Tethered Uni-Rotor Network

Design, Modeling, Control, and Simulation for a Novel Eternal Flight System

---

A Dissertation

Presented to

the faculty of the School of Engineering and Applied Science

UNIVERSITY OF VIRGINIA

---

in partial fulfillment

of the requirements for the degree

DOCTOR OF PHILOSOPHY

by

JUSTIN MICHAEL SELFRIDGE

May 2017

Approval Sheet

This Dissertation
is submitted in partial fulfillment of the requirements
for the degree of

DOCTOR OF PHILOSOPHY

Author Signature: 

This Dissertation has been read and approved by the examining committee:

Advisor:	Gang Tao
Committee Member:	Zongli Lin
Committee Member:	Harry Powell
Committee Member:	Farzad Hassanzadeh
Committee Member:	Haibo Dong

Accepted for the School of Engineering and Applied Science:

Craig H. Benson, School of Engineering and Applied Science

May 2017

Dedicated to my affectionate parents, my loving wife Calla, and my beautiful daughter Natalie.

Abstract

This research presents a new concept vehicle called the Tethered Uni-Rotor Network (TURN). The system is intended to attain eternal flight, by collecting enough solar power during the day to stay aloft through the night. This capability enables atmospheric satellites, which offer the same services as existing satellites, but permits increased capabilities from their close proximity and low signal latency. There is a great commercial interest in achieving this goal, and several research groups are striving for this aviation milestone, but existing designs encounter severe limitations. This document introduces a novel concept vehicle which captures the best features of both rotorcraft and glider design methodologies, while reducing their respective limitations. The vehicle is a tethered system, with complex nonlinear dynamics, interactions between multiple rigid bodies, and requires a unique perspective to implement the controller architecture. First, the plant dynamics are established, which models the entire nonlinear system, formulates the dynamics acting on each subcomponent, establishes a multibody dynamic structure within a matrix framework, and develops novel trimming and linearization processes applicable to such a multibody system. Then, the control system is derived, which presents the overall control methodology, and develops an LDS based model reference adaptive control (MRAC) architecture, which is implemented on three distinct control loops. An extensive simulation study outlines the vehicle sizing and parameters, reviews the disturbance rejection capabilities, formulates multisine signal injection for system identification, investigates parameter convergence within the LDS based MRAC system, evaluates reference tracking for an output feedback embodiment, and discusses inertial translation by coordinating maneuvers among several of the rigid body components. This initial effort is part of a larger spiral development process, so a future testing plan is laid out for a series of prototype vehicles. The outcome of this research will show that the TURN approach is a feasible concept design, capable of being adequately controlled, while offering greatly increased aerodynamic efficiency. It has immediate commercialization potential at a smaller scale, can alleviate design issues inherent in airborne wind energy platforms, and may be the answer to achieving eternal flight.

Acknowledgements

I would like to acknowledge and extend my gratitude, to the several groups and individuals who have helped bring this research project to fruition.

To the University of Virginia, for accepting me into their doctoral program. This has allowed me to learn, explore, research, and disseminate knowledge, while working on this dissertation.

To my three mentors and program sponsors at NASA Langley: Sheri Hoadley, Mark Moore, and Carey Buttrill. Without your continuous support through internships and independent contracting projects, I would not have had the financial means to dedicate my time to this endeavor.

To the colleagues and cohorts that I have worked beside at NASA Langley for the past six years. Always willing to entertain and evaluate new and unconventional ideas, and offer insights from unique and differing perspectives.

To my good friend Jim Wolfe, who has been a great sounding board during the most stressful times, and who has a knack for reducing insurmountable problems down trivial and manageable tasks.

To my loving wife, Calla Selfridge, who has endured through the odd hours and pressing deadlines. Who gave me the space and time I needed to see this research through to completion; without which, the quality would have most certainly suffered.

Finally, and most notably, to my faculty advisor, Gang Tao. Whose insight and advice has guided my development process throughout this journey; but also permitted enough latitude for me to forge my own path. Prescribing seemingly impossibly high standards, always pushed me to put forth the best possible effort with the highest quality results.

Contents

List of Figures

List of Tables

List of Acronyms

AOA	Angle of Attack
AR	Aspect Ratio
At-Sat	Atmospheric Satellite
AWE	Airborne Wind Energy
CFD	Computational Fluid Dynamics
CG	Center of Gravity
DARPA	Defense Advanced Research Projects Agency
EOM	Equations of Motion
FEA	Finite Element Analysis
FSO	Free-Space Optical
GEO	Geosynchronous
HALE	High-Altitude Long-Endurance
HFG	High-Frequency Gain
HOT	Higher Order Terms
HPA	Human Powered Aircraft
HPF	High-Pass Filter
HTA	Heavier-Than-Air
L/D	Lift-to-Drag ratio
LEO	Low Earth Orbit
LHP	Left Half Plane
LPF	Low-Pass Filter
LTA	Lighter-Than-Air
LTI	Linear Time-Invariant
MIMO	Multiple-Input Multiple-Output
MRAC	Model Reference Adaptive Control
OHS	Outboard Horizontal Stabilizer
RGA	Relative Gain Array
RHP	Right Half Plane
SISO	Single-Input Single-Output
T/C	Thickness-to-Chord ratio
TURN	Tethered Uni-Rotor Network
UAV	Unmanned Aerial Vehicle
VTOL	Vertical Takeoff and Landing

Physical Constants

Environmental Properties	
acceleration due to gravity	$g = 9.807\,\mathrm{m\,s^{-2}}$
density of air at sea level	$\rho = 1.225\,\mathrm{kg\,m^{-3}}$
Hub Simulation Properties	
weight	$w_H = 19.6\,\mathrm{N\ (kg\,m\,s^{-2})}$
mass	$m_H = 2.0\,\mathrm{kg}$
radius	$r_H = 0.5\,\mathrm{m}$
Tether Simulation Properties	
length	$l_T = 12.0\,\mathrm{m}$
diameter	$d_T = 4.0 \times 10^{-4}\,\mathrm{m}$
density	$\rho_T = 1000\,\mathrm{kg\,m^{-3}}$
weight	$w_T = 0.0148\,\mathrm{N\ (kg\,m\,s^{-2})}$
mass	$m_T = 0.0015\,\mathrm{kg}$
drag coefficient	$c_{dT} = 1.0$
Satellite Simulation Properties	
weight	$w_S = 31.1\,\mathrm{N\ (kg\,m\,s^{-2})}$
mass	$m_S = 3.18\,\mathrm{kg}$
moment inertia (x)	$J_{xS} = 2.81\,\mathrm{kg\,m^2}$
moment inertia (y)	$J_{yS} = 0.11\,\mathrm{kg\,m^2}$
moment inertia (z)	$J_{zS} = 2.72\,\mathrm{kg\,m^2}$
wingspan	$b_S = 3.5\,\mathrm{m}$
chord length	$c_S = 0.2\,\mathrm{m}$
motor thrust	$F_S = 0.47\,\mathrm{N\ (kg\,m\,s^{-2})}$
wing lift coefficient	$c_{lS} = 0.60$
wing drag coefficient	$c_{dS} = 0.01$
aspect ratio	$AR = 17.5$
lift-to-drag ratio	$L/D = 33.15$

List of Symbols

State Space Parameters

n	number of system states
m	number of control inputs
x	system state vector
u	control input vector
y	measured output vector
z	numerator polynomial (zeros)
p	denominator polynomial (poles)
d	desired response polynomial
A	state matrix
B	input matrix
C	output matrix
D	feedforward matrix
G	open-loop transfer matrix
W	closed-loop transfer matrix
Z	numerator transfer matrix (zeros)
P	denominator transfer matrix (poles)

State Designations

ϕ	roll	rad
θ	pitch	rad
ψ	yaw	rad
x	forward	m
y	right	m
z	downward	m
ω	angular rate	$\mathrm{rad\,s^{-1}}$
v	linear velocity	$\mathrm{m\,s^{-1}}$
α	angle of attack	rad
δ	relative position	m

Geometric Parameters

r	position vector	m
A	area	$\mathrm{m^2}$
C	centroid location	m

Physical Parameters

g	gravity	$\mathrm{m\,s^{-2}}$
ρ	density	$\mathrm{kg\,m^{-3}}$
m	mass	kg
J	moment of inertia	$\mathrm{kg\,m^2}$
F	force	N
M	moment	N m
τ_w	wall shear stress	Pa

Common Matrices

I	identity matrix
R	rotation matrix

Trigonometric Functions

s_*	sine function
c_*	cosine function
t_*	tangent function

Mathematical Symbols

Δ	difference or change
$\mathbb{R}$	set of real numbers
∂	partial derivative

Notation

Frame Designations

`A,B,C,D`	tether indexing
F	fuselage frame
H	hub frame
M	motor frame
N	inertial frame
P	propeller frame
S	satellite frame
T	tether frame

Model Designations

`lin`	linearized model
`sat`	satellite stabilization model
`tet`	tether arm inner-loop model
`hub`	central hub outer-loop model

Subscripts

c	centrifugal component
d	drag component
g	gravity component
i	inboard component
l	lift component
o	outboard component

Operators

`det`	determinant operator
`diag`	diagonal operator
`rank`	rank operator
`sgn`	sign operator
`tr`	trace operator
`Re`	real part of a complex number
`Im`	imaginary part of a complex number
`min`	minimum operator
`max`	maximum operator

Chapter 1

Introduction

Flight has always captured man's imagination, which is evidenced by the great variety of aerial vehicles that exist today. Everything from fixed-wing to rotorcraft; satellites to spaceships; mono-wing to quadrotor. However, despite the wide variety of flying vehicles, not one of them has attained eternal flight. Accomplishing this feat is one of the great challenges still facing the aviation community.

Chapter Motivation

Achieving eternal flight opens the doors to atmospheric satellites. These are a new breed of unmanned aircraft that attempt to collect enough solar power during the day to stay aloft throughout the night. Existing satellites have a great number of capabilities that enrich our lives; however, their distance from the surface of the earth precludes certain types of transmission capabilities. Once eternal flight is achieved, that vehicle can serve the same role as ordinary satellites, but its close proximity will allow for real-time two-way communications, like wireless broadband internet. And with active controls, an atmospheric satellite would not be constrained to geosynchronous orbits, like our existing satellite technology.

Chapter Objectives

Many projects are under way to achieve this goal, but most of these research efforts follow the same design methodology; each attempting to make a conventional tube-and-wing airframe that is lighter, more aerodynamic, and with higher aspect ratio wings. Unfortunately, this approach is limited by material, solar cell, and battery technology, and has exhausted the limits of improvement. This concept introduces a completely new aerial vehicle structure, which uses the best features of fixed-wing and rotorcraft designs. Combining the best features of different classes of aircraft, expands the capabilities beyond what either one can achieve on its own.

Chapter Outline

Before discussing the particulars of the dynamic model, controller design, and simulation results, for this new class of unmanned aircraft, a top-level overview of the system and its benefits are reviewed. This chapter motivates the need for an eternal flight vehicle, introduces the radical new concept aircraft, lists the most notable alternative embodiments, and outlines the remainder of the presented research.

Section 1.1 describes the *Motivation for Eternal Flight*, which discusses the impact this new aircraft could have on the aviation community. It reviews existing and future satellite demand, and summarizes different classes of satellites currently in use. It illustrates the desired commercial interest, current research efforts, and limitations with existing designs.

Section 1.2 presents the *Radical New Concept Vehicle*, which introduces the Tethered Uni-Rotor Network (TURN) system. It describes the attributes of fixed-wing glider and helicopter designs, summarizes how the TURN methodology utilizes the best features of both, lists the benefits that arise from this vehicle configuration, and summarize the pertinent control objectives.

Section 1.3 showcases *Alternative Embodiments* for this type of aircraft, which further motivates the research effort. It presents various TURN vehicle sizes, illustrates one which can compete with existing drones, and describes notable benefits when applied to airborne wind energy platforms.

Section 1.4 lists the remaining topics within a *Research Outline*, which serves as a road map guiding the remainder of the research presentation. It overviews the sections for the dynamic system model, controller development, simulations results, an outline of future work, and final conclusions.

1.1 Motivation for Eternal Flight

Satellites are an amazing feat of engineering. Various classes of satellites have offered a wide range of capabilities, each of which have provided dramatic improvements to our quality of life. Yet, our society is beginning to demand an increase in functionality, beyond what these systems can offer. An eternal flight vehicle offers the promise of satiating this demand, so a great deal of commercial and government interest has been focused on such systems. Despite new research efforts, no existing platform has fully achieved eternal flight. Several methodologies are being used within eternal flight programs, but there are serious limitations with existing approaches, so a new concept is required. This research presents a novel alternative approach, which exceeds existing capabilities, outpaces current research efforts, and may be the answer to attain eternal flight.

1.1.1 Existing and Future Satellite Demand

Satellites have had a profound impact on our society and have drastically improved our quality of life by enabling technology that could not have been accomplished any other way. In 1957, the first satellite system was launched into orbit. Within 15 years time, standardized designs produced

highly capable platforms which delivered essential services. Since then, satellites have connected the world through telecommunications, delivered precise locations with geopositional navigation, and enabled imaging and sensor systems to significantly increase our understanding of our planet as well as the entire universe. Even though satellites are the most expensive aerospace products on a dollar per pound basis, their unique capability provides an unrivaled benefit.

Despite all their advances over the years, there is still a need for even greater capabilities while delivered at a lower cost. Society has developed an increased appetite for omnipresent communications, surveillance capabilities, and instant access to information. More recently, the expectation is for these services to be achievable in real-time as on-demand services. These new capabilities are not well met by existing satellites, and will require a new solution with several orders of magnitude lower signal latency, greater operational flexibility, and dramatically lower costs.

1.1.2 Classes of Satellites

Various types of satellites are currently in practice, each having its own strengths and weaknesses. Several well known satellite systems are depicted in Figure 1.1 for reference. Geosynchronous satellites offer a continuous coverage capability with a single satellite. Low Earth Orbit satellites

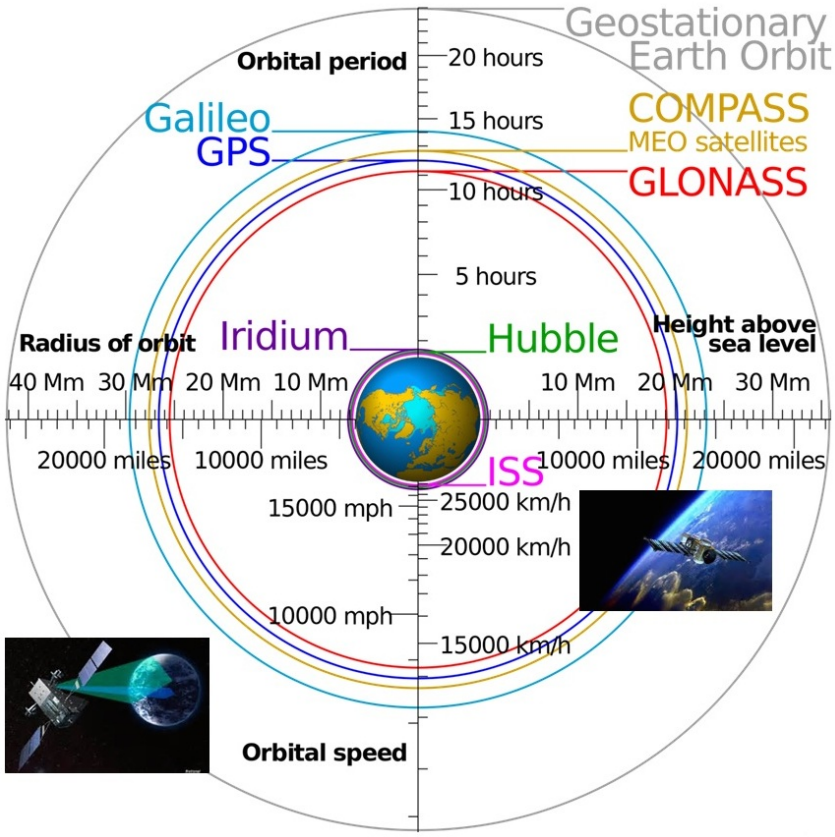

FIGURE 1.1: Illustration of various satellite systems and their attributes.

Satellite Type	**GEO**	**LEO**	**AT-Sat**
Product	XM Ecostar	Motorola Iridium	Global Observer
Distance above Earth (mi)	22,230	500	10
Coverage Diameter (mi)	7926	2300	500
Fleet Required	1	50-60	1
Satellite Cost	$300M	$50M x50	< $20M
Launch & Insurance Cost	$100M	$25M x50	< $1M
Ideal Signal Delay	> 250	5-40	0.1

TABLE 1.1: Comparison between GEO, LEO, and AT-Sat systems.

are fifty times closer for improved single latency, power requirements, and imaging resolution; but require a fleet to be operational. Atmospheric satellites are another fifty times closer for even better latency, power, and resolution; and are reusable with extremely low capital costs. The summary in Table 1.1 provides a comparison between the different varieties of satellites.

Geosynchronous Satellites

Geosynchronous (GEO) satellites remain over a fixed location above the earth and provide continuous surveillance or communication. Because they are the farthest distance from Earth, they provide the largest coverage area, but also suffer from long transmission delay, called signal latency. Because of this delay, real-time two-way communications with GEO satellites is impractical; however, they are very effective with one-way communications across a large and constant coverage area. Power loss of a signal is inversely proportional to the transmission distance, so these satellites require considerably more power because of their extreme distances. With such a broad coverage area, frequency reuse is extremely limited. Coverage at high latitude locations is challenging due to very low looking angles from the satellites, which increases signal obstruction and losses from building, trees and mountains.

Low Earth Orbit Satellites

Low Earth Orbit (LEO) satellites are about fifty times closer to Earth, which lowers their signal latency, but also decreases their coverage area. Because, LEO satellites require a constant orbit, they are unable to maintain a fixed reference location above the earth. Therefore, a large fleet of LEO satellites is needed to maintain continuous coverage over any specific location. This leads to very high capital costs associated with both manufacturing the fleet and the cost to launch and insure all of the satellites. Although their proximity reduces signal latency, it is still extremely difficult to achieve two-way digital data transmission, and they are unable to attain broadband speeds.

Atmospheric Satellites

Atmospheric satellites (AT-Sats) are a new breed of aircraft designed to operate at altitudes around 60,000 feet. This altitude offers air density and winds aloft which require the lowest power consumption while minimizing weather concerns. Even with a single vehicle, AT-Sats can offer continuous coverage because they operate over relatively fixed locations. Their proximity to Earth is another fifty times closer than LEO satellites, so their signal latency is extremely low, which greatly reduces the required transmission power, and allows the entire payload to shrink in size. Lower altitudes also lead to a reduced coverage area; about the size of a single urban area with the most direct lines of communication, or the size of several states for the full coverage area. Cost of deployment and recovery is very low because the aircraft is able to takeoff and land. Thus, it is expected that the total system cost for AT-Sats are several orders of magnitude less than other satellite solutions, with the added benefit of upgrading and refurbishing satellite payloads as equipment ages. At this time, existing high-altitude long-endurance (HALE) aircraft can only maintain flight for several weeks at a time, and lack the highly reliable and persistent capabilities that satellites offer.

1.1.3 Commercial Interest

Existing satellites have a great number of capabilities that enrich our lives; however, their distance from the surface of the earth precludes certain types of surveillance and transmission capabilities. Once eternal flight is achieved, that vehicle can serve the same role as ordinary satellites, but its close proximity will allow for real time two-way communications, such as wireless broadband internet. Furthermore, unlike our existing satellite technology, atmospheric satellites are equipped with active controls and are not constrained to geosynchronous orbits. Finally, an ability to takeoff and land allows for more scheduled routine maintenance and more frequent system payload upgrades, while reducing the cost to launch and insure the satellite. This desired capability has attracted giant technology firms. In the past two years, both Google and Facebook have entered into AT-Sat development, each purchasing aerospace companies focused on aircraft for this mission.

In March 2014, Facebook offered $60 million to purchase Titan Aerospace, and ended up buying Ascenta for $20 million; reported by (Pepitone, 2014, Mar 4) and (Garside, 2014, Mar 28). Zuckerberg stated, "In our effort to connect the whole world with *Internet.org*, we've been working on ways to beam internet to people from the sky,". Ascenta is a spin-off of the QinetiQ Zephyr aircraft, and the intent is to use free-space optical (FSO) communication technology, which transmits large amounts of information at high speeds across space using invisible infrared laser beams.

A month later, Google purchased Titan Aerospace; reported by (Etherington, 2014, Apr 14) and (Barr and Albergotti, 2014, Apr 14). The company focuses on collecting real-time, high-resolution images of the earth, but its platforms can also carry atmospheric sensors and support voice and data services. This type of technology would be instrumental to Google activities, such as its mapping division. "It is still early days, but atmospheric satellites could help bring Internet access to millions of people, and help solve other problems, including disaster relief and environmental damage like deforestation," claimed a Google spokesman in a public announcement.

FIGURE 1.2: Current research efforts attempting to develop AT-Sat capabilities.

1.1.4 Current Research Efforts

Several commercial and government research groups are attempting to design feasible AT-Sat vehicles which can attain eternal flight, documented in (Eshel, 2013, Aug 13). The problem reduces down to an energy balance relationship, where solar energy collected during the day must be sufficient to sustain the system throughout the night. Some approaches are investigating balloon and airship embodiments, but lightweight tube-and-wing structures dominate the majority of current design paths. Many of the current research efforts are depicted in Figure 1.2.

Google X Project Loon

Google X set out on a mission to deliver 4G-LTE internet speeds, which are accessible to remote areas across the planet (Lardinois, 2017, Feb 16). Project Loon utilizes a large network of balloons within the stratosphere which drift with prevailing winds. Changing the buoyancy, thus adjusting the altitude, offers limited directional control by placing the balloons in regions with different wind speeds and directivity. Trajectories start at the most southern latitudes and eventually spiral their way to the equator with prevailing winds. As a one-way operation, the balloons are active for 50 to 100 days before requiring descent and payload pickup. In June of 2013, Google X began their pilot program and initiated test flights originating from New Zealand. Clearly these investments showcase the interest that exists in developing platforms as an alternative to conventional satellites.

DARPA Projects

Over the past decade, DARPA has investigated several concepts through research efforts including the ISIS and Vulture programs (Fletcher, 2008, Mar 6). The objective of both approaches was to stay aloft for years at a time, utilizing advanced solar cells as a renewable energy source. ISIS was a Lighter-Than-Air (LTA) concept which utilized enormous hydrogen/helium filled vehicles. This approach achieves a difference in buoyancy between the internal volume and the density of the atmosphere. However, operating at high altitudes with very low air densities, required extremely large volumes of gas with equally large surface areas to contain it. Vulture researched fixed-wing concepts utilizing ultra-lightweight structure techniques. The aircraft had very low wing loading which provided substantial surface areas for solar cells, and minimized both the cruise velocity and required power, but the structure was extremely delicate with Mylar wing surfaces. Each of these DARPA programs exceeded $150 million, and intended to achieve a large-scale flight demonstrator.

Commercial Efforts

Several aerospace companies have been developing their own solutions. Lockheed placed a bottom strut across the fuselage elements to achieve greater effective wing spar depth. However, without trussing between the fuselage elements this approach does not provide significant improvement, and wire crisscrossing trusses between each fuselage element at flight speeds would dramatically increase drag. Aurora utilized a combination Z-wing arrangement. Each wing element docks together during flight with a hinge element that does not transmit bending moments, allowing each wing element to fly at inclination angles better suited to capture the solar flux for energy storage. Boeing utilized an Outboard Horizontal Surface (OHS) to minimize the induced drag and augment the pitch trimming capability. Only Boeing was selected for the Phase II DARPA Vulture program. However, after detailed studies, this concept showed questionable feasibility and was descoped into a focused effort to advance the energy storage and capture technologies.

QinetiQ Zephyr

In 2010, the QinetiQ Zephyr 7 aircraft set the world record for high-altitude long-endurance flight, which remained airborne over New Mexico for a two week midsummer period, announced by (Ridden, 2010, Dec 29). And unofficial attempts, not verified by the FAI, have claimed flight durations approaching three weeks. The Zephyr has a tube-and-wing structure design, weighs 110 pounds, and carries a payload of less than five pounds. With a 74 foot wingspan, it reduced the wing loading to less than one pound per square foot. While the Zephyr achieved an altitude of 70,741 feet, it was not able to maintain that height during night operation. Energy collected from solar cells during daylight operation, was not quite sufficient to meet the energy requirements for night operation. Essentially, the aircraft relied on its altitude as potential energy, while power was being consumed from the batteries. The Zephyr is highly reflective of all the other aircraft concept approaches currently pursued and provides many indicators relating to future concept feasibility.

1.1.5 Limitations with Existing Approaches

Clearly, the interest in developing AT-Sat vehicles is gaining a great deal of momentum. With the exception of the Google X Project Loon and the DARPA ISIS concept, nearly all design methodologies focus on extremely lightweight materials applied to a conventional tube-and-wing structure. Several variants of wing-tail configurations have been devised, but each concept maintains a similar structural approach, which places as much weight as possible across the span to decrease bending moments on the wing root. Now consider the shortcomings of the most prominent designs.

Project Loon is severely limited because with an uncontrolled flight, the balloons can drift aimlessly over different countries, thus it is only being tested in the southern hemisphere. Besides, each balloon must be collected and redeployed after a period of several weeks, so this is not a true eternal flight solution. Airships, like DARPA ISIS, would be an ideal solution if winds aloft could be ignored. Unfortunately, the vehicles have such high drag that during a majority of the yearly seasons, and at a majority of latitudes, the power requirements to overcome even modest winds exceed a feasible solution. Meanwhile, DARPA Vulture had a relatively small payload, was extremely sensitive to winds, and had huge wing root bending moments absorbed through its thin wings. Both DARPA programs, ISIS and Vulture, were canceled due to a lack of feasibility while closing the day-night energy balance required for staying aloft without excessive altitude loss.

Zephyr used the most advanced lithium-sulfur batteries, with more than twice the specific energy of any other lithium rechargeable batteries at that time. This extremely light battery system enabled the vehicle to claim a world record, but it was also the limiting factor preventing longer flights. With lithium-sulfur chemistry, the specific energy seriously degrades within twenty recharge cycles, so it is no wonder why the system could not maintain flight for more than three weeks. Also, lithium-sulfur batteries can only provide very low power discharges rates, so during night operation, the Zephyr batteries were not able to provide enough power to maintain a constant altitude.

To successfully compete with existing satellite technology, an operational AT-Sat product must demonstrate a minimum level of proficiency. It must be capable of controlled flight, remain airborne indefinitely throughout the year, and only need to land for routine maintenance. It needs a sufficiently large margin of error to operate at high latitudes, overcome seasonal wind, and accommodate solar flux variations. It cannot utilize altitude energy storing, because weather effects would hamper the station-keeping ability, and line of sight communication is reduced at lower altitudes. For these reasons, a new concept approach is needed to tackle the eternal flight problem.

1.2 Radical New Concept Vehicle

Current design methodology for HALE aircraft aims to expand the capabilities of what tube-and-wing concepts can achieve, but has reached the limits of what structural materials can accomplish. Unfortunately, current energy collection and storage technology is insufficient to attain eternal flight with this approach. The question this study asks is whether a new form of vehicle is possible, and proposes a unique advanced concept design which has never been previously explored.

The objective of the vehicle design is to reduce structural mass, maintain a robust structural configuration, and simultaneously increase the lift-to-drag ratio. A tensegrity approach minimizes compression load paths by putting as much of the structural load into tensile load paths, where advanced carbon composites provide incredible strength to weight. The concept combines the best features of both high efficiency glider and helicopter designs, reduces the deficiencies within each class of aircraft, and yields better attributes than either can provide on their own. This new approach dramatically lowers structural weight, greatly reduces drag, and provides a far more robust structure in weather than existing structures.

1.2.1 Glider Versus Helicopter

In the next few sections, a novel unmanned aerial vehicle (UAV) will be presented. This unique system combines the best features of both gliders and helicopters while minimizing each of their respective deficiencies. Before introducing the concept vehicle, pros and cons of both gliders and helicopters will be considered, which will better illustrate the benefits of this radical new design.

Glider Attributes

Gliders (or sailplanes) are some of the most aerodynamically efficient vehicles, because they strive to minimize the amount of drag acting on the system. One of the primary methods available to engineers to accomplish this, is by using long slender wings, thereby increasing the aspect ratio, which is the ratio between the wingspan and the chord length. Figure 1.3 showcases such an aircraft. Although high aspect ratio wings are desirable from an aerodynamic drag perspective, there are limitations with this approach. Making the wing more slender introduces flexibility, which can experience bend and twist during flight. Furthermore, longer wings are subjected to greater bending moments at the wing root, which is the attachment point between the fuselage and wing.

FIGURE 1.3: Glider with high aspect ratio wings.

FIGURE 1.4: Helicopter with sagging rotors.

Additional structural material is needed to reinforce this connection point in order to counteract this large moment. And gliders, like all fixed-wing aircraft, need forward velocity to generate airflow over the airfoil which produces lift. Thus, these systems cannot hover or takeoff vertically.

Helicopter Attributes

Unlike fixed-wing aircraft, helicopters have desirable vertical takeoff and landing (VTOL) and hovering capabilities. Consider a helicopter at rest on a tarmac, as presented in Figure 1.4. The rotor blades are generally so thin, that they bend and deflect under their own weight. Yet, these flimsy structures are capable of lifting a substantially heavy vehicle once they are spinning, because centrifugal forces provide stiffening throughout the rotor element. Unfortunately, helicopter rotors are not aerodynamically efficient. They suffer from triangular span loading, meaning outboard sections are primarily responsible for producing lift, while the inboard sections are quite ineffectual. Furthermore, the rotor mechanism is extremely complex and must withstand forces that are thousands of times greater than the force from acceleration due to gravity.

Best of Both Worlds

This research introduces a completely new aerial vehicle concept, incorporating features from both glider and helicopter methodologies. Gliders utilize extremely efficient wings, but must also mitigate flexibility and large bending moments between the wing and the fuselage. Helicopters have centrifugal stiffening which support large payloads on flimsy rotors, but suffer from inefficient triangular span loading from a decreasing velocity distribution across the rotor. This research explores a new concept that combines the best attributes of both types of aircraft, while minimizing the deficiencies of each. The overall approach aims to use centrifugal stiffening to mitigate flexibility and bending moments commonly found in gliders, while replacing inefficient helicopter rotors with extremely aerodynamic high aspect ratio airfoils.

1.2.2 Introducing the Tethered Uni-Rotor Network

Without further ado, lets unveil this revolutionary new concept vehicle. This research introduces a novel UAV a called the Tethered Uni-Rotor Network (TURN), illustrated in Figure 1.5. The system utilizes a unique alternative approach, which exceeds existing capabilities, outpaces current research efforts, and may be the answer to attain eternal flight.

Vehicle Layout

The TURN system has a central hub which stores the vehicle payload. Several high tensile, small diameter cable tethers radiate outwards from the central hub. At the end of each tether, a satellite body is attached at the outboard position. Each satellite contains all the components typically found on an aircraft system, including: an airfoil lifting section, small propellers delivering propulsion,

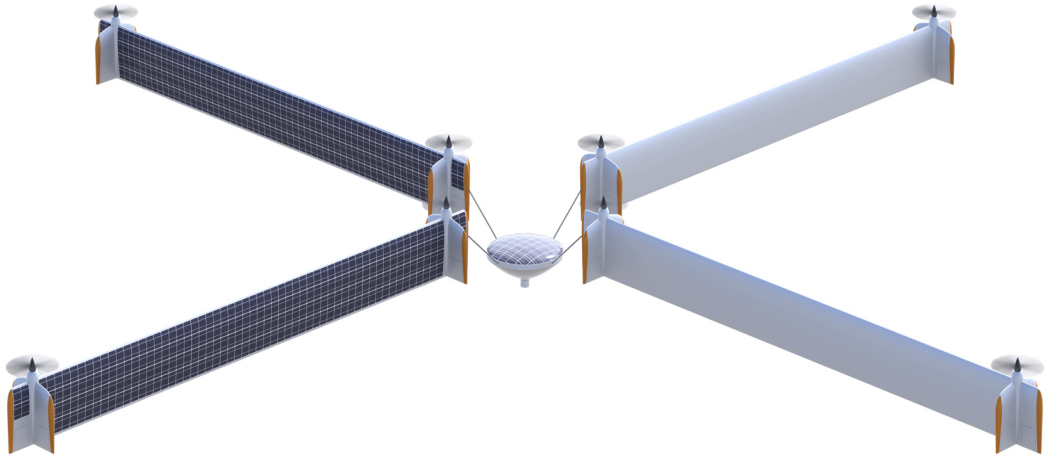

FIGURE 1.5: Introducing the Tethered Uni-Rotor Network (TURN) system; depicted in VTOL flight.

several stabilizers and control surfaces, and a fuselage containing batteries, hardware, and sensors. Each satellite resembles a flying-wing system, which provides all the lift, propulsion and control for the TURN system. Two propellers, mounted on the leading edge of the wing, are located near each of the wingtips. Immediately behind the props, vertical stabilizers and control surfaces are located directly in the prop wash. The concept was named *Tethered Uni-Rotor Network* because a network of aircraft systems are tethered together to form a much larger singular rotor system.

Hover Operation

During flight, the vehicle operates in a perpetual state of rotation. Each of the satellite bodies drive the rotation of the system with their respective propulsion systems, which have an optimum twist and pitch designed for the rotation rate. This propulsion technique is opposite that of a conventional helicopter rotor, where a torque is applied to the central shaft, which requires a counter-torque to prevent the helicopter body from spinning in the reverse direction. Since this is a tip driven system, there is no torque transmitted back to the central hub. Because the system is spinning, centrifugal forces keep the tethers taught and mitigate bending moments commonly present within thin wing sections. As the satellite bodies move through the air, lift is generated on each of the winged airfoil sections, which is enough to counteract the weight of the satellite, and a distributed portion of the weight of the central hub. Having described the hover equilibrium operation, the next paragraph describes how the system is dynamically controlled.

Flight Operation

Individual satellites are controlled through their propeller and control surfaces, and the central hub is controlled by coordinating the tether forces imparted from the satellite vehicles. Two types of translation are considered, vertical and horizontal, which have a parallel in helicopter terminology as "collective" and "cyclic" commands. Each type of translation has two associated control modes which can be implemented through different control inputs.

Vertical translation uses "collective" commands where each satellite adjusts its settings in unison. Adjusting throttle increases or decreases the velocity of the satellite, and thus the angular rate of the TURN system. This changes the amount of airflow over the wing, which increases or decreases the total amount of lift generated, and causes the vehicle to ascend or descend. Alternatively, adjusting the pitch of each satellite through the elevator control surface, causes each satellite to nose up or down, thus the entire system will climb or fall as each satellite moves through a spiral trajectory.

Horizontal translation is achieved with "cyclic" commands, where the control inputs are changed in a sinusoidal fashion throughout the rotation. The first cyclic command is applied to the rudder control surface, which manipulates the amount of tension on the tether. At one point in the rotation there is maximum pull from the tension, and exactly opposite that point there is a minimum tension force. This imbalance causes the TURN system to translate horizontally. Another approach uses cyclic elevator commands to achieve horizontal translation. At one point in the rotation a satellite passes a low elevation, and at the exact opposite point the satellite traverses a high elevation. This essentially tilts the plane of rotation, which inclines the thrust vector coming from the airfoils, and yields a horizontal force component. This type of thrust vectoring is identical to how traditional multirotors translate horizontally.

Takeoff and Landing Operation

One of the most common questions after describing the TURN system is, "How does the vehicle takeoff and land?" Since the tethers makeup approximately 80% of the inboard section, it is only practical to have them fully extended during normal flight operations. During takeoff, the tethers are nearly completely retracted, and the satellite bodies are oriented upward in a tail-sitter configuration; where this flight mode is depicted within Figure 1.5. Each satellite has enough control inputs to manipulate its own independent VTOL operation, so they all takeoff in unison, moving vertically with no system rotation, and carry the central hub along with them. Once an operational altitude is reached, the satellites traverse outward as the tethers are extended. Then, each satellite slowly pitches forward to initiate the rotation process. Originally, the system weight was completely supported by thrust from the propellers, but throughout the transition process, the wing sections begin to carry more of the load. Once the transition is complete, the satellites are in their forward-flight orientation, the wings provide all the lift needed for the system, and the propulsion system simply provides enough thrust to overcome aerodynamic drag. Landing the aircraft follows a procedure exactly opposite that of takeoff.

Design Considerations

Several system design variations were considered while devising the TURN vehicle. Some alternatives offer clear benefits, while others represent an engineering tradeoff.

The number of tether arms is somewhat flexible. A single arm is not feasible because there is no means of counter-balancing the rotating system. Two arms can balance one another, but the central hub is free to swing like a hammock, so this should only be employed as a last resort to recover a vehicle in the event the other arms become disabled. Three arms are the minimum number needed to completely stabilize the central hub while offering the greatest benefit from centrifugal stiffening; however, cyclic control is slightly more difficult because the arms are not directly opposing each other. With four tether arms, as with any even number, cyclic control is simplified because opposite pairs of tether arms directly balance each other out through the central hub. Any number of tether arms greater than three is possible, and can offer redundancy in the event of a local failure; however, distributing the system mass across more arms decreases the amount of beneficial centrifugal stiffening working on each satellite. For this analysis, four tether arms were selected to simplify the controls development, while investigating three arms will be reserved for future work.

The number of propulsion systems is highly subjective, where each offers unique advantages and disadvantages. Earliest designs considered a single prop located at the outermost wingtip of the satellite. With a minimum number of motor systems, it was originally believed to be the simplest embodiment. However, with only a single motor system, each satellite lacks independent VTOL capabilities. Without a VTOL transition process, the tether retracting mechanism must be powerful enough to overcome centrifugal forces while pulling the tether in. Thus, the vehicle would incur a cost from carrying an oversized mechanism used only briefly during landing. This research considers a vehicle design with two motors, because that is the smallest number of systems that still offers VTOL capabilities. Using more motors can increase weight and system complexity, but may also offer some notable benefits. Four motors placed in a rectangular arrangement would eliminate the need for stabilizers and control surfaces, because the satellite could use a quadrotor control methodology. Alternatively, placing a multitude of prop systems across the leading edge of the airfoil has aerodynamic benefits, because forced air over the wing helps maintain laminar flow.

Stabilizer and control surface placement is intimately related with the layout and number of motor systems. As previously mentioned, when using four motors, stabilizers and control surfaces can be eliminated entirely, because a quadrotor controls approach does not require them. Adjusting motor angular rates is a powerful technique, but it is it not energy efficient in comparison to control surfaces. Similarly, thrust vectoring, which directly adjusts the orientation of the motors, can reduce the number of aerodynamic surfaces; but altering the plane of a spinning prop is another energy expensive maneuver. The model considered in this research has vertical stabilizers located behind the props, with several control surfaces that mirror the functionality of an elevator and rudder. This configuration simplifies the controls implementation because forces and moments are aligned with primary axes, so system inputs are more closely matched with system outputs. Angled stabilizers that eliminate a small drag surface would offer a slight aerodynamic advantage, but a "ruddevator" has significant cross-coupling between inputs and outputs, and is reserved for future research.

1.2.3 System Benefits

Many unique benefits arise from the TURN system. It has the same advantageous centrifugal stiffening as a traditional helicopter rotor, except thin tether filaments replace wasted material that have detrimental aerodynamic properties. Because the outboard section is free to pivot about the tether connection point, there is no adverse bending moment typically found at the wing root with fixed-wing gliders. This permits a much higher aspect ratio, an increased lift-to-drag ratio, and lower thickness-to-chord ratio, than can be attained by a traditional tube-and-wing style aircraft. Consider some of the system benefits in more detail.

High Aspect Ratios

It is well understood that higher aspect ratio wings improve aerodynamic efficiency, but the fraction of wing weight to vehicle weight is another closely related performance indicator. Typical aircraft wings are commonly 10-20% of the gross aircraft weight. Due to aeroelastic and structural constraints the majority of these aircraft rarely exceed aspect ratios of ten. The current paradigm for HALE aircraft research, is to increase the aspect ratio of a tube-and-wing design, and then push the envelope of what exotic new materials are capable of. While targeting aspect ratios of 20-25, they all experience similar wing weight fractions around 40-50% of the total aircraft, which is indicative that the wing receives extra material to reinforce the flimsy structure. Conversely, most rotorcraft blades, which generate all the lift for a helicopter, have aspect ratios of 40-50 and typically only represent 2-3% of the gross helicopter weight. Clearly, applying centrifugal stiffening to thin structures is a highly effective method for attaining significantly greater aspect ratios while reducing the weight of the lifting surface. The TURN system does not rely on large wing chords to provide a thick structural spar depth, rather it utilizes a tensegrity structural approach which permits high aspect ratios within very thin and lightweight airfoil structures.

Centrifugal Stiffening

High aspect ratio wings are especially susceptible to bending moments created by opposing lift and weight forces. Mitigating bending moments through centrifugal stiffening is one of the most desirable attributes of the TURN system methodology. Because centrifugal forces are acting on the wing sections, very little material is needed within the spar to counteract the bending moment. This structural stiffening permits very thin wing airfoils and dramatically increased aspect ratios, which achieves increased laminar flow with extremely low levels of induced and parasitic drag. The NASA/AeroVironment Helios, shown in Figure 1.6, is an example of a HALE aircraft experiencing very high bending moments across a large wing span. The Helios failed during a test flight because the wing fluttered from a lack of structural stiffness, documented in (Noll et al., 2004, Jan).

Higher centrifugal forces can be attained by increasing the rotational velocity of the system, but this is not desirable because it increases the power requirements. Centrifugal forces can also be achieved at lower tip speeds by having a large mass at the outer most portion of the rotor. Thus,

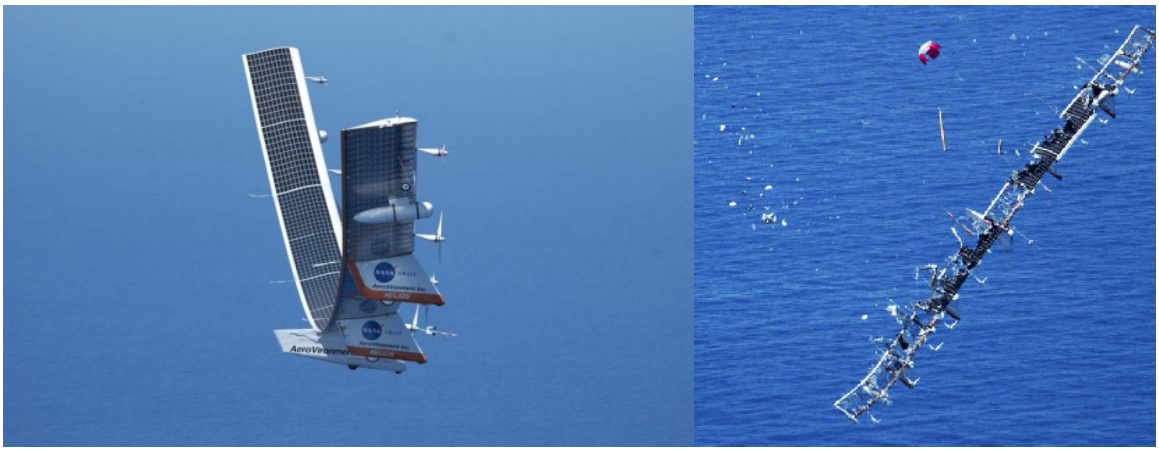

FIGURE 1.6: Helios aircraft with severe bending moment and the outcome from a lack of stiffness.

the design places as much of the vehicle mass at the largest rotation radius possible, thereby reducing the rotor-wing speed. Approximately 80% of the entire vehicle system mass is located in the satellite bodies, which is predominantly the battery system which provides energy during night operations. Placing the battery mass at the outer fuselage maximizes the centrifugal force and provides the most structural stiffening to alleviate the bending moment exerted on the wing spar. Traditional rotor blades run high tip speeds (around 600 to 850 ft/sec) to achieve high radial accelerations, typically thousands of times greater than the acceleration of gravity. But the TURN system, utilizing a large tip mass, only needs about twice the acceleration of gravity, to provide sufficient stiffening within the system.

Tether

A major detriment with helicopter rotor aerodynamics, is that only the outermost portions contribute any significant lift. The majority of the innermost sections are quite ineffectual, but are still subjected to induced drag. With this concept, each satellite has a large radius of rotation, with the tether making up the inner 80% of that radius, thereby eliminating an underutilized structure. The nondimensional cross-sectional drag coefficient for a cylindrical cable is extremely high, about 1.00 compared to a typical airfoil of 0.04; so at first glance the tether drag may appear to significantly increase the parasitic drag. However, the tether is made of advanced aerospace grade compressed Spectra, which provides incredible strength-to-weight. This allows the tether cable diameter to be very small because it is extremely structurally efficient at carrying tensile loads. Combined with the fact that the average tether speed is only 40% of the tip speed, the resulting tether drag merely constitutes around 5-10% of the total vehicle drag.

High Lift-to-Drag Ratios

Attaining eternal flight must resolve the conflict between the forces needed to keep the system aloft versus the power required to do so. Thus, a high lift-to-drag (L/D) ratio is extremely important.

Several mechanisms accomplish this through: low thickness-to-chord ratio, elliptical wing load distribution, and improved rotor disk loading. This unique geometry permits L/D ratios that exceed what either helicopters or gliders can achieve on their own.

Previously mentioned, centrifugal forces allow for very high aspect ratios, but this structural stiffening has another benefit. The low resulting bending moment allows for very thin airfoil sections which have low thickness-to-chord (t/c) ratios. Because the satellites have very large diameters, the system can cruise at relatively low airspeeds; and the use of low t/c airfoils is especially important for aircraft operating at a low Reynolds number. This condition maintains laminar flow for a greater portion of the airfoil by insuring that laminar separation does not occur, which achieves extremely low levels of induced and parasitic drag.

Helicopter rotors develop lift across their entire diameter, where nearly all the thrust is generated from the outer 25% of the rotor blade. This is described as a triangular load distribution, which has poor lift efficiency resulting from high induced drag. A more ideal scenario is an elliptic load distribution across the lifting surface, which lowers the induced drag, and increases the overall L/D ratio. With this concept, the tether comprises the innermost 80% of the arm, so the satellites have a large radius of rotation which enables the wings to achieve elliptic span loading.

Helicopter rotors perform in close proximity of the downwash of the blade rotating in front of it, which increases the required angle of attack for lift generation, and also leads to high induced drag. With the TURN concept, each satellite has a large spatial separation, so they operate independently of the other downwash fields. A reduction in downwash induced drag can be visualized from a rotor disc loading perspective, as seen in Figure 1.7. Extremely large tether diameters creates a toroid shaped downwash field generated from the traversed rotation of the satellites. A conventional rotor with 20 foot radius has a swept disc area of 1256 square feet. Meanwhile, the same 20 foot lifting surface with an 80 foot tether traverses a swept area of 11,304 square feet, which is vastly greater than the span of the satellite alone. Because the total rotor disc area is directly related to the induced drag, the TURN approach offers a distinct advantage over conventional rotor designs.

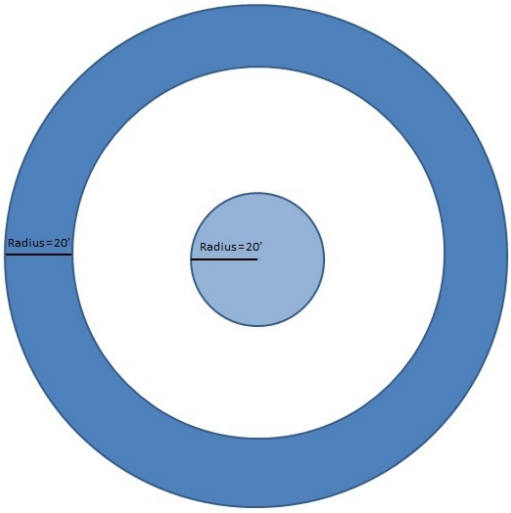

FIGURE 1.7: Simplified traversed rotor disk area.

Rotating System

Another favorable aerodynamic characteristic of the TURN concept allows for larger payload volumes. Traditional fixed-wing vehicles produce lift from their cruise speed, meaning they require airflow over the wing to generate lift. Of course, this forward velocity also incurs a drag penalty. Conventional HALE concepts require that payload volumes move at the same speed as the rest of the vehicle, which can result in substantial parasitic drag from bulky antenna or optic payloads. Unlike typical designs, the TURN vehicle alleviates this condition. All the lift generation is achieved within the moving satellites, which is independent from the stationary hub. This means larger and aerodynamically inefficient payload volumes can be incorporated into the central hub without incurring similar drag penalties, because the payload is isolated from the cruise speed components which generate lift. Furthermore, the system is less sensitive to payload weight because a significant portion of the vehicle mass is already concentrated within the satellite bodies.

1.2.4 Control Problem and Objectives

After being introduced to the TURN system, it is intuitive how such a vehicle could achieve greater aerodynamic efficiency, outperform both fixed-wing and rotorcraft style aircraft, and put an eternal flight capability within reach. What is not immediately obvious, is whether such an aircraft can be adequately stabilized and controlled. From the earliest phases of the conceptual design for the TURN system, the largest identified risk and the major issue to be resolved, pertained to the controller development for this novel architecture. A prominent hurdle with the TURN configuration, is the uniqueness of its layout. As such, there are no existing dynamic models, control developments, or simulation studies that can claim the TURN methodology is a viable concept design. The focus of this research, addresses these concerns in several ways. First, it derives a multibody dynamic model that accurately depicts the nonlinearity and interactions between the several rigid body components. Next, it utilizes a unique controls methodology, which decomposes the system into several control loops, and develops an adaptive controller framework to mitigate modeling uncertainty. Finally, a simulation study helps evaluate the effectiveness of the controller architecture when applied to the nonlinear system dynamics. The objective is to demonstrate that each satellite can stabilize its local state, each tether arm can manipulate forces acting on the central hub, and coordinated maneuvers can achieve translation for the central hub within the inertial frame.

1.3 Alternative Embodiments

While the primary mission for the TURN concept focuses on HALE communication platforms, several other compelling missions would benefit directly from the unique capabilities offered by the TURN advanced concept. These unique advantages include: extremely high L/D ratio, stationary central hub, centrifugal stiffening allowing lightweight structure design, large swept rotor area with extremely low effective disc loading, and an ability to alter the effective disc loading by changing the tether radius. During the course of this research, NASA Langley has already begun

	sUAV	Camera	Small AT-Sat	AT-Sat
Geometry				
Outer Diameter (ft)	70	200	400	800
Inner Diameter (ft)	56	160	320	640
Span (ft)	7	20	40	80
Chord (ft)	0.5	1.0	1.0	1.5
Aspect Ratio	18.6	26.7	53.3	71.1
Swept Lift Surface (ft^2)	1385	11310	45239	180956
Forces				
Rotational Rate (rpm)	20	8	4	2.25
Outer Tip Speed (ft/sec)	73	83	84	94
Inner Tip Speed (ft/sec)	59	67	68	75
Reynolds Number (avg)	233023	466045	532623	898802
Centrifugal Accel (g's)	3.89	1.78	0.89	0.56
Angle vs Horizon (deg)	1.62	4.02	7.99	13.59
Tether Tension (lbf)	55.64	107.96	141.99	310.14
Weights				
Gross Weight (lbf)	52.8	226.6	591.9	2185.1
Satellite Weight/Element (lbf)	14.3	60.5	158.0	583.3
Payload Weight (lbf)	4.7	22.7	59.2	218.7
Disk Loading (lbf/ft^2)	0.038	0.020	0.013	0.012
Drag and Power				
Induced Drag (lbf)	167	638	1363	4835
Parasite Drag (lbf)	29	95	303	1294
Tether Drag (lbf)	9	31	180	602
Power Required (watts)	205	764	1846	6731
Specific Power (watts/lbf)	3.88	3.37	3.12	3.08

TABLE 1.2: Comparison between three-armed TURN concepts at various sizes and payloads.

to consider this concept for an atmospheric observatory and a Mars flight vehicle; and methods applied to this very unique multibody dynamic problem have been adopted to model a robotic legged lander system for an asteroid capture vehicle. Only a small portion of the larger number of applications are presented here. This section reviews different vehicle sizes, describes a competitive commercial TURN system, and offers advantages to alternative airborne wind energy platforms.

1.3.1 Various TURN Vehicle Sizes

Although initially designed to support AT-Sat payloads, this unique design methodology is not a one-size-fits-all proposition; rather a wide range of different scale vehicles can be implemented. Table 1.2 presents several payload sizes spanning from small UAVs to full satellite equivalent payloads. The vehicle characteristics shown are not optimized, but merely result from simple sizing sensitivities yielding reasonable configurations. A particularly useful tracking metric while comparing the TURN concept to other approaches is the specific power, which is the ratio of the power required to maintain flight per vehicle pound.

It is interesting to compare the TURN concept to the recently successful winner of the Sikorsky Human Powered Helicopter prize, showcased in Figure 1.8. The Aerovelo Atlas is a four rotor, 121 pound human-powered vehicle, where a 160 pound pilot managed to keep the aircraft aloft for 64 seconds. Despite its light weight, the system has a massive footprint, comprising a 156

FIGURE 1.8: Aerovelo Atlas, the winner of the Sikorsky Human Powered Helicopter competition, with a highlighted rotor disk area.

foot diameter with a total rotor lift area of 13,700 square feet. The combined lifted weight of 281 pounds, with a human power output of 750 watts, indicates the vehicle has a specific power of 2.67 watts/lbf. This was accomplished with an incredibly flimsy structure that provided no design to ultimate load or safety margins.

While sizing the TURN structure, a factor of three was used for the total safety margin over design load, thus the specific power is slightly higher across all vehicle scales than what was required by Atlas. However, at a similar vehicle weight, the TURN concept is able to achieve a specific power close to 3.5 watts/lbf, which is only 31% greater than the Atlas. As another point of comparison, the Zephyr 7 is a 110 pound vehicle and calculated to cruise at approximately 550 watts. With a specific power of 5 watts/lbf, this is 45% greater than the TURN concept at a similar weight.

1.3.2 Competition for Existing UAVs

Over the past decade, unmanned aerial vehicles have been the most aggressive growth sector within the aerospace industry, and recent reports indicate that this market is just beginning to bloom. The Teal Group, a market analysis firm specializing in the aerospace and defense sectors, recently released several forecasts pertaining to the UAV industry. Their 2015 report (Teal Group, 2015, Aug 14) estimated that, "UAV production will soar from current worldwide UAV production of $4 billion annually to $14 billion, totaling $93 billion in the next ten years," and goes on to state that the market demographic is: 72% military, 23% consumer, and 5% civil. A more recent market study (Teal Group, 2016, Jul 7) focusing exclusively on the civilian sector, "estimates that non-military UAS production will soar from $2.6 billion worldwide in 2016 to $10.9 billion in 2025, a 15.4% compound annual growth rate," and will total $65 billion over the next decade.

Now consider a price-sensitive consumer that does not require an eternal flight capability. Hovering ability for the drone would be a desirable feature, but this customer is more concerned with the available flight endurance. Emergency situation monitoring, remote medical supply delivery, agricultural health assessment, and land surveying and mapping, are all UAV applications that fit this demographic. With one small revision, a TURN aircraft could easily service this sector. Solar cells represent a vast majority of the vehicle expense, so if price is a driving factor, and an eternal flight capability is not a requirement, then eliminating this component from a TURN vehicle makes it a very formidable competitor within this existing marketplace.

While `http://www.uavglobal.com` provides a more comprehensive listing of UAVs and their specifications, this analysis evaluated four comparable and commercially available fixed-wing aircraft, displayed in Figure 1.9. Each vehicle is nearly a ten foot wingspan, carries approximately five pounds of payload, and flies for about 90 minutes. Falcon, produced by Falcon Unmanned, is the smallest vehicle with the shortest flight duration. The wing and tail are merely affixed to a carbon pole, so it lacks a formal fuselage and has the least professional design. Aeromapper 300, by Aeromao, is the next size up in both wingspan and endurance. This aircraft is a full carbon composite construction and is on the upper-end of a hobby grade system. The best overall performer is the Tempest, by UASUSA. Developed for tornado research conducted at the University

FIGURE 1.9: Tempest (top left) was the fastest most versatile solution; other UAVs considered are: Falcon (top right), Aeromapper (bottom left), and Penguin BE (bottom right).

of Colorado, its sailplane inspired design is the fastest vehicle, and it has the widest ranges for payload and flight time. UAV Factory offers the Penguin BE, which is their only electric vehicle. It has the largest wingspan and is significantly heavier than the other aircraft; most likely because it was derived from their gas powered UAV designs. A summary of key attributes are listed in Table 1.3. Values were obtained from specification sheets, inferred from images within product brochures, or calculated using simple modeling techniques. The table also includes a fictitious aggregate system which serves as a basis for comparison against a comparable TURN aircraft.

Starting with a 10 foot wingspan, and a 12.5 aspect ratio, the chord length and wing area were calculated as 0.80 feet and 8.0 square feet, respectively. This size wing, while traveling 40 mph with a reasonable lift coefficient of 0.60, would generate approximately 20 pounds of lift, which comprises a 15 pound aircraft and a 5 pound payload. The tail area was set at 1.75 square feet, because common tail sizes were typically between 17-27% of the wing area. A drag coefficient of 0.06 was used, which assumes a lift-to-drag ratio of ten. With a combined surface area of 9.75 square feet, the drag force was slightly under 2.4 pounds, thus the power requirements to overcome aerodynamic drag at the cruise velocity slightly exceeds 190 watts. Assuming an 80% propeller efficiency, means the battery system must provide 238 watts of power for the aircraft to maintain its velocity. This represents a specific power of 11.9 watts/lbf, compared to the expected TURN value of 3.88 watts/lbf, which is greater than a factor of three improvement over existing designs. Depending on payload and rotation rate, an identically sized battery powering a TURN vehicle, should achieve flight durations ranging from 4.5 to 7.5 hours.

	Falcon	Aeromapper	Tempest	Penguin	Aggregate
Wingspan (ft)	8.0	9.8	10.6	10.8	10.0
Chord Length (ft)	0.69	0.89	0.70	0.78	0.80
Aspect Ratio (-)	11.5	11.0	15.0	13.8	12.5
Wing Area (ft)	5.52	8.72	7.42	8.42	8.00
Tail Area (ft)	1.50	1.85	1.30	1.50	1.75
Prop Diameter (in)	15	10	16	14	15
Vehicle Weight (lbf)	9.0	11.8	10.0	32.8	15.0
Payload Weight (lbf)	2.0	1.4	8.0	6.2	5.0
Cruise Velocity (mph)	31.1	37.3	50.0	49.2	40.0
Max Velocity (mph)	51.8	56.0	98.0	80.5	75.0
Min Flight Time (min)	60	90	90	110	90
Max Flight Time (min)	90	100	180	140	120

TABLE 1.3: Comparison between various commercial UAVs and a fictitious aggregate system.

While the prospect of an eternal flight system is extremely tantalizing, developmental milestones need to remain pragmatic. The best means of reducing risk and advancing the research project forward, is to adopt a spiral development methodology. Rather than attempt the biggest and most complex project in a single pass, this approach works iteratively. Smaller, more manageable, and less expensive scaled vehicles demonstrate unproven technology. The success and shortcomings of the current vehicle provide "lessons learned" which are incorporated into the next more complex design. Because this scale system represents an immediate commercialization opportunity, it has been defined as the first step in the spiral development life cycle. This TURN embodiment is such an important stepping stone, that the remainder of this research will focus on this scale vehicle.

1.3.3 Airborne Wind Energy Platform

Traditional wind turbines are only economical where winds routinely reach 12-18 mph, which represents less than 15% of the world surface. With their growing size and cost, these systems have reached a plateau because they are not scalable. Thus, there has been renewed interest in airborne wind energy (AWE) techniques, with a comprehensive reference provided by (Ahrens et al., 2013). Small aircraft, or "energy kites," fly in circles while performing the same function as ground-based wind turbine tips, which deliver over 75% of the energy capture. Propellers on the aircraft act as electric alternator generators which extract the wind energy and transmit it down the tether to the ground. Makani is an energy kite under development by X, the research division for Google, and an illustration of their concept is provided in Figure 1.10.

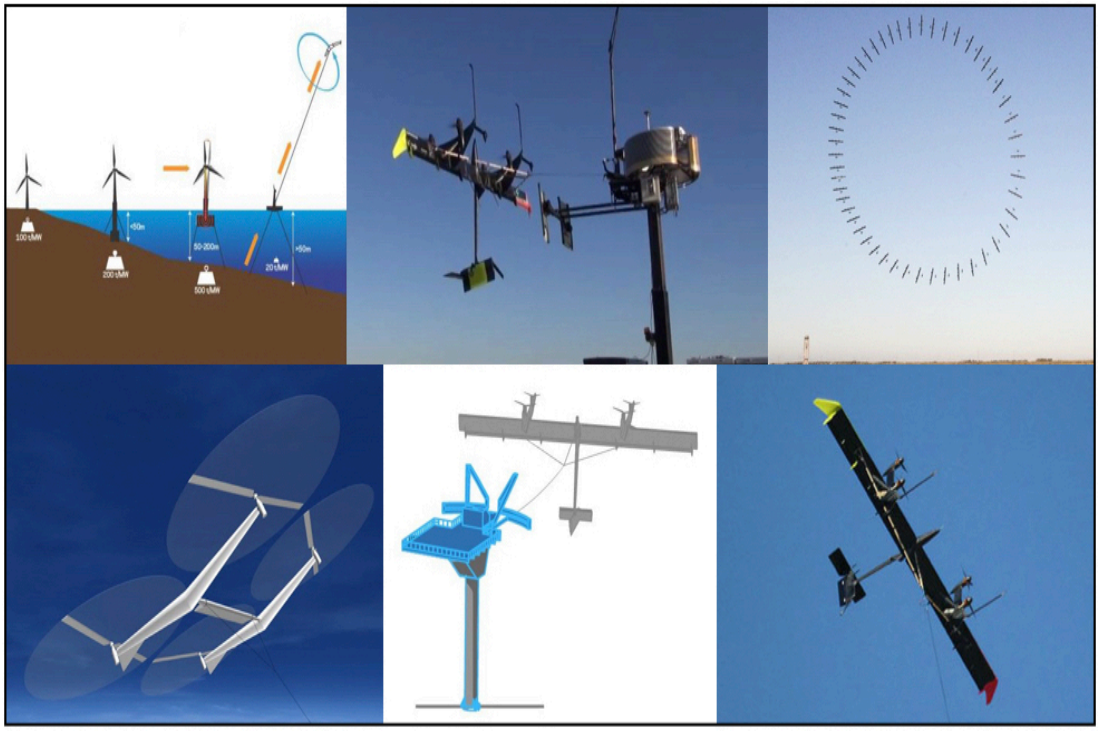

FIGURE 1.10: Depiction of AWE platform and the Makani system demonstration.

While ground-based wind turbine tower structures experience huge bending moments requiring massive concrete pads, an AWE approach does not transmit any bending moment down the tether. This is particularly appealing for off-shore application because it eliminates large and expensive mooring platforms. Long tethers eliminate 90% of the structural material required for a traditional tower, resulting in lower material and installation costs. Energy kites reach higher altitudes, so they can be installed in a greater number of locations, and they are able to reach stronger and steadier winds generating up to 50% more energy. Because they are more aerodynamically effective, energy kites can collect more power at any given wind speed.

Despite the touted advantages, the Makani solution has notable shortcomings. Tethers for such large systems experience substantial aerodynamic drag. The entire tether section moves at the aircraft velocity, which is around 200-300 ft/sec for the the Makani system. This results in high tether drag, thereby reducing the amount of collected energy. Because the tether orientation is orthogonal to the aircraft, a significant bending load is imparted on the wing. Controls are available to adjust the flight trajectory and mitigate disturbances, but do not to actively manipulate the rate or direction of the system, which would be needed to coordinate alignments with other neighboring AWE systems. Finally, during hover, an inefficient multirotor design uses more of the stored energy.

Consider what happens when a conventional Makani aircraft is replaced with a TURN concept vehicle. For starters, while hovering during idle winds, an energy consuming multirotor platform would be replaced with a more efficient concept which was designed to attain eternal flight. Energy collection would be further improved because a TURN embodiment has a higher lift-to-drag

ratio compared to other airborne wind concepts. By connecting the anchoring ground tether to the TURN central hub, this stationary component would not have translational velocity or experience aerodynamic drag. This nearly eliminates the drag on the primary tether which: increases tether angles relative to the horizon, permits smaller land use, and retains more of the collected energy. Because the TURN approach incorporates centrifugal stiffening, the rotating tethers and their energy kites would maintain tensile loading, allowing for a lighter weight solution.

1.4 Research Outline

Preliminary performance results are compelling and indicate the TURN concept is feasible in achieving a day-night energy balance, but the major risk identified early on is the ability to maintain control of the multibody dynamics inherent in the design. Therefore, this research focuses on delivering a detailed multibody model of the system dynamics, an advanced adaptive controls analysis and architecture, and a representative simulation of the system flight characteristics. It considers both standard and non-ideal operating conditions, and investigates real world disturbances which may introduce dynamic instabilities. The following describes subsequent chapter subject matter.

Chapter 2 discusses pertinent research topics in the *Literature Review*, which covers HALE aircraft, tethered systems, multibody dynamics, and some previous publications from the author. Chapter 3 familiarizes the reader with the vehicle by providing a *Plant Development*, which models the rigid body components, describes their dynamics, introduces the numerical multibody simulation structure, and develops the trimming and linearization processes. Chapter 4 performs the *Controls Analysis*, which summarizes the overall controller methodology, describes three distinct controller subsystems, and implements an LDS based model reference adaptive control (MRAC) architecture. Chapter 5 presents the *Simulation Study*, which introduces the prototype system, trims the simulated prototype vehicle, and simulates the nonlinear dynamic TURN model running the LDS based MRAC on each of the three control loops. Chapter 6 describes the *Prototype Development Plan* which lays out subsequent steps for this research beyond the PhD, by introducing a series of prototype vehicles and their associated testing plan. Chapter 7 closes the paper with *Conclusion*. Furthermore, the reader may reference several appendices which address various topics in control theory including: basic fundamentals, SISO and MIMO state feedback control, state estimators and reduced state estimators, system identification methods, and adaptive control techniques.

Chapter 2

Literature Review

This chapter reviews the relevant literature, both general theory within technical publications and practical applications performed by research groups, which pertain to the research and development of the tethered uni-rotor network (TURN) concept vehicle. It reviews: high-altitude long-endurance (HALE) aircraft, tethered systems, multibody dynamic problem formulations, adaptive control theory and architecture, and several publications developed by the author.

Chapter Motivation

Eternal flight vehicles have received a great deal of attention in recent years. Most current attempts utilize long and slender wing sections to increase the aspect ratio and reduce the amount of drag. Two prominent designs are either a single long flexible wing that bends under its own weight, or slender wing sections attached through hinged joints. Both designs have inherent problems with the amount of flexibility in the wing sections and the control techniques to mitigate the bend and twist dynamics. Other pertinent areas of research for this project include tethered systems and multibody dynamic models. Most of the currently available research have certain aspects that are applicable to this project, but also include serious limitations or simplifying assumptions which are not appropriate for the TURN modeling effort. Finally, there are many complexities heading into this research; for instance: uncertain multibody interactions, highly nonlinear dynamics, sparse existing research to develop upon, no available wind tunnel data, and the a lack of computational fluid dynamic (CFD) analysis. Thus, adaptive controls techniques are of paramount importance.

Chapter Objectives

First and foremost, the goal of the literature review is to ascertain whether this type of aerial vehicle already exists. After a substantially broad investigation, it appears this concept is as novel as first anticipated. So then, the next task is to survey design methodologies that have the most similar mission requirements, typically HALE aircraft, and find out their existing capabilities. After that, attention is focused on the TURN model, specifically the mathematical description the tether, where the objective is to understand existing approaches and to explore what alternative multibody

techniques are available. Once the system is accurately modeled, the next assignment investigates the means of putting the vehicle into practice; accomplished though suitable adaptive control techniques. Finally, it is important that the reader be cognizant of existing publications from the author, pertaining to the current TURN research effort.

Chapter Outline

Before discussing the intricacies of the TURN system development, a comprehensive assessment of the current state of the art is in order. This chapter reviews the literature for: existing vehicle designs that attempt eternal flight, and background theory needed for the TURN system analysis.

Section 2.1 investigates *HALE Aircraft*, which are high-altitude long-endurance systems that seek an eternal flight capability. It looks at existing designs pursued by various research groups, and reviews applicable feasibility studies applied to a wide range of embodiments.

Section 2.2 reviews *Tethered Systems*, which are unconventional vehicles that make use of flexible cables as part of their primary structure. References were extremely scarce for systems that operate in atmospheric environments, so it primarily looks at tethers used within space applications.

Section 2.3 addresses *Multibody Dynamics*, which is a type of numerical routine used to model and study the behavior of a dynamic system comprised of rigid body elements. It covers several available approaches and addresses their applicability to the TURN research development.

Section 2.4 summarizes *Adaptive Control* research; which is commonly used on systems with parameters that are unknown and/or changing over time. Adaptive control aids the TURN research development, by tuning control parameters in real-time, which overcomes modeling inaccuracies.

Section 2.5 describes *Publications From the Author*, which precede this more comprehensive research analysis. It summarizes model reference adaptive control techniques that are incorporated into this project, and presents research publications that specifically address the TURN system.

Section 2.6 lists several *Reference Textbooks*, which were used frequently throughout the research development process. It includes: linear system theory, fundamentals of feedback control systems, and various works on adaptive control.

Section 2.7 offers some *Background Material*, which is a listing of the controls topics offered in each of the appendices. It begins with the most introductory material, and subsequently builds upon the previous foundations into more complex subject matter.

2.1 HALE Aircraft

Prior to the ambition of reaching for eternal flight, aerospace companies and research groups were very interested in aircraft that exhibit long flight endurance while operating at high altitudes. Thus, much research has been applied toward these types of HALE aircraft.

A down select procedure for eternal flight missions is outlined by (Nickol et al., 2007). It reviews sixteen heavier-than-air (HTA) and lighter-than-air (LTA) concepts, which include a combination of heavy-fuel and solar regeneration technologies. Of course, heavy-fuel concepts do not qualify as eternal flight vehicles, and they deemed the LTA concept is not practical from its large size and technical risk. Concerning the solar regenerative concepts, the research concludes that a feasible solution with available technology does not exist. A breakthrough in solar array and battery performance are the determining factors for achieving eternal flight with existing concept vehicles.

An optimization framework, for assessing solar powered HALE aircraft design, is described by (Mattos et al., 2013). It addresses structural design, aerodynamics, vehicle dynamics, stability, and payload weight as points within the optimization routine. Although this research takes existing HALE designs to their optimal limit, it is still is not enough to achieve eternal flight with existing solar cell and battery technologies.

Similar to the previous optimization approach, (Xian-Zhong et al., 2013) attempts to define the key parameters that could enable eternal flight from solar powered aircraft. Their focus is to enhance the payload capacity by redistributing the wing load using lighter structural materials. Although the analysis is based on existing technologies, the findings are limited in scope to certain latitudes with optimal solar radiance.

While not a formal analysis, optimization, or design, (Xiongfeng et al., 2014) provides an informative trade study which reviews various solar powered aircraft that are attempting to achieve eternal flight. It presents the general constraints with common aircraft configurations, outlines what is needed to satisfy the energy balance relationship, and describes an operational "black area" that cannot be breached by existing solar powered airplanes.

Flexibility is one of the largest existing deficiencies within fixed-wing HALE aircraft. To help overcome this, (Ricciardi et al., 2013) provides an aeroelastic gust load analysis for a variety of HALE aircraft currently under development. It applies a nonlinear aeroelastic model to both a joint wing design and a flying wing configuration, but it does not evaluate the feasibility of attaining eternal flight with any particular concept vehicle.

Another nonlinear aeroelastic model, presented by (Cesnik and Su, 2005), is used to analyze fully flexible HALE aircraft. A finite element framework utilizes a rigid body model with flexible joints, and applies a one-dimensional nonlinear beam model to all the structural members of the aircraft. This approach is used to simulate both single wing and joint wing designs, and then compares the nonlinear results to linearized rigid models.

2.2 Tethered Systems

What enables the TURN concept to be so compelling, is also the very feature that makes it hard to model, analyze and simulate: the mathematical description of the tether. These types of systems are not new, but most of the research on tethered structures is centered around space applications, which are not subjected to atmospheric conditions.

A comprehensive survey of the literature on the subject is provided by (Chen et al., 2014). Topics on tethered systems include: dynamic modeling, deployment and retrieval, trajectory generation and control, attitude and motion control, and vibration modeling. Because it develops the dynamics for tethered systems operating in space, the model includes the effects of gravity; but since it is focused on space applications, it does not make any provisions for aerodynamic drag, which is present within the TURN dynamics.

An analysis of a very long tether is presented by (Woo and Misra, 2013), but the derivations focus on a space elevator application. Primary concerns regarding the consistently growing stress distribution, from the cumulative weight of the tether, are addressed using Lagrangian formulations. However, the emphasis of the model is on the strength of the tether, rather than its dynamics, which is not particularly applicable to the TURN vehicle.

A similar tethered structure is modeled by (Pizarro-Chong and Misra, 2008). They have a central body with multiple branches, described as a "hub-and-spoke" configuration, which directly mirrors the TURN design. However, their derivations encompass straight and massless tether sections as simplifying assumptions, so their model cannot accommodate aerodynamic drag and the effects of gravity required for the TURN simulations.

2.3 Multibody Dynamics

As will be shown, unique challenges are inherent in modeling the TURN tether element. Including both the effects of gravity and aerodynamic drag necessitate that the system be modeled as a set of multiple interconnected rigid bodies. An unintended benefit of this approach, is this formulation lends itself very well to modeling flexibility within structures, such a long and slender TURN rotor.

Some research, such as (Keshmiri et al., 1996), use Lagrangian mechanics to analytically model multiple entities; including their elasticity and vibrational frequency modes. However, this formulation requires multiple integrals, which are cumbersome to derive, do not scale well when altering the number of elements, and are not favorable for numerical routines. Unfortunately, it also requires that the system dynamics have a closed-form solution, which the TURN model cannot satisfy.

Orbital motion of tethered satellites operating in space are addressed by (Schutte and Dooley, 2005). While, they consider multiple linked rigid bodies, their derivations treat the tether as a single rigid body link, which is only suitable for space applications. Because it does not account for tether bending arising from the force of gravity and aerodynamic drag, this approach cannot accurately depict the TURN system tether dynamics.

Extremely flexible aircraft modeled with a multibody dynamic approach is presented by (Zhao and Ren, 2011). It incorporates the coupled effects of flight dynamics, aeroelasticity, and control, and the trim state is solved using a dynamic relaxation method. This approach is similar to the presented research because it is an iterative technique; however, their approach perturbs the system with external loads, which is a feature that is not available with a tether component.

A general multibody formulation devised by (Stoneking, 2007), shows the most promise for implementing the TURN system dynamics. Although the intended application is for tethered space structures, the model is accommodating enough to incorporate gravitational and aerodynamic drag forces. The dynamics are assembled in a matrix framework, which is well suited for numerical environments like Matlab, and is easily scaled to model a greater number of rigid body elements.

2.4 Adaptive Control

A great number of research publications exist on the topic of adaptive control. It has origins in parameter estimation, which can utilize recursive least squares or gradient descent methods; and where controller parameters can be estimated using either direct or indirect methods. It is common in more recent research, to propose adjustments to the controller structure which attempt to achieve a more capable controller, while knowing less about the plant; examples include: gain scheduling, σ-modification, and e-modification. One of the most versatile methods for reducing the amount of *a priori* information required of the plant, is to use a matrix decomposition of the high-frequency gain (HFG) matrix. This technique is used multiple times throughout the presented research, so this literature review focuses on this smaller subset within adaptive controls literature.

An early publication applying model reference adaptive control (MRAC) to multiple-input multiple-output (MIMO) dynamic systems is produced by (Hsu et al., 2001). They present a MIMO analog of the Lyapunov-based MRAC single-input single-output (SISO) design, and use a decomposition of the HFG matrix, to relax the SISO assumption that the sign of the HFG must be known.

Several months later, the previous publication was expanded upon by (Imai et al., 2001). They also worked with a matrix decomposition of the HFG matrix for MIMO MRAC controllers. However, they extend the MRAC solution to a more general case, to plants with a relative degree that is greater than one, and then present three possible factorizations.

Around that same time, (Ortega et al., 2001) worked to reduce the *a priori* knowledge placed on the HFG matrix. This work shows it is possible to globally and adaptively stabilize linear multivariable systems; and relaxes the restrictive symmetry condition, using an immersion and invariance approach, typically required to solve the problem.

With all this new development around matrix decompositions, a unification of multivariable MRAC was documented by (Tao, 2003a). This work: considers both discrete-time and continuous-time models; is based on LDU, SDU and LDS decompositions of the HFG matrix of controlled systems; and offers a unified framework for system parameterization, controller structures, error models, adaptive laws and stability analysis.

This line of research was continued by (Costa et al., 2003). They provide a control parameterization derived from the HFG matrix using an SDU decomposition; such that: S is symmetric positive definite, D is diagonal, and U is unity upper triangular. Therefore, only the signs of the entries of D, thus the signs of the leading principal minors of the HFG matrix, are assumed to be known.

More recently, attention was turned toward implementing such a control architecture on a nonlinear aircraft model, by (Guo et al., 2011). They apply a MIMO state-feedback output-tracking MRAC control scheme to the multivariable system. This controller maintains a simpler structure than that of an output-feedback design, but allows the plant-model matching conditions to be much less restrictive than those for state-tracking, where such a control scheme is useful when the plant-model matching conditions for state-tracking cannot be satisfied.

2.5 Publications From the Author

Several publications from the author precede this research effort. Some pertain to controlling a quadrotor platform, but the developed adaptive control techniques are subsequently applied in this document. Others present early research on the modeling and control of the TURN concept.

Prior research derived a multivariable MRAC scheme for a quadrotor (Selfridge and Tao, 2014a), which was subsequently published in a journal (Selfridge and Tao, 2014b). It employed a state-feedback output-tracking design, with a less restrictive matching condition than a comparable state-tracking design. The adaptive control law was based on a parameterization of an LDS matrix decomposition of the HFG matrix, which reduces the amount of *a priori* knowledge needed for the plant. This control architecture was directly applied within the TURN satellite entities.

A similar topic reviewed an output-feedback output-tracking controller design, which was applied to a quadrotor system (Selfridge and Tao, 2016). It also considered a multivariable MRAC structure, that utilized an LDS decomposition of the HFG matrix, which again reduced the amount of *a priori* knowledge placed on the plant. The primary benefit of output-feedback rather than state-feedback, is that not all of the system states need to be directly available; rather the controller works exclusively with a smaller number of measured states. For the TURN controller, the relative positions between the central hub and the outlying satellites are not measured, so this controller methodology offers a practical solution even though those states are not directly known.

The first of two publications (Selfridge and Tao, 2015b), pertaining to the TURN concept vehicle, introduced the research community to the modeling effort that describes the: nonlinear system dynamics, numerical multibody simulation structure, and the unique requirements for trimming and linearizing such a nonlinear multibody problem. Although the TURN system layout and geometry has evolved since this publication, it still represents a substantial portion of the modeling content described in *Chapter 3: Plant Development*.

A second publication (Selfridge and Tao, 2015a) presented the initial controls analysis. It outlined the controller methodology, and introduced the unique requirements needed for the inner-loop and outer-loop control systems, which handle stabilization and navigation, respectively. A relative gain array (RGA) was evaluated, which determined that decentralized control techniques are suitable. Controls development began with a SISO solution and expanded to a more involved MIMO controller; which helps to mitigate cross-coupling between inputs and outputs, and which provides the framework needed to develop the adaptive controls architectures. Some of the features in this

publication needed minor revisions to work with the more recently updated TURN embodiment, but the underlying theoretical development is the same as in *Chapter 4: Controls Analysis*.

2.6 Reference Textbooks

Several textbooks were used so frequently throughout this research process, that they deserve a special mention. Topics pertaining to linear algebra are addressed in (Holt, 2017), and (Khalil, 2002) describes the intricacies of nonlinear systems. Fundamentals of feedback control for dynamic systems are from (Franklin et al., 2010), whereas (Goodwin et al., 2001) elaborates more completely on MIMO control techniques. Comprehensive and detailed presentations of adaptive control are presented by (Tao, 2003b), while the most recent adaptive control methodology, L1 adaptive control, was founded by (Hovakimyan and Cao, 2010).

2.7 Background Material

Introductory material is presented in *Appendix A: Control Theory Fundamentals*, which addresses transfer functions/matrices, system eigenvalues, poles and zeros, controllability and observability, and decentralized control techniques. The simplest type of state feedback control structure is a single-input single-output plant, addressed in *Appendix B: SISO State Feedback*, which creates a desired system response, provides a canonical transformation, and develops the controller theory. The SISO controller is expanded to a MIMO framework in *Appendix C: MIMO State Feedback*, which modifies the applicable theory, provides a revised canonical transformation, specifies the matrix formulation, and illustrates how to achieve the desired closed-loop response. Estimation techniques are useful when system states are unknown, as described in *Appendix D: State Estimation*, which presents the theory, showcases the estimation error reduction process, and extends the development to include reduced order estimators. Finally, system identification techniques are useful when the plant parameters are unknown or changing over time, described in *Appendix E: System Identification*, which introduces parameter estimation and their associated errors, develops the adaptive laws with a stability analysis, and addresses parameter convergence.

Chapter 3

Plant Development

This chapter expands the preliminary analysis performed on the Tethered Uni-Rotor Network (TURN) concept system, and derives the complete system dynamics required for controls development (Selfridge and Tao, 2015b). It outlines how each component of the system is modeled, which then yields the equations of motion (EOM) for the vehicle. These dynamics are implemented in a multibody dynamics structure which govern the TURN simulations running in Matlab. Finally, the nonlinear system is trimmed and linearized which is the starting point for the controller development.

Chapter Motivation

The TURN vehicle is a radical departure from both conventional fixed-wing and rotorcraft designs, but this concept offers greater flight capabilities by combining the best features of both classes of aircraft. However, existing models of aircraft dynamics are not applicable to this concept vehicle, so a complete set of mathematical relationships describing the TURN dynamics needs to be established. Prior to developing prototypes and building full scale vehicles, simulation and analysis is required to provide insight into how the system behaves. Before starting the controller development, the nonlinear dynamic system model needs to be linearized so that control theory can be applied. And prior to linearizing the model, a set of initial conditions must be identified which put the system in a steady state equilibrium condition. All these future objectives begin with modeling, so developing the equations of motion, finding trimmed control inputs, and obtaining a linearized model of the system, are all crucial steps toward developing the TURN vehicle.

Chapter Objectives

The goal of this chapter is to develop a complete and accurate mathematical description of the TURN system. The models must provide sufficient accuracy to evaluate the system, but also be modular enough to accept more sophisticated models throughout the development process. Different vehicle geometries at various scales will be evaluated, so the models must be general enough to accommodate multiple configurations. Parameter files are used to store the vehicle geometry and physical attributes, so alternative designs can be evaluated by simply changing the parameter files.

The first objective of this chapter is to define the system, develop the equations of motion, and implement the system dynamics within a Matlab simulation environment. The system is reduced to a collection individual subcomponents, where each component has a description, some physical parameters, and an assigned coordinate frame. As the vehicle moves through space, various forces and moments act on each of the subcomponents. The external forces and moments are calculated for each individual entity at their current state, and then summed together to provide the total force and moment acting on that particular rigid body. All the relationships between the subcomponents are compiled into a multibody dynamics structure, which executes the numerical routine responsible for the nonlinear simulation.

The next goal of this chapter takes the developed TURN dynamics, and expresses those relationships in a form suitable for control analysis. Before applying controls, the system must operate in a steady state equilibrium point, such as hover. Trimming is the process of finding states and control inputs which attain a particular equilibrium point. The trimming routine begins with an educated guess value for the system initial conditions, and then runs an optimization routine which identifies the states and control inputs required to attain a force and moment balance within the system. Once the vehicle is trimmed, a linearization routine takes the nonlinear equations of motion and determines the state space matrices needed for the controls analysis.

Chapter Outline

Before undertaking any controls development for the TURN system, a complete and accurate description of the vehicle dynamics is required. This chapter develops all the dynamic models needed to mathematically describe the physical plant used during the design and analysis process.

Section 3.1 focuses on *Modeling*, which showcases the main features of the TURN vehicle. It then decomposes the system into individual subcomponents, describes the properties and geometries of each subcomponent, and assigns coordinate frames used during the modeling process.

Section 3.2 derives the *Dynamics* of the TURN system, which are the mathematical relationships that describe the equations of motion of the vehicle. It identifies all the pertinent forces and moments acting on each subcomponent, and uses first principles to obtain those force and moment values.

Section 3.3 implements the *Simulation*, which models the vehicle within the Matlab environment. It formulates a multibody dynamic structure based on a numerical routine, presents a generalized approach to execute the routine, and then applies the theory to implement the TURN models.

Section 3.4 addresses *Trimming* the vehicle, which seeks to obtain the set of states and control inputs that achieve hover. While TURN is in hover, the system is operating in a steady state static equilibrium condition, which is the starting point for linearization and controls development.

Section 3.5 performs *Linearization* on the system, which takes the nonlinear system dynamics and identifies linear relationships surrounding the hover operating point. Values obtained from the partial derivatives are used to populate the state space matrices needed for the controls analysis.

3.1 Modeling

Modeling the TURN system is the first step towards deriving the system dynamics, building the simulations, and performing the control analysis. This section presents the overall vehicle structure, describes the individual subcomponents, introduces coordinate frames typically located at the center of gravity (CG) of the body, and identifies various forces that act on each subcomponent.

3.1.1 System Overview

Four tethered satellite vehicles rotate around a central hub, illustrated in Figure 3.1. Each satellite has a flying-wing configuration, where the long and slender airfoil lifting surface with a single elevator is the predominant feature. At the end of each wingtip, there is a propeller mounted on a fuselage, a vertical stabilizer with a rudder, and an aileron control surface. Centrifugal forces keep the tethers taught, while lifting forces acting on the wing sections support each satellite and the central hub. Individual satellites are controlled through their propellers and control surfaces, and the central hub is articulated by manipulating tether forces coming from the satellite vehicles. The axes for the inertial frame $\{N\}$ are designated as: `+X:North; +Y:East; +Z:Down`.

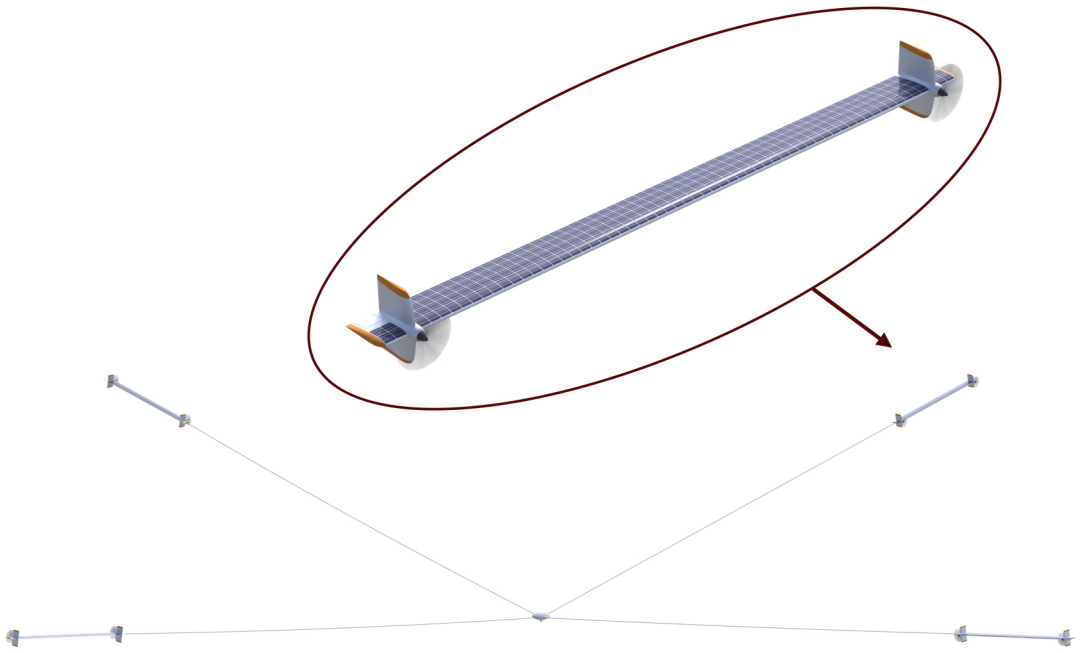

FIGURE 3.1: Complete Tethered Uni-Rotor Network (TURN) system.

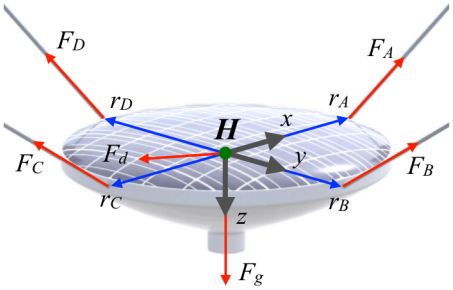

FIGURE 3.2: Diagram of the hub model.

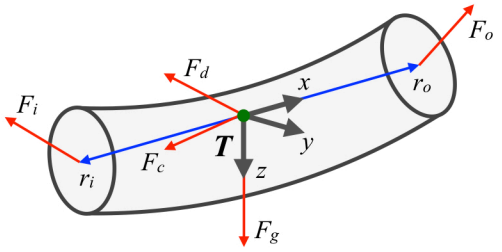

FIGURE 3.3: Diagram of the tether model.

3.1.2 Hub Description

The central hub is a rigid body which houses the vehicle payload and connects all the tether arms, illustrated in Figure 3.2. It has mass m_H and moment inertia $J_H = \texttt{diag}\{\, J_{Hx},\, J_{Hy},\, J_{Hz} \,\}$ expressed in the hub frame $\{H\}$. The four tethers are arbitrarily labeled as `A`, `B`, `C`, and `D`, to distinguish them from one another. Position vectors (r_A, r_B, r_C, r_D) relate the tether anchor points to the CG of the hub. Forces that act on the hub include gravity, tension from the tethers, and aerodynamic forces as the hub moves through space. The frame associated with the hub is located at the CG of the rigid body component, with: `+X:TetherA; +Y:Right; +Z:Down`.

3.1.3 Tether Description

Each tether is modeled as a chain of rigid body elements connected together with spherical joints, depicted in Figure 3.3. Each element has a cylindrical shape with mass m_T and moment inertia $J_T = \texttt{diag}\{\, J_{Tx},\, J_{Ty},\, J_{Tz} \,\}$ expressed in the tether frame $\{T\}$. Two position vectors, r_i and r_o, emanate from the CG of the element to the inboard and outboard endpoints, respectively. Each tether element has four forces acting on it. Two forces, F_i and F_o, come from the joint constraints and are located on each endpoint of the rigid body. Gravity and aerodynamic drag make up the other two forces, F_g and F_d. The frame of each tether element is located at the CG of the rigid body element, where: `+X:Outward; +Y:Right; +Z:Down`.

3.1.4 Satellite Description

The satellites are secured to the tethers, and are the entities that provide lift and contain all the control inputs which manipulate the TURN system; where Figure 3.4 depicts a layout of the satellite system. Each of the vehicles move through the inertial frame as a rigid body structure, with mass m_S and moment inertia $J_S = \texttt{diag}\{\, J_{Sx},\, J_{Sy},\, J_{Sz} \,\}$ expressed in the satellite frame $\{S\}$. External forces and moments that act on the vehicle come from: gravity, the propulsion system, and aerodynamic effects. Aerodynamic forces and moments are generated from: the wing section, vertical stabilizers, rudders, ailerons, and an elevator. The frame origin of the satellite is located at the CG of the vehicle, and its coordinate frame is oriented as: `+X:Nose; +Y:Right; +Z:Down`.

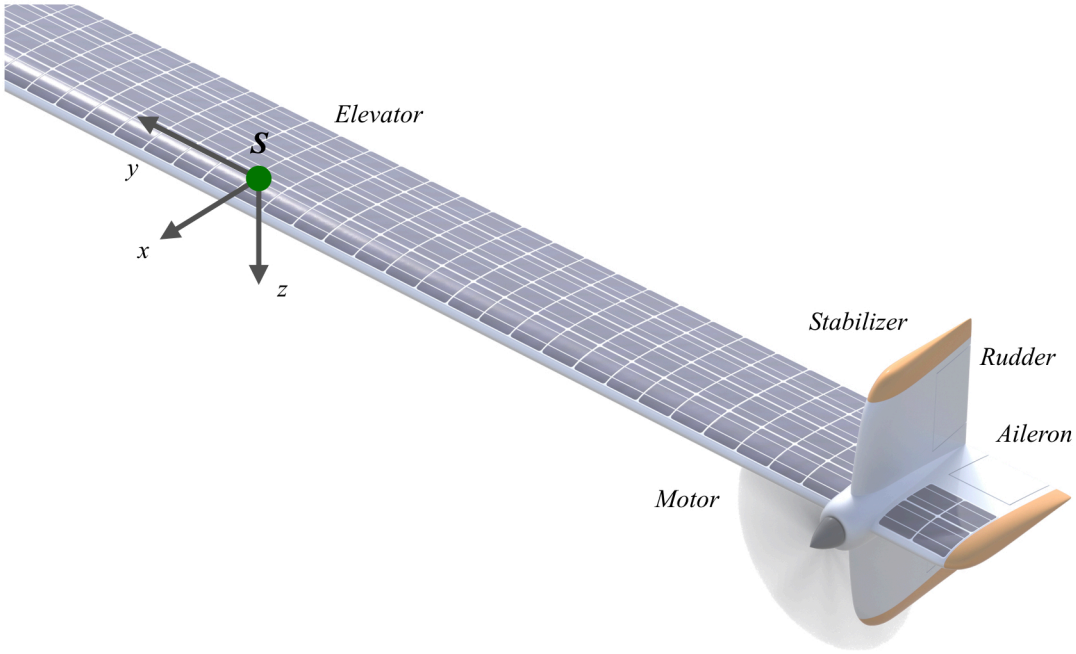

FIGURE 3.4: Diagram of the satellite model.

3.1.5 Aerodynamic Surfaces

Each satellite has several aerodynamic surfaces influencing the dynamic behavior of the system. The wing is fixed relative to the satellite body; while vertical stabilizers, rudders, ailerons, and the elevator, articulate while controlling the aircraft. The relative airflow vector across these structures, described by the angle of attack (AOA), is directly related to the force on each component. The objective is to determine the location of these applied forces, and obtain a position vector relative to the CG of the satellite. While standard airfoils commonly provide the location of the applied force, usually described as a percentage of the chord length, the force on more generic surfaces will act through the geometric center of the structure. Knowing the position, orientation, and centroids, of these entities is required to implement the simulation routine.

Centroids of simple shapes, like rectangles and triangles, can be determined from defined formulas. However, future TURN designs may incorporate tapered edges or utilize non-orthogonal angles, so a more general solution is sought. Each surface is described by a collection of coordinates, and defined with a closed, planar, and non-self-intersecting geometry. Vertices are listed in their occurrence along the perimeter, defined so the initial point (x_0, y_0) is equivalent to the final point (x_n, y_n), and indexed in a counter-clockwise direction to ensure the value of the area remains positive. The area A of such a polygon is described by (Johnson, 1960)

$$A = \frac{1}{2} \sum_{i=0}^{n-1} (\, x_i \, y_{i+1} - x_{i+1} \, y_i \,) \tag{3.1}$$

and used in the following relationships

$$
\begin{aligned}
C_x &= \frac{1}{6A} \sum_{i=0}^{n-1} (x_i + x_{i+1}) (x_i \, y_{i+1} - x_{i+1} \, y_i) \\
C_y &= \frac{1}{6A} \sum_{i=0}^{n-1} (y_i + y_{i+1}) (x_i \, y_{i+1} - x_{i+1} \, y_i)
\end{aligned}
\tag{3.2}
$$

which yields the centroid of the polygon, with coordinates (C_x, C_y). Finally, each planar representation is transformed into three dimensional space with a rotation matrix, which is covered in further detail while presenting the derivations for the system dynamics.

3.1.6 Modular Satellite Configuration

A representation of the satellite was modeled in Matlab, to facilitate simulations and generate animations. This depiction of the satellite model is illustrated in Figure 3.5. The satellite structure was coded with modularity in mind, where all the attributes and dimensions of the system are stored in a customizable parameter file. This file can be modified to reflect other system configurations, such as evaluating alternative prototype designs or assessing vehicles at differing scales. Then, the simulation takes the satellite characteristics and geometric relationships, developed in this section, and calculates the forces and moments acting on the vehicle, as described in the subsequent section.

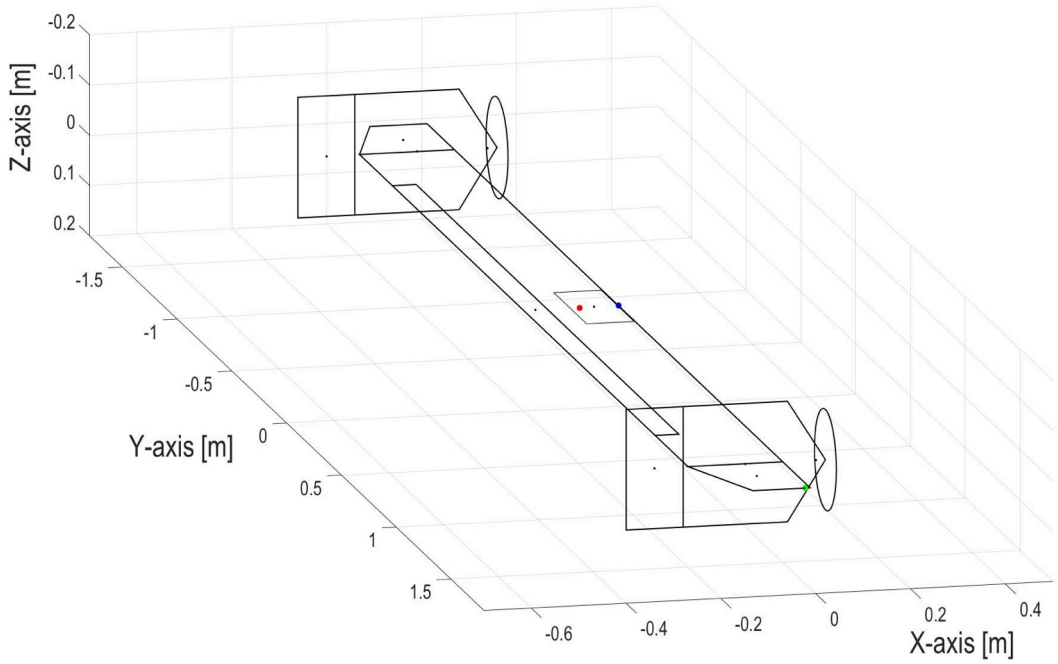

FIGURE 3.5: Representation of the satellite system within the simulation environment.

3.2 Dynamics

The modeling process defined all of the individual subcomponents that make up a TURN system, outlined geometric descriptions for each of those subcomponents, and identified the forces acting on them. This section identifies the dynamics of the system, which describes the mathematical expressions for all the forces and moments acting on each individual subcomponent. This establishes the equations of motion that are used to execute the numerical simulation and to perform the controls analysis (Durham, 2013).

3.2.1 Overview

Following sections outline the various forces and moments that act on all of the subcomponents within the TURN system. Then, the total force and moment acting on each rigid body element, is the summation of all the individual forces and moments acting on that body. Position vectors define locations where forces act on the rigid body, typically located at the center of gravity or at the geometric center for aerodynamic control surfaces. The forces and position vectors determine the applied moments, through the relationship

$$M = r \times F \tag{3.3}$$

where the cross product of the position vector r and the force vector F, are used to calculate the resultant moment M for that particular subcomponent.

3.2.2 Common Forces

Many forces are common to all the TURN subcomponents. Such forces include: gravity, centrifugal force, and aerodynamic lift and drag forces. The gravity vector always points downward, which is positive z in the inertial frame, and is expressed by

$$F_g = mg \, [\, 0 \; 0 \; 1 \,]^T \tag{3.4}$$

where F_g is the force of gravity, m is the mass of the element, and $g = 9.806 \; m/s^2$ is the acceleration due to gravity. Because TURN operates in a state of rotation, nearly all subcomponents are subjected to a centrifugal force. This force is expressed as

$$F_c = m \, (\omega \times (\omega \times r)) \tag{3.5}$$

where the centrifugal force vector F_c is determined by the mass m, angular rate vector ω, and position vector r, of the element. Similarly, all rigid bodies experience aerodynamic drag, and many provide aerodynamic lift. Lift and drag forces are governed by the lift/drag equation, through

$$F_* = \frac{1}{2} \, \rho \, v^2 \, A \, c_*, \quad * = l, d \tag{3.6}$$

where the lift F_l and drag F_d forces are dictated by the density of air ρ, relative velocity of airflow across the element v, cross-sectional area A, and the lift c_l and drag c_d coefficients.

3.2.3 Hub Forces

Primary forces acting on the hub include: gravity, tension from the tethers, and aerodynamic drag. Gravity was previously described, and tether tension is accounted for within the simulation environment. Aerodynamic drag is a direct extension of (3.6), modeled as

$$F_{Hd} = [\ F_{Hdx}\ F_{Hdy}\ F_{Hdz}\ ]^T,\ \ F_{Hd*} = c_{Hdf*} v_{H*}^2 \tag{3.7}$$

for $* = x, y, z$. The formula illustrates linear relationships between the hub drag forces F_{Hd*} and the squared velocity of the relative airflow across the hub v_{H*}, which are scaled by nondimensional drag coefficients c_{Hdf*}. Similar relationships exist between the hub drag moments M_{Hd*}, and the squared hub angular rates ω_{H*}, scaled by nondimensional drag coefficients c_{Hdm*}, described by

$$M_{Hd} = [\ M_{Hdx}\ M_{Hdy}\ M_{Hdz}\ ]^T,\ \ M_{Hd*} = c_{Hdm*} \omega_{H*}^2 \tag{3.8}$$

for $* = x, y, z$. The nondimensional coefficients, c_{Hdf*} and c_{Hdm*}, map the aerodynamic drag relationships for the hub, and are based on the geometry of the rigid body. Initial values for these coefficients are obtained by estimating terminal velocity and maximum aerodynamic torque on the hub. Aerodynamic drag force and moment are expressed in the hub frame and act at the hub CG.

3.2.4 Tether Forces

Each tether element has five forces acting on it. Two forces, F_{Ti} and F_{To}, come from the inner and outer joint constraints, and are accounted for within the simulation structure. The force of gravity F_{Tg}, and the centrifugal force F_{Tc}, have been previously described. The final force is aerodynamic drag F_{Td}, which is modeled with (3.6). The tether moves through the inertial frame with velocity v_T. Adjusting for wind moving across the tether section, yields the relative airflow, also described in the inertial frame. Using the orientation of the section, along with a rotation matrix, this vector is transformed into the tether frame. The relative airflow vector acts at the CG of the tether element, and the component that is perpendicular to the tether gives the velocity v, which is used in

$$F_{Td} = \frac{1}{2}\,\rho\, v^2\, A_T\, c_{Td} \tag{3.9}$$

where ρ is the density of air, A_T is the cross-sectional area of the tether element, and c_{Td} describes the nondimensional drag coefficient around a cylindrical body.

3.2.5 Satellite Forces

TURN satellites contain all the available control inputs, so stabilizing and maneuvering the system is accomplished entirely through these entities. Each satellite applies its own control locally, and then all the satellites execute coordinated maneuvers to control the complete TURN system. Therefore, an accurate assessment of the dynamic behavior of the satellite system is needed for both simulations and controller design.

Each satellite is modeled as subcomponents, which include: airfoil wing, propellers mounted to fuselages, vertical stabilizers with rudders, ailerons, and an elevator. Each subcomponent has a designated frame and a position vector which points from the frame origin to the CG of the satellite. Rotating between frames is accomplished with an Euler rotation matrix R, given as

$$R(\phi,\theta,\psi) = \begin{bmatrix} c_\theta c_\psi & -c_\phi s_\psi + s_\phi s_\theta c_\psi & s_\phi s_\psi + c_\phi s_\theta c_\psi \\ c_\theta s_\psi & c_\phi c_\psi + s_\phi s_\theta s_\psi & -s_\phi c_\psi + c_\phi s_\theta s_\psi \\ -s_\theta & s_\phi c_\theta & c_\phi c_\theta \end{bmatrix} \tag{3.10}$$

where the attitude of the subcomponent (roll, pitch, and yaw) is given by (ϕ, θ, ψ), and s_* and c_* describe the sine and cosine functions, respectively.

Gravitational force and centrifugal force have already been presented, but three other forces need to be addressed; propulsion from the propellers, skin friction drag acting on the fuselages, and contributions from aerodynamic surfaces. Lift and drag profiles provide a mapping between local AOA and the lift and drag coefficients, which determines the local force vector as a function of relative airflow, and is then mapped from a local frame to the satellite frame. Because forces arising from aerodynamic surfaces are not located at the CG of the satellite, they will produce moments described by (3.3). Finally, the total force and moment on the satellite is the summation of individual forces and moments acting on all of the subcomponents.

Propulsion Model

A propulsion system consists of a motor and a propeller. The rotor, which is expressed in the propeller frame $\{P\}$, spins with angular rate ω_P, and generates forces and moments described by

$$F_P = [\ F_{Px}\ F_{Py}\ F_{Pz}\ ]^T, \quad M_P = [\ M_{Px}\ M_{Py}\ M_{Pz}\ ]^T. \tag{3.11}$$

The inner workings of a brushless DC motor, and the aerodynamic intricacies of a fixed pitch propeller may be addressed in future developments. For this initial analysis, a simplified propulsion model is utilized as a first approximation to describe the dynamics. Blade flapping and side airflow are neglected, so the force and moment from the propeller only have components in the z-axis of rotation; therefore, (3.11) reduces to

$$F_P = [\ 0\ 0\ F_{Pz}\ ]^T, \quad M_P = [\ 0\ 0\ M_{Pz}\ ]^T. \tag{3.12}$$

This simplified model exhibits a linear relationship between the force and moment (F_{Pz}, M_{Pz}) delivered from the propulsion system, and the squared rotor angular rate ω_P, which are scaled by nondimensional coefficients. The relationships are expressed as

$$F_{Pz} = c_{Pf}\,\omega_P^2, \quad M_{Pz} = c_{Pm}\,\omega_P^2 \tag{3.13}$$

where c_{Pf} and c_{Pm} are the nondimensional propeller coefficients for the force and moment, respectively. Future prototypes may incorporate a canted motor, which necessitates defining a motor frame $\{M\}$, such that

$$F_M = R(\phi_P, \theta_P, 0)\,F_P \tag{3.14}$$

maps the force from the propeller frame to the motor frame, where a yaw angle was omitted because it aligns with the axis of the motor. Similarly, the moment in the motor frame is described by

$$M_M = r_M \times F_M + R(\phi_P, \theta_P, 0)\,M_P \tag{3.15}$$

where r_M is the position vector from the CG of the satellite to the motor frame.

Skin Friction Drag

As the satellite moves through space, the fuselage is subjected to skin friction; a type of drag force from the airflow grabbing the fuselage surface. This force is expressed in the fuselage frame $\{F\}$, and the skin friction drag coefficient is defined as

$$c_{Fd} = \frac{\tau_w}{\frac{1}{2}\,\rho\,U_\infty^2} \tag{3.16}$$

where ρ is the density of air, U_∞ is the free-stream velocity, and τ_w is the wall shear stress, given by

$$\tau_w = \mu \frac{\partial v}{\partial y}\bigg|_{y=0} \tag{3.17}$$

where μ is the dynamic viscosity air, v is the fluid velocity along the boundary, and y is the distance above the boundary layer. Using the fluid velocity as the free-stream velocity, with $U_\infty = v$, and substituting the skin friction drag coefficient relationship into the drag equation, yields a much simplified relationship

$$\begin{aligned} F_{Fd} &= \frac{1}{2}\,\rho\,v^2\,A\,c_{Fd} \\ &= \frac{1}{2}\,\rho\,v^2\,A\left(\frac{\tau_w}{\frac{1}{2}\,\rho\,v^2}\right) \\ &= A\,\tau_w \end{aligned} \tag{3.18}$$

which directly relates the wall shear stress τ_w to the drag force F_{Fd}, through the surface area A.

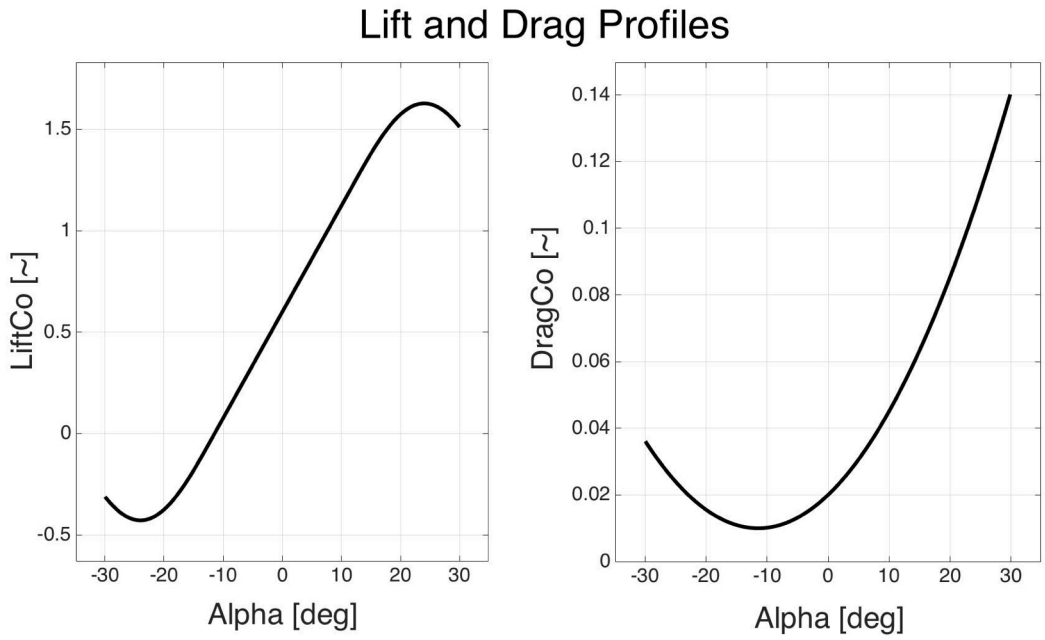

FIGURE 3.6: Profile curves describing lift and drag coefficients as a function of angle of attack.

Lift and Drag Profiles

Several prototypes are planned as part of the spiral development design process, and different wing geometries will be evaluated during these design iterations. Furthermore, various types of airfoils are used across the control surfaces, and these differences need to be accurately modeled within the simulation. Therefore, a Matlab function was developed to implement custom lift and drag profiles for each of the different control surfaces. The simulation stores lift and drag attributes including: zero angle lift coefficient c_L, zero angle drag coefficient c_D, linear range and slope, and maximum and minimum values for the lift coefficient. The program takes these parameters, and calculates the lift and drag coefficients as a function of the AOA of the surface. Sample lift and drag profiles are depicted in Figure 3.6.

Aerodynamic Surfaces

Aerodynamic surfaces on the satellite include: the wing, vertical stabilizers with rudders, ailerons, and an elevator. Each surface has its own lift and drag profile to accurately represent the sub-component. Within the simulation, the satellite moves through the inertial frame with a known velocity. Adjusting for wind across each surface, yields a relative airflow expressed in the inertial frame. The attitude of the satellite forms a rotation matrix which converts the relative airspeed vector from the inertial frame into the local satellite frame. For each surface, the the airspeed vector is projected onto a plane parallel with the cross-section of the surface. This projection determines

the relative AOA and the magnitude of the airflow over the surface. The AOA is fed into the previously described lift and drag profile function, which returns the lift and drag coefficients (c_L, c_D) for that particular angle and surface. The magnitude of the airspeed v, together with c_L or c_D, are passed into the lift and drag equation (3.6) which yield values for the lift force and drag force. These magnitudes are converted into vectors, such that the drag force acts parallel to the airflow, and the lift force acts perpendicular to the airflow. Force vectors are located at the quarter-chord of the wing surface, and at the geometric center for all other surfaces. Each surface has a position vector pointing from the CG of the satellite to the point where the aerodynamic force acts, and then individual moments are calculated with (3.3).

3.3 Simulation

Having defined the TURN system dynamics, the final step toward implementing the equations of motion, is to establish the relationships between all the rigid body elements. This section formulates the multibody dynamics problem through an illustrative generic example, applies the theory to a satellite vehicle, a tethered model, and the complete TURN system, and then explains how the numerical routine is implemented in Matlab.

3.3.1 Multibody Dynamics Motivation

Simple elements, like springs and dampers, have an exact representation between forces and states, so a closed-form solution can be attained. However, with the tether dynamics, the states and forces are intertwined. The state of the tether determines the amount and direction of airflow across the section, which influences the magnitude of the drag force. However, the magnitude and direction of the drag force, affect the current state of the tether. This forms a mathematical vicious circle, so no closed-form solution exists. Therefore, a numerical approach is required to represent the tether within the TURN dynamic model.

Several techniques are available to model a multibody dynamic system. There are laborious hand derivations, like Kane's method and Lagrangian mechanics, but changes to the model or to the number of elements requires a completely new derivation. The following uses a method described by (Stoneking, 2007), which is similar to a finite element analysis (FEA) approach, inasmuch that each section is modeled as a smaller building block. While, FEA techniques linearize a system early in the process, and thus are only suitable for small perturbations, this approach maintains the nonlinearities within the dynamic relationships.

The TURN simulation utilizes a novel multibody dynamic implementation. The technique keeps nonlinearities within the model, is appropriate for numerical integration, and allows the structure to be assembled through inspection. This approach offers the most accurate model, and is modular enough to accommodate various prototypes and revisions throughout the development process.

3.3.2 Preliminaries

The system is decomposed into rigid body elements connected together with spherical joints. Some states in the simulation structure are represented in the inertial frame, while others portrayed in a local body frame. This section describes the dynamics of a rigid body, the rotation matrix between coordinate frames, how to express derivatives in different coordinate frames, and a common notation used within the multibody development.

Rigid Body Dynamics

A dynamic model which governs a rigid body under external forces and moments is described by

$$m\dot{v} = \Sigma F, \quad J\dot{\omega} + \omega \times J\omega = \Sigma M \tag{3.19}$$

where $\Sigma F \in \mathbb{R}^3$ and $\Sigma M \in \mathbb{R}^3$ represent the summation of all external forces and moments acting on the body, v is the velocity vector in the inertial frame, ω is the angular rate vector, m represents the scalar mass of the element, and $J \in \mathbb{R}^{3\times3}$ is the moment inertia matrix.

Rotation Matrix

While developing the equations of motion, some elements need to be transformed from the inertial frame to its local body frame. When working with Euler angles, the rotation from the body frame to the inertial frame is given by the rotation matrix R, described by

$$R(\phi,\theta,\psi) = \begin{bmatrix} c_\theta c_\psi & -c_\phi s_\psi + s_\phi s_\theta c_\psi & s_\phi s_\psi + c_\phi s_\theta c_\psi \\ c_\theta s_\psi & c_\phi c_\psi + s_\phi s_\theta s_\psi & -s_\phi c_\psi + c_\phi s_\theta s_\psi \\ -s_\theta & s_\phi c_\theta & c_\phi c_\theta \end{bmatrix} \tag{3.20}$$

where sine and cosine terms (s_*, c_*) act on the attitude (ϕ, θ, ψ) of the element. Rotation matrices possess a special property where the inverse is equal to the transpose, $R^{-1} = R^T$, so mapping from the inertial frame to the body frame is accomplished with R^T.

Derivatives

Differentiation is performed with respect to a local frame. The relationship

$${}^N\frac{d}{dt}(v) = {}^B\frac{d}{dt}(v) + {}^N\omega^B \times v = \dot{v} + {}^N\omega^B \times v \tag{3.21}$$

equates the time derivatives in the body frame $\{B\}$, to the inertial frame $\{N\}$.

Notation

Two operators are introduce to keep the notation clean. The cross product of two vectors is equivalent to the matrix multiplication of a skew symmetric matrix and a vector, so that $\tilde{x}y = x \times y$, where

$$\tilde{x} = \begin{bmatrix} 0 & -x_3 & x_2 \\ x_3 & 0 & -x_1 \\ -x_2 & x_1 & 0 \end{bmatrix} \tag{3.22}$$

is the skew symmetric matrix of x. Similarly, a double cross product can be represented in matrix form, so that $\bar{x}y = x \times (x \times y)$, where

$$\bar{x} = \begin{bmatrix} -x_2^2 - x_3^2 & x_1 x_2 & x_1 x_3 \\ x_1 x_2 & -x_1^2 - x_3^2 & x_2 x_3 \\ x_1 x_3 & x_2 x_3 & -x_1^2 - x_2^2 \end{bmatrix} \tag{3.23}$$

is the matrix equivalent of the double cross product of x.

3.3.3 General Multibody Structure

This subsection establishes the groundwork for implementing the multibody dynamic routine. Before addressing the specifics of the TURN models, it is important to have a solid notion of how the numerical routine is assembled. First, the structure for two connected rigid bodies will be discussed. Next, a more general case will be made for multiple rigid bodies. Finally, a technique is presented which eliminates redundant states from the simulation structure.

Two Rigid Bodies

A two-body system, depicted in Figure 3.7, is the simplest case to consider . An inner body B_i is connected to an outer body B_o with a spherical joint at point G. The connection point has a joint force F_G and joint torque T_G, which are arbitrarily designated as acting in a positive sense on the inner body. Position vectors r_i and r_o extend from each CG to the connection point, and both bodies have an external force, F_i and F_o, and an external torque, T_i and T_o, acting on them.

Euler's equation outlines the two rotational relationships as

$$\begin{aligned} J_i \dot{\omega}_i &= T_i - \omega_i \times H_i + T_G + r_i \times F_G \\ J_o \dot{\omega}_o &= T_o - \omega_o \times H_o - T_G - r_o \times F_G \end{aligned} \tag{3.24}$$

where J_* is the moment of inertia, ω_* is the angular rate vector, and H_* is the angular momentum of the rigid body, for $* = i, o$. When there are no momentum storage devices, the angular momentum term is expressed as $H_* = J_* \omega_*$. Newton's Law yields the translational relationships as

$$m_i \dot{v}_i = F_i + F_G, \quad m_o \dot{v}_o = F_o - F_G \tag{3.25}$$

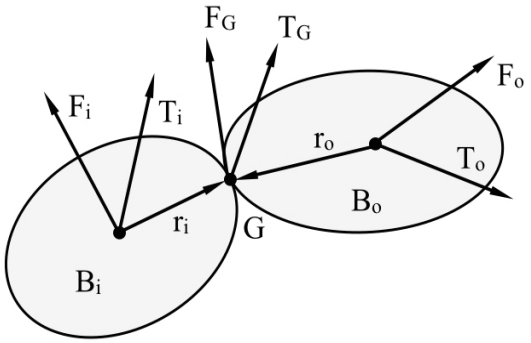

FIGURE 3.7: Two rigid body model.

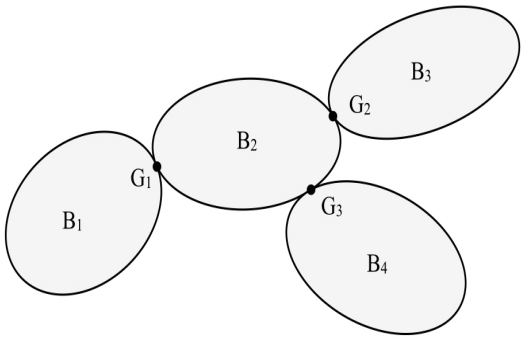

FIGURE 3.8: Multiple rigid body model.

where m_* is the mass, and v_* is the velocity vector of the rigid body, for $* = i, o$. A fifth relationship models the velocity of the joint constraint which is shared by both rigid bodies

$$v_G = v_i + \omega_i \times r_i = v_o + \omega_o \times r_o \tag{3.26}$$

which is equivalent to

$$\dot{v}_i + \dot{\omega}_i \times r_i + \bar{\omega}_i r_i = \dot{v}_o + \dot{\omega}_o \times r_o + \bar{\omega}_o r_o. \tag{3.27}$$

after differentiating within the inertial frame $\{N\}$.

Rotation matrices R are employed to convert between coordinate frames, identity matrices I enforce consistent dimensions, and the five dynamic equations are rearranged to accommodate a matrix structure. These operations produce

$$\begin{bmatrix} J_i & 0 & 0 & 0 & -\tilde{r}_i R_i^N \\ 0 & J_o & 0 & 0 & \tilde{r}_o R_o^N \\ 0 & 0 & m_i I_3 & 0 & -I_3 \\ 0 & 0 & 0 & m_o I_3 & I_3 \\ -R_N^i \tilde{r}_i^T & R_N^o \tilde{r}_o^T & -I_3 & I_3 & 0 \end{bmatrix} \begin{bmatrix} \dot{\omega}_i \\ \dot{\omega}_o \\ \dot{v}_i \\ \dot{v}_o \\ F_G \end{bmatrix} = \begin{bmatrix} T_i - \tilde{\omega}_i H_i + T_G \\ T_o - \tilde{\omega}_o H_o - R_o^i T_G \\ F_i \\ F_o \\ R_N^i \bar{\omega}_i r_i - R_N^o \bar{\omega}_o r_o \end{bmatrix} \tag{3.28}$$

which is the complete two-body dynamic model structure.

Multiple Rigid Bodies

The previous section laid the foundation for consolidating the equations of motion into a single matrix framework. This section builds upon that concept and further generalizes the system dynamics for multiple rigid bodies. An illustrative example of a four-body system is depicted in Figure 3.8. A connectivity table identifies the inner and outer bodies of each joint, presented in Table 3.1. Each joint connects two bodies, where i and o designate the inner and outer body, respectively.

	G1	G2	G3
B1	i		
B2	o	i	i
B3		o	
B4			o

TABLE 3.1: Sample four-body connectivity table.

Equations of motion are assembled by inspection using the connectivity table. The matrix relationship for a generic multiple rigid body system is given by

$$\begin{bmatrix} \bar{J} & 0 & \bar{R} \\ 0 & \bar{M} & \bar{I} \\ \bar{R}^T & \bar{I}^T & 0 \end{bmatrix} \begin{bmatrix} \dot{\omega} \\ \dot{v} \\ F \end{bmatrix} = \begin{bmatrix} \tau \\ \mathcal{F} \\ \mathcal{C} \end{bmatrix}. \tag{3.29}$$

Denote N as the total number of rigid body elements. The states of the system are stored in the first column vector, where $\omega \in \mathbb{R}^{3N}$ contains the angular velocities, $v \in \mathbb{R}^{3N}$ contains the linear velocities, and $F \in \mathbb{R}^{3(N-1)}$ contains the joint constraint forces. The right column vector stores the external torques in $\tau \in \mathbb{R}^{3N}$, the external forces in $\mathcal{F} \in \mathbb{R}^{3N}$, and the constraint relationships in $\mathcal{C} \in \mathbb{R}^{3(N-1)}$. The left matrix is populated with submatrices. Matrices $\bar{J}$ and $\bar{M}$ are each $\mathbb{R}^{3N\times 3N}$ diagonal matrices, which contain the masses and moment inertias for each rigid body element. The modified rotation matrix $\bar{R}$, and the modified identity matrix $\bar{I}$, are both $\mathbb{R}^{3N\times 3(N-1)}$, and follow the same structure as the connectivity table.

The modified identity matrix $\bar{I}$, has negative 3×3 identity matrices for inner body connections, and positive 3×3 identity matrices for outer body connections, formed as

$$\bar{I} = \begin{bmatrix} -I_3 & 0 & 0 \\ I_3 & -I_3 & -I_3 \\ 0 & I_3 & 0 \\ 0 & 0 & I_3 \end{bmatrix}. \tag{3.30}$$

The modified rotation matrix $\bar{R}$, follows an identical sign convention, but is populated with position vectors and rotation matrices, described by

$$\bar{R} = \begin{bmatrix} -\tilde{r}_{11}R_1^N & 0 & 0 \\ \tilde{r}_{21}R_2^N & -\tilde{r}_{22}R_2^N & -\tilde{r}_{23}R_2^N \\ 0 & \tilde{r}_{32}R_3^N & 0 \\ 0 & 0 & \tilde{r}_{43}R_4^N \end{bmatrix}. \tag{3.31}$$

This concludes the generalized procedure for implementing the dynamics of a generic multibody system. Because this approach utilizes a matrix structure, it is extremely favorable for running numerical simulations within a Matlab environment. Furthermore, this approach offers a degree

of modularity that is not available with other multibody formulations. Revising the model layout, or altering the number of rigid body elements, is reduced to a simple matter of bookkeeping.

Redundant State Elimination

The previous derivation was developed from a very intuitive standpoint, where all the interactions between the internal and external forces and moments were accounted for. Although this provides the maximum amount of information pertaining to the system, this formulation includes redundancy in the number of states. Reducing the system to a minimal number of states helps decrease the computational load while executing the simulation.

To formulate a minimal set, assume the internal forces acting on the joints are not of interest. Define an alternative state vector x, which includes the velocity of a single component and the angular rates of all the rigid bodies. Redundant states, which are the remaining rigid body velocities, are placed in an auxiliary vector y. The current task finds an alternative description to eliminate redundant states y and internal joint forces F. The state vector and auxiliary vector are defined as

$$x = \begin{bmatrix} \omega_1 \\ \vdots \\ \omega_N \\ v_1 \end{bmatrix}, \quad y = \begin{bmatrix} v_2 \\ \vdots \\ v_N \end{bmatrix} \tag{3.32}$$

where the velocity of interest, $v_1 \in \mathbb{R}^3$, is appended to the original angular rate vector to form x, and the remaining redundant states form y. The submatrices described in (3.29) need to be partitioned to account for this change in dimension. Define the new system as

$$\begin{bmatrix} \tilde{J} & 0 & \tilde{R} \\ 0 & \tilde{M} & \tilde{I} \\ \tilde{R}^T & \tilde{I}^T & 0 \end{bmatrix} \begin{bmatrix} \dot{x} \\ \dot{y} \\ F \end{bmatrix} = \begin{bmatrix} \tau \\ \mathcal{F} \\ \mathcal{C} \end{bmatrix} \tag{3.33}$$

where $\bar{J}$ and $\bar{R}$ increase in size, and $\bar{M}$ and $\bar{I}$ decrease in size, such that

$$\tilde{J} = \begin{bmatrix} \bar{J} & 0 \\ 0 & m_1 I_3 \end{bmatrix} \in \mathbb{R}^{3(N+1)\times 3(N+1)}, \quad \tilde{R} = \begin{bmatrix} \bar{R} \\ \bar{I}(1:3,:) \end{bmatrix} \in \mathbb{R}^{3(N+1)\times 3(N-1)} \tag{3.34}$$

and

$$\tilde{M} = \bar{M}(4{:}3N, 4{:}3N) \in \mathbb{R}^{3(N-1)\times 3(N-1)}, \quad \tilde{I} = \bar{I}(4{:}3N, :) \in \mathbb{R}^{3(N-1)\times 3(N-1)}. \tag{3.35}$$

Now decouple $\dot{x}$ from $\dot{y}$ and F using elementary row operations. Introduce two unknown coefficient matrices, α and β which are both $\mathbb{R}^{3(N+1)\times 3(N-1)}$. The row operated system is described by

$$\left[\begin{bmatrix} \tilde{J} & 0 & \tilde{R} \end{bmatrix} + \alpha \begin{bmatrix} 0 & \tilde{M} & \tilde{I} \end{bmatrix} + \beta \begin{bmatrix} \tilde{R}^T & \tilde{I}^T & 0 \end{bmatrix} \right] \begin{bmatrix} \dot{x} \\ \dot{y} \\ F \end{bmatrix} = \tau + \alpha\mathcal{F} + \beta\mathcal{C} \tag{3.36}$$

which is equivalent to

$$\left[\begin{array}{ccc} \tilde{J}+\beta\tilde{R}^T & \alpha\tilde{M}+\beta\tilde{I}^T & \tilde{R}+\alpha\tilde{I} \end{array}\right] \left[\begin{array}{c} \dot{x} \\ \dot{y} \\ F \end{array}\right] = \tau + \alpha\mathcal{F} + \beta\mathcal{C}. \tag{3.37}$$

Next, solve for α and β so that $\dot{y}$ and F have no influence on the system dynamics, which yields

$$\alpha = -\tilde{R}\tilde{I}^{-1}, \quad \beta = \tilde{R}\tilde{I}^{-1}\tilde{M}\tilde{I}^{-T} \tag{3.38}$$

so the desired form of the system dynamics reduces to

$$\left(\tilde{J}+\beta\tilde{R}^T\right)\dot{x} = \tau + \alpha\mathcal{F} + \beta\mathcal{C} \tag{3.39}$$

which is the set of differential equations used in the numerical routine. Submatrices $\tilde{J}$, $\tilde{M}$, and $\tilde{I}$ are all constant matrices which are known in advance; therefore, $-\tilde{I}^{-1}$ and $\tilde{I}^{-1}\tilde{M}\tilde{I}^{-T}$ are also constant matrices, and only need to be calculated prior to running the simulation. Thus, solving for α and β at each time increment only requires the multiplication of $\tilde{R}$ with these known constant matrices.

3.3.4 TURN Multibody Models

Previous content illustrated the general theory for implementing a numerical routine capable of modeling a multibody dynamics system within a Matlab simulation environment. The current discussion takes that general theory and applies it to several models that will be used throughout the remainder of the analysis. It presents a *Free Satellite Model* where an individual satellite operates as a flying wing without any tethers, a *Tether Arm Model* which is a single tethered system constrained to a fixed point, and a *Full System Model* which captures the complete TURN dynamics.

Beginning with the simplest starting point and adding capabilities over time, is the most logical progression for the development process. Thus, studying the *Free Satellite Model* is the ideal jumping-off point before working with more complex models. Technically, because this is a single rigid body structure, there is no formal requirement to utilize the multibody dynamics framework with this model. But to maintain consistency across all simulations, the multibody routine coded in Matlab is still used, but instructed to work with just the single element. This approach will be useful when expanding into planned future work. At a later time, flexibility within the wing section should be investigated, so a distinction must be made between rigid and flexible models. When takeoff and landing is considered in greater detail, the VTOL transition process is better studied as a single vehicle before tackling the added complexities of the full multibody dynamics system.

Part of the TURN development will build a scaled model prototype of the system. Before the complete system is flown in free flight, several development stages will work with a single satellite vehicle flying around a fixed pole, which will help evaluate hardware components and collect flight data. System identification techniques applied to the collected flight data will characterize the satellite and tether dynamics, which can be compared against simulation data to validate and

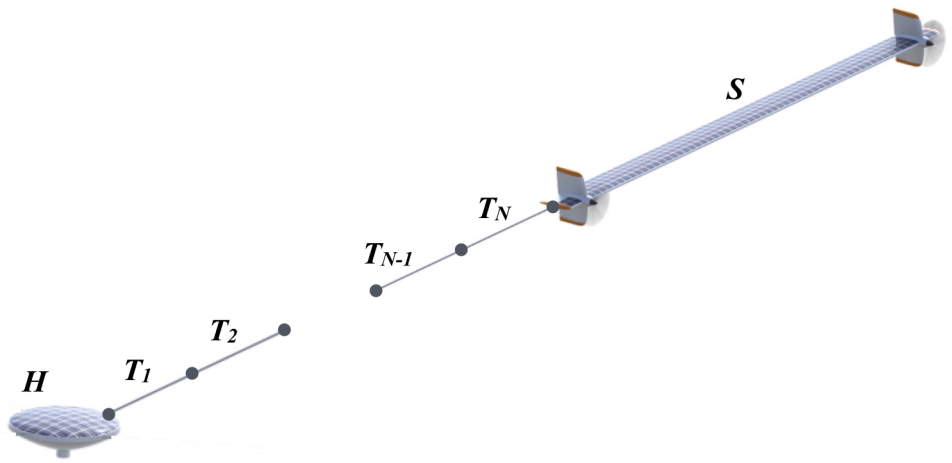

FIGURE 3.9: Diagram of the *Tether Arm Model*.

	G_1	G_2	$\dots$	G_N
H	i			
T_1	o	i		
T_2		o	i	
$\vdots$			$\ddots$	
T_N			o	i
S				o

TABLE 3.2: Connectivity table for the *Tether Arm Model*.

refine the simulation parameters. Therefore, a model of a single satellite system, described as the *Tether Arm Model*, shown in Figure 3.9, is needed for this future work.

The multibody structure requires one more rigid body than the number of constraints, so the central hub H must be included within the model. It should not translate with respect to the inertial frame, so it is modeled as an extremely large mass with no gravitational force acting on the element. The hub should mimic a bearing, and thus be constrained to only rotate freely around the vertical axis. So, moment of inertias J_x and J_y are assigned extremely large values, while J_z was prescribed a value of nearly zero. This provides a very good representation for a pole fixed in the inertial frame.

A single chain of n rigid bodies model the tether, which starts with the central hub H connected to tether link T_1, works outward to tether link T_n, and finishes with the satellite S element. The connectivity table has a very simple structure, provided in Table 3.2, which forms the reduced modified rotation matrix $\tilde{R}$ and the reduced modified identity matrix $\tilde{I}$, as described previously.

A complete TURN vehicle is represented by the *Full System Model*; including: the hub, four tether arms with satellites, and no external constraints on the system, as illustrated in Figure 3.10. While,

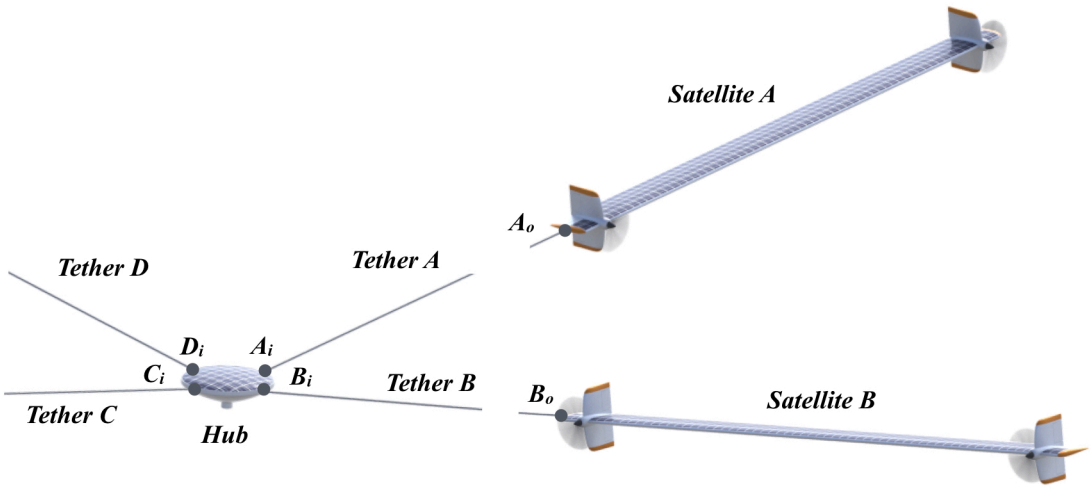

FIGURE 3.10: Diagram of the *Full System Model*.

	A_i	B_i	C_i	D_i	A_o	B_o	C_o	D_o
H	i	i	i	i				
T_A	o				i			
T_B		o				i		
T_C			o				i	
T_D				o				i
S_A					o			
S_B						o		
S_C							o	
S_D								o

TABLE 3.3: Connectivity table for the *Full System Model*.

several connectivity tables are possible, the most desirable configuration is one where simulation code can easily scale to accommodate different numbers of tether elements, or additional rigid bodies to model flexibility in the wing section. Because future work will incorporate a flexible wing into the model, an extra level of modularity was designed to accommodate this addition.

Rather than have a single massive framework comprising all the individual elements, the approach uses several smaller multibody objects to assemble the complete multibody system. For example, a multibody structure models a tether as a single chain of elements. Similarly, the rigid bodies for a satellite are housed in their own self-contained multibody structure. Finally, these subcomponents are used to make up the larger TURN system through nine distinct objects: the central hub, four flexible tether objects, and four flexible satellite objects. A connectivity table for this embodiment is shown in Table 3.3, where each tether and satellite object represent a smaller multibody subsystem.

3.4 Trimming

Modeled system dynamics establish how the system moves, and the multibody structure implements those equations of motion within the simulation. This section addresses trimming, which seeks the set of states and control inputs that attain a steady state equilibrium point. In other words, the set of values that where the system states and control inputs remain constant.

Trimming is an important milestone for several reasons. First, it obtains the values for specific flight conditions, like hover and forward flight. These steady state values are also needed to perform linearization, which is required to begin the controls analysis. Finally, the trimmed state values are used as system initial conditions prior running a simulation.

The TURN aircraft has a complicated nonlinear model with intertwined states and control inputs, so an analytic approach to determine equilibrium points is not possible. Matlab has built-in functions which can trim certain classes of problems; however, the special structure of the TURN multibody structure precludes the use of these existing functions. This section addresses limitations with traditional trimming routines applied to multibody dynamics problems, presents an alternative approach using nonlinear optimization techniques, and presents the specific procedure used to trim the TURN system models.

3.4.1 Problem Formulation

The objective is to find the system states $x(t)$ and control inputs $u(t)$ to attain an equilibrium point, which means the system is not accelerating. Achieving zero acceleration requires a force and moment balance within all the elements. Thus, the goal is to find values where the forces and moments sum to zero for every rigid body within the system. Following sections illustrate deficiencies with current trimming techniques, and then outlines a solution to overcome the problem.

Limitations When Trimming Multibody Systems

Many types of modeling problems are formulated as decoupled rigid bodies which are connected together through springs and dampers. Figure 3.11 illustrates this common modeling form. With

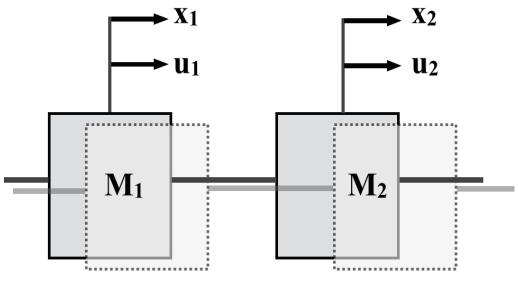

FIGURE 3.11: Typical model to trim.

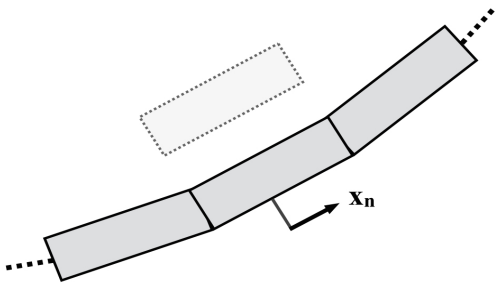

FIGURE 3.12: Multibody model to trim.

this arrangement, the masses and their states are independent of one another, so a single state can be perturbed while the others remain static. In the multibody dynamics structure, the rigid bodies must maintain joint constraints, so the states of the rigid bodies are not independent. Perturbing a single rigid body element leads to a disjoined chain structure, depicted in Figure 3.12. This is not a viable solution, so an alternative trimming procedure is needed to alleviate this concern.

Optimization Function

Trimming is a type of optimization problem (Lawson and Hanson, 1995). The Matlab function, `lsqnonlin`, is designed to solve nonlinear least-squares curve fitting problems. The input is defined as a vector $x \in \mathbb{R}^n$ with initial condition x_0, and the output $f(x)$ is a vector as a function of x, which can be described by

$$f(x) = [\ f_1(x)\ f_2(x)\ \cdots\ f_n(x)\ ]^T . \tag{3.40}$$

The optimization routine solves

$$\min_x \|f(x)\|_2^2 = \min_x \left(\ f_1(x)^2 + f_2(x)^2 + \cdots + f_n(x)^2\ \right) \tag{3.41}$$

which minimizes the squared Euclidean norm of the vector function.

Trimming Process Overview

Trimming is accomplished with two loops: an inner-loop and an outer-loop. The inner-loop starts at a tether anchor point and works outward to the satellite. An optimization is run on each tether element to achieve a force balance within that body, which is repeated all the way out to the satellite. After the satellite has been optimized, the entire tether arm satisfies a force balance condition. However, the lift generated by the satellite is dictated by its attitude, which is based on the initial values used at the central hub; so there is no assurance that the generated lift equals the required lift. An outer-loop optimization incrementally adjusts the hub rotation and anchor point forces, runs the inner-loop optimization again, and reevaluates the amount of lift generated. The outer-loop optimization continues until there is a force and moment balance within the entire system.

3.4.2 Implementing the Optimization Routine

An overview of the trimming process described the several different optimizations needed to trim the TURN vehicle. These include a tether force balance, tether projection, satellite force balance, and hub force balance. Following sections describe each of the steps in greater detail.

Tether Force Balance

Consider a single tether element. The goal is to identify a steady state equilibrium point, which is the unique orientation of the rigid body that achieves a force and moment balance. The forces to

consider include: the inner and outer joint constraint forces, F_{Ti} and F_{To}, a centrifugal force F_{Tc}, aerodynamic drag F_{Td}, and gravity F_{Tg}. Now consider the innermost tether section, where the inboard position, velocity, force on the tether joint constraint, and the angular rate of the central hub, are all initialized with suitable starting values. The orientation of the element dictates the CG location and the direction of the relative airflow across the tether section. Thus, these attitude states determine the drag force, centrifugal force, and outboard endpoint force. The optimization adjusts the orientation of the tether element until the force balance equality

$$F_{Ti} + F_{Tc} + F_{Td} + F_{Tg} + F_{To} = 0 \tag{3.42}$$

is satisfied. A similar relationship balances the moments acting on the tether element.

Tether Projection

The previous section outlined a process that takes an inboard tether state, balances the forces within the element, and returns the outboard tether state. Tether projection describes a program loop that sequentially balances all the elements within a tether arm. The loop starts with both the anchor force and the angular rate of the hub, and applies the optimization to the inner most tether element. The outboard states of this first element become the inboard states for the next element. The loop proceeds outward through each section until it reaches the final tether element. The outboard states of the final tether section are used as the anchor position, velocity and force for the satellite body.

Satellite Force Balance

The satellite optimization is very similar to the tether optimization. The tether endpoint states were determined from the tether projection loop, but the satellite attitude and control inputs are still unknown. As a starting point, the satellite is initialized with zero attitude, zero control surface deflection, and a reasonable guess value for throttle input. Inputs to the optimization include: tether endpoint states, tether endpoint forces, satellite orientation, and satellite control inputs. For this particular attitude, the program evaluates the centrifugal force and aerodynamic forces and moments, calculates the summation of forces and moments on the satellite, and compares this value to zero. The optimization incrementally adjusts the orientation of the satellite and the applied control inputs until the net forces and moments are reduced to zero. This completes the inner-loop.

Hub Force Balance

Previous sections described the inner-loop which balances an entire tether arm including the satellite entity. That process began with an initial guess for the hub anchor force and system angular rate. Using these initial guess values, the lift generated from the satellite may not equal the lift force needed for the system. Therefore, an outer-loop optimization is needed to balance the hub forces. The optimization compares the current lift generated by the satellite against the force required to

support the weight of the entire system. It also balances the moment generated by the tether force with the rotational aerodynamic drag from the spinning hub. If the net forces and moments are nonzero, the optimization routine adjusts the angular rate and anchor forces on the hub, and runs another inner-loop optimization. This iterative process continues until the central hub and satellite achieve static equilibrium. Once the TURN system is completely balanced, the states and control inputs are stored as initial conditions for the simulation and as operating points for linearization.

3.4.3 Obtaining Initial Guess Values

All the optimization routines require initial conditions to begin each process. Values for the inner-loop optimizations, including the tether elements and the satellite, are initialized at each new iteration within the projection loop. However, the outer-loop initial conditions, which are the system angular rate and anchor forces on the central hub, are still unaccounted for. This section presents the derivations which yield approximate values that are suitable for initializing the outer-loop optimization. It determines the lift force, linear velocity, and position of the satellite, which are subsequently used to estimate the hub angular rate and anchor forces.

Satellite Lift Force

Masses for all the rigid body elements are known, so the first step calculates the total weight of the system. Assuming n represents the number of tether arms on the vehicle, the vertical component of the lift force vector, generated from each satellite wing, must support $1/n$ of the total weight of the system. The program stores the required vertical lift force F_S which is used in the next section.

Satellite Velocity

The lift equation is governed by

$$F_S = \frac{1}{2}\,\rho\, v_S^2\, A\, c_{SL} \tag{3.43}$$

where F_S is the previously calculated vertical lift force from the satellite, ρ is the density of air, v_S is the forward linear velocity of the satellite, A is the planform area of the wing, and c_{SL} is the lift coefficient of the satellite wing. The only unknown value in this relationship is the velocity of the satellite, so rearrange terms such that

$$v_S = \sqrt{\frac{2\,F_S}{\rho\, A\, c_{SL}}} \tag{3.44}$$

which yields the forward velocity v_S required to achieve the desired satellite lift force F_S. This equality assumes a level flight condition, but the trimmed satellite attitude will have a slightly nonzero inclination, so the actual trimmed velocity is expected to be slightly greater.

Satellite Position

During flight the tether will curve from aerodynamic drag forces and from the force of gravity. The amount of curvature is unknown until after the optimization routine. As a starting point, assume the tether has no curvature and projects straight out toward the satellite. The hub anchor position, the length of the tether, and the satellite anchor position all have known dimensions. Thus, they can be summed together to obtain r_S, an approximate initial radius for the satellite.

System Angular Rate

While operating in a trimmed state, the angular rate of the satellite will match that of the central hub. The next step uses the approximate satellite radius and linear velocity, to estimate the angular rate of the central hub. Relating the satellite radial length r_S and linear velocity v_S through

$$\omega_H = \omega_S = \frac{v_S}{r_S}. \tag{3.45}$$

yields ω_H and ω_S, the estimated angular velocities of the hub and satellite, respectively.

Hub Anchor Force

A final set of calculations estimate each component of the force vector acting on the central hub anchor points. The estimated satellite radial length r_S and the hub angular rate ω_H are used to determine the pull from the centrifugal force F_x, described by

$$F_x = m_S \, r_S \, \omega_H^2 \tag{3.46}$$

where m_S is the satellite mass. A lateral force from rotational aerodynamic drag F_y, is given as

$$F_y = \frac{1}{n} \frac{c_{Hdmz} \, \omega_H^2}{r} \tag{3.47}$$

where $M_{Hdz} = c_{Hdmz} \, \omega_H^2$ describes the z-axis moment on the hub for a particular angular rate, r is the distance from the hub CG to the tether anchor point, and the $1/n$ term equally distributes the force among each of the satellite anchor points. The vertical force component F_z, is influenced by gravity g and the mass of the hub m_H described by

$$F_z = -\frac{1}{n} \, m_H \, g \tag{3.48}$$

where the $1/n$ term distributes the gravitational force among each tether arm, and the negative sign is needed to remain consistent with the coordinate frame designation.

3.5 Linearization

Thus far, the TURN plant has a set of nonlinear dynamics implemented within the simulation and a process for obtaining trimmed states and control inputs around a desired operating point. The last step toward developing the TURN plant description, takes the nonlinear system and identifies a linear models around those trimmed operating points. Linearization is an important topic because the vast majority of the controls theory is applied to linear systems. Linearizing a multibody dynamic problem has many of the same hurdles as with trimming, so this research utilizes the alternative trimming technique and adapts it to the linearization process for multibody dynamic systems. This section presents the Taylor series expansion of a nonlinear model, describes how the partial derivatives form the state space matrices within the linear system, addresses issues with linearizing multibody dynamics problems, and proposes an alternative approach.

3.5.1 Taylor Series Expansion

The equations of motion of the plant are expressed in compact form as $\dot{x}(t) = f(x(t), u(t))$ where $x(t) \in \mathbb{R}^n$ are the n states of the plant and $u(t) \in \mathbb{R}^m$ are the m control inputs. Denote an operating point as $\hat{x}$ and $\hat{u}$, so that perturbations are described by $\Delta x = x - \hat{x}$ and $\Delta u = u - \hat{u}$.

A Taylor series expansion for the nonlinear system is described by

$$\dot{x} = f(x,u) \cong f(\hat{x},\hat{u}) + \left.\frac{\partial f}{\partial x}\right|_{(\hat{x},\hat{u})} (x - \hat{x}) + \left.\frac{\partial f}{\partial u}\right|_{(\hat{x},\hat{u})} (u - \hat{u}) + HOT \tag{3.49}$$

and disregarding the higher order terms (HOT), yields the form

$$\Delta\dot{x} = f(\hat{x},\hat{u}) + A\Delta x + B\Delta u \tag{3.50}$$

where matrices defined as

$$A = \begin{bmatrix} \frac{\partial f_1}{\partial x_1} & \frac{\partial f_1}{\partial x_2} & \cdots & \frac{\partial f_1}{\partial x_n} \\ \frac{\partial f_2}{\partial x_1} & & & \\ \vdots & & \ddots & \vdots \\ \frac{\partial f_n}{\partial x_1} & & \cdots & \frac{\partial f_n}{\partial x_n} \end{bmatrix}, \quad B = \begin{bmatrix} \frac{\partial f_1}{\partial u_1} & \frac{\partial f_1}{\partial u_2} & \cdots & \frac{\partial f_1}{\partial u_m} \\ \frac{\partial f_2}{\partial u_1} & & & \\ \vdots & & \ddots & \vdots \\ \frac{\partial f_m}{\partial u_1} & & \cdots & \frac{\partial f_m}{\partial u_m} \end{bmatrix}. \tag{3.51}$$

represent the state matrix A, and the input matrix B, used in state space form.

When an operating point is also an equilibrium point, meaning the derivatives are exactly equal zero, then $f(\hat{x},\hat{u}) = 0$ and the system reduces to $\Delta\dot{x} = A\Delta x + B\Delta u$, where future equations omit the Δ symbol for readability.

3.5.2 Process Applied to Multibody Systems

For simple systems with closed form solutions, the partial derivative terms that form the A and B matrices may be obtained by hand calculations. Because the TURN system requires a numerical routine, and does not have a closed-form solution, this is not a viable option. Matlab has built-in functions that linearize a wide range of systems. However, the Matlab process is expecting a model that resembles Figure 3.11, which is not suitable for multibody problems.

An alternative approach is used. For each entry in the A matrix, select a single state (x_j) at equilibrium. Adjust this value by a small increment δ in both directions of its nominal trimmed value (x_j^+, x_j^-), while all other states are kept at their equilibrium values. For reference, call this the *ideal perturbed state vector*. Traditional trimming routines run the system dynamics at this point; but for a multibody problem, the perturbed system resembles Figure 3.12, which is not a valid configuration.

The ideal perturbed state vector does not maintain the physical constraints of the problem, so an alternative vector is sought. The goal is to find the set of states that are as close as possible to the ideal perturbed state vector, and call this new set the *actual perturbed state vector*. Run `lsqnonlin` optimization to find the "closest match", which minimizes the Euclidean norm of the difference between the ideal perturbed state vector and the actual perturbed state vector.

Using x_j^+ and x_j^-, two optimizations return two actual perturbed state vectors $\bar{x}_j^+$ and $\bar{x}_j^-$. These state vectors are passed into the system dynamics, which return two derivative function vectors

$$f_j^+ = f(\bar{x}_j^+, u), \quad f_j^- = f(\bar{x}_j^-, u). \tag{3.52}$$

Working through each row of the derivative vector yields the partial derivatives

$$\frac{\partial f_i}{\partial x_j} \approx \frac{f_{ji}^+ - f_{ji}^-}{x_j^+ - x_j^-} = \frac{f_{ji}^+ - f_{ji}^-}{2\delta}. \tag{3.53}$$

A Matlab code runs through an iterative loop which applies this process to each derivative function vector f_j, and each system state vector x_j; for $i = 1, \ldots, n$, and $j = 1, \ldots, n$. This process yields the values which populate the state matrix A; and an identical process is implemented with the control inputs u, to derive the input matrix B.

3.5.3 Structure of a Linearized TURN Satellite

Subsequent chapters will first outline the states and control inputs needed to implement the linearization process, and then present the satellite parameters used to obtain the numerical values within the state space matrices. However, some of the motivation for the controller development is based on the internal structure of the linearized system, so a general description is provided here.

A more complete description of the system states and control inputs will be developed in the next chapter. For the purposes of this subsection, the twelve system states are a collection of rotational

and translational terms, and their derivatives, described by

$$x_{\mathtt{sat}}(t) = \left[\ \phi,\ \theta,\ \psi,\ x,\ y,\ z,\ \dot{\phi},\ \dot{\theta},\ \dot{\psi},\ \dot{x},\ \dot{y},\ \dot{z}\ \right]^T \in \mathbb{R}^{12} \tag{3.54}$$

which describes the state vector. Six control inputs are control surface deflections for the ailerons, elevator, rudders, and stabilizers, as well as the angular rate of the motor systems, given as

$$u_{\mathtt{lin}}(t) = [\ \delta_{ai},\ \delta_{ao},\ \delta_e,\ \delta_r,\ \delta_s,\ \omega\ ]^T \in \mathbb{R}^6 \tag{3.55}$$

which describes the control input vector.

Applying the linearization process to the unconstrained satellite vehicle yields

$$A_{\mathtt{lin}} = \begin{bmatrix} 0_{3\times3} & 0_{3\times3} & I_{3\times3} & 0_{3\times3} \\ 0_{3\times3} & 0_{3\times3} & 0_{3\times3} & I_{3\times3} \\ A_{rr} & 0_{3\times3} & 0_{3\times3} & A_{rt} \\ A_{tr} & 0_{3\times3} & 0_{3\times3} & A_{tt} \end{bmatrix} \in \mathbb{R}^{12\times12} \tag{3.56}$$

which is the state matrix of the linearized system, where

$$\begin{aligned} A_{rr} &= \begin{bmatrix} 0 & 0 & 0 \\ 0 & a_{rr(22)} & 0 \\ 0 & 0 & a_{rr(33)} \end{bmatrix} \quad A_{rt} = \begin{bmatrix} 0 & 0 & 0 \\ 0 & 0 & a_{rt(23)} \\ 0 & a_{rt(32)} & 0 \end{bmatrix} \\ A_{tr} &= \begin{bmatrix} 0 & a_{tr(12)} & 0 \\ a_{tr(21)} & 0 & a_{tr(23)} \\ 0 & a_{tr(32)} & 0 \end{bmatrix} \quad A_{tt} = \begin{bmatrix} a_{tt(11)} & 0 & a_{tt(13)} \\ 0 & a_{tt(22)} & 0 \\ a_{tt(31)} & 0 & a_{tt(33)} \end{bmatrix} \end{aligned} \tag{3.57}$$

are the submatrices within the state matrix, and where subscripts r and t denote groupings of rotational and translational terms, respectively. Similarly, the linearization process yields

$$B_{\mathtt{lin}} = \begin{bmatrix} & & & 0_{6\times6} & & \\ b_{(11)} & b_{(12)} & 0 & 0 & 0 & 0 \\ b_{(21)} & b_{(22)} & b_{(23)} & 0 & 0 & 0 \\ 0 & 0 & 0 & b_{(34)} & b_{(35)} & 0 \\ 0 & 0 & b_{(43)} & 0 & 0 & b_{(46)} \\ 0 & 0 & 0 & b_{(54)} & b_{(55)} & 0 \\ b_{(61)} & b_{(62)} & b_{(63)} & 0 & 0 & 0 \end{bmatrix} \tag{3.58}$$

which is the input matrix of the linearized system. These matrices represent the starting point for all the controls development in the next chapter.

Chapter 4

Controls Analysis

All the groundwork for deriving and modeling the equations of motion, which describe the nonlinear dynamics implemented within the multibody simulation, were presented in the previous chapter; which concluded by trimming and linearizing the simulated Tethered Uni-Rotor Network (TURN) system. With this foundation in place, it is time to address the primary focus of this research effort: controlling this novel and extremely unconventional unmanned aerial vehicle (UAV). Early controls development for the TURN system were published in (Selfridge and Tao, 2015a), but this current effort works with an improved vehicle design, and implements more sophisticated control strategies. This chapter opens with a general description of the control objective, along with a preliminary analysis of how to accomplish the task with the prescribed plant. Then, it investigates three distinct control loops, which are responsible for: controlling the satellite, managing the tether arms, and manipulating the central hub.

Chapter Motivation

From early on, the ability to adequately control the TURN system was identified as the largest risk, while attempting to implement this unique concept design. Whereas, new aircraft designs can utilize existing wind tunnel data and control derivatives from other similar aircraft, there is no existing model or research to initiate the TURN development. Because this vehicle is a radical departure from conventional design methodologies, there is no preexisting dogma that claims a particular control strategy is best suited for this type of architecture. Developing and evaluating the control system within a simulation environment is of paramount importance for several reasons.

For starters, realize that the full TURN system does not have any direct control over the central hub. Stabilizing and maneuvering the hub, as well as the rest of the system, is implemented indirectly by coordinating the tension in the tether arms. This is accomplished by manipulating the control inputs that act on each individual satellite vehicle. Investigating how the controller performs amidst these multibody interactions is a necessary first step before tackling vehicle design improvements.

Before addressing the specifics of the controller architecture, a more general understanding of what needs to be accomplished, is in order. Because the TURN vehicle represents an intertwined multi-body dynamic model, a single all-encompassing controller structure is ill-advised; rather, it should be decomposed into several smaller structures, which are more manageable subsystems to control. Because the system dynamics are largely unknown, a reliance on adaptive control techniques is needed to mitigate the risk inherent from the inaccuracies of the untested simulation model. Similarly, a minimal number of requirements should be placed on the *a priori* knowledge of the plant. For all these reasons, successfully implementing the TURN controller within a simulation, is the first step towards advancing the project to the next level.

Finally, as part of the larger development program, a prototype system will be constructed to: test avionics hardware, collect flight data, perform system identification, and validate existing simulation models. But as previously shown, the dynamics are highly nonlinear, so paper analysis and hand derivations are not sufficient enough to develop the controllers for the first prototypes. With no other data to work with, the controller presented in this work represents the first that will be implemented. Evaluating this controller within a simulation environment, will help to gain confidence in both the controller and the vehicle dynamics before executing it on a physical prototype.

Chapter Objectives

The primary goal of this initial research is to demonstrate that the TURN vehicle is a viable design concept; and that a feasible controller architecture exists, which can successfully navigate the system, and mitigate disturbances. Prerequisite knowledge that is needed before applying these techniques is available for review in the numerous appendices. In general, they begin by presenting fundamental concepts, and then graduate to more advanced strategies.

Before jumping into the specifics of the controls design, the goal is to provide a top-level understanding of the overall methodology. This both, yields a road map leading the development process, and provides motivation for the proposed controller architecture. This chapter illustrates the rationale for decomposing the TURN vehicle into three distinct control systems: stabilization to control the satellite, an inner-loop to manage the tether arms, and an outer-loop to manipulate the central hub. Then it outlines the required characteristics of the plant, which must be present within the TURN system, to implement the controls strategies.

After developing a firm foundation, the next objective is to develop the controllers for each of the three subsystems. All the satellite states are directly measured, so state feedback is employed for the stabilization process. Inner-loop control is responsible for managing the relative positions of the satellites with respect to the central hub, but these states are not available for measurement, so output feedback is used to work around this limitation. Both of these controllers utilize a type of multiple-input multiple-output (MIMO) model reference adaptive control (MRAC), which incorporate an LDS decomposition of the high-frequency gain (HFG) matrix into the adaptation process. The intent it to show how this approach includes plant uncertainty within the estimation scheme, thereby reducing the amount of information needed *a priori*. Finally, the outer-loop system has

dual modes of control available for each translation, so this chapter will present a novel controls approach which borrows techniques commonly used within complementary filter designs.

Chapter Outline

Before assessing any eternal flight capabilities, or showcasing any prototype flight demonstrators, the TURN vehicle must exhibit an ability to be controlled during flight. This chapter focuses on the controls theory and analysis to address this issue.

Section 4.1 provides a *General Description* of the development process, which makes the TURN control problem more tractable. It describes the controller methodology through an alternative perspective, defines the control subsystems, and draws parallels to the simulation development.

Section 4.2 investigates the *Plant Attributes*, which are pieces used within the controller derivations. It describes the modified left interactor matrix, HFG matrix, LDS decomposition, necessary assumptions placed on the plant, and applicability to a TURN system configuration.

Section 4.3 derives an *LDS Based MRAC Architecture*, which is applicable for all output tracking controller designs. It parameterizes the control law, defines the tracking error, incorporates the LDS decomposition, obtains suitable adaptive laws, and reviews the stability properties of the system.

Section 4.4 performs a *Satellite Assessment* to analyze in greater detail, the only TURN component with control inputs. It establishes the system state space realization; reviews control input mixing, the relative gain array, and controllability; and implements the desired system response.

Section 4.5 achieves *Stabilization Via State Feedback MRAC*, which is responsible for controlling each independent satellite vehicle with state feedback. It is a MIMO MRAC architecture, which uses an LDS decomposition of the HFG matrix, and is suitable when all states are directly measured.

Section 4.6 considers the *Inner-Loop Via Output Feedback MRAC*, which manages each tether arm through output feedback. It is also a MIMO MRAC architecture, which again uses an LDS decomposition of the HFG matrix, but is more appropriate when states are not available for measurement.

Section 4.7 discusses the *Outer-Loop Via Complementary Filter*, which manipulates the central hub. It describes the two available control modes for each translation, how they are blended together with high-pass and low-pass filters, and then implemented through collective and cyclic commands.

4.1 General Description

At first glance, controlling the TURN vehicle appears to be a very complicated undertaking, which will require full cooperation from a great number of different entities. However, this research will show that a slight shift in perspective makes the control problem much more tractable. This section provides a general description of the TURN controller structure, which serves as a road map, and guides the remainder of the research development. The overall controller methodology illustrates an alternative perspective, which helps define what the controller needs to accomplish to move the

system globally. Then it addresses how to achieve the control objective, by describing the roles of three distinct control loops. Finally, it draws a parallel between the current controls analysis and both the simulation study and the prototype hardware development.

4.1.1 Control Methodology

Prior to diving into the specifics of the control theory, an overview of the control methodology serves as a road map, which guides the control development process. It starts with the most general description within the inertial frame, and moves toward the specifics in the local satellite frames. It provides an alternative perspective which is needed to redefine standard conventions, describes the approach used to maneuver the system globally, and then illustrates how this is accomplished by manipulating tension within the tethers.

Alternative Perspective

Controlling the TURN vehicle appears to be a very complicated task. With many different states, multiple tethers and satellites, and force interactions pulling on the central hub, the problem appears to require full cooperation from all entities involved. In many ways, the coordinated effort resembles a highway traffic system. When viewed from above, the number of vehicles and potential routes make the traffic system appear unmanageable. However, driving is a very simple task as as seen from the driver seat. As long as each driver adheres to basic rules, such as: stay centered within a lane, keep a safe following distance, and obey traffic signals; the complex driving system becomes much more tractable.

A similar approach can be applied to the TURN vehicle. Imagine sitting on the hub while peering at an individual satellite; which is operating in a trimmed state, and free of external disturbances. From this perspective the satellite will maintain a static position relative to the hub; it will appear to be "fixed" in space, with respect to that vantage point. The control objective is to identify meaningful relative positions of the satellite with respect to the central hub, and then apply control signals to manipulate the relative states of the satellite. By altering these relative states, the force vector of the tether, which is anchored at the central hub, also changes. Manipulating these tether anchor forces, can be used to influence the state of the central hub, and thus control the entire TURN system.

Redefine Standard Conventions

Because the TURN system exhibits a unique configuration, well established aviation terminology is not suitable to adequately describe this application. Roll and pitch are synonymous, because there is no "nose" or "side" to differentiate between them. Roll and pitch describe the same flight maneuver for any prescribed heading within the inertial frame. Likewise, yaw is arbitrary, because the system rotates constantly. Yaw only has meaning when referring to an instrument, like a camera system, which needs to maintain a static heading. Accounting for the custom TURN geometry, only two inertial descriptions are needed: vertical translation and horizontal translation.

Translation in the Inertial Frame

Borrowing from rotorcraft terminology; vertical translation utilizes collective control inputs, where the inputs adjust in unison; and horizontal translation uses cyclic control inputs, where the inputs are applied sinusoidally throughout the rotation cycle. Both horizontal and vertical translations each have two control modes available to induce each type of motion. For both, one mode achieves a faster transient dynamic response, while the other mode exhibits a slower steady state response.

Vertical Translation: For vertical translation, the first mode applies an elevator command, which is the faster dynamic response mode. This command changes the satellite pitch angle, which points the nose of the satellite up or down. With all satellites pointing upward or downward, the system enters into a spiral climb or descent. The other mode applies collective throttle commands, which is the slower dynamic response. This command adjusts the satellite velocity, which changes the amount of airflow over the wing, and subsequently influences the lift force acting on each satellite. Changing the lift force on each the satellites in unison, results in a climb or a descent.

Horizontal Translation: Similarly, two cyclic control modes exist for horizontal translation. The first mode applies cyclic stabilizer commands, which is the faster dynamic response mode. This introduces a lateral force on the satellite, which alters the radial tension in the tethers acting on the hub. The command is cyclic, so at one point in the rotation, there is a maximum outward tension, and at the opposite side, there is a minimum radial tension. Because the forces are imbalanced, the TURN system translates horizontally in the direction of the maximum tension. Cyclic complementary aileron commands can also achieve horizontal translation, which is the slower dynamic response. This command influences the relative vertical position of the satellites, so each satellite flies through the same low elevation point on one side of the rotation, and a high elevation point on the directly opposite side. This coordinated flight has the effect of tilting the entire rotor plane of the system, and thus reorients the overall force vector, which causes the system to move horizontally. This type of thrust vectoring to achieve translation, is exactly how traditional multirotors travel laterally.

Tether Manipulation Through the Satellite

Whereas, the previous section described a collection of coordinated maneuvers among the satellites, which achieves a linear velocity within the central hub, the next task formulates how that control will be implemented. Recognize that the central hub has no control inputs of its own, so all control is accomplished through the satellites, which indirectly influence the central hub through tether forces. Each tether connection point has three force vector components: a radial force from centrifugal stiffening, a horizontal force overcoming aerodynamic drag, and a vertical force exerted from the weight of the hub. The next subsections look at each force component in detail, and describe how manipulating satellites acts as a proxy for exerting tether forces on the central hub.

Centrifugal Force Component: Because the system is constantly rotating, a centrifugal force creates a radial tension, which pulls outward on the hub anchor point. Adjusting the lateral force on the satellite, changes the magnitude of the radial force acting on the hub. A lateral satellite force away from the hub increases the radial tension, while a lateral force toward the hub decreases the radial

tension. Vertical stabilizers influence the lateral force acting on the satellite, and subsequently the radial force on the central hub. Radial force manipulation is the most stable subsystem, because the forces from the control surfaces are closely aligned with the tether, and stabilizing centrifugal forces are self-correcting for any yaw disturbances on the satellite.

Aerodynamic Drag Force Component: Because the tether and satellites are moving through a fluid, an aerodynamic drag creates a horizontal tension, which pulls laterally on the hub anchor point. Adjusting the relative horizontal position away from its trimmed operating point, changes the magnitude of the horizontal force acting on the hub. A relative satellite position leading the trim position increases the horizontal tension, and a relative satellite position lagging the trim position decreases the horizontal tension. Complementary throttle commands adjust the motor forces, which influence the forward satellite position relative to its trim point. Lateral force manipulation is the most cumbersome subsystem, because the high lift-to-drag ratio satellite has very small motor forces relative to its mass, so there is limited control bandwidth to implement the command.

Weight Force Component: Because the tether arms support the weight of the hub, a gravitational force is offset by a vertical tension, which pulls upward on the hub anchor point. Adjusting the relative vertical position away from its trimmed operating point, changes the magnitude of the vertical force acting on the hub. A relative satellite position above the trim point increases vertical tension, and a relative satellite position below the trim point decreases the vertical tension. Complementary aileron commands influence the vertical satellite position relative to its trim point. Because the aileron forces are closely aligned with the satellite CG, vertical force manipulation is a relatively docile subsystem. However, some cross-coupling introduces a pitch disturbance, where the satellite is free to pivot around an axis parallel to the tether, with limited restoring forces.

4.1.2 Control Loop Definitions

Previous sections described the road map for using satellites to influence the tether tension on the hub, which subsequently moves the TURN system globally. Using that as guide, indicates that three distinct control loops are required for the control architecture, so the current task assesses how each the controllers operate to realize that process. Whereas, the previous description started globally and worked toward specifics, this section starts with the innermost foundation and builds upon itself. Stabilization controllers work directly on each of the satellite vehicles, inner-loop controllers are responsible for adjusting relative positions between the hub and satellites, and an outer-loop controller coordinates these activities, which dictate the locomotion of the entire system.

Stabilization Control Manages the Satellite

Consider an unconstrained satellite vehicle, maintaining a level attitude, while operating in forward flight. Vehicle pitch is articulated with the elevator, and the pair of ailerons influence both roll and vertical translation of the vehicle, through differential and complementary inputs, respectively. Complementary commands applied to the rudders, throttles, and vertical stabilizers influence the

yaw, forward velocity, and lateral velocity, respectively. These are idealized relationships, so some cross-coupling is to be expected. For example, the predominant state impacted by the complementary aileron command is vertical translation, but there will also be some torques generated which influence the satellite pitch. Hovering the unconstrained satellite while in a vertical orientation, utilizes an identical control process. The only difference being a rotated coordinate frame and the motors support some additional weight when the wing section is not used. Because all the states are available for measurement, full state feedback control is most appropriate. This control loop works with the *Free Satellite Model* described in the previous chapter.

Inner-Loop Control Manages the Tether Arm

Having full control of the satellite, next consider the tether arms. Inner-loop control manages each tether arm; such that, relative positions of the satellites act as proxies, which mirror the component forces of the tether, and are used to influence the central hub. Thus, relative satellite positions outside trimmed operating points are considered to be system outputs, and component forces arising from tether anchor points are defined as the system inputs. Whereas, all the satellite states are available for measurement, the relative satellite positions with respect to the central hub are not directly known, so an output feedback controller is employed. This control loop works with the *Tether Arm Model* described in the previous chapter.

Outer-Loop Control Manages the Central Hub

With a means of managing the tether arms, consider the complete TURN system. Outer-loop control manages the central hub; such that, the components of the tether force vectors are used to influence the state of the hub, which moves the TURN vehicle vertically and horizontally within the inertial frame. Thus, the controller determines the desired tether forces, and the inertial states of the central hub are deemed the system outputs. Unlike the satellite and tether control loops, the outer-loop has more control inputs than are required to manipulate the system outputs; which represents an underdetermined linear system with an infinite number of solutions. Furthermore, each translation has two modes of control available, which need to work harmoniously. A novel controls approach is devised which borrows techniques commonly used with complementary filter designs. This control loop works with the *Full System Model* described in the previous chapter.

4.1.3 Controller Structure

An overview of the complete TURN controller structure is provided in Figure 4.1. The desired inertial states are fed into the outer-loop controller $C_{\texttt{Hub}}$, which determines the desired tether forces for each of the four tether arms. Each tether arm runs its own inner-loop controller $C_{\texttt{Tet}}$, which takes the desired forces and determines appropriate satellite relative positions. Each of these positions outside the trimmed operating point is fed into the stabilization control loop $C_{\texttt{Sat}}$ which determines the forces and moments applied to each satellite body. The control inputs applied to

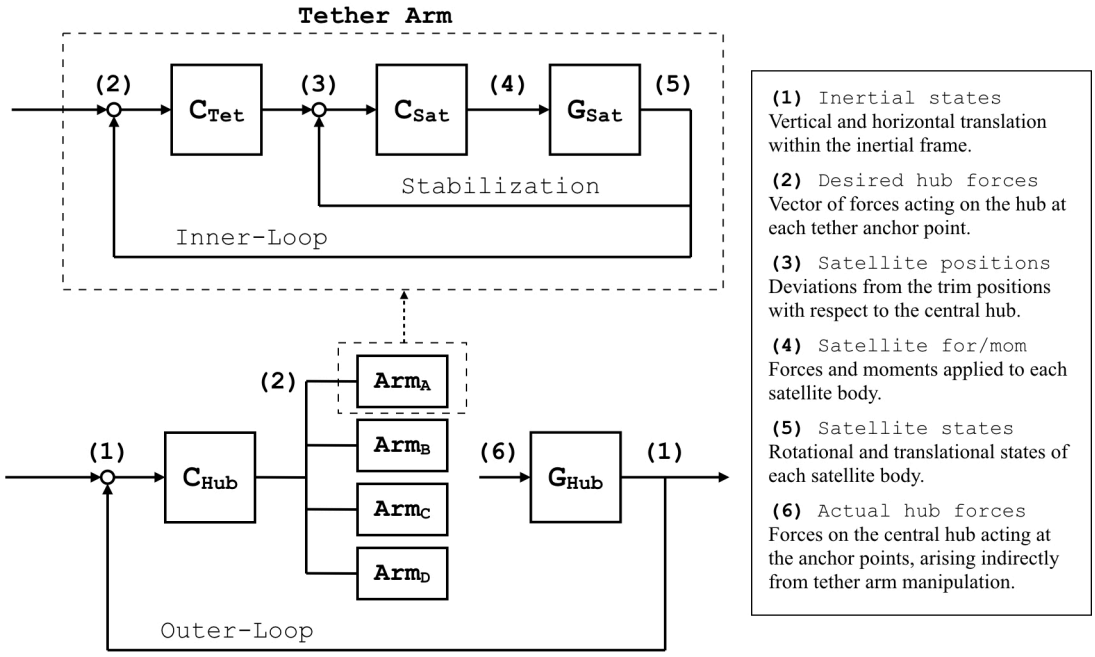

FIGURE 4.1: Block diagram of the controller structure.

the satellite plant G_{Sat}, yield the states of each satellite vehicle. The tether arms have no direct control over the central hub, but the relative positions of each satellite influence the tether forces acting on the central hub, which act as inputs to the central hub plant dynamics G_{Hub}, where the output is the translational states expressed in the inertial frame.

4.1.4 Parallel with Simulation Study and Prototype Development

The TURN project follows a spiral development life cycle. Because of its novel design, very little existing research aids the investigation. To minimize risk during early development, small incremental steps are taken to: learn about the system, collect flight data, and refine simulation models. More advanced techniques are introduced over time, building upon previous lessons learned.

The first TURN prototype demonstration will be an unconstrained flying wing satellite, which showcases: its VTOL capabilities, a transformational flight process, and the forward flight configuration. This vehicle will help evaluate avionics hardware, and system identification will improve the satellite simulation model before adding the complexities of the tether interactions.

The next iteration implements a tether arm flight. For this model, a single satellite is constrained to a fixed pole. The main objective is to: identify trimmed control inputs, assess the capabilities of the output-feedback controller, and perform system identification on the tether arm subcomponent. Collected data is compared to simulation data, and both the dynamic model and the controller gains are revised to more closely match the physical system.

The next milestone is a coordinated flight, where four satellites are connected to a constrained central hub. The primary objective is to: maintain equal spacing between the satellites, and test coordinated flight maneuvers. Equal spacing between satellites is a prerequisite before graduating to more elaborate maneuvers. Then, coordinated flights are used to demonstrate collective and cyclic commands within a controlled environment, before advancing to a free flight demonstration.

The final stage implements the free flight model, which is the fully unconstrained TURN system. The objective is to: demonstrate hover abilities, and achieve waypoint navigation through coordinated flight maneuvers. Once a flying prototype is available, the research will investigate disturbance rejection on the prototype, and evaluate the effectiveness of the various adaptive controllers.

Of course, the controllers need to be validated and refined through simulation analysis, prior to implementing them on prototype vehicles. The simulation study, has an identical parallel with the anticipated prototype development, where each of the three control loops are investigated in turn. A more complete description of the simulations is presented within *Chapter 5: Simulation Study*.

4.2 Plant Attributes

Three distinct controller architectures will be presented in subsequent sections. But first, some preliminary discussion is in order. To begin, this section describes the system to be controlled; the plant. Then, it outlines the relationship between the interactor matrix and the HFG matrix, summarizes the LDS decomposition, and presents the assumptions that need to be satisfied prior to implementing the control strategies. Finally, it concludes with an overview of how these general conditions are applicable for the TURN configuration.

4.2.1 Plant Description

Consider a general MIMO linear time-invariant (LTI) system, described in state space form as

$$\dot{x}(t) = A\,x(t) + B\,u(t), \quad y(t) = C\,x(t) \tag{4.1}$$

with the following vector signals: $x(t) \in \mathbb{R}^n$ is the state vector, $u(t) \in \mathbb{R}^m$ is the control input, and $y(t) \in \mathbb{R}^m$ is the system output; and the following state space matrices: $A \in \mathbb{R}^{n\times n}$ is the state matrix, $B \in \mathbb{R}^{n\times m}$ is the input matrix, and $C \in \mathbb{R}^{m\times n}$ is the output matrix. The plant has m inputs and m outputs, such that the relationship between these signals is described by

$$y(t) = G(s)\,[u](t) \tag{4.2}$$

where $G(s) \in \mathbb{R}^{m\times m}$ is the plant transfer matrix, and the variable s denotes the Laplace transform variable or the time differentiation operator, such that $s[x](t) = \dot{x}(t)$. The plant transfer matrix can be expressed as

$$G(s) = C\,(sI - A)^{-1}B \tag{4.3}$$

which is comprised of the system state space matrices, previously described.

The transfer matrix $G(s)$ may be unknown, but is assumed to be nonsingular; meaning it is normally full rank, except for a finite number of values for s. The transfer matrix is also expressed as

$$G(s) = Z(s)P^{-1}(s) \tag{4.4}$$

where $Z(s) \in \mathbb{R}^{m\times m}$ and $P(s) \in \mathbb{R}^{m\times m}$ are both right co-prime polynomial matrices, and $P(s)$ is column proper (Goodwin et al., 2001). The nature of multivariable derivations necessitates indexed matrix elements, so consider

$$i = 2, 3, \ldots, m, \quad j = 1, 2, \ldots, m-1, \quad k = 1, 2, \ldots, m \tag{4.5}$$

to be a standardized index used throughout the remainder of the derivations.

4.2.2 Interactor Matrix and the High-Frequency Gain Matrix

A modified left interactor matrix of $G(s)$ is described by

$$\xi_m(s) = \begin{bmatrix} d_1(s) & 0 & \ldots & 0 \\ h^m_{21}(s) & d_2(s) & \ddots & \vdots \\ & \ddots & & \\ \vdots & \ddots & d_{m-1}(s) & 0 \\ h^m_{m1}(s) & \ldots & h^m_{m\,m-1}(s) & d_m(s) \end{bmatrix} \tag{4.6}$$

where $h^m_{ij}(s)$ are polynomials, and $d_k(s)$ are monic stable polynomials. From (Tao, 2003b), it is known that a strictly proper and full rank transfer matrix $G(s)$, has a modified left interactor matrix $\xi_m(s)$, which has a stable inverse and represents the zero structure of $G(s)$ at infinity. The modified left interactor matrix $\xi_m(s)$, is related to the HFG matrix of $G(s)$, through the relationship

$$K_p = \lim_{s\to\infty} \xi_m(s)\, G(s) \tag{4.7}$$

where $K_p \in \mathbb{R}^{m\times m}$ is finite and nonsingular. For the remainder of this document, the modified left interactor matrix $\xi_m(s)$, will simply be referred to as the *interactor matrix*, for brevity.

4.2.3 LDS Decomposition

When the HFG matrix K_p, has all nonzero leading principal minors Δ_k, there exists a non unique matrix decomposition, given by

$$K_p = L\, D\, S \tag{4.8}$$

where $L, D, S \in \mathbb{R}^{m \times m}$, $S = S^T > 0$, L is a unity lower triangular matrix, and

$$D = \texttt{diag}\left\{ \texttt{sgn}\left[\Delta_1\right] \kappa_1, \texttt{sgn}\left[\frac{\Delta_2}{\Delta_1}\right] \kappa_2, \ldots, \texttt{sgn}\left[\frac{\Delta_m}{\Delta_{m-1}}\right] \kappa_m \right\} \tag{4.9}$$

where `sgn[]` is the sign operator, and $\kappa_k > 0$, are arbitrary gain values.

4.2.4 Plant Assumptions

Following sections will introduce both state feedback and output feedback multivariable MRAC architectures, applied to the stabilization and inner control loops, respectively. The following list of conditions, which encompasses both the state feedback and output feedback designs, are required for implementing multivariable model reference adaptive control:

1. All zeros of $G(s)$ have negative real parts, indicating they are stable;
2. The plant must be (A, B) controllable and (A, C) observable;
3. The transfer matrix $G(s)$ is strictly proper, full rank, with a known interactor matrix $\xi_m(s)$;
4. There is a known upper bound $\bar{\nu}$ on the observability index of $G(s)$, and;
5. All leading principle minors of the HFG matrix K_p, are nonzero and their signs are known.

Transmission zeros of a MIMO system cause $G(s)$ to lose rank, so that a control input $u(t) \neq 0$ exists where $y(t) = G(s)u(t) = 0$; meaning the control input has no influence on the output. Condition (1) ensures that no transmission zeros exist which can cause $G(s)$ to lose rank, which may cause the system to become uncontrollable. Condition (2) is needed for stable plant-model matching for the state feedback design. Condition (3) is needed to select a reference model, (4) is needed to filter the input and output signals for the output feedback design, and (5) ensures that the adaptation laws converge in the proper direction.

4.3 LDS Based MRAC Architecture

This section presents a general procedure that can be applied to multivariable output tracking designs. Traditional MIMO MRAC architecture requires *a priori* knowledge of the HFG matrix K_p, which is based on the transfer matrix $G(s)$. But when the system $G(s)$ is unknown, identifying K_p is not be feasible. A more flexible control structure would allow for adaptive control when $G(s)$ and K_p are not uniquely known. Incorporating the plant uncertainty into the adaptation process relaxes this requirement. This research, built upon work from (Guo et al., 2011), is based on an LDS decomposition of the HFG matrix K_p, which only requires knowledge of the signs of its principal minors. Following subsections outline a process, which eliminates the need to know specific values of K_p, and only requires knowledge of the structure of K_p. This allows for adaptive control when $G(s)$ and K_p are not completely known in advance. Because all three TURN control loops utilize output tracking, this LDS methodology is directly applicable to each subsystem.

4.3.1 Control Law Parameterization

Whether working with state feedback or output feedback, the first objective is to parameterize the control law, with the following form

$$u(t) = \Theta^{*T}\,\omega(t) \tag{4.10}$$

where Θ^* contains the true parameter values, and $\omega(t)$ is a regressor signal vector. Whether the parameter values are known or unknown, substituting (4.10) into (4.2) yields

$$\bar{y}(t) = G(s)\,\Theta^{*T}[\omega](t) \tag{4.11}$$

which describes the desired system output. The structure of the control law (4.10) will vary between controller architectures, but when the parameters are appropriately selected, the desired system response (4.11) will match a prescribed reference model system described by

$$\bar{y}(t) = \bar{G}(s)\,[r](t) \tag{4.12}$$

where $\bar{G}(s)$ is the intended system response, given a bounded reference signal $r(t)$. When the true parameter values Θ^* are known, a fixed controller attains the desired system response. However, adaptive control is concerned with the scenario when the parameter values are unknown, and must be updated from adaptive laws. The time-varying estimate of the parameters is described by $\Theta(t)$, which is used in the adaptive version of the parameterized control law

$$u(t) = \Theta^{T}(t)\,\omega(t) \tag{4.13}$$

where substituting (4.13) into (4.2) yields

$$y(t) = G(s)\,[\Theta^{T}\omega](t) \tag{4.14}$$

which is the actual system output; as dictated by the current, and possibly incorrect, assessment of the parameter values. The parameter estimate error $\tilde{\Theta}(t)$, described by

$$\tilde{\Theta}(t) = \Theta(t) - \Theta^* \tag{4.15}$$

is the difference between the estimated parameter values and the true parameter values.

4.3.2 LDS Decomposition Formulation

Express the output tracking error $e(t) \in \mathbb{R}^m$, as the difference between the actual and desired system outputs, and manipulate variables

$$e(t) = y(t) - \bar{y}(t) = G(s)\,[\tilde{\Theta}^{T}\omega](t) \tag{4.16}$$

such that the tracking error is expressed in terms of the parameter estimation error. Utilizing (4.7), substitute the the HFG matrix K_p, and the interactor matrix ξ_m, in place of $G(s)$, which forms

$$e(t) = \xi_m^{-1}(s)\, K_p\, [\tilde{\Theta}^T \omega](t) \tag{4.17}$$

and then incorporating the gain matrix decomposition $K_p = LDS$, yields

$$\xi_m(s)\, [e](t) = LDS\, \tilde{\Theta}^T(t)\, \omega(t). \tag{4.18}$$

which is an alternative representation of the output tracking error.

To fully realize the benefit of the LDS decomposition, the controller needs to utilize the simplified matrix structures. Rearrange terms

$$L^{-1}\xi_m(s)\, [e](t) = DS\, \tilde{\Theta}^T(t)\, \omega(t) \tag{4.19}$$

where the inverse is guaranteed to exist, because L is defined as a unity lower triangular matrix. Eliminate the unity on the diagonal in L^{-1}, by establishing a new matrix $\Lambda^* = L^{-1} - I_m$, where

$$\Lambda^* = \begin{bmatrix} 0 & 0 & & \dots & 0 \\ \lambda^*_{21} & 0 & & & \vdots \\ \vdots & \ddots & \ddots & & \\ \lambda^*_{m-1\,1} & & \ddots & 0 & 0 \\ \lambda^*_{m1} & \lambda^*_{m2} & \dots & \lambda^*_{m\,m-1} & 0 \end{bmatrix} \tag{4.20}$$

such that $\lambda^*_{ij} = 0$, on its diagonal and upper triangle. Introducing Λ^* requires some additional parameter vectors

$$\begin{aligned} \lambda^*_2 &= \lambda^*_{21} \in \mathbb{R} \\ \lambda^*_3 &= [\, \lambda^*_{31},\, \lambda^*_{32}\,]^T \in \mathbb{R}^2 \\ &\vdots \\ \lambda^*_{m-1} &= [\, \lambda^*_{m-1\,1},\, \dots,\, \lambda^*_{m-1\,m-2}\,]^T \in \mathbb{R}^{m-2} \\ \lambda^*_m &= [\, \lambda^*_{m1},\, \dots,\, \lambda^*_{m\,m-1}\,]^T \in \mathbb{R}^{m-1} \end{aligned} \tag{4.21}$$

where $\lambda_{ij}(t)$ are the estimates of the true matrix elements λ^*_{ij}, and $\lambda_i(t)$ are the estimates of the true row vectors λ^*_i. Finally, incorporating Λ^* into (4.19), yields

$$\Lambda^*\, \xi_m(s)\, [e](t) + \xi_m(s)\, [e](t) = DS\, \tilde{\Theta}^T(t)\, \omega(t). \tag{4.22}$$

4.3.3 Error Model

Introduce a stable filter $f(s) = 1/h(s)$, where an arbitrary stable monic polynomial $h(s)$, is selected with a degree equal to the maximum degree of the interactor matrix $\xi_m(s)$. Operating on both sides of (4.22), with $f(s)I_m$, leads to

$$\Lambda^* \, \xi_m(s) \, f(s) \, [e](t) + \xi_m(s) \, f(s) \, [e](t) = DS \, f(s) \, [\tilde{\Theta}^T \omega](t) \tag{4.23}$$

which can be more compactly noted by

$$\Lambda^* \, \bar{e}(t) + \bar{e}(t) = DS \, f(s) \, [\tilde{\Theta}^T \omega](t) \tag{4.24}$$

after defining the filtered tracking error $\bar{e}(t)$, as

$$\bar{e}(t) = \xi_m(s) \, f(s) \, [e](t) = [\, \bar{e}_1(t), \, \bar{e}_2(t), \, \ldots, \, \bar{e}_m(t) \,]^T \tag{4.25}$$

where $\bar{e}_k \in \mathbb{R}$. Using the parameter vectors from (4.21), and denoting $\eta_i(t)$, as

$$\eta_i(t) = [\, \bar{e}_1(t), \, \bar{e}_2(t), \, \ldots, \, \bar{e}_{i-1}(t) \,]^T \in \mathbb{R}^{i-1}, \tag{4.26}$$

the $\Lambda^* \, \bar{e}(t)$ term can be expressed as

$$\Lambda^* \, \bar{e}(t) = [\, 0, \, \lambda_2^{*T} \eta_2(t), \, \lambda_3^{*T} \eta_3(t), \, \ldots, \, \lambda_m^{*T} \eta_m(t) \,]^T \tag{4.27}$$

which can be substituted into (4.24), to yield the following revised error equation

$$\big[\, 0, \, \lambda_2^{*T} \eta_2(t), \, \lambda_3^{*T} \eta_3(t), \, \ldots, \, \lambda_m^{*T} \eta_m(t) \,\big]^T + \bar{e}(t) = DS \, f(s) \, [\tilde{\Theta}^T \omega](t). \tag{4.28}$$

Uncertainty within L has already been incorporated into (4.21), but uncertainty within DS is still unaccounted for. Denote $\Psi^* = DS$, as the true unknown parameter, and let $\Psi(t)$ represent the estimate of Ψ^*. Estimation errors are the difference between the estimates and their true values, so

$$\tilde{\Psi}(t) = \Psi(t) - \Psi^*, \text{ and } \quad \tilde{\lambda}_i(t) = \lambda_i(t) - \lambda_i^* \tag{4.29}$$

represents the all estimation errors for the entire LDS decomposition of K_p.

Define two auxiliary signals, where the first

$$\zeta(t) = f(s) \, [\omega](t) \tag{4.30}$$

is a filtered regressor signal, and the second

$$\rho(t) = \Theta^T(t) \, \zeta(t) - f(s) \, [\Theta^T \omega](t) \tag{4.31}$$

is the difference between, the parameter estimate acting on the filtered regressor signal, and the filtered adaptive parameterized control law (4.13).

Define the estimation error $\epsilon(t)$, as

$$\epsilon(t) = \bar{e}(t) + \Psi(t)\,\rho(t) + \left[\,0,\, \lambda_2^T(t)\eta_2(t),\, \lambda_3^T(t)\eta_3(t),\, \ldots,\, \lambda_m^T(t)\eta_m(t)\,\right]^T \tag{4.32}$$

then, solve for $\bar{e}(t)$ in the error equation (4.28), and substitute that relationship into the estimation error equation (4.32), which becomes

$$\epsilon(t) = DS\,\tilde{\Theta}^T(t)\,\zeta(t) + \tilde{\Psi}(t)\,\rho(t) + \left[\,0,\, \tilde{\lambda}_2^T(t)\eta_2(t),\, \tilde{\lambda}_3^T(t)\eta_3(t),\, \ldots,\, \tilde{\lambda}_m^T(t)\eta_m(t)\,\right]^T \tag{4.33}$$

and expresses $\epsilon(t)$ completely in terms of the parameter estimate errors.

4.3.4 Adaptive Laws

The estimates do not always equal their true values, so parameters must be updated from adaptive laws. Recall, the parameter errors are described by

$$\tilde{\Theta}(t) = \Theta(t) - \Theta^*, \quad \tilde{\Psi}(t) = \Psi(t) - \Psi^*, \quad \tilde{\lambda}_i(t) = \lambda_i(t) - \lambda_i^* \tag{4.34}$$

and since true parameter values are constant, derivatives of parameter errors are described by

$$\dot{\tilde{\Theta}}(t) = \dot{\Theta}(t), \quad \dot{\tilde{\Psi}}(t) = \dot{\Psi}(t), \quad \dot{\tilde{\lambda}}_i(t) = \dot{\lambda}_i(t). \tag{4.35}$$

Select a normalizing signal $m(t)$, described by

$$m^2(t) = 1 + \zeta^T(t)\,\zeta(t) + \rho^T(t)\,\rho(t) + \sum_{i=2}^{m} \eta_i^T(t)\,\eta_i(t) \tag{4.36}$$

then the expression for the estimation error $\epsilon(t)$, suggests the following adaptive laws

$$\dot{\Theta}^T(t) = -\frac{D\,\epsilon(t)\,\zeta^T(t)}{m^2(t)}, \quad \dot{\Psi}(t) = -\frac{\Gamma\,\epsilon(t)\,\rho^T(t)}{m^2(t)}, \quad \dot{\lambda}_i(t) = -\frac{\gamma_i\,\epsilon_i(t)\,\eta_i(t)}{m^2(t)} \tag{4.37}$$

where the adaptive gains are $\Gamma \in \mathbb{R}^{m\times m}$ and $\gamma_i \in \mathbb{R}$, and selected such that $\Gamma = \Gamma^T > 0$ and $\gamma_i > 0$.

4.3.5 Stability Analysis

To evaluate the closed-loop stability, define a positive definite function $V(\tilde{\Theta}(t), \tilde{\Psi}(t), \tilde{\lambda}_i(t))$

$$V = \mathtt{tr}\left[\,\tilde{\Theta}(t)\,S\,\tilde{\Theta}^T(t)\,\right] + \mathtt{tr}\left[\,\tilde{\Psi}^T(t)\,\Gamma^{-1}\,\tilde{\Psi}(t)\,\right] + \sum_{i=2}^{m} \tilde{\lambda}_i^T(t)\,\gamma_i^{-1}\,\tilde{\lambda}_i(t) \tag{4.38}$$

which serves as a measure of the estimation errors, and where `tr[]` denotes the trace of a matrix. Take the time derivative of V, and substitute in the adaptive laws (4.37), to obtain

$$\dot{V} = \frac{-2}{m^2(t)} \left[\mathtt{tr} \left[\tilde{\Theta}(t)\, SD\, \epsilon(t)\, \zeta^T(t) \right] + \mathtt{tr} \left[\tilde{\Psi}(t)\, \epsilon(t)\, \rho^T(t) \right] + \sum_{i=2}^{m} \tilde{\lambda}_i^T(t)\, \epsilon_i(t)\, \eta_i(t) \right] \tag{4.39}$$

which, after substituting appropriate terms, reduces to

$$\dot{V} = -\frac{2\, \epsilon^T(t)\, \epsilon(t)}{m^2(t)} \leq 0 \tag{4.40}$$

and shows that it is negative semi-definite. With $\dot{V} \leq 0$, the adaptive laws ensure that all the estimation signals are bounded: $\Theta(t) \in L^\infty$, $\Psi(t) \in L^\infty$, and $\lambda_i(t) \in L^\infty$. It also shows that $\epsilon(t)/m(t) \in L^2 \cap L^\infty$, which implies that $\dot{\Theta}(t) \in L^2 \cap L^\infty$, $\dot{\Psi}(t) \in L^2 \cap L^\infty$, and $\dot{\lambda}_i(t) \in L^2 \cap L^\infty$.

After reviewing the adaptive law properties, the following results can be established. The multivariable output tracking MRAC system, updated from the adaptive laws (4.37), and applied to the plant (4.2), guarantees closed-loop signal boundedness and asymptotic output tracking

$$\lim_{t \to \infty} e(t) = \lim_{t \to \infty} (y(t) - \bar{y}(t)) = 0 \tag{4.41}$$

for any given initial conditions. The proof of this theorem is lengthy and can be derived from multivariable MRAC theory developed in (Tao, 2003b), for the basic design without using an LDS decomposition of K_p.

4.4 Satellite Assessment

Arguably, the most important TURN component to discuss during the controls analysis, is an unconstrained satellite vehicle. Since it is the only structure that has control inputs, it deserves special attention. This entity is directly responsible for all the takeoff and landing, transformational flight, and forward flight capabilities. Once this subsystem is analyzed and adequately controlled, all other control structures will be developed directly upon it. Following content presents: the linearized state space description, a process for control input mixing, an assessment of the controllability and observability for the satellite, and an explanation of how the plant satisfies the required assumptions for implementing the controllers.

4.4.1 State Space Description

Controls development will work exclusively with a state space representations of the plant systems. This section defines the: system states, control inputs, and system outputs; which are used to perform the linearization process and to carry out the controller development.

System States: There are twelve total states $x_{\texttt{sat}}(t)$, which describe the satellite vehicle. The first three are attitude angles (ϕ, θ, ψ), which convey satellite orientation. The next three describe the position of the vehicle (x, y, z), expressed in the inertial frame. The final six states are the derivatives of the initial six; angular rates and linear velocity, respectively. Thus, the following vector

$$x_{\texttt{sat}}(t) = \Big[\ \phi,\ \theta,\ \psi,\ x,\ y,\ z,\ \dot{\phi},\ \dot{\theta},\ \dot{\psi},\ \dot{x},\ \dot{y},\ \dot{z}\ \Big]^T \in \mathbb{R}^{12} \tag{4.42}$$

contains all the available states which describe the plant dynamics as a function of time.

Control Inputs: Each satellite has a total of nine control inputs: a single elevator with pairs of motors, stabilizers, rudders, and ailerons. However, the motors, stabilizers, and rudders are only articulated through complementary control inputs, thus three signals are duplicates. So only six unique control inputs influence the dynamics of the vehicle. The first two inputs are the deflection of the aileron control surfaces (δ_{ai}, δ_{ao}), expressed in radians. Since ailerons apply both complimentary and differential inputs, each surface must be uniquely identified. Next is the deflection of the elevator (δ_e), expressed in radians. The final three convey the pairs of complementary control inputs. Because each pair applies the same command, only one input signal is needed to describe each of them. The first two are the rudder and stabilizer (δ_r, δ_s), also expressed in radians. Finally, the propulsion unit (ω), expressed in radians per second. Thus, the following vector

$$u_{\texttt{lin}}(t) = [\ \delta_{ai},\ \delta_{ao},\ \delta_e,\ \delta_r,\ \delta_s,\ \omega\ ]^T \in \mathbb{R}^6 \tag{4.43}$$

contains all the available control inputs which influence the linearized model of the satellite vehicle.

System Outputs: Six system outputs $y_{\texttt{sat}}(t)$, are needed to adequately characterize the disposition of the unconstrained flying satellite vehicle. They are defined as the attitude and linear position of the aerial system. Thus, the following vector

$$y_{\texttt{sat}}(t) = [\ \phi,\ \theta,\ \psi,\ x,\ y,\ z\ ]^T \in \mathbb{R}^6 \tag{4.44}$$

contains all the available system outputs which describe the plant.

State Matrices: A general representation of the state matrix $A_{\texttt{lin}}$, and input matrix $B_{\texttt{lin}}$, was provided in the linearization process derived in *Chapter 3: Plant Development*. However, a small modification, described in the next subsection, is still needed before developing the controller. The only matrix left to define, is the output matrix $C_{\texttt{sat}}$, for the unconstrained satellite model, given as

$$C_{\texttt{sat}} = \Big[\ \ I_{6\times 6} \quad 0_{6\times 6}\ \ \Big] \in \mathbb{R}^{6\times 12} \tag{4.45}$$

which depicts a direct mapping between particular states and the desired system outputs.

4.4.2 Control Input Mixing

The linearization process yielded an input matrix $B_{\texttt{lin}}$, where all six unique control inputs mapped directly to their respective physical components. However, it is advantageous when the inputs are specified in terms of forces and moments. This is desirable, because it is more intuitive while developing the controller, and it provides a stronger correlation between input-output channels.

The goal is to define an alternative control input vector, such that

$$u_{\texttt{sat}}(t) = [\ M_x,\ M_y,\ M_z,\ F_x,\ F_y,\ F_z\ ]^T \in \mathbb{R}^6 \tag{4.46}$$

which is comprised of forces and moments in the body frame of the satellite. Notice how each of the control inputs very closely matches its associated system output. By incorporating this change, the intent is to modify the original linearized system

$$\dot{x}_{\texttt{sat}}(t) = A_{\texttt{lin}}\, x_{\texttt{sat}}(t) + B_{\texttt{lin}}\, u_{\texttt{lin}}(t) \quad \Rightarrow \quad \dot{x}_{\texttt{sat}}(t) = A_{\texttt{sat}}\, x_{\texttt{sat}}(t) + B_{\texttt{sat}}\, u_{\texttt{sat}}(t) \tag{4.47}$$

into an equivalent representation of the system dynamics, but with favorable properties for assessing the vehicle layout design and developing the controller architecture. Since no modifications are needed for the state matrix, and in an effort to keep the subscript notation clean, the linearized state matrix $A_{\texttt{lin}}$, is denoted as

$$A_{\texttt{sat}} = A_{\texttt{lin}} \tag{4.48}$$

which indicates that it is equivalent to the state matrix $A_{\texttt{sat}}$, of the unconstrained satellite vehicle.

Next, consider the control input part of the dynamics. A relationship defined by

$$u_{\texttt{lin}}(t) = B_{\texttt{mix}}\, u_{\texttt{sat}}(t) \tag{4.49}$$

with a control input mixing matrix $B_{\texttt{mix}}$, provides the mapping between the different control input vectors. This matrix is structured as

$$B_{\texttt{mix}} = \begin{bmatrix} -b_\phi & 0 & 0 & 0 & 0 & b_z \\ b_\phi & 0 & 0 & 0 & 0 & b_z \\ 0 & b_\theta & 0 & 0 & 0 & 0 \\ 0 & 0 & b_\psi & 0 & 0 & 0 \\ 0 & 0 & 0 & 0 & b_y & 0 \\ 0 & 0 & 0 & b_x & 0 & 0 \end{bmatrix} \in \mathbb{R}^{6\times 6} \tag{4.50}$$

such that matrix elements relate the applied forces and moments directly to their intended physical control inputs, and the negative sign indicates differential control is used by the ailerons to execute roll commands. The control input mixing matrix $B_{\texttt{mix}}$, must be populated to satisfy the relationship

$$B_{\texttt{sat}} = B_{\texttt{lin}}\, B_{\texttt{mix}} \tag{4.51}$$

to preserve consistent dynamics from the transformation depicted within (4.47), but the diagonal must contain terms for the inverse of the moment inertias and mass of the satellite, to relate forces and moments directly to their respective states. Using elements with the linearized input matrix, define the control input mixing coefficients as

$$\begin{array}{ll} b_\phi = 1/(2J_x b_{(11)}) & b_x = 1/(m b_{(46)}) \\ b_\theta = 1/(J_y b_{(23)}) & b_y = 1/(m b_{(55)}) \\ b_\psi = 1/(J_z b_{(34)}) & b_z = 1/(2m b_{(61)}) \end{array} \tag{4.52}$$

where $b_{(**)}$ cancel out each of their appropriate linearized terms, and the fact that two ailerons influence both roll and vertical translation are accounted for within b_ϕ and b_z.

Applying the mixing matrix to the original input matrix, forms the revised input matrix as

$$B_{\mathtt{sat}} = \begin{bmatrix} 0_{3\times3} & 0_{3\times3} \\ 0_{3\times3} & 0_{3\times3} \\ B_{rm} & B_{rf} \\ B_{tm} & B_{tf} \end{bmatrix} \in \mathbb{R}^{12\times6} \tag{4.53}$$

with subscripts m and f denoting force and moment inputs, respectively. The submatrices are expanded as

$$\begin{gathered} B_{rm} = \mathtt{diag}\{\ 1/J_x,\ 1/J_y,\ 1/J_z\ \} \quad B_{tf} = \mathtt{diag}\{\ 1/m,\ 1/m,\ 1/m\ \} \\ B_{tm} = \begin{bmatrix} 0 & b_{tm(12)} & 0 \\ 0 & 0 & b_{tm(23)} \\ 0 & b_{tm(32)} & 0 \end{bmatrix} \quad B_{rf} = \begin{bmatrix} 0 & 0 & 0 \\ 0 & 0 & b_{rf(23)} \\ 0 & b_{rf(32)} & 0 \end{bmatrix} \end{gathered} \tag{4.54}$$

where B_{rm} and B_{tf} are the predominant input-output mappings, submatrices B_{tm} and B_{rf} preserve the cross-coupling inherent in the system dynamics, and $B_{\mathtt{sat}}$ is a more appropriate structure which exhibits stronger correlations between the control inputs and the system outputs.

4.4.3 Controllability and Observability

Two very important system properties, controllability and observability, are obtained directly from the MIMO state space matrices: $A_{\mathtt{sat}}$, $B_{\mathtt{sat}}$, and $C_{\mathtt{sat}}$; which are described in greater detail in *Appendix A: Control Theory Fundamentals*. A portion of the general controllability matrix $\mathbb{C}_{\mathtt{sat}}$, and a portion of the general observability matrix $\mathbb{O}_{\mathtt{sat}}$, are derived next.

The first twelve columns of the controllability matrix $\mathbb{C}_{\mathtt{sat}}$, are given by

$$\mathbb{C}_{\mathtt{sat}} = [\ B_{\mathtt{sat}},\ A_{\mathtt{sat}}B_{\mathtt{sat}}\ ] = \begin{bmatrix} 0_{3\times3} & 0_{3\times3} & B_{rm} & B_{rf} \\ 0_{3\times3} & 0_{3\times3} & B_{tm} & B_{tf} \\ B_{rm} & B_{rf} & A_{rt}B_{tm} & A_{rt}B_{tf} \\ B_{tm} & B_{tf} & A_{tt}B_{tm} & A_{tt}B_{tf} \end{bmatrix} \tag{4.55}$$

which is always full rank, thus the system is fully controllable; and where

$$\mu_i = 2 \qquad \texttt{for } \; i = 1, \ldots, 6 \tag{4.56}$$

describe the controllability indexes.

The first twelve rows of the observability matrix $\mathbb{O}_{\texttt{sat}}$, are given by

$$\mathbb{O}_{\texttt{sat}} = [\, C_{\texttt{sat}},\, C_{\texttt{sat}} A_{\texttt{sat}} \,]^T = I_{12\times 12} \tag{4.57}$$

which is also always full rank, thus the system is fully observable; and where

$$\nu_i = 2 \qquad \texttt{for } \; i = 1, \ldots, 6 \tag{4.58}$$

describe the observability indexes.

This is a very important result for the TURN system. Because the system is both fully controllable and fully observable, the greatest number of options are available for developing the controls framework. As previously described, satisfying these conditions is a requirement for the MRAC controllers, which are simulated in the next chapter.

4.4.4 Satisfying Plant Assumptions

To implement the controllers, the plant assumptions must be satisfied. Even with the aid of computer software programs, such as Matlab, the size and complexity of the transfer matrix in its general form does not shed any valuable insight; therefore, some reasonable assumptions are used to proceed. An aircraft can be idealized as a rigid body under the influence of aerodynamic effects, which contribute damping. Removing these effects represents the worst case scenario, which is a rigid body with no damping forces contributing stability. Because the inputs are forces and moments that map directly to their respective states, such an idealized system is described by

$$G_{\texttt{sat}}(s) = \texttt{diag} \left\{ \; \frac{1}{J_x s^2},\; \frac{1}{J_y s^2},\; \frac{1}{J_z s^2},\; \frac{1}{m s^2},\; \frac{1}{m s^2},\; \frac{1}{m s^2} \; \right\} \tag{4.59}$$

which exhibits second order dynamics across all input-output channels. Using the relationship $K_{p\texttt{sat}}(s) = \lim_{s\to\infty} \xi_{m\texttt{sat}}(s) G_{\texttt{sat}}(s)$, yields

$$\begin{aligned} \xi_{m\texttt{sat}} &= \texttt{diag} \{\; s^2,\; s^2,\; s^2,\; s^2,\; s^2,\; s^2 \;\} \\ K_{p\texttt{sat}} &= \texttt{diag} \{\; J_x^{-1},\; J_y^{-1},\; J_z^{-1},\; m^{-1},\; m^{-1},\; m^{-1} \;\} \end{aligned} \tag{4.60}$$

for the interactor matrix $\xi_{m\texttt{sat}}$, and the HFG matrix $K_{p\texttt{sat}}$.

The numerators of $G_{\texttt{sat}}(s)$ are all unity (no Laplace terms), thus the transfer matrix has no system zeros, so condition (1) is always satisfied. Furthermore, it is strictly proper, always full rank, and has a known interactor matrix, satisfying condition (3). From the diagonal structure of $K_{p\texttt{sat}}$, which is populated with physical parameters (known to be positive), the leading principle minors are all

positive terms, satisfying condition (5). The previous section indicated that the system is both fully controllable and fully observable, which satisfies condition (2); and since each input-output channel has an observability index of two, an upper bound for the observability index is known, which satisfies condition (4).

4.5 Stabilization Via State Feedback MRAC

Influencing the states of each satellite vehicle is the foundation from which all other control loops are built upon. Before considering the adaptive control implementation, this section first describes the theory to develop a nominal state feedback output tracking controller for a MIMO system. It presents a state tracking design, and summarizes the limitations with the required matching condition; then it reviews how an output tracking design is more flexible, and can relax such strict matching conditions. Finally, it builds upon that foundation, and parameterizes the control law, which is used in the LDS based MRAC architecture, for the stabilization loop on the TURN satellite. A theoretical background is provided in *Appendix C: MIMO State Feedback*.

4.5.1 Motivation for State Feedback

Both state feedback and output feedback control designs can be applied to MRAC; however, state tracking requires a strict matching condition between the plant and model, and output feedback requires a more complicated controller structure. Previous sections detailed the twelve states that describe the unconstrained satellite vehicle: inertial position, attitude angles, linear velocity, and angular rates. With the available sensors mounted on the satellite, all twelve of these states can be directly measured. Thus, the controller for the unconstrained satellite vehicle utilizes state feedback with output tracking, based on an LDS decomposition of the HFG matrix, which keeps the simple state feedback structure, while relaxing the required matching condition.

4.5.2 State Tracking

The goal of state feedback state tracking control is to design a control input $u(t)_{\text{sat}} \in \mathbb{R}^m$, which influences the system

$$\dot{x}_{\text{sat}}(t) = A_{\text{sat}}\, x_{\text{sat}}(t) + B_{\text{sat}}\, u_{\text{sat}}(t) \tag{4.61}$$

such that all signals in the closed-loop system are bounded, and the state vector signal $x(t)_{\text{sat}} \in \mathbb{R}^n$, asymptotically tracks a reference state vector signal $\bar{x}_{\text{sat}}(t) \in \mathbb{R}^n$. The desired system response of the closed-loop system, is described by a reference system

$$\dot{\bar{x}}_{\text{sat}}(t) = \bar{A}_{\text{sat}}\, \bar{x}_{\text{sat}}(t) + \bar{B}_{\text{sat}}\, r_{\text{sat}}(t) \tag{4.62}$$

where a bounded reference signal $r(t)_{\text{sat}} \in \mathbb{R}^m$ is applied to the reference model which include stable reference state matrix $\bar{A}_{\text{sat}} \in \mathbb{R}^{n\times n}$, and reference input matrix $\bar{B}_{\text{sat}} \in \mathbb{R}^{n\times m}$. The control

law is selected as

$$u_{\mathtt{sat}}(t) = K_x\, x_{\mathtt{sat}}(t) + K_r\, r_{\mathtt{sat}}(t) \tag{4.63}$$

with controller gains $K_x \in \mathbb{R}^{m\times n}$, and $K_r \in \mathbb{R}^{m\times m}$. When the gains are selected such that

$$\bar{A}_{\mathtt{sat}} = A_{\mathtt{sat}} + B_{\mathtt{sat}}\, K_x, \quad \bar{B}_{\mathtt{sat}} = B_{\mathtt{sat}}\, K_r \tag{4.64}$$

then the necessary state tracking matching condition is satisfied. Choosing K_x and K_r, which honor the relationships in (4.64), achieves the desired control objective by producing a closed-loop system governed by

$$\dot{x}_{\mathtt{sat}}(t) = \bar{A}_{\mathtt{sat}}\, x_{\mathtt{sat}}(t) + \bar{B}_{\mathtt{sat}}\, r_{\mathtt{sat}}(t) \tag{4.65}$$

once the control law (4.63) is substituted into the system plant (4.61).

4.5.3 Matching Condition Limitations

Consider the general structure of the unconstrained TURN satellite vehicle, where the state space matrices are described by $A_{\mathtt{sat}}$ and $B_{\mathtt{sat}}$. The goal of state tracking is to identify a closed-loop system $\bar{A}_{\mathtt{sat}}$, such that the matching condition from (4.64), forces all of the states to follow prescribed trajectories. However, when $A_{\mathtt{sat}}$ and $B_{\mathtt{sat}}$ are sparse matrices, it is difficult or impossible to identify a suitable state gain K_x, that can accomplish the task.

Partition the state feedback gain into appropriate equally sized submatrices

$$K_x = \begin{bmatrix} K_{11} & K_{12} & K_{13} & K_{14} \\ K_{21} & K_{22} & K_{23} & K_{24} \end{bmatrix} \in \mathbb{R}^{6\times 12} \tag{4.66}$$

and, consider the closed-loop system structure described in terms of the submatrices, given by

$$\begin{bmatrix} 0_{3\times 3} & 0_{3\times 3} & I_{3\times 3} & 0_{3\times 3} \\ 0_{3\times 3} & 0_{3\times 3} & 0_{3\times 3} & I_{3\times 3} \\ A_{rr}+B_{rm}K_{11}+B_{rf}K_{21} & B_{rm}K_{12}+B_{rf}K_{22} & B_{rm}K_{13}+B_{rf}K_{23} & A_{rt}+B_{rm}K_{14}+B_{rf}K_{24} \\ A_{tr}+B_{tm}K_{11}+B_{tf}K_{21} & B_{tm}K_{12}+B_{tf}K_{22} & B_{tm}K_{13}+B_{tf}K_{23} & A_{tt}+B_{tm}K_{14}+B_{tf}K_{24} \end{bmatrix} \tag{4.67}$$

which at first appears to be sufficiently populated. However, each of the submatrices of $A_{\mathtt{sat}}$ and $B_{\mathtt{sat}}$, are either diagonal or only contain a couple of elements. As such, each element of $\bar{A}_{\mathtt{sat}}$ may only contain a single coefficient influenced by K_x, which also needs to be shared among the other twelve columns. The sparse nature of the plant matrices, and the limited options for elements within those matrices, make the matching condition (4.64), difficult or impossible to satisfy.

4.5.4 Output Tracking

To alleviate the state tracking matching condition, an output tracking controller is presented. The goal of state feedback output tracking control is to influence the system

$$y_{\mathtt{sat}}(t) = G_{\mathtt{sat}}(s)\,[u_{\mathtt{sat}}](t) \tag{4.68}$$

by designing a control input $u_{\mathtt{sat}}(t)$, such that all the signals in the closed-loop system are bounded, and the system output $y_{\mathtt{sat}}(t) \in \mathbb{R}^m$, asymptotically tracks a reference output $\bar{y}_{\mathtt{sat}}(t) \in \mathbb{R}^m$; which means the error signal decays to zero, $\lim_{t\to\infty}(y_{\mathtt{sat}}(t) - \bar{y}_{\mathtt{sat}}(t)) = 0$. A bounded reference signal $r_{\mathtt{sat}}(t)$ is applied to the reference system

$$\bar{y}_{\mathtt{sat}}(t) = \bar{G}_{\mathtt{sat}}(s)\,[r_{\mathtt{sat}}](t), \quad \bar{G}_{\mathtt{sat}}(s) = \xi_{\mathtt{sat}}^{-1}(s) \tag{4.69}$$

where the closed-loop transfer matrix $\bar{G}_{\mathtt{sat}}(s)$ is described by

$$\bar{G}_{\mathtt{sat}}(s) = C_{\mathtt{sat}}\left(sI - A_{\mathtt{sat}} - B_{\mathtt{sat}}K_x\right)^{-1} B_{\mathtt{sat}}K_r \tag{4.70}$$

and $\xi_{\mathtt{sat}} = \mathtt{diag}\{\, d_1(s), \cdots, d_m(s)\,\}$ is the interactor matrix, where $d_k(s)$ are the desired closed-loop characteristic polynomials of degree l_k (Guo et al., 2009). The HFG matrix K_p, is related to the control gains K_x and K_r by the relationship

$$K_x = K_p^{-1}K_0, \quad K_r = K_p^{-1} \tag{4.71}$$

where the k^{th} row of K_0 is described by

$$K_{0k} = -c_k A_{\mathtt{sat}}^{l_k} - d_{k1}c_k A_{\mathtt{sat}}^{l_k-1} - \cdots - d_{kl_k-1}c_k A_{\mathtt{sat}} - d_{kl_k}c_k \tag{4.72}$$

where c_k is the k^{th} row of the $C_{\mathtt{sat}}$ matrix, and d_{k*} are desired characteristic polynomial coefficients.

4.5.5 Relaxed Matching Condition

Whereas state tracking control requires a strict matching condition, described by (4.64), the structure of the output tracking controller is more flexible. The gain matrices K_x and K_r are defined in terms of K_0, which encompasses the terms for the desired closed-loop characteristic polynomials given by $d_k(s)$. These polynomials can be arbitrarily tailored to suit any desired system response. The only restriction on the selection of $d_k(s)$ is that the degree of each polynomial must match the degree of the satellite vehicle plant interactor matrix $\xi_{\mathtt{sat}}(s)$, which is common for any traditional pole placement controller design.

4.5.6 Adaptive State Feedback Controller Design

When the state and input matrices $A_{\mathtt{sat}}$ and $B_{\mathtt{sat}}$ are known, the state feedback gains K_x and K_r can be uniquely determined (Goodwin et al., 2001). However, when $A_{\mathtt{sat}}$ and $B_{\mathtt{sat}}$ are either unknown or changing, then static values for K_x and K_r are not appropriate. The uncertainty associated with the nominal controller motivates the development of the adaptive controller, where the parameters of $A_{\mathtt{sat}}$ and $B_{\mathtt{sat}}$ are estimated to determine the appropriate feedback gains.

The goal of the adaptive control algorithm is to have the system output $y_{\mathtt{sat}}(t)$, track a desired reference output $\bar{y}_{\mathtt{sat}}(t)$, given by (4.69), and to have the tracking error

$$e_{\mathtt{sat}}(t) = y_{\mathtt{sat}}(t) - \bar{y}_{\mathtt{sat}}(t) \tag{4.73}$$

decay to zero exponentially. Let K_x^* and K_r^* denote the true but unknown feedback gains, and $K_x(t)$ and $K_r(t)$ be their current time-varying estimates. The feedback control law becomes

$$u_{\mathtt{sat}}(t) = K_x(t)\, x_{\mathtt{sat}}(t) + K_r(t)\, r_{\mathtt{sat}}(t) \tag{4.74}$$

where controller gains, $K_x(t)$ and $K_r(t)$, are updated from adaptive laws. Uncertainties within the $A_{\mathtt{sat}}$ and $B_{\mathtt{sat}}$ matrices, propagate into uncertainty within the plant transfer matrix $G_{\mathtt{sat}}(s)$; but these are accounted for in the HFG matrix K_p, where the LDS decomposition of K_p is incorporated into the adaptation process.

4.5.7 Control Structure

Using the estimates of the gain matrices $K_x(t)$ and $K_r(t)$ within the control law (4.74), and substituting into the state space description (4.61), yields

$$\begin{aligned} \dot{x}_{\mathtt{sat}}(t) &= (A_{\mathtt{sat}} + B_{\mathtt{sat}}\, K_x^*)\, x_{\mathtt{sat}}(t) + B_{\mathtt{sat}}\, K_r^* r(t) \\ &\qquad + B_{\mathtt{sat}}\, [\, (K_x(t) - K_x^*)\, x_{\mathtt{sat}}(t) + (K_r(t) - K_r^*)\, r_{\mathtt{sat}}(t)\,]\,, \\ y_{\mathtt{sat}}(t) &= C_{\mathtt{sat}}\, x_{\mathtt{sat}}(t) \end{aligned} \tag{4.75}$$

so the output tracking error is expressed as

$$e_{\mathtt{sat}}(t) = \bar{G}_{\mathtt{sat}}(s)\, K_p\, [\, \tilde{\Theta}_{\mathtt{sat}}^T\, \omega_{\mathtt{sat}}\,](t) + C_{\mathtt{sat}}\, e^{(A_{\mathtt{sat}} + B_{\mathtt{sat}}\, K_x^*)t}\, x_{\mathtt{sat}}(0) \tag{4.76}$$

where

$$\omega_{\mathtt{sat}}(t) = \big[\, x_{\mathtt{sat}}^T(t),\, r_{\mathtt{sat}}^T(t)\, \big]^T \tag{4.77}$$

is the regressor signal, the matrices

$$\Theta_{\mathtt{sat}}^* = [\, K_x^{*T},\, K_r^{*T}\,]^T, \quad \Theta_{\mathtt{sat}}(t) = [\, K_x^T(t),\, K_r^T(t)\,]^T \tag{4.78}$$

are the unknown constant parameter matrix and its time-varying estimate, and

$$\tilde{\Theta}_{\mathtt{sat}}(t) = \Theta_{\mathtt{sat}}(t) - \Theta_{\mathtt{sat}}^* \tag{4.79}$$

describes the current parameter estimation error. When there is no estimation error, the gain estimates equal their true values, such that $K_x(t) = K_x^*$ and $K_r(t) = K_r^*$. This indicates the tracking error goes to zero, $\lim_{t\to\infty} e_{\mathtt{sat}}(t) = 0$, because the estimation error $\tilde{\Theta}_{\mathtt{sat}}(t)$ is zero, and the stability

of $A_{\mathtt{sat}} + B_{\mathtt{sat}}\, K_x^*$ ensures that

$$C_{\mathtt{sat}}\, e^{(A_{\mathtt{sat}}+B_{\mathtt{sat}}\, K_x^*)t}\, x_{\mathtt{sat}}(0) \tag{4.80}$$

converges to zero exponentially.

4.5.8 Comments

State tracking implementations are more restrictive than their output tracking counterparts. This is because state tracking requires a certain amount of matching within the internal matrix structure, which consequently makes this realization more sensitive to parameter uncertainties. Meanwhile, output tracking MRAC utilizes the interactor matrix; thus only the relative degree of the system must be matched, rather than the internal matrix structure of the system. This relaxed condition is more easily satisfied, and is less sensitive to parameter uncertainties. While the output tracking MRAC design does not require restrictive system matrix matching conditions, which are needed for a state tracking MRAC design, it still achieves the practically meaningful system requirement of tracking a desired output trajectory.

4.6 Inner-Loop Via Output Feedback MRAC

Now that the satellite vehicles have an appropriate control architecture, the next development looks at the inner-loop controller, which manages the tether arms that impart forces on the central hub. First, this section presents the theory for a nominal MIMO output feedback output tracking controller design, which describes how the controller parameters within the controller structure influence the system to track the desired reference model. Then it expands to the output feedback MRAC control structure, which parameterizes the adaptive control law, into a form suitable for the LDS based MRAC architecture. This theory was originally devised for a quadrotor application in (Selfridge and Tao, 2016), but the approach is equally applicable to the inner-loop output feedback TURN control system.

4.6.1 Motivation for Output Feedback

The goal of the inner-loop control system, is to adjust the satellites in a meaningful way, such that the tethers impart a set of desired forces on the central hub. The added difficulty with this control methodology, is that the relative velocities of the satellites with respect to the central hub are not directly measured. Declare the control inputs as the three satellite relative positions with respect to the central hub, which directly influence their respective tether forces. Forward satellite position maps to a horizontal tether force, vertical satellite position maps to a vertical tether force, and lateral satellite position maps to the radial tension tether force. Thus the control input for the tether

is defined as

$$u_{\texttt{tet}}(t) = [\ \delta_x,\ \delta_y,\ \delta_z\ ]^T \in \mathbb{R}^3 \tag{4.81}$$

which is passed as a reference command into the stabilization control loop. Six states are defined as the three relative velocities of the satellite with respect to the central hub ($\dot{\delta}_x$, $\dot{\delta}_y$, $\dot{\delta}_z$), and the three components of the force vector acting on the central hub (F_x, F_y, F_z). Therefore,

$$x_{\texttt{tet}}(t) = \left[\ \dot{\delta}_x,\ \dot{\delta}_y,\ \dot{\delta}_z,\ F_x,\ F_y,\ F_z\ \right]^T \in \mathbb{R}^6 \tag{4.82}$$

describes the inner-loop state vector. Tether forces imparted on the hub are the signals that are measured and tracked, so

$$y_{\texttt{tet}}(t) = [\ F_x,\ F_y,\ F_z\ ]^T \in \mathbb{R}^3 \tag{4.83}$$

forms the output vector. The control objective is to find a control signal $u_{\texttt{tet}}(t)$ for the plant with unknown transfer matrix $G_{\texttt{tet}}(s)$ such that the inner-loop system output $y_{\texttt{tet}}(t)$ tracks a desired response $\bar{y}_{\texttt{tet}}(t)$. The closed-loop system must be stable with bounded signals for any given bounded input signals. Because some of the states for the inner-loop TURN system are not directly available for measurement, an output feedback design is the necessary controller structure.

4.6.2 Reference Model

The reference model expresses the desired system response. It is described by

$$\bar{y}_{\texttt{tet}}(t) = \bar{G}_{\texttt{tet}}(s)\,[r_{\texttt{tet}}](t) \tag{4.84}$$

where $\bar{y}_{\texttt{tet}}(t) \in \mathbb{R}^3$ is the desired system output and $r_{\texttt{tet}}(t) \in \mathbb{R}^3$ is the bounded piecewise continuous external reference signal. Matrix $\bar{G}_{\texttt{tet}}(s) \in \mathbb{R}^{3\times 3}$ is the reference transfer matrix, which describes the desired closed-loop system dynamics. The expression

$$\bar{G}_{\texttt{tet}}(s) = \xi_{\texttt{tet}}^{-1}(s) \tag{4.85}$$

illustrates the relationship between the interactor matrix and the reference model transfer matrix.

4.6.3 Controller Structure

The controller structure for output feedback (Ioannou and Sun, 1996), is given as

$$u_{\texttt{tet}}(t) = \Theta_{\hat{u}}^T\,\hat{u}(t) + \Theta_{\hat{y}}^T\,\hat{y}(t) + \Theta_y\,y_{\texttt{tet}}(t) + \Theta_r\,r_{\texttt{tet}}(t), \tag{4.86}$$

where

$$\Theta_{\hat{u}} = [\Theta_{\hat{u}1}, \ldots, \Theta_{\hat{u}\hat{\nu}-1}]^T, \quad \Theta_{\hat{y}} = [\Theta_{\hat{y}1}, \ldots, \Theta_{\hat{y}\hat{\nu}-1}]^T. \tag{4.87}$$

Matrices Θ_y, Θ_r, and all the sub matrices within $\Theta_{\hat{u}}$ and $\Theta_{\hat{y}}$, are each $\mathbb{R}^{3\times 3}$. The upper bound on the observability index of $G_{\texttt{tet}}(s)$ is given by $\hat{\nu}$, and $\hat{u}(t)$ and $\hat{y}(t)$ are filtered input and output signals,

which are described by

$$\hat{u}(t) = F(s)\,[u_{\texttt{tet}}](t), \quad \hat{y}(t) = F(s)\,[y_{\texttt{tet}}](t) \tag{4.88}$$

with

$$F(s) = I_0(s)/\Lambda(s), \quad I_0(s) = [\, I_m,\, sI_m,\, \ldots,\, s^{\hat{\nu}-2} I_m \,]^T \tag{4.89}$$

where $I_m \in \mathbb{R}^{3\times 3}$ is an identity matrix, and $\Lambda(s)$ is a monic stable polynomial of degree $\hat{\nu} - 1$.

4.6.4 Controller Parameters

When the plant is known, the true parameter values $\Theta^*_{\hat{u}}$, $\Theta^*_{\hat{y}}$, Θ^*_y, and $\Theta^*_r = K_p^{-1}$, exist and satisfy the relationship (Mirkin and Gutman, 2005)

$$\Theta^{*T}_{\hat{u}}\, I_0(s)\, P_{\texttt{tet}}(s) + \left(\Theta^{*T}_{\hat{y}}\, I_0(s) + \Theta^*_y \Lambda(s)\right) Z_{\texttt{tet}}(s) = \Lambda(s)\,(P_{\texttt{tet}}(s) - \Theta^*_r\, \xi_{\texttt{tet}}(s)\, Z_{\texttt{tet}}(s)) \tag{4.90}$$

where $Z_{\texttt{tet}}(s) \in \mathbb{R}^{3\times 3}$ and $P_{\texttt{tet}}(s) \in \mathbb{R}^{3\times 3}$ are both right co-prime polynomial matrices, and $P_{\texttt{tet}}(s)$ is column proper, such that

$$G_{\texttt{tet}}(s) = Z_{\texttt{tet}}(s)\, P^{-1}_{\texttt{tet}}(s) \tag{4.91}$$

is an alternative description of the inner-loop transfer matrix. The plant-model transfer matrix matching equation is attained by post multiplying (4.90) by $P^{-1}_{\texttt{tet}}(s)$, dividing through by $\Lambda(s)$, and substituting in (4.85). This yields

$$I_m - \Theta^{*T}_{\hat{u}}\, F(s) - \Theta^{*T}_{\hat{y}}\, F(s)\, G_{\texttt{tet}}(s) - \Theta^*_y\, G_{\texttt{tet}}(s) = \Theta^*_r\, \bar{G}^{-1}_{\texttt{tet}}(s) G_{\texttt{tet}}(s) \tag{4.92}$$

which, after multiplying through by $u_{\texttt{tet}}(t)$, becomes

$$u_{\texttt{tet}}(t) - \Theta^{*T}_{\hat{u}}\, \hat{u}(t) - \Theta^{*T}_{\hat{y}}\, \hat{y}(t) - \Theta^*_y\, y_{\texttt{tet}}(t) = \Theta^*_r\, \bar{G}^{-1}_{\texttt{tet}}(s)[y_{\texttt{tet}}](t). \tag{4.93}$$

Subtracting $\Theta^*_r\, r_{\texttt{tet}}(t)$ from both sides, and using the relationships (4.84) and (4.85), yields

$$K_p\left(u_{\texttt{tet}}(t) - \Theta^{*T}_{\hat{u}}\, \hat{u}(t) - \Theta^{*T}_{\hat{y}}\, \hat{y}(t) - \Theta^*_y\, y_{\texttt{tet}}(t) - \Theta^*_r\, r_{\texttt{tet}}(t)\right) = \xi_{\texttt{tet}}(s)\,[\, y_{\texttt{tet}} - \bar{y}_{\texttt{tet}}\,](t). \tag{4.94}$$

Consider what happens when the control law (4.86) is populated with the true values $\Theta^*_{\hat{u}}$, $\Theta^*_{\hat{y}}$, Θ^*_y, and Θ^*_r. The left side of (4.94) completely cancels, which leaves

$$\xi_{\texttt{tet}}(s)\,[\, y_{\texttt{tet}} - \bar{y}_{\texttt{tet}}\,](t) = 0 \tag{4.95}$$

and implies that $\lim_{t\to\infty}(y_{\texttt{tet}}(t) - \bar{y}_{\texttt{tet}}(t)) = 0$. When the parameters are known, the output feedback model reference controller is designed to reduce the tracking error to zero, exponentially.

4.6.5 Adaptive Output Feedback Controller Structure

The output feedback model reference controller accomplishes the control objective when the parameters are perfectly known. When the parameter values are not known, they must be estimated using MRAC techniques. To utilize the LDS based MRAC derivation, the adaptive control law must be parameterized into an appropriate form. Define

$$\Theta^*_{\texttt{tet}} = [\ \Theta^{*T}_{\hat{u}},\ \Theta^{*T}_{\hat{y}},\ \Theta^*_y,\ \Theta^*_r\ ]^T \tag{4.96}$$

as the true and unknown constant parameters, and let

$$\Theta_{\texttt{tet}}(t) = [\ \Theta^T_{\hat{u}}(t),\ \Theta^T_{\hat{y}}(t),\ \Theta_y(t),\ \Theta_r(t)\ ]^T \tag{4.97}$$

be their estimates. Then

$$\tilde{\Theta}_{\texttt{tet}}(t) = \Theta_{\texttt{tet}}(t) - \Theta^*_{\texttt{tet}} \tag{4.98}$$

represents the current estimation error, and the vector

$$\omega_{\texttt{tet}}(t) = [\ \hat{u}^T(t),\ \hat{y}^T(t),\ y^T_{\texttt{tet}}(t),\ r^T_{\texttt{tet}}(t)\ ]^T \tag{4.99}$$

is the system regressor signal. This parameterized structure is now in an adaptive control law form, which is suitable for the LDS based MRAC architecture previously presented.

4.6.6 Comments

If the tether system parameters were completely known, then true values within the state matrix $A_{\texttt{tet}}$ and the input matrix $B_{\texttt{tet}}$, which dictate the transfer matrix $G_{\texttt{tet}}(s)$, could be utilized to implement a non-adaptive output feedback model reference control architecture. However, when there is uncertainty within the model, $A_{\texttt{tet}}$ and $B_{\texttt{tet}}$ have unknown values. These errors propagate into the structure of $G_{\texttt{tet}}(s)$, and subsequently the output feedback gains. Using adaptive control allows the system to accommodate this uncertainty within the model.

An MRAC design using either state feedback, as developed in (Selfridge and Tao, 2014a), or output feedback, developed in (Selfridge and Tao, 2016), has the guaranteed stability property and tracking performance described as part of the LDS derivation. This applies for any time-varying reference trajectory $\bar{y}_{\texttt{tet}}(t)$, for any bounded and piecewise continuous reference signal $r_{\texttt{tet}}(t)$, and for any full-order MIMO linearized model. A PID control design does not have such desired properties. It can only stabilize lower-order systems with *a priori* system parameter knowledge, and can only ensure asymptotic tracking for constant reference signals. MRAC can tolerate a large range of system parameter uncertainties, while PID control cannot.

Finally, when the tether arm moves into a different trimmed flight pattern, say to execute a steady state outer-loop command, then the internal structure of $G_{\texttt{tet}}(s)$ changes, so traditional MRAC with a constant K_p is not appropriate. The LDS decomposition presented in this work, includes the

uncertainty of K_p within the adaptation process, so the system can adapt to the new structure of the changing transfer matrix.

4.7 Outer-Loop Via Complementary Filter

Now that the tether arms are suitably managed through the inner-loop architecture, the final task considers the outer-loop controller derivation, which is used to translate the central hub though the inertial frame. Multiple modes of control are available while working with the TURN outer-loop system; however, simultaneously incorporating dual modes for each type of translation, presents some unanticipated challenges. This section reviews each of the outer-loop control modes, summarizes the difficulties devising a unified controller framework, presents a novel alternative approach to the problem, and describes the implementation on the actual TURN vehicle.

4.7.1 Integrating Two Control Modes

Earliest sections within this chapter described that each of the inertial translations have two control modes available to them. Vertical translation uses collective commands: where adjusting the elevator directly pitches each satellite; or through changing the throttle commands, which alters the angular rate of the system, and subsequently influences the overall lift generated from the wings. Horizontal translation makes use of cyclic commands: where adjusting the stabilizers directly pulls on the tether; or through changing the complementary aileron commands, which alters the rotor plane of the system, and subsequently influences the orientation of the vectored thrust.

Each mode can be categorized as having a fast or slow dynamic response. The fast response is characterized when the applied input immediately effects the system. Both the elevator for vertical and the stabilizers for horizontal, directly impact the system dynamics by immediately deviating from the trimmed operating point. Conversely, the slow dynamic response is characterized when the applied input must alter the steady state operation of the system, before the command has any influence on the system response. For instance, throttle adjustments in the vertical mode, must change the angular rate of the system, before the lift force is altered. Similarly, aileron adjustments in the horizontal mode, must alter the rotor plane, before vectored thrust takes effect. To put it another way, the slow dynamic response must move the system into a new trimmed equilibrium operating point, before the maneuver is executed.

A simplified approach might suggest that only a single control mechanism be utilized for each type of translation. But each of the two modes have their own set of benefits, so it is better to incorporate each of their strengths in an efficient means. Ideally, disturbance rejection should be handled by the faster dynamic response. Although it is the more jarring and aggressive maneuver, it can immediately mitigate unanticipated perturbations which arise unexpectedly. On the other side of the coin, the slower steady state type of response is better suited for executing reference signal commands. Since these actions are expected to last for longer durations, it makes sense to move the operating point of the system into a new steady state condition.

4.7.2 Limitations With Traditional Controller Structures

The intent is to devise a means of harmoniously enacting both of the available control modes; where the fast mode mitigates disturbances, and the slow mode executes reference commands. But from the controller perspective, the effects of a reference signal versus that of an external disturbance are indistinguishable. Essentially, the controller applies a corrective input based on the current error signal, which draws no distinction between a commanded reference change and an unanticipated system disturbance. It appears that executing this type of control requires a distinction between a commanded input utilizing the slow mode, and an unexpected disturbance utilizing the fast mode.

At first glance, perhaps a boolean condition could be used to execute the two different types of commands. Some control architectures make use of switching statements, which enact different control methodologies based on the current state of the system. However, because the source of the error signal is indistinguishable, this approach is rather limited in application. Furthermore, this technique can lead to a discontinuous nonlinearity, as the controller flips from one control mode to another. Finally, consider the dynamic response when a step reference signal is commanded. It would be beneficial to use the faster dynamic to begin executing the maneuver, and then seamlessly transition into the slower dynamic while running for an extended period of time. A smooth transition, which harmoniously blends the two control modes together, is not easily implemented with a discrete boolean logic condition. Instead, it will require a new mindset applied to the problem, which is presented next.

4.7.3 Alternative Approach Utilizing A Complementary Filter

Up to this point, the conceptual differentiation between the fast and slow response, has resided within the time domain. An alternative approach, is to consider the frequency domain, and incorporate the two modes together utilizing high-pass and low-pass filters. Rather, than have a distinct and abrupt transition, this approach seamlessly blends the control modes together, which ensures that the appropriate dynamic response is used in turn.

A similar technique is widely utilized within avionics hardware, while performing vehicle attitude estimation (Hughes, 1986). A complementary filter, takes measurements from accelerometer and rate gyro sensors, and calculates the roll and pitch angles for the vehicle. One set of angles is obtained from initializing and integrating the angular rates provided by the rate gyro. This provides a very rapid assessment of the attitude of the vehicle, but suffers in the long run from sensor drift. The other set of angles are calculated using trigonometry based on the vector components of the accelerometer. While, this is highly susceptible to noise in the short term, it provides very reliable values over time. The complementary filter is designed around a specific cutoff frequency, which dictates the respective time constants, and yields a weighting factor applied to each of the filtered signals. The result, is that the attitude estimation sees a very fast response from the rate gyro estimate, but utilizes the accelerometer estimates to correct for gyro drift over time.

While a traditional complementary filter is used to calculate attitude estimates, an identical methodology can be applied to combine each of the two modes for the TURN outer-loop system. Although this application is an extremely common data fusion technique for avionic sensor integration; it appears that this approach has never been used to merge two complementary control input signals.

4.7.4 Complementary Filter Derivation

With a solid understanding of how to achieve the desired control objective, it is it time to unveil the specifics, which detail how the complementary filter is put into practice (Euston et al., 2008).

First, identify a cutoff frequency f_c, measured in hertz, which serves as the dividing line between the high and low frequency components. The cutoff frequency is related to the time constant τ, through the following relationship

$$\tau = \frac{1}{2\pi f_c} \tag{4.100}$$

thus, the units for the time constant are given in seconds. The following definitions

$$H(s) \triangleq \frac{\tau s}{\tau s + 1}, \quad L(s) \triangleq \frac{1}{\tau s + 1} \tag{4.101}$$

are Laplace domain transfer functions, where $H(s)$ is the high-pass filter (HPF), and $L(s)$ is the low-pass filter (LPF). Then, the complementary signal $\beta_C(s)$, is a linear combination of both the high frequency signal $\beta_H(s)$, and the low frequency signal $\beta_L(s)$, through the following equality

$$\beta_C(s) = \left(\frac{\tau s}{\tau s + 1}\right) \beta_H(s) + \left(\frac{1}{\tau s + 1}\right) \beta_L(s) \tag{4.102}$$

where both of the transfer functions signify a weighting factor applied to each signal.

Of course, Laplace terms are quite abstract, and not easily implemented within the time domain of the physical world. Thus, the final task is to modify (4.102), such that the Laplace terms disappear, which puts the equation into a more practical form. Define a weighting gain as

$$\alpha = \frac{\tau s}{\tau s + 1} \tag{4.103}$$

which is identical to the HPF transfer function. After some derivations

$$\frac{1}{\tau s + 1} = \frac{\tau s + 1}{\tau s + 1} - \frac{\tau s}{\tau s + 1} = 1 - \alpha \tag{4.104}$$

yields another weighting gain, which is equivalent to the LPF transfer function. Therefore, the complementary control signal $\beta_C(s)$ can be revised, such that

$$\beta_C(s) = \alpha\, \beta_H(s) + (1 - \alpha)\, \beta_L(s) \tag{4.105}$$

where the weighting gains are now constant quantities, and their sum equals unity. Because (4.105) is free of all Laplace terms, it can be directly converted back into the time domain

$$\beta_C(t) = \alpha\,\beta_H(t) + (1-\alpha)\,\beta_L(t). \tag{4.106}$$

In practice, this will be implemented with a discrete-time controller, so the equivalent time domain expression for the weighting gain in (4.103), is provided by

$$\frac{\tau}{\tau + \frac{1}{s}} \quad \Rightarrow \quad \frac{\tau}{\tau + \Delta T} \tag{4.107}$$

where ΔT is the time step duration for the digital controller.

4.7.5 Implementation on the TURN System

Depending on how the problem is structured, the outer-loop control implementation for the TURN system can be very straight forward or extremely complex.

First consider the most complex scenario. The hub is represented with twelve states, consisting of: three attitude angles, three position descriptions, three angular rates, and three linear velocities. A total of twelve inputs are available, from the four anchor force vectors, which each have three orthogonal components. Finally, there is added complexity where the body frame, which implements the control, is constantly spinning with respect to the inertial frame, which monitors the system output. Having more control inputs than a realistic number of system outputs, and dealing with nonlinear trigonometric terms to account for the system rotation, makes this a very difficult controls problem. Furthermore, without extensive simulations or prototype flight data, it is unclear how much state interaction or input-output coupling is present. Venturing down this path for the first iteration, is not consistent with the spiral development methodology.

Instead, consider a more tractable starting point. The earliest sections in this chapter described an approach, which serves as a road map to guide this process. Based on the TURN geometry, movement within the inertial frame is accomplished entirely through vertical translation and horizontal translation, which are implemented with collective and cyclic commands, respectively. Furthermore, it has already been established that each translation only has two control modes to consider, and the previous sections illustrated how to blend the control signals together using a complementary filter approach. Therefore, this final controls development considers the outer-loop system as two distinct SISO subsystems.

Treating each translation as its own independent SISO subsystem, greatly simplifies the problem. Each translation can be described as a two-state SISO LTI system, which has very straight forward dynamics. Each can be considered as a spring-mass-damper system, where there is no restorative

force acting on the position state. Both of the state space models are described by

$$\begin{aligned} \dot{x}_*(t) &= A_* x_*(t) + B u_*(t) \\ \begin{bmatrix} v_* \\ a_* \end{bmatrix} &= \begin{bmatrix} 0 & 1 \\ 0 & -d_* \end{bmatrix} \begin{bmatrix} p_* \\ v_* \end{bmatrix} + \begin{bmatrix} 0 \\ 1/m \end{bmatrix} F_*, \qquad \text{for } * = \texttt{vert}, \texttt{horz} \end{aligned} \tag{4.108}$$

which are populated with the position p, velocity v, acceleration a, mass m, input force F, and linear damping term d, for both the vertical and horizontal translation models.

For vertical translation, the force is equally distributed among each of the four tether arms. So the commanded change in force, off of the nominal condition, for each individual tether arm is

$$\frac{\Delta F_{\texttt{vert}}}{4} = \Delta F_{*\texttt{vert}} \tag{4.109}$$

where $* = \texttt{A}, \texttt{B}, \texttt{C}, \texttt{D}$ designate each of the tether arms.

Horizontal translation requires one additional step to account for the rotation of the system within the inertial frame. Designate $\bar{\psi}$ as the desired heading, and ψ as the actual heading of the body frame of the central hub. When a tether arm is directly aligned with the intended direction, the radial force adjustment acts in the desired direction. The total force acting on the central hub is allocated such that, half comes from the aligned tether, another half comes from the opposite tether acting in an opposite sense, and the other two tethers have no contribution. A more general relationship is needed to depict a similar mechanism across the entire rotation cycle. Using

$$\frac{\Delta F_{\texttt{horz}}}{2} \cos\left[\left(\psi + \frac{i\pi}{2}\right) - \bar{\psi}\right] = \Delta F_{*\texttt{horz}} \tag{4.110}$$

where $i = 0, 1, 2, 3$ is a numerical index that maps to each of the respective tether arms, designated by $* = \texttt{A}, \texttt{B}, \texttt{C}, \texttt{D}$. When all four tether arms apply their respective forces, the total force acting on the central hub sums to the desired value of $F_{\texttt{horz}}$, which provides a continuous application across the entire rotation cycle. Similarly, the force components that are not aligned with the intended direction are directly canceled out from opposing pairs of tether arms.

Chapter 5

Simulation Study

All the theory needed to develop the nonlinear dynamic model and the adaptive control architecture has been laid out for the Tethered Uni-Rotor Network (TURN) concept vehicle. But at this stage it is nothing more than theory. Thus far, there has been no tangible output validating the feasibility or practicality of this novel concept system design. This chapter remedies the situation by presenting a simulation analysis performed on a smaller scale, commercially viable, TURN aircraft. It begins with a preliminary analysis to familiarize the reader with the vehicle properties and sizing used during the simulation, and investigates each of the three control loops applied to the nonlinear multibody dynamic model of the TURN system.

Chapter Motivation

From a conceptual standpoint, the TURN architecture presents an unmanned aerial vehicle (UAV), that has the potential to drastically outperform both rotorcraft vehicles and standard tube-and-wing style aircraft. The ultimate confirmation that a TURN vehicle can achieve such performance will come from a proof-of-concept prototype demonstration. However, similar to plant modeling and controller development, because the vehicle has a unique configuration there is very little information which aids the initial design process. A simulation study helps assess the system performance prior to committing to a prototype design. Furthermore, the simulation routine will play an extremely important role in the spiral development process. Once flight data has been obtained from a prototype, and the simulation model has been revised to more accurately represent the system dynamics, the simulation routine will serve as a tool to aid future vehicle designs.

For this current research effort, the simulation study is needed for several important reasons. First, it helps specify values and parameters for the satellite layout and sizing. While developing this chapter and the simulations contained herein, the satellite dimensions underwent continuous revisions, enhancing stability and control authority, while reducing moment arms that introduce dynamic cross-coupling. Next, it validates the results of theoretical developments, such as the trimming routine, linearization process, and adaptive control implementation. Finally, it uncovers system dynamics and response characteristics that were originally unanticipated, such as throttle response and the interactions between the multiple rigid bodies that comprise the complete system.

Chapter Objectives

The main goal of this chapter is to accurately simulate a TURN vehicle, at a scale that has immediate commercial viability, such that simulation results aid the design process for the initial prototype. The outcome of this chapter should quantify the sizing parameter for a specific embodiment of a TURN system, verify the trimming and linearization processes work as anticipated, confirm that the general form of the state space representations match the results obtained for this specific instance, and verify the controllability and observability of the simulated system. It must establish a prescribed dynamic response within the bounds of the system performance capabilities, successfully demonstrate reference tracking, identify the threshold of the disturbance rejection boundaries, and confirm that the LDS based model reference adaptive control (MRAC) architecture adapts to uncertainty within the nonlinear plant.

Chapter Outline

Before developing a prototype demonstration for the TURN system, a reliable and accurate simulation model is required to aid the design process. This chapter performs a detailed simulation study which depicts the nonlinear system dynamics and evaluates each of the three control loops.

Section 5.1 performs a *Preliminary Analysis*, which introduces the simulation study. It presents the vehicle sizing and parameters, obtains the set of trimmed satellite states and control inputs, reviews the linearized state space model, and confirms controllability and observability within the system.

Section 5.2 covers the *Satellite Vehicle Stabilization Loop Simulation*, which utilizes state feedback control. It establishes a desired system response, specifies appropriate controller gains, demonstrates disturbance rejection capabilities, and compares single and multivariable controller performance.

Section 5.3 presents the *Tether Arm Inner-Loop Simulation*, which utilizes output feedback. It validates the tether arm trimming process, develops multisine signals for system identification, demonstrates parameter convergence with MRAC, and illustrates the output tracking performance.

5.1 Preliminary Analysis

All the necessary theoretical developments are in place, which provide a complete TURN plant description and a foundation for the controller implementation. Some preliminary analysis is needed before addressing each of the control loops. This section summarizes the sizing and parameters used to populate the simulation vehicle, describes the trimming routine applied to the unconstrained satellite, presents state space matrices of the linearized model, and confirms the controllability and observability matrices match the developed theory.

5.1.1 Vehicle Sizing and Parameters

Implementing the simulation routine, requires numerical values to populate the model. Various scales of TURN systems were previously presented, so the current task determines the most prudent size to investigate for the remainder of this analysis. Future work will utilize a spiral development methodology during the prototyping process; which does not look at the largest embodiment, or even one that might attain eternal flight. Rather, the goal is to consider a layout that can easily validate early dynamic models within the simulation; while at a scale that offers the best possibility of attracting future funding, thereby allowing the project to advance to the next level.

After introducing the TURN vehicle in a previous chapter, a smaller embodiment was presented which would be a formidable competitor within the existing UAV market. This scale offers an ideal starting point before advancing to larger and more complex designs, and an opportunity for immediate commercialization. Thus, the remainder of this document analyzes a system that meets these requirements. A listing of the pertinent sizes and parameter values is provided in Table 5.1.

Hub		
Weight	19.6 N	4.41 lbf
Mass	2.0 kg	0.14 slug
Radius	0.5 m	1.64 ft
Tether		
Length	12.0 m	39.4 ft
Diameter	4.0e-4 m	1/64 in
Density	1000 kg/m^3	1.94 slug/ft^3
Weight	0.0148 N	3.3e-3 lbf
Mass	0.0015 kg	1.0e-4 slug
Drag Co	1.0	-
Satellite		
Weight	31.1 N	7.01 lbf
Mass	3.18 kg	0.22 slug
Inertia(x)	2.81 kg-m^2	66.9 lb-ft^2
Inertia(y)	0.11 kg-m^2	2.61 lb-ft^2
Inertia(z)	2.72 kg-m^2	64.5 lb-ft^2
Wingspan	3.5 m	11.5 ft
Chord	0.2 m	0.66 ft
Thrust	0.47 N	0.10 lbf
Wing Lift Co	0.60	-
Wing Drag Co	0.01	-
Aspect Ratio	17.5	-
L/D Ratio	33.2	-

TABLE 5.1: Vehicle sizing and parameters that make up the TURN simulation model.

5.1.2 Trimmed Satellite States and Inputs

A set of trimmed states and control inputs are needed to obtain the linearized model of the free flying satellite system. The goal is to find this set of parameters such that the system exhibits a force and moment balance throughout the system, which requires that all the second derivatives are exactly equal to zero. The trimming optimization routine can be simplified, because some states and control inputs are known in advance.

While the satellite maintains a level flight condition, all the attitude and angular rate states are known to be zero. Similarly, there is no lateral or vertical translation in a trimmed flight condition, so those states are set to zero as well. A particular airspeed is needed to generate lift over the wing surface to counter balance the aircraft weight. So, the only two states that change in the inertial frame, are the forward position and velocity, but forward acceleration is still required to be zero.

When operating in forward flight, several control inputs should maintain neutral positions. Ailerons, stabilizers, and rudders, are all used to influence states that are trimmed to values of zero, so these control inputs do not need to be included within the trimming optimization process. Only two control inputs need to be adjusted to achieve a trimmed condition: throttle and elevator. Throttle values are adjusted to overcome the aerodynamic drag that arises as the satellite maintains its forward velocity. Elevator deflection is desired to be as close to zero as possible, but it still needs to be an adjustable parameter to balance a pitch moment that may arise.

After running the trim optimization process, the following velocity, elevator deflection, and prop angular rate, were obtained to maintain a trimmed flight condition:

$$V_x = 12.58 \text{ m/s} \qquad \delta_E = -0.0045 \text{ rad} = -0.256 \text{ deg} \quad \Omega_T = 684.9 \text{ rad/sec} \tag{5.1}$$

A motor angular rate of 685 rad/sec, yields a throttle force of 0.469 N (0.1 lbf) for each motor, which indicates that 0.938 N (0.2 lbf) is needed to balance the total aerodynamic drag. With a vehicle weight of 31.1 N (7.01 lbf), the lift-to-drag (L/D) ratio is calculated as 33.15. Considering that traditional tube-and-wing aircraft have L/D ratios around 10, and helicopter rotors are upwards of 50-60, the L/D ratio for the TURN simulation is reasonable.

A high L/D ratio is one of the primary attributes that make the TURN system very aerodynamically efficient. However, this presents some notable limitations while prescribing the desired response characteristics on the forward velocity controller. Consider that the drag force is 33.15 times smaller than the lift force. Thus, the throttle forces are very small with respect to the total vehicle mass. As such, the throttle dynamics are rather slow with respect to other control input-output pairs.

5.1.3 State Space Model of Linearized Satellite

This section uses the trimmed states and control inputs previously described, and presents the results of the linearization process applied to an unconstrained satellite vehicle. The general structure

of the linearized state matrix $A_{\texttt{sat}}$, was previously shown to be

$$A_{\texttt{sat}} = A_{\texttt{lin}} = \begin{bmatrix} 0_{3\times3} & 0_{3\times3} & I_{3\times3} & 0_{3\times3} \\ 0_{3\times3} & 0_{3\times3} & 0_{3\times3} & I_{3\times3} \\ A_{rr} & 0_{3\times3} & 0_{3\times3} & A_{rt} \\ A_{tr} & 0_{3\times3} & 0_{3\times3} & A_{tt} \end{bmatrix} \in \mathbb{R}^{12\times12} \tag{5.2}$$

but the submatrices, given as

$$\begin{aligned} A_{rr} &= \begin{bmatrix} 0 & 0 & 0 \\ 0 & -24.37 & 0 \\ 0 & 0 & -0.903 \end{bmatrix} \quad A_{rt} = \begin{bmatrix} 0 & 0 & 0 \\ 0 & 0 & -1.939 \\ 0 & 0.072 & 0 \end{bmatrix} \\ A_{tr} &= \begin{bmatrix} 0 & -0.043 & 0 \\ 9.803 & 0 & 13.41 \\ 0 & -43.65 & 0 \end{bmatrix} \quad A_{tt} = \begin{bmatrix} -0.047 & 0 & 0.777 \\ 0 & -1.067 & 0 \\ -1.559 & 0 & -3.473 \end{bmatrix} \end{aligned} \tag{5.3}$$

are now populated with values from the linearization process. Next, the linearized control input matrix was determined to be

$$B_{\texttt{lin}} = \begin{bmatrix} & & & 0_{6\times6} & & \\ -4.911 & 4.911 & 0 & 0 & 0 & 0 \\ 7.17e{-}3 & 7.17e-3 & 24.58 & 0 & 0 & 0 \\ 0 & 0 & 0 & 0.926 & 0.029 & 0 \\ 0 & 0 & 0.043 & 0 & 0 & 8.62e{-}4 \\ 0 & 0 & 0 & -4.214 & 9.130 & 0 \\ 2.687 & 2.687 & 8.779 & 0 & 0 & 0 \end{bmatrix} \tag{5.4}$$

which leads to the control input mixing matrix, given as

$$B_{\texttt{mix}} = \begin{bmatrix} -0.0363 & 0 & 0 & 0 & 0 & 0.0586 \\ 0.0363 & 0 & 0 & 0 & 0 & 0.0586 \\ 0 & 0.3842 & 0 & 0 & 0 & 0 \\ 0 & 0 & 0.3966 & 0 & 0 & 0 \\ 0 & 0 & 0 & 0 & 0.0345 & 0 \\ 0 & 0 & 0 & 365.02 & 0 & 0 \end{bmatrix} \tag{5.5}$$

and subsequently determines the satellite control input matrix, calculated as

$$B_{\texttt{sat}} = \begin{bmatrix} & & & 0_{6\times6} & & \\ 0.3563 & 0 & 0 & 0 & 0 & 0 \\ 0 & 9.4427 & 0 & 0 & 0 & 8.402e{-}4 \\ 0 & 0 & 0.3674 & 0 & 9.939e{-}4 & 0 \\ 0 & 0.0164 & 0 & 0.3148 & 0 & 0 \\ 0 & 0 & -1.6714 & 0 & 0.3148 & 0 \\ 0 & 3.3729 & 0 & 0 & 0 & 0.3148 \end{bmatrix} \tag{5.6}$$

$$\begin{bmatrix}
0 & 0 & 0 & 0 & 0 & 0 & 0.356 & 0 & 0 & 0 & 0 & 0 \\
0 & 0 & 0 & 0 & 0 & 0 & 0 & 9.443 & 0 & 0 & 0 & 8.40e\text{–}4 \\
0 & 0 & 0 & 0 & 0 & 0 & 0 & 0 & 0.367 & 0 & 9.94e\text{–}4 & 0 \\
0 & 0 & 0 & 0 & 0 & 0 & 0 & 0.016 & 0 & 0.315 & 0 & 0 \\
0 & 0 & 0 & 0 & 0 & 0 & 0 & 0 & –1.671 & 0 & 0.315 & 0 \\
0 & 0 & 0 & 0 & 0 & 0 & 0 & 3.373 & 0 & 0 & 0 & 0.315 \\
0.356 & 0 & 0 & 0 & 0 & 0 & 0 & 0 & 0 & 0 & 0 & 0 \\
0 & 9.443 & 0 & 0 & 0 & 8.40e\text{–}4 & 0 & –6.540 & 0 & 0 & 0 & –0.610 \\
0 & 0 & 0.367 & 0 & 9.94e\text{–}4 & 0 & 0 & 0 & –0.120 & 0 & 0.023 & 0 \\
0 & 0.016 & 0 & 0.315 & 0 & 0 & 0 & 2.619 & 0 & –0.015 & 0 & 0.244 \\
0 & 0 & –1.671 & 0 & 0.315 & 0 & 0 & 0 & 1.783 & 0 & –0.336 & 0 \\
0 & 3.373 & 0 & 0 & 0 & 0.315 & 0 & –11.74 & 0 & –0.491 & 0 & −1.093
\end{bmatrix}$$

FIGURE 5.1: Controllability matrix for the linearized unconstrained satellite vehicle.

where the inverse of the moment inertias (0.3563, 9.4427, 0.3671) directly relate moments to their respective rotational states, the inverse of the mass (0.3148) directly relate forces to their respective translational states, and the remaining elements incorporate the cross-coupling terms which preserve the system dynamics of the original linearized model.

5.1.4 Controllability and Observability

The general form of the reduced controllability matrix $\mathbb{C}_{\mathtt{sat}}$, was previously shown as

$$\mathbb{C}_{\mathtt{sat}} = [\, B_{\mathtt{sat}},\ A_{\mathtt{sat}}B_{\mathtt{sat}} \,] = \begin{bmatrix} 0_{3\times3} & 0_{3\times3} & B_{rm} & B_{rf} \\ 0_{3\times3} & 0_{3\times3} & B_{tm} & B_{tf} \\ B_{rm} & B_{rf} & A_{rt}B_{tm} & A_{rt}B_{tf} \\ B_{tm} & B_{tf} & A_{tt}B_{tm} & A_{tt}B_{tf} \end{bmatrix} \tag{5.7}$$

and the general form of the reduced observability matrix $\mathbb{O}_{\mathtt{sat}}$, was found to be a $\mathbb{R}^{12\times12}$ identity matrix. The simulation verified these results, where the first twelve rows of the observability matrix matches an identity matrix, and the first twelve columns of the controllability matrix maintain the form described by (5.7), and are displayed in Figure 5.1.

5.2 Satellite Vehicle Stabilization Loop Simulation

The foundation for successfully implementing a TURN vehicle begins with the ability to adequately control each satellite vehicle. Before introducing dynamic complexities from the tether arm, it is prudent to assess the flight characteristics of a completely unconstrained, free flying satellite vehicle. This section assigns the desired response characteristics, assembles the appropriate controller gains, assesses the disturbance rejection capabilities, and showcases how a multiple-input multiple-output (MIMO) controller outperforms its single-input single-output (SISO) controller counterpart.

5.2.1 Desired System Response

With a full state feedback design, the desired closed-loop system response can be arbitrarily selected (Franklin et al., 2010). For illustrative purposes, this analysis will implement similar response characteristics on each of the different input-output channels. In future developments, each subsystem may have a uniquely optimized dynamic response to accommodate other design considerations, such as power consumption or disturbance rejection. A detailed account of the system response characteristics is provided in *Appendix B: SISO State Feedback*.

The goal is to obtain the real and imaginary parts of the complex roots, σ and ω, respectively. As a starting point, the desired percent overshoot should be close to $M_p = 5\%$, for all system outputs. So solve for the damping ratio as

$$\zeta = \sqrt{\frac{\ln(M_p)^2}{\pi^2 + \ln(M_p)^2}} = \sqrt{\frac{\ln(0.05)^2}{\pi^2 + \ln(0.05)^2}} = 0.69. \tag{5.8}$$

Two inputs, F_x from throttle and M_z from rudder, have notably slower dynamics. Their desired settling time, within 1% of steady-state, should be around 2.0 seconds, while the remaining outputs can accommodate 0.75 seconds. Obtain the real part ($\sigma = \texttt{Re}[\lambda]$) of the complex root with

$$\sigma = \frac{4.6}{t_s} \qquad \sigma_f = \frac{4.6}{0.75} = 6.13 \qquad \sigma_s = \frac{4.6}{2.0} = 2.30 \tag{5.9}$$

with natural frequencies given by

$$\omega_n = \frac{\sigma}{\zeta} \qquad \omega_{nf} = \frac{6.13}{0.69} = 8.88 \qquad \omega_{ns} = \frac{2.30}{0.69} = 3.33 \tag{5.10}$$

then the damped natural frequencies become

$$\omega = \omega_n \sqrt{1 - \zeta^2} \qquad \omega_f = 8.88\sqrt{1 - 0.69^2} = 6.43 \qquad \omega_s = 3.33\sqrt{1 - 0.69^2} = 2.41 \tag{5.11}$$

which yields the imaginary parts ($\omega = \texttt{Im}[\lambda]$) of the complex roots. The complex pair with the faster dynamics form their desired characteristic polynomial as

$$\alpha_f(s) = (s + 6.13 + 6.43j)(s + 6.13 - 6.43j) = s^2 + 12.27s + 78.96 \tag{5.12}$$

with polynomial coefficients of $\alpha_{f0} = 78.96$ and $\alpha_{f1} = 12.27$, and the other complex pair with the slower dynamics form their desired characteristic polynomial as

$$\alpha_s(s) = (s + 2.30 + 2.41j)(s + 2.30 - 2.41j) = s^2 + 4.6s + 11.10 \tag{5.13}$$

with polynomial coefficients of $\alpha_{s0} = 11.10$ and $\alpha_{s1} = 4.6$.

5.2.2 Controller Gains

After using the linearized state space matrices, incorporating the desired response polynomials, and following the procedure outlined in the previous chapter, the controller gains can be obtained. The state feedback gain K_x, is evaluated as

$$K_x = \begin{bmatrix} -221.7 & 0 & 0 & 0 & 0 & 0 & -34.43 & 0 & 0 & 0 & 0 & 0 \\ 0 & -5.78 & 0 & 0 & 0 & 0 & 0 & -1.29 & 0 & 0 & 0 & 0.21 \\ 0 & 0 & -27.77 & 0 & 0 & 0 & 0 & 0 & -12.52 & 0 & -0.19 & 0 \\ 0 & 0.14 & 0 & -35.29 & 0 & 0 & 0 & 0 & 0 & -14.47 & 0 & -2.47 \\ -31.15 & 0 & -42.60 & 0 & -250.9 & 0 & 0 & 0 & 0 & 0 & -35.58 & 0 \\ 0 & 138.7 & 0 & 0 & 0 & -250.9 & 0 & 0 & 0 & 4.95 & 0 & -27.94 \end{bmatrix} \tag{5.14}$$

the reference gain K_r is solved as

$$K_r = \begin{bmatrix} 221.7 & 0 & 0 & 0 & 0 & 0 \\ 0 & 5.78 & 0 & 0 & 0 & 0 \\ 0 & 0 & 27.77 & 0 & 0 & 0 \\ 0 & 0 & 0 & 35.29 & 0 & 0 \\ 0 & 0 & 0 & 0 & 250.9 & 0 \\ 0 & 0 & 0 & 0 & 0 & 250.9 \end{bmatrix} \tag{5.15}$$

and the high frequency gain (HFG) matrix is given by

$$K_p = \begin{bmatrix} 0.3563 & 0 & 0 & 0 & 0 & 0 \\ 0 & 9.4427 & 0 & 0 & 0 & 0 \\ 0 & 0 & 0.3674 & 0 & 0 & 0 \\ 0 & 0 & 0 & 0.3148 & 0 & 0 \\ 0 & 0 & 0 & 0 & 0.3148 & 0 \\ 0 & 0 & 0 & 0 & 0 & 0.3148 \end{bmatrix} \tag{5.16}$$

which has its main diagonal populated with values that are the inverse of the moment inertias and mass of the satellite vehicle.

5.2.3 Disturbance Rejection

While the inner-loop relies heavily on reference tracking, and the outer-loop focuses on coordinated maneuvers, the stabilization loop is predominantly concerned with disturbance rejection. Each satellite vehicle is designed to have control influence over all six degrees of freedom; which includes the three rotational axes and the three translational axes. Although, the satellite layout attempts to align forces with the CG and to minimize off-axis moment arms, it is impossible to completely eliminate cross-coupling between system outputs. This simulation assesses the interaction between such states, and identifies the boundaries of the disturbance rejection capabilities.

The simulation runs for 14.0 sec, and introduces six disturbances, equally spaced at two second increments, with each lasting 0.1 sec in duration. All control surface deflections are designed so a positive command rotates the surface to produce a positive sense on the intended axis. All disturbances have a negative sense, which allows the controller to implement a positive command

correction. The magnitude of the disturbance was iteratively selected as the largest value which did not saturate the control surface. The disturbances begin with three moments applied to the roll, pitch, and yaw axes, and then introduces three forces applied to the forward, lateral, and vertical axes. The magnitudes of each disturbance are given as

$$\begin{aligned} M_x &\Rightarrow -20.0\ \text{Nm} & F_x &\Rightarrow -15.0\ \text{N} \\ M_y &\Rightarrow -1.0\ \text{Nm} & F_y &\Rightarrow -20.0\ \text{N} \\ M_z &\Rightarrow -3.0\ \text{Nm} & F_z &\Rightarrow -15.0\ \text{N} \end{aligned} \tag{5.17}$$

and the results are displayed on the following three figures. Figure 5.2 shows plots of the deviations from the trim point for all twelve system states, Figure 5.3 illustrates plots of the applied forces and moments expressed in the body frame, and Figure 5.4 provides plots of the control input commands implemented directly by the physical components.

The most notable effect conveyed in the simulations, is the influence the control surfaces have on the throttle. When a control surface articulates to mitigate a disturbance, the aerodynamic drag on the satellite increases; thus the throttle must adjust to compensate for this additional force. Because the simulation is testing the bandwidth of the disturbance rejection capabilities, each of the control surfaces come very close to their maximum deflection of 30 degrees. These extreme deflections introduce considerable drag, which in some cases is as high as twice the magnitude of the trimmed throttle force. As such, cross-coupling shows up in throttle commands, and the X-axis translation and force plots. The magnitudes of the simulated disturbances are quite extreme, with forces that

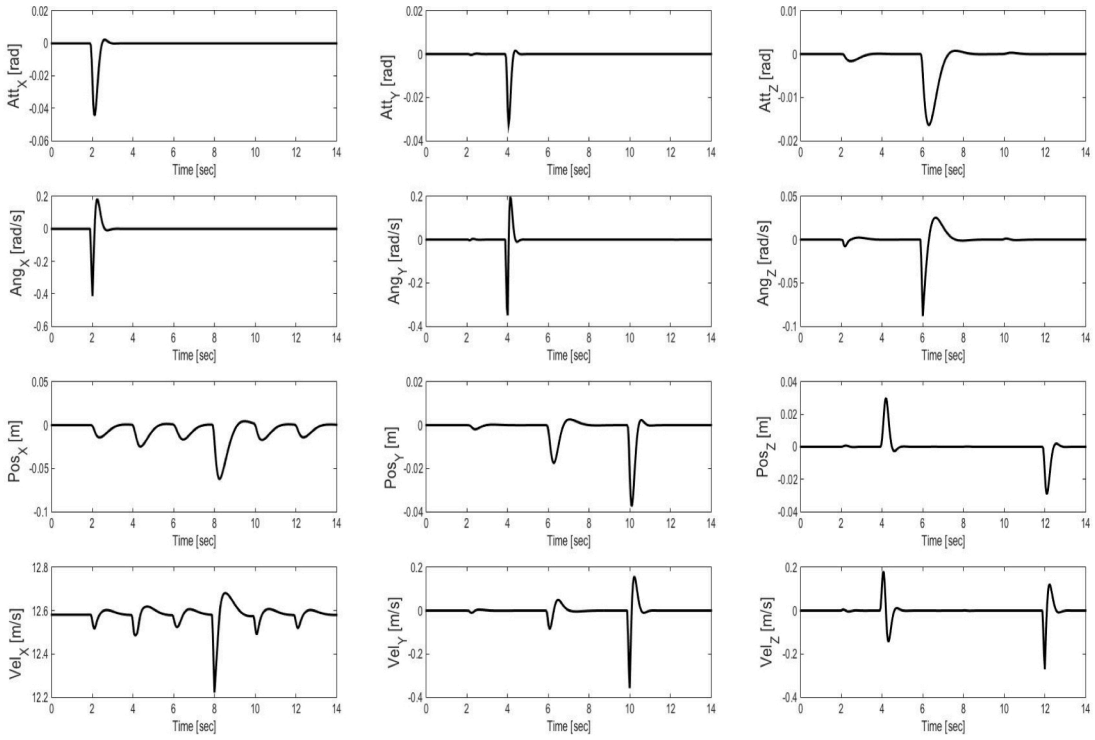

FIGURE 5.2: Satellite disturbance rejection: Plots of satellite system states.

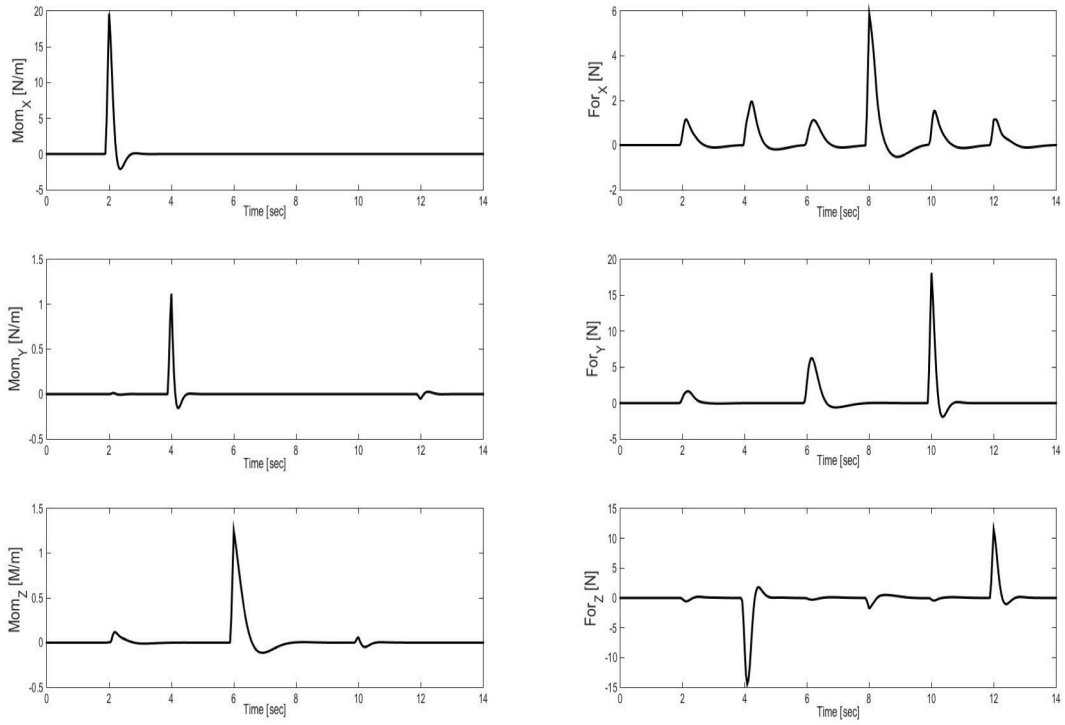

FIGURE 5.3: Satellite disturbance rejection: Plots of satellite forces and moments.

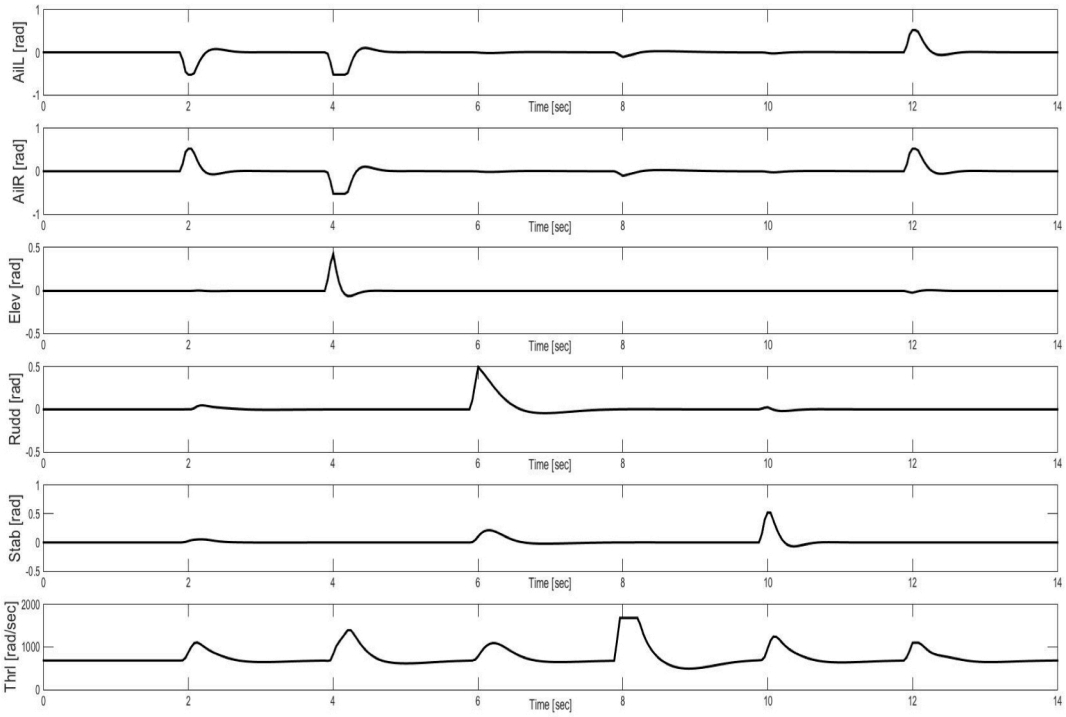

FIGURE 5.4: Satellite disturbance rejection: Plots of satellite control inputs.

are 50-66% of the total weight of the vehicle, which are unlikely to be encountered in practice.

Aside from throttle compensation, nearly all of the command inputs are decoupled from one another. Roll from the ailerons is nearly completely isolated, yaw from the rudders has a small interaction with the stabilizers, throttle does not adversely impact any other states, and lateral and vertical translations from the stabilizers and ailerons are predominantly independent from every other state. The single exception is the pitch command enacted by the elevator. Altering this state rotates the thrust vector of the motors in the inertial frame, which induces a vertical translation, and invokes a complementary aileron corrective command input. This coupling is inherent in the vehicle dynamics and cannot be eliminated through adjustments to the satellite layout.

Finally, it is interesting to note how the structure of the control input mixing matrix $B_{\texttt{mix}}$, reflects the simulated commands of the physical control inputs. Because the disturbances mirror the indexing within $u_{\texttt{sat}}$, and the plots are arranged in the same order as $u_{\texttt{lin}}$, the significant perturbations within Figure 5.4 match the sign and placement of the elements within $B_{\texttt{mix}}$.

5.2.4 SISO vs MIMO Response

Working directly with SISO subsystems is an efficient design technique while evaluating how the satellite layout achieves a desired response for a specific input-output channel. It also provides a valuable confirmation that the MIMO controller applies a comparable control input, while tracking

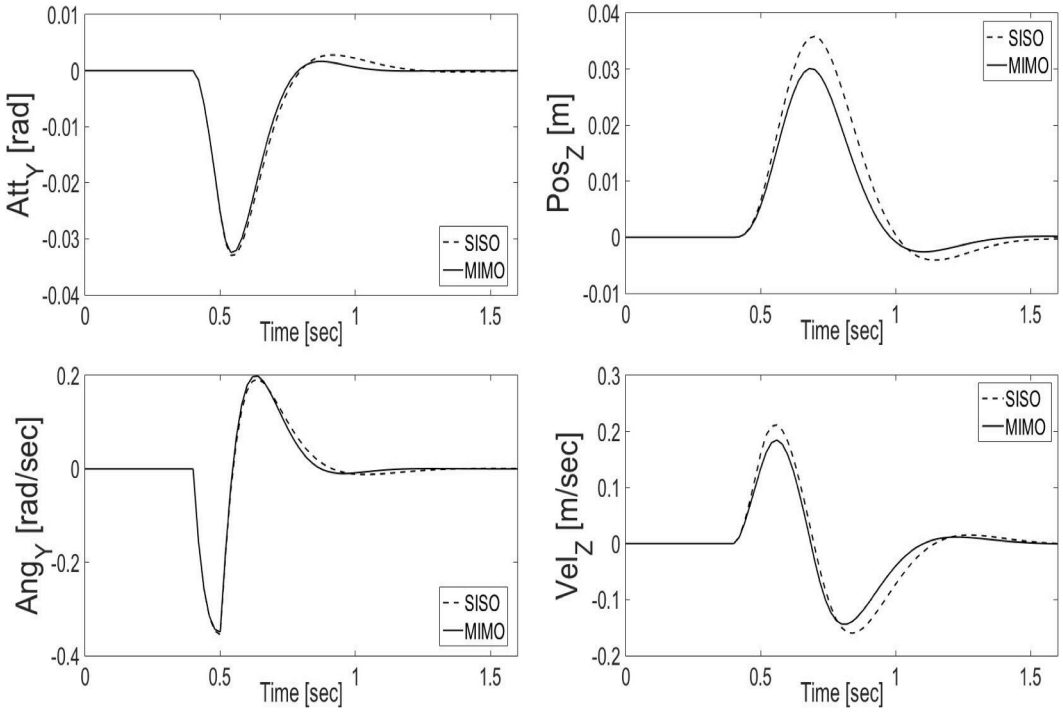

FIGURE 5.5: A comparison between SISO and MIMO controller system outputs.

reference signals and mitigating disturbances, within the system. However, a MIMO controller accounts for the cross-coupling with a system, which leads to a better system output. The next simulation offers a comparison between SISO and MIMO controllers, and demonstrates this effect.

Figure 5.5 applies the same pitch disturbance as the previous set of simulations, but more closely reviews the interactions between the pitch rotation and the vertical translation states. The two signals on each plot represent the system response from SISO and MIMO controllers. First, the similarity between each of the signals indicates that MIMO controller is implementing the desired characteristic response that was designed for the SISO subsystem. Second, each of the subplots show an improvement in performance with the MIMO controller. The rotational states return to equilibrium slightly faster, and the amplitude of the translation states is reduced by about 15%.

5.3 Tether Arm Inner-Loop Simulation

A stabilization loop implemented on the unconstrained satellite forms a solid foundation, but the real test is utilizing output feedback when some of the states are not directly measured. This section confirms the trim routine works on the TURN tether arm subsystem, introduces multisine signal injection to facilitate parameter estimation, addresses the inner-loop MRAC architecture setup, and reviews the output tracking capabilities of the output feedback MRAC system.

5.3.1 Plots of Trimmed Tether Arm

Previous sections described a process for trimming the TURN multibody dynamic models. This section presents the results of that effort, by displaying two figures depicting a trimmed system.

Figure 5.6 conveys several perspective views of a trimmed tether arm. Values for density, diameter, and mass of the tether, were assigned larger values which exaggerate effects of drag and gravity, to showcase the trimming capability. Notice, the tether bends uniformly in the vertical direction from gravity, and the horizontal curvature becomes more pronounced outward as drag increases. Finally, the satellite center of gravity aligns with the tether endpoint force vector, as expected.

Figure 5.7 displays the states of a trimmed TURN satellite in the inertial frame. The satellite flies in a circle around the hub, so the horizontal position and velocity are sinusoidal. The central hub rotates at a constant angular rate, as seen in the upper right corner. All other states maintain static equilibrium, so the value of those states remain very near their trimmed values.

5.3.2 Multisine Signal Injection

When running the MRAC adaptive control architecture, ensuring the parameter estimates converge to their true values requires persistent excitation to make the signal “rich” enough. Multisine signal injection accomplishes this task. The process applies a summation of sinusoidal inputs to the system, which excites the system dynamics so the adaptation continues with new measurements.

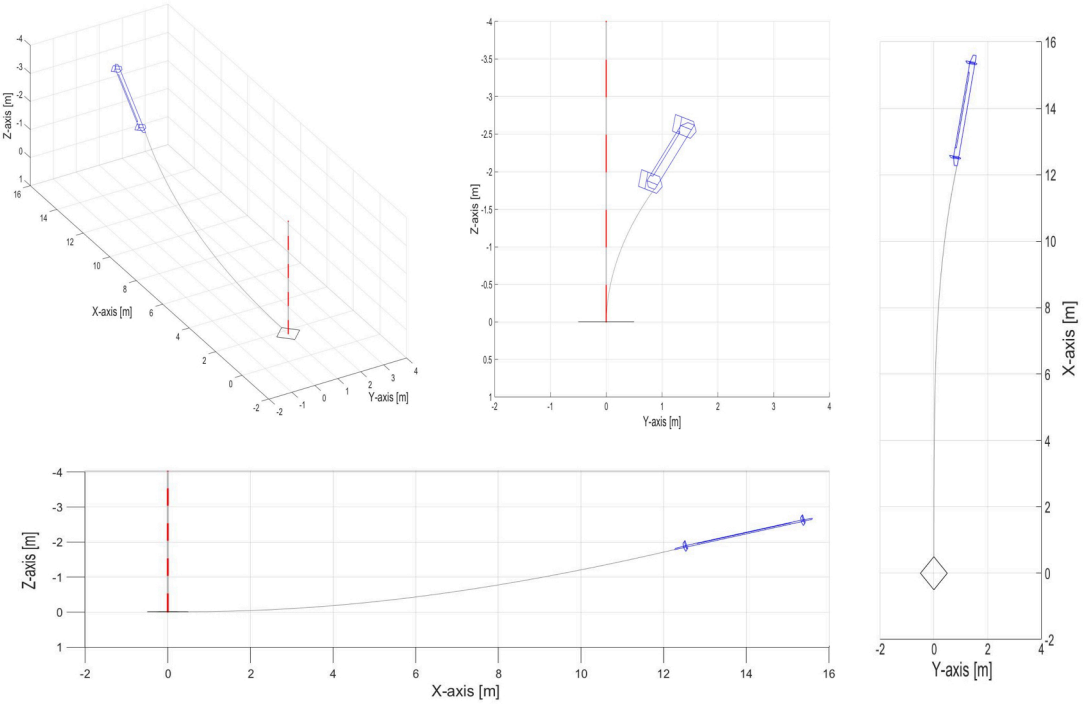

FIGURE 5.6: Animation views of the rendered trimmed tether arm, with exaggerated parameters.

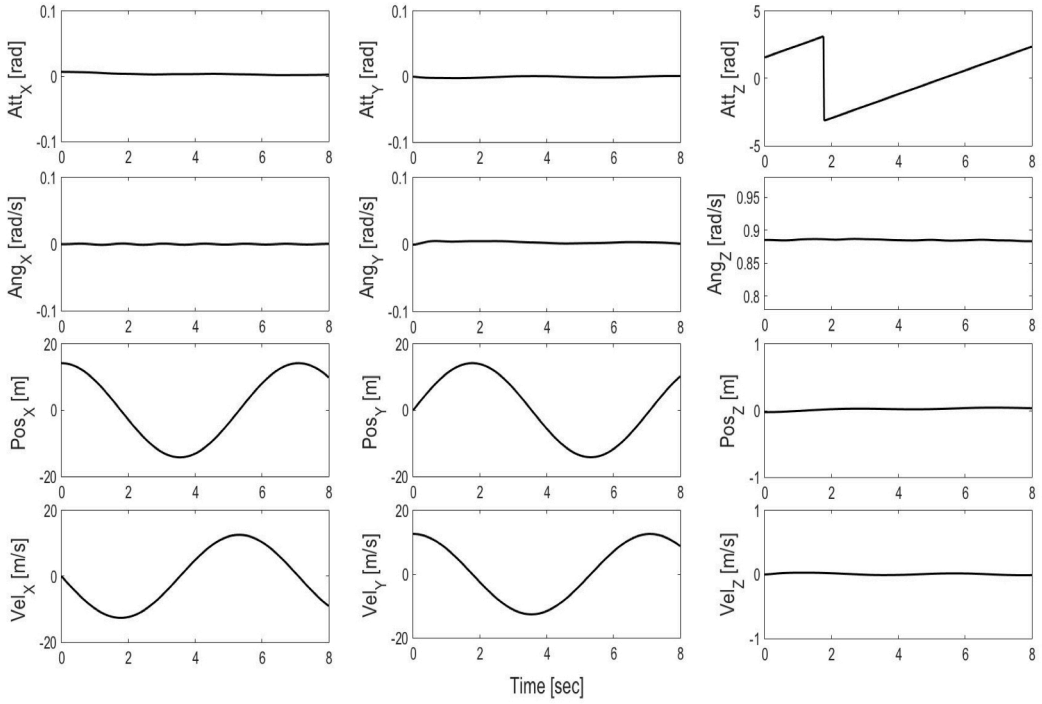

FIGURE 5.7: Plots of trimmed tether arm states, expressed in the inertial frame.

A constant control input contains a single frequency at zero. Sinusoidal inputs with frequency ω and amplitude A, contribute two frequencies at $\pm\omega$. From (Tao, 2003b), a persistently exciting control signal, for an m input system, can be implemented with

$$u_i(t) = \sum_{j=1}^{m_o} A_{ij} \cos(\omega_{ij} t) \tag{5.18}$$

where $A_{ij} \neq 0$, and ω_{ij} are all distinct, for $i = 1, 2, \cdots, m$. The number of frequency components is an integer specified by m_o, and must observe the inequality

$$m_o \geq \frac{n+1}{2} \tag{5.19}$$

to introduce enough signal excitation. This approach ensures the estimate errors go to zero, exponentially. However, this design does not utilize phase shifts within the summed harmonics.

According to (Morelli, 2000), adding appropriately designed phase shifts introduces orthogonality within the sinusoidal inputs. This achieves excitation with a reduced amount of control input, and ensures the signal injection values all return to zero at the same time. Their theory was expanded in (Morelli, 2003), to account for multiple input systems.

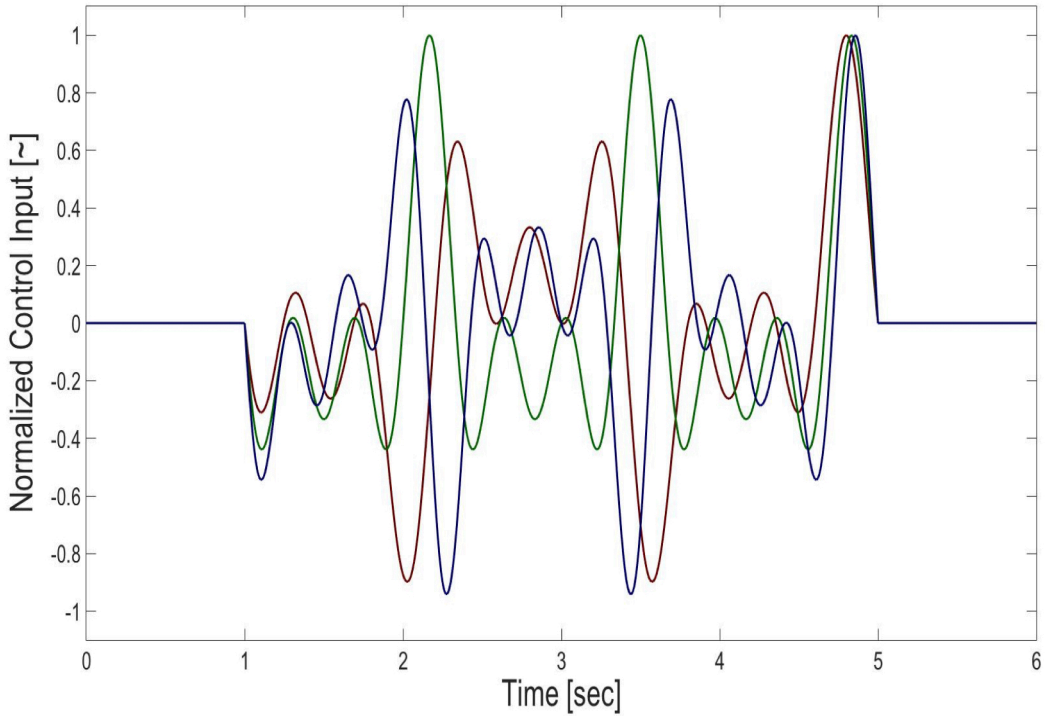

FIGURE 5.8: Sample multisine function output, developed for three control signals.

The multisine signal is described by

$$u_i(t) = \sum_{j=1}^{m_o} A_{ij} \cos\left(\frac{2\pi j t}{T} + \phi_{ij}\right) \tag{5.20}$$

where T is the duration of the excitation, and ϕ_{ij} are the phase angles to be selected for each of the harmonic components. The goal is to select the phase angles such that the *peak factor*, described by

$$PF(u_i) = \frac{[\max(u_i) - \min(u_i)]/2}{\sqrt{\left(u_i^T u_i\right)/N}} = \frac{\|u_j\|_\infty}{\|u_j\|_2} \tag{5.21}$$

is minimized. The last term in the equality, named the *crest factor*, only holds true when the control inputs oscillate symmetrically about zero. The remainder of their research outlines a process for generating frequencies within an appropriate range, an optimization routine to minimize the peak factor, and an iterative loop that adjusts the phase shift offset so each input begins and ends at zero. A fictitious set of multisine signals, with three control inputs, is demonstrated in Figure 5.8.

For the TURN simulation, there are twelve total states, which requires a minimum of seven unique frequencies per input channel. Because the throttle has slow dynamics, and high frequencies have a diminished system output, the desired frequency band was initially set as 0.0 Hz to 0.5 Hz. Selecting a frequency step size as $\Delta f = 0.01$, allows for eight unique frequencies per input channel, so using $\Delta f = 1/T$, the duration of the multisine signal was determined to be 100 sec. One of the conditions is that the minimum frequency observes the inequality $f_{\min} \geq 2/T$, so the final frequency set begins at 0.02 Hz, works upward in 0.01 Hz step sizes, increments through six control inputs and eight frequencies per channel, and ends at 0.49 Hz. The optimization and phase shift offset were applied, and a set of custom multisine signals were created for the TURN simulation.

5.3.3 Inner-Loop MRAC with Signal Injection

Having generated a set of persistently exciting control input signals, the next task utilizes those commands on the tether arm subsystem, while running the LDS based MRAC architecture. The second order adaptive filter was selected as

$$f(s) = 1/h(s) \quad \texttt{with} \quad h(s) = (s + 4 + 4i)(s + 4 - 4i) = s^2 + 8s + 32 \tag{5.22}$$

which is centered between the fast and slow dynamics prescribed for the closed-loop systems. Before running the simulation, all the time-varying gain values must be initialized, which include the state feedback gains and the matrices for the $LDS = K_p$ decomposition. A discrepancy must exist between the true parameter values and their time varying estimates for adaptation to occur. Prior to the simulation, the HFG matrix K_p and the state feedback gain matrix K_x are initialized at 95% of their true values, then the LDS matrices are determined. Setting $L = I_6$ satisfies the unity lower diagonal condition. Diagonal matrix D doubles as an adaptive gain setting, so specifying a

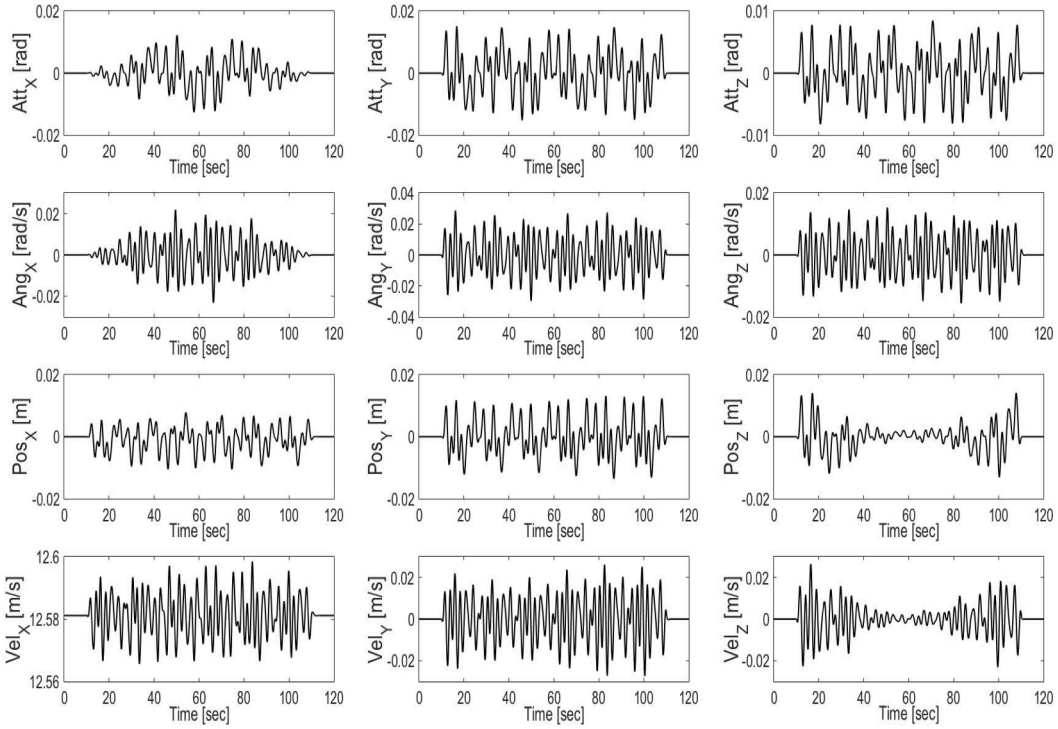

FIGURE 5.9: Multisine signal injection: Plots of satellite system states.

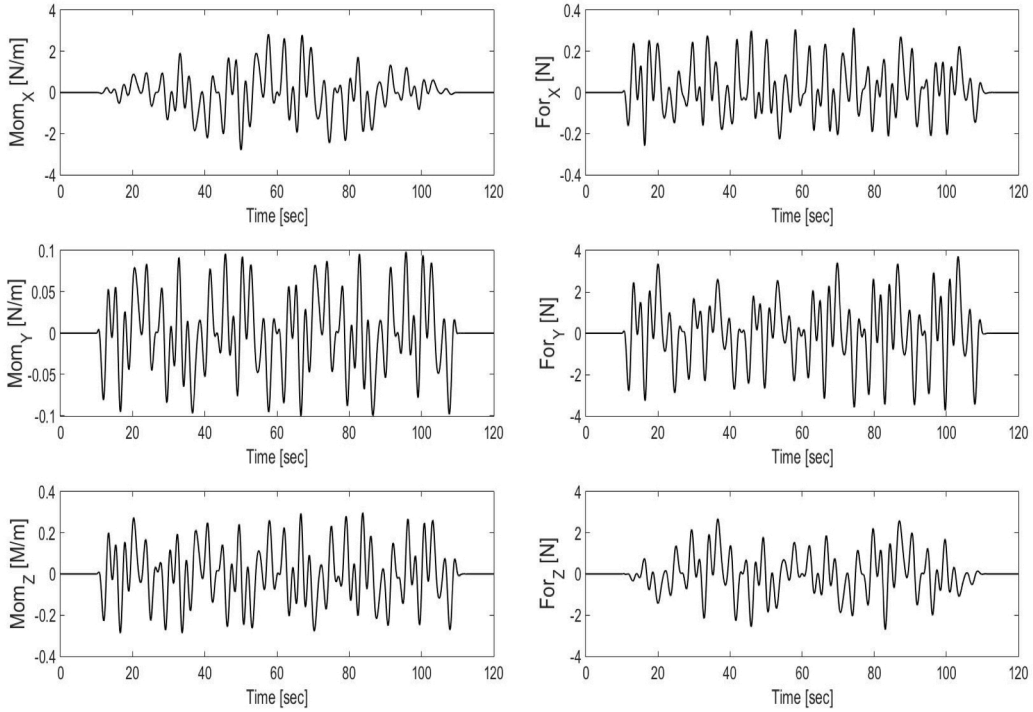

FIGURE 5.10: Multisine signal injection: Plots of satellite forces and moments.

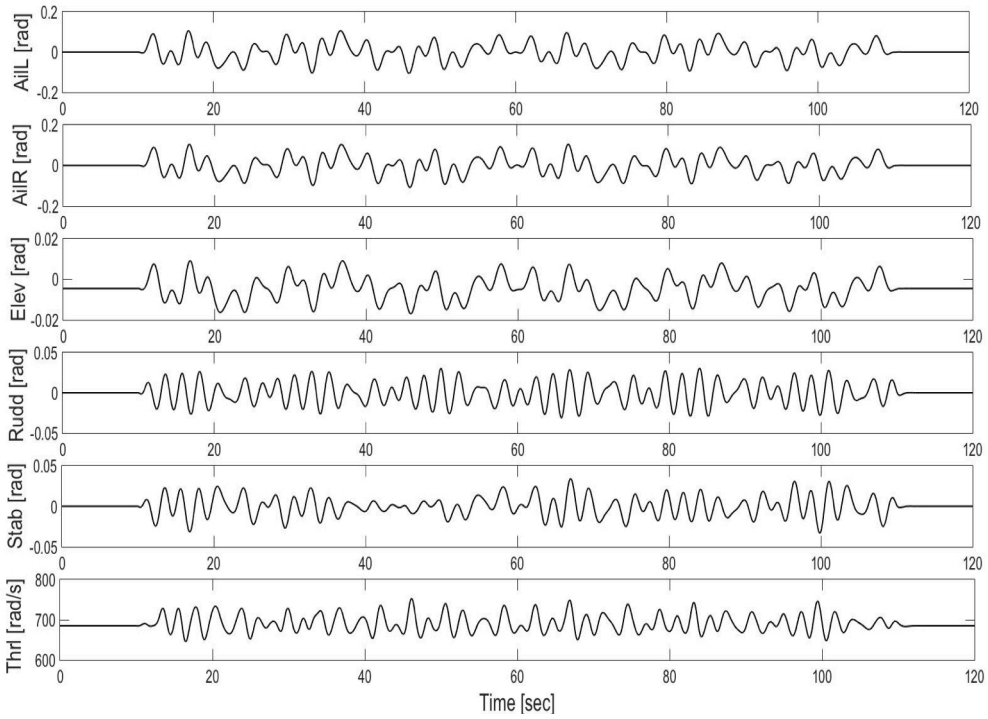

FIGURE 5.11: Multisine signal injection: Plots of satellite control inputs.

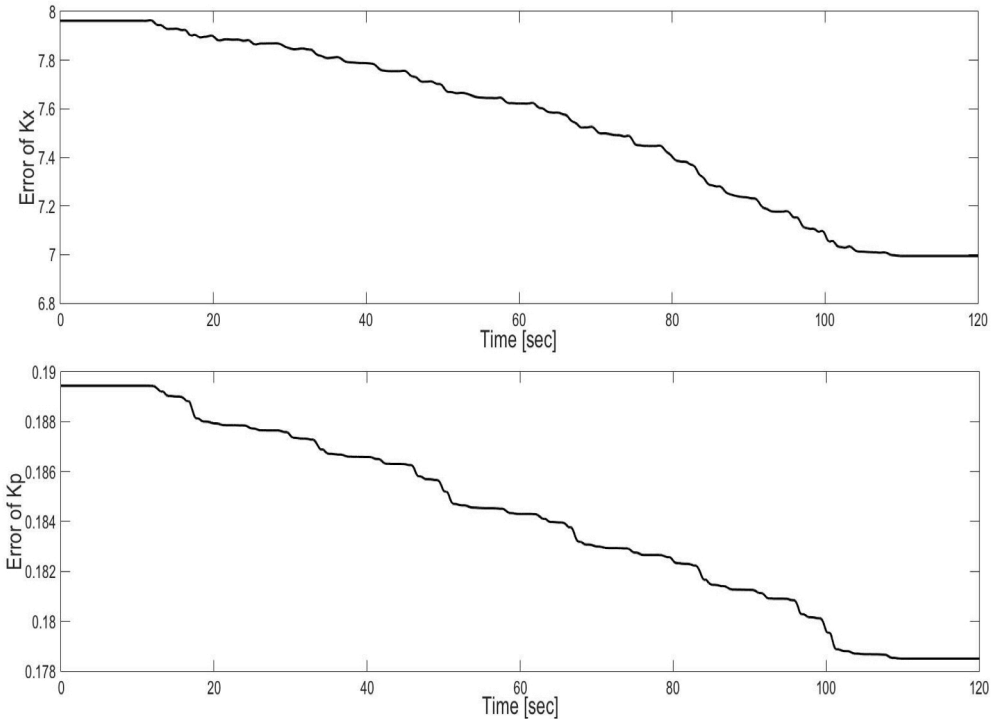

FIGURE 5.12: Multisine signal injection: Tether arm parameter estimation errors.

gain value of $d = 100,000$, the matrix is initialized as $D = dI_6$. The final matrix is subsequently initialized as $S = K_p/d$, to maintain the decomposition equality.

Four figures illustrate the results of this simulation. A 100.0 sec multisine signal injection time span, with 10.0 sec of padding on either end, yield a 120.0 sec simulation duration. When the multisine signal is generated, each signal has a magnitude around unity. To implement them on the TURN tether arm, each input signal was scaled to 40% of the maximum allowable range for that control input. Figure 5.9 shows plots of the deviations from the relative trim points for all twelve system states, Figure 5.10 illustrates the plots of the applied forces and moments expressed in the body frame, Figure 5.11 provides plots of the control input commands implemented directly by the physical components, and Figure 5.12 plots the Frobenius norm of the parameter estimation error matrices, which serves as a measure of the error within the adaptation process.

The first plots shows that the system states remain bounded and maintain reasonable values. The second plots convey that the forces and moments are applied uniformly throughout the signal injection process. The third plot is a direct depiction of the scaled multisine signal inputs. Finally, the fourth plot illustrates that the adaptation process is working correctly, and the parameter estimate errors are diminishing over time. Admittedly, the rate of convergence is rather sluggish. Increasing the adaptive gains, the frequency of the multisine inputs, or the magnitude of the control input scaling, may accelerate the adaptation process, but can also degrade the transient performance if left unchecked. Future research may review alternative embodiments, such as eliminating elements that are known to be zero from the adaptation process, or using an indirect MRAC architecture to first estimate the state space matrices, as illustrated in *Appendix E: System Identification*.

5.3.4 Output Tracking MRAC

The stabilization loop for the unconstrained satellite was shown to effectively reject disturbances, but before implementing coordinated maneuvers with the outer-loop acting on the central hub, the inner-loop for the tether arms needs to demonstrate successful reference tracking. The primary objective of this controller is to articulate the relative positions of each satellite with respect to the central hub, thereby imparting a set of tether forces that can manipulate the translation of the entire TURN vehicle within the inertial frame.

The simulation runs for 20.0 sec, and applies reference commands that are deviated 0.1 m from their trimmed operating points, for each of the three relative translations. The forward translation is influenced by the slower throttle dynamics, so the reference command starts at 1.0 sec, holds the command for a 5.0 sec duration, and returns to neutral for another 5.0 sec. The lateral and vertical translations work with much faster dynamics, so they are each cycled through with 2.0 sec durations. A lateral reference command is implemented between 11.0 sec and 13.0 sec, and allowed to settle between 13.0 sec and 15.0 sec. A vertical reference command is implemented between 15.0 sec and 17.0 sec, and allowed to settle for the remainder of the simulation. The results are displayed in the following three figures. Figure 5.13 shows plots of the deviations from the relative trim points for all twelve system states, Figure 5.14 illustrates the plots of the applied forces and

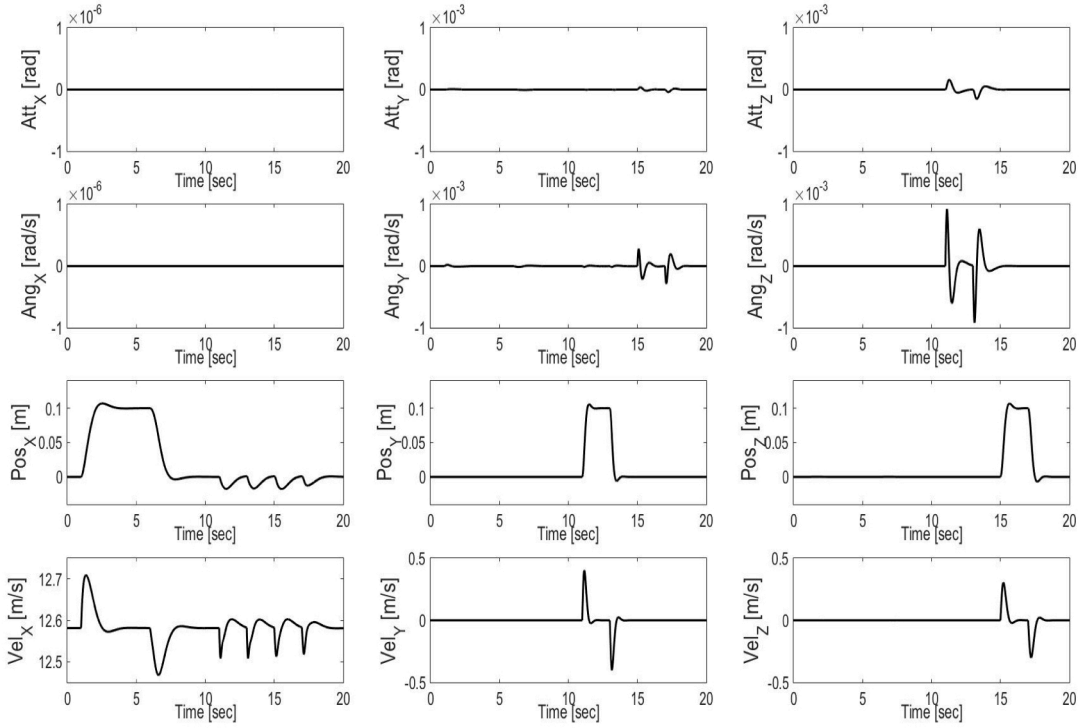

FIGURE 5.13: Tether arm reference tracking: Plots of satellite system states.

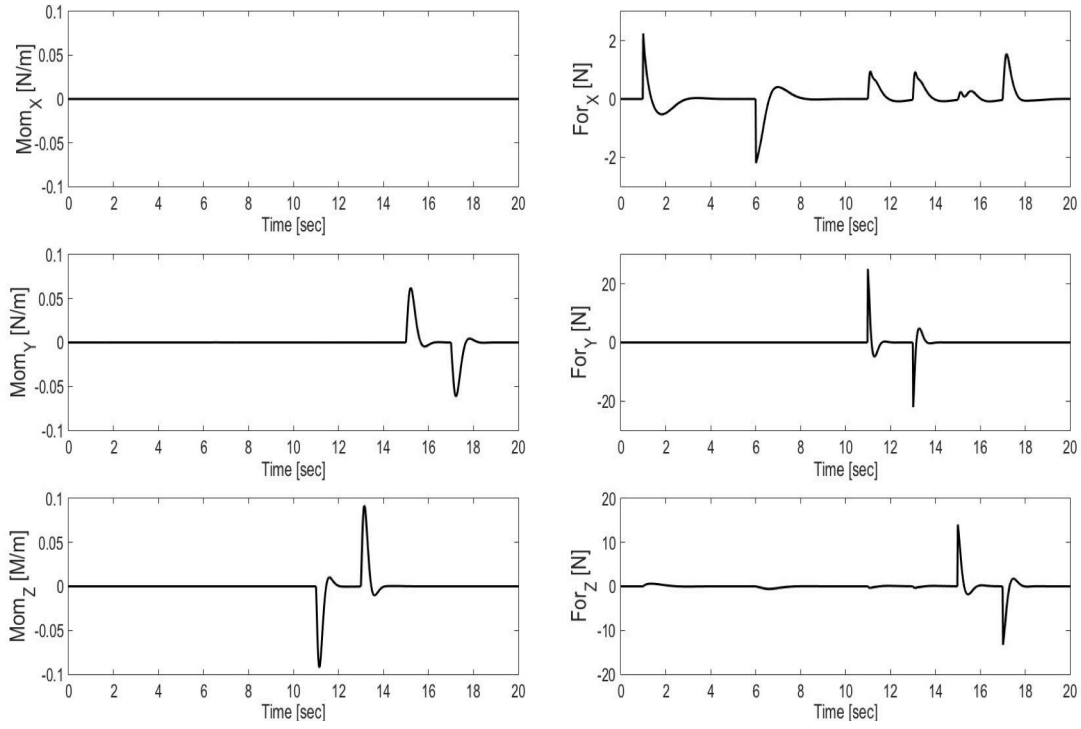

FIGURE 5.14: Tether arm reference tracking: Plots of satellite forces and moments.

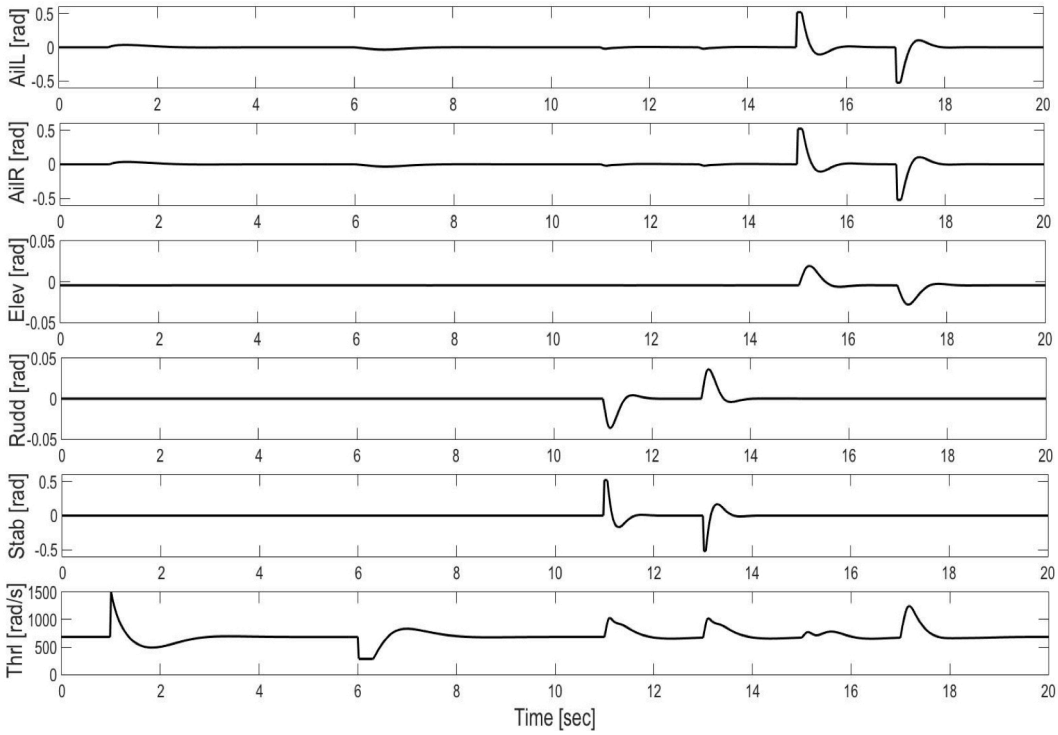

FIGURE 5.15: Tether arm reference tracking: Plots of satellite control inputs.

moments expressed in the satellite body frame, and Figure 5.15 provides plots of the control input commands implemented directly by the physical components.

As before, the throttle commands are susceptible to cross-coupling from control surface articulation. However, the output tracking capability of the relative forward position, exhibits a nearly identical desired response characteristic to that which was designed for the unconstrained satellite subsystem. Notice that there is a slight saturation in the throttle command as the system returns to the neutral position. This is because there is a bias designed into the motor bandwidth, where the thrust is allowed to greatly exceed the trimmed value, but is not allowed to fall below a minimum setting. This means the system is highly capable of tracking fore relative positions, but has a reduced ability to track aft relative positions. Future research may investigate this phenomenon further, and possibly incorporate an air brake utilizing differential rudder commands which would increase the aerodynamic drag and offset the throttle. Lateral and vertical translations perform admirably, achieving their desired system response, with negligible cross-coupling in other states.

Chapter 6

Prototype Development Plan

Theory, analysis, and simulations are all valid endeavors, and serve as extremely useful tools. However, when discussing the merit and feasibility of a completely new concept vehicle, a series of plots will never be as convincing as a prototype system which successfully demonstrates a flight capability. The only way to truly claim the Tethered Uni-Rotor Network (TURN) vehicle is a valid design concept, is to showcase its performance on a physical platform.

Chapter Motivation

While this first research effort constitutes a drastic improvement toward understanding the requirements when implementing a TURN system; at the present moment, none are currently in existence. So, there is still much work to be done. The primary intent of this body of research was to devise a practical controls methodology, and to simulate it on this novel system. With that objective accomplished, this chapter looks toward the future, and identifies the tasks needed to move beyond the analysis phase and into a prototype production program.

A simulation is only as good as the assumptions underlying its model. The presented model is more than sufficient while demonstrating the controller operating during normal flight; however, additional modeling will be needed to accurately represent the transformational flight mechanism, and to aid the design process while advancing to the next level. Even with sophisticated analysis, computational dynamics, and detailed modeling efforts; models always contain some discrepancies from their physical counterparts. Some systems, like conventional aircraft, have a sufficient design history where new designs have a degree of validation through comparison with historical data. However, radically new concepts, like the TURN vehicle, have little basis for comparison, so providing a physical proof of concept is of utmost importance.

Chapter Objectives

The primary goal of this chapter is to outline the future work plan, which will make a case for additional research funding, and will describe the immediate next steps once funding is secured.

The majority of upcoming work focuses on three efforts: increasing the fidelity of the simulation, developing hardware prototypes, and implementing a testing plan utilizing those prototypes.

The main development methodology for this research project follows a spiral design process, which is a cyclic design cycle rather than a traditional linear progression. Instead of developing a single high fidelity model, each cycle utilizes prototypes to obtain a greater understanding of the conceptual system. Early models are simple and only attempt to capture the most dominant system characteristics. Similarly, early prototypes are developed quickly and inexpensively, which serve as a proof of concept. Finally, simulation models are compared against flight data collected from the prototypes, where a validation process is the crucial step moving from one iteration to the next.

This doctoral dissertation represents the first iteration of the simulation development. The immediate next step is to develop a suitable prototype platform that can compliment the theoretical developments. Once the simulation results are compared against the collected flight data, the computer models can be updated, and the next set of highest-risk activities can be addressed in the subsequent prototype. This section outlines the plan of action that guides this cyclic development process. It presents the next round of improvements to the dynamic models within the simulation, outlines the next three envisioned prototype vehicles, and establishes the objectives of the testing plan that will be employed on those systems.

Chapter Outline

Simulations serve as useful design tools, but real system validation comes from hardware demonstrations. The only way to claim that the TURN system works as expected, is to implement the vehicle in the real world. This chapter focuses on improvement to the simulation, upcoming prototype vehicles, and a testing plan that progresses the TURN research and design effort.

Section 6.1 presents upcoming *Simulation Improvements*, which will increase the fidelity of the main TURN analysis tool. It accounts for additional propulsion dynamics, discusses numerical aerodynamic modeling, and addresses aspects of the takeoff/landing and transformational flight process.

Section 6.2 describes the *Prototype Vehicles*, which are used in the spiral development process. It illustrates how each of the vehicles serve a unique purpose for each stage of development, and how they progress from simple models to more sophisticated and higher fidelity designs.

Section 6.3 outlines the *Testing Plan*, which is carried out on each of the prototype vehicles. It showcases that with each new model, a new set of hurdles and uncertainties are introduced, so the procedure follows a natural progression from simple tasks to more risky maneuvers.

6.1 Simulation Improvements

With both time and funding constraints, this research limited its scope of work to the highest risk activity: developing and evaluating a controller architecture for the TURN concept. To that end,

only the most important features of the dynamic model were captured to achieve this goal; including, nonlinear dynamic behavior, interactions between the TURN components, and a reasonable depiction of the system flight characteristics. This is a perfect start to provide a comparison against the first prototype vehicle, but more can be done to aid the future design process. Following sections address: the existing situation and current limitations, and then what needs to be done and how will it be accomplished. These sections describe notable improvements that are planned for the following entities: propulsion model, computational fluid dynamics, flexible non-symmetrical satellite wing, and vertical takeoff and landing (VTOL) and transformational flight capabilities.

6.1.1 Propulsion Model

Very little modeling was developed for the propulsion system. It consists of a basic single-axis model, which instantaneously applies the force and moment as a function of the angular rate. It only accounts for airflow directly aligned with the propeller axis, and it does not characterize or model the downwash field as the channel of air moves through the propeller.

In reality, airflow can come from any direction in three dimensional space, so the propellers will experience lateral forces and moments, as well as blade flapping effects. A motor time constant should be incorporated, which introduces a delay in the system dynamics. Characterizing the propeller downwash field is extremely important, because it describes forced air moving across aerodynamic surfaces. The current model uses relative airspeed to determine forces generated by stabilizers and control surfaces. While this is a perfectly reasonable assumption during forward flight operation, it does not work for VTOL period, where the satellite has no relative velocity.

To overcome this, a more sophisticated motor dynamic model will be incorporated which moves beyond the single axis assumption. It will include a mathematical model of the airflow channel where the velocity of air is both a function of: distance from the prop plane, and distance from the rotation axis. Characterizing the physical aspects of the propeller and motor system will be done with hardware testing. Using a load cell and some sample motors and propellers, the propulsion unit will be ramped up and down, and collected data will characterize the dynamic response.

6.1.2 Computational Fluid Dynamics

One of the great benefits of the current aerodynamic model, is that it is extremely modular and compartmentalized. Mathematical relationships are clearly defined, because everything is modeled using first principles. Calculations are straight-forward, because they are based on simple geometric properties, such as assuming forces are located at the centroids of control surfaces. Implementing an alternative vehicle design is as simple as adjusting some planar coordinates which describe the aerodynamic surface. Finally, it is easier to assess the impact of alternative designs, because each component acts independently from one another.

However, this aerodynamic modeling approach has not been validated against flight data collected from a prototype system. Until a prototype vehicle is built and flown, there is no way to gauge

the accuracy of the simulation, or to known what areas need the most improvement. Even with a comparison to a physical system, there will still be deficiencies within the model, because it does not account for aerodynamic interactions between all the different structures, and it does not represent the airflow across the entire component, just an idealized force acting at a single point.

A supplementary tool to aid the design process will include a computational fluid dynamics (CFD) analysis. For a given satellite layout, while operating at a specified attitude and velocity, and commanding a particular set of control inputs, the CFD model will return force and moment values arising from the aerodynamics across the surfaces of the vehicle. Running this process once for a trimmed condition is manageable, but attempting to run the CFD model in real-time within the dynamic model is unlikely. Therefore, a lookup table will be assembled and added to the dynamic model, which includes discrete entries for all the variables that can be adjusted. Then the simulation simply runs a linear interpolation to obtain values between the those specified. Because building a lookup table is a labor intensive task, it will be reserved for final layout assessments, and correlating flight data from prototype platforms.

6.1.3 Flexible Non-Symmetrical Satellite Wing

Two features are expected to be revised prior to the second generation prototype: the rigidity and symmetry within the satellite wing model. To better focus the research effort on the controls development, these implementations were selected for the first approach, because they are the most straight-forward embodiments. Each satellite is modeled as a rigid body, which is a valid assumption during normal operations when centrifugal stiffening is present. However, when each satellite lacks centrifugal stiffening while in VTOL flight mode, this very long and slender body will be subjected to various bend and twist moments. Furthermore, each satellite is modeled symmetrically from left to right. But, while the system rotates in free flight, the outboard section moves faster than the inboard section, which does not maintain a symmetrical profile. Ideally, a greater portion of the satellite weight should be placed on the outboard section, to gain the most from centrifugal stiffening, which necessitates a non-symmetrical wing planform.

Modeling flexibility within the wing is readily achievable, because the simulation structure is already equipped to account for additional rigid bodies. Each satellite structure can be remodeled using multiple rigid bodies with a prescribed amount of stiffness between each joint. Meanwhile a non-symmetric wing will be designed to achieve better aerodynamic performance, where different motors and propellers will be optimized for their respective relative airflow. Also, the wing will be revised, such that it has different angle of attack and airfoil shapes at different radial lengths, which will further optimize the aircraft aerodynamics.

This will take place after both the CFD analysis and first prototype flights, which will provide greater insight into potential revisions. Then alternative designs will be assessed with the CFD structure, and run within the simulation environment. Finally, these improvements would be implemented on the next generation of prototype model.

6.1.4 Satellite VTOL and Transformational Flight

As previously mentioned, the current model does not include a precise characterization of the airflow through the propulsion system, and forces are only applied at the centroid of aerodynamic surfaces. During takeoff and landing, the satellites are oriented vertically, and remain fairly static during their hover. Because there is no forward velocity, the existing model does not perceive any relative airflow acting across the aerodynamic structures. Thus, the control surfaces have no effect. Similarly, a transformational flight capability depicts the system moving from a vertical orientation through to the forward flight configuration. Because the model cannot accurately depict the satellite VTOL maneuver, it also cannot model the transformational flight process.

Once the propulsion model is revised, and after the CFD analysis has produced a look-up-table for the aerodynamic forces and moments, the model will be in a form that can accurately represent the satellite vehicles operating in their vertical orientation. With those capabilities available, the takeoff and landing simulation for the system can be considered. After takeoff and landing has been successfully simulated, attention will focus on the transformational flight process. A linear piece-wise continuous controller will handle the transition corridor. The system will be trimmed at different forward attitude angles, and controller gains will be obtained for each incremental step. As the vehicle moves through the transition process, each of the linear models, and their respective controller allocations, will be applied to the system until it attains a forward flight configuration.

6.2 Prototype Vehicles

True to the spiral development philosophy, several prototypes are slated to aid the TURN design and analysis. A commercially available acrobatic model aircraft is the easiest and most economical entry point to test new avionics and control theories. A custom half scale prototype with composite construction, more closely resembles the TURN methodology at a manageable scale. A full system demonstrator is the final step to bring the TURN concept vehicle to market. The following subsections describe each prototype vehicle and its purpose within the spiral development cycle.

6.2.1 Acrobatic Model Airplane

The first prototype vehicle embodies the greatest amount of risk, because there is no available flight data to contribute toward the design, thus all preliminary design work is based on unverified simulation models. However, the dynamics within the simulation cannot be validated until the first prototype is flown. Similarly, the avionics hardware and sensors have never been implemented on a real flight platform; they have only been bench tested within a controlled environment. The first prototype vehicle falls into a viscous circle, where it is risky to fly without some validation, but confidence within the components is only attained through flying the system.

Description: To minimize the amount of risk with the first prototype, the selected embodiment is a small commercially available model aircraft; named the *Malibu III*, manufactured by *TechOne*

FIGURE 6.1: The *Malibu III*, manufactured by TechOne Hobby, serves as the initial prototype.

Hobby, and depicted in Figure 6.1. The vehicle is made of very light and forgiving EPP foam, so it is extremely durable and crash resistant. Because it is designed for aerobatic flights, it has a very high power to weight ratio. The system has a 33.2 inch wingspan, is listed as under 175 grams, which is less than a 0.4 pound vehicle weight, and comes equipped with nine inch props and landing gear.

Purpose: The objective of this vehicle is to minimize risk, while developing custom avionics and testing initial controller algorithms. This platform was selected as the first prototype vehicle, because it is mostly assembled and nearly ready to fly out of the box. Plus, it has many desirable features for a maiden prototype platform. As a commercially available system, it represents a completed design with stable and controllable flight characteristics. Its durable construction allows it to withstand mishaps from early flight attempts, and its lightweight is desirable from a safety standpoint. As an aerobatic aircraft, it has a slow flight capability, so the angular rate of the prototype can be reduced while testing new techniques. Although, it does not represent many of the characteristics of the TURN system, it is a very docile system, which is ideal for proving out other unknowns; including the: avionics, data logging, controller design, system identification algorithms, and coordinated maneuvers. Utilizing a ready made vehicle with stable flight characteristics is the ideal means to implement the custom and untested sensors, avionics, hardware, and software.

6.2.2 Half Scale Prototype

Whereas, the first prototype assessed untested avionics and control algorithms on a stable platform; the second prototype takes the next incremental step, and implements a prototype system that more closely mirrors the TURN concept.

Description: The scaled prototype is much more representative of a TURN aircraft design. It has the characteristic flying wing configuration; equipped with dual propulsion units, ailerons, and

vertical stabilizers with rudders, located at each of the wingtips, and a single centrally located elevator. This is expected to be close to a half scale prototype, so its size is still practical for indoor flight testing within a warehouse environment. The wingspan will be about four feet, with sixteen feet of tether, which equates to a total outer diameter of forty feet. To minimize flexibility and increase stability, a slightly smaller aspect ratio, and slightly larger aerodynamic surfaces, are anticipated. The vehicle will be a custom design, fabricated with carbon fiber Kevlar construction, and expected to weight about twenty pounds.

Purpose: The objective of the second prototype is to learn the characteristic aerodynamics of the satellite vehicle, revise the system dynamics within the simulation, and evaluate the effectiveness of the controller designs. Early dynamic models have simplifying assumptions which did not account for all the aerodynamics. Wing tip vortices and interactions between the various surfaces were not modeled. Because the system is rotating, it has differential velocity over the wing surface, which may impact the relative heading of the satellite. Finally, other aerodynamic features that are unique to the TURN system, might not have been accurately depicted. These are significant aerodynamic effects that contributes to the flight capability of the vehicle, and should be accounted for in the simulation model. Comparing the simulation dynamics and the CFD model to the collected flight data, is the best means of gaining confidence within the primary analysis tool. The goal of this prototype is to observe the system dynamics, and refine the simulation and CFD models, to more accurately reflect these aerodynamic features.

6.2.3 Full System Demonstrator

The half scale prototype will shed valuable insight into the vehicle dynamics, which will lead to an improved dynamic model, and a better understanding of the TURN system behavior. A final prototype builds upon that foundation, and delivers a full scale demonstrator, which is able to compete with existing small unmanned aerial vehicle (UAV) systems. The intent of this vehicle is to address lingering concerns prior to developing a commercially available TURN platform.

Description: The following description is based entirely on preliminary analysis work, and is subject to change, once data is collected and evaluated from preliminary prototype models, and after revised simulation and CFD models become available. The full scale TURN vehicle is expected to have an eighty foot diameter, which utilize eight foot wingspan satellites. With a chord length of only five inches, the system will approach an aspect ratio of close to twenty. Control surface positions and sizes may change once new data is received, but they are anticipated to be in nearly the same positions, but have slightly smaller relative sizes, as the half scale prototype. Finally, the hub will be revised to carry a payload and incorporate a retracting mechanism for takeoff and landing.

Purpose: The most obvious purpose of the full system demonstrator, is to showcase a commercially viable product. While, the first prototypes tested hardware, collected aerodynamic flight data, and validated computer models; this vehicle is primarily designed to be representative of a fully completed system. The intent is to investigate the features needed for practical application; such as, degree of flexibility within the slender wing, takeoff and landing capabilities, payload carrying

capacities, flight endurance, and a pilot user interface. This system will follow the same testing procedure as the other prototypes, which will yield valuable information about the vehicle characteristics at this larger size. As a worst case scenario, the collected data will shed insight into what revisions are needed to improve the performance of the vehicle; and if all goes well, this TURN system embodiment will be a formidable competitor within the UAV industry.

6.2.4 Subsequent Prototype Development

The previous three subsections outlined the *Acrobatic Model Airplane*, the *Half Scale Prototype*, and the *Full System Demonstrator*, respectively. These prototypes represent a very reasonable research development path, which is attainable with a relatively modest budget, and has a high chance of success for bringing a commercial product to market. Of course, the most tantalizing aspect of the TURN concept vehicle, is its promise of putting eternal flight within reach. Unfortunately, at this point, there are no formal plans for larger and more elaborate prototypes. However, producing a commercially viable product, which is able to generate revenue and showcase an unprecedented flight capability, is a tremendous milestone. One that would inevitably lead to continued TURN research and development, which would be focused on the eternal flight endeavor.

6.3 Testing Plan

Each prototype platform is a natural progression, moving from simple vehicles to more complex systems, where each new milestone builds upon the previous foundation. For all the prototypes, a nearly identical testing procedure is adopted; which minimizes risk, by first demonstrating fundamental capabilities, and then incrementally advances to more complex maneuvers. This section describes the four major testing progressions applied to each prototype system.

6.3.1 Free Flying Satellite

Testing a new prototype is preformed through incremental steps, to ensure that more risky maneuvers are built upon a firm foundation. Each new round of prototype testing begins with a single unconstrained satellite vehicle; which validates all hardware, sensors, and actuators; and demonstrates the new system in flight. Operating this system utilizes the stabilization control loop, which is the foundation of the entire TURN control methodology. The first series of tests focus on getting the satellite from takeoff all the way through to forward flight.

Hover: Every subsequent test begins with getting the satellites into the air, so hover testing is the first task. Before leaving the safety of the ground, the vehicle is commanded to around 95% of its hover throttle value, and the control gains are evaluated by sending reference commands. If the response looks good, the throttle is increased slightly to just barely attain hover, and then the stabilization response is observed. Finally, the vehicle is elevated above its ground effect, where the controller gains could be further adjusted.

Transition: No flight data will be available, so the transition process is accomplished with small incremental steps. The vehicle is brought into hover, and then commanded to maintain a small forward angle. Flight data is collected for this new equilibrium point, and a custom set of gains are devised for that spot in the transition. The process is repeated for the next incremental forward angle, and continues until the vehicle has reach forward flight. Each of the gains are used in a piecewise linear continuous controller, which is a type of gain scheduling that uses linear interpolation between recorded operating points.

Forward Flight: Once the satellite has completed the transformational flight process, it is ready for the forward flight assessment. The test essentially flies the unconstrained vehicle, as a means of evaluating the handling characteristics and system performance. The goal is to make sure that each degree of freedom within the system has an appropriate amount of control authority available.

6.3.2 Constrained Satellite

This is the least risky tethered test because it only involves a single tethered satellite circumnavigating a fixed point. Now that the satellite is constrained with a tether, the main goals are to collect important system identification data, which characterize the tether dynamics, validate the computer simulation model, and develop the inner-loop control mode used to manage this subsystem. This round of testing uses techniques like; doublets, signal injection, and disturbance rejection.

Doublets: This technique has been utilized since the earliest days of aviation. Doublets are a quick maneuver designed to perturb a single input, and then quickly bring the vehicle back to its steady state. The doublets begin with small magnitudes at low frequencies, and gradually move up to larger command inputs. At some point the doublet will be deemed "too aggressive," at which point the test is complete. The data is post processed and the values of the most aggressive doublets are used to assign limits while designing appropriate control gains for the system.

Signal Injection: Doublets are a quick means of assessing vehicle dynamics and evaluating controller gain selection, but a more thorough system identification process is accomplished with multisine signal injection. This process operates the feedback controlled system, and superimposes a summation of sinusoidal signals on top of the existing control inputs. These signals excite the system dynamics at several frequencies, which generate new measurements that are used in the system identification process. The data is post processed and compared against the the existing simulation model, and revisions are made as needed, until the computer model matches the collected data.

Disturbance Rejection: Having obtained an accurate dynamic description from the signal injection process, the next order of business assesses how robust the system is to disturbances. Wind gusts are the most notable disturbances the system must reject, but generating a static wind condition which acts on the entire vehicle is infeasible, so a series of controlled experiments is presented as an alternative. Consider a wind gust acting on the nose of a satellite, which creates a longitudinal force. An identical type of force can be implemented by adjusting the throttle command; so to mimic this type of disturbance, code is added which alters the motors outside the control loop. The control law is unaware of the motor adjustment, and only acts on the measurements which indicate

a tracking error. Similarly, the elevator and complementary ailerons can be tested by dropping a mass in the middle of a flight, where the decreased payload simulates a force acting in the vertical direction, which the control surfaces must mitigate. These experiments can be easily modeled in the simulation environment, so collected data may further validate the computer model.

6.3.3 Constrained TURN

While the previous tests investigated the behavior of a single tethered satellite vehicle, the constrained TURN tests increase the level of difficulty, by working with four satellites in unison. By adding several tethered vehicles, a new set of complications need to be addressed; however, this series of tests still reduces the amount of risk by constraining the hub. Controlling the complete TURN system requires coordination between all the satellites to achieve the outer-loop control, so the objective of these tests is to evaluate the effectiveness of the controller to simultaneously manage multiple entities. This series of tests investigates coordinated maneuvers; such as, equal spacing, collective commands, and cyclic commands.

Equal Spacing: The first tethered test with multiple vehicles needs to demonstrate an ability to maintain equal spacing. Without this capability, all other coordinated maneuvers are futile. Begin with the satellites in a VTOL hover state, with no rotation about the central hub. Each satellite should be able to hold its respective position. Once the reference signal increases the desired angular rate of the central hub, the satellites begin their forward transformational flight process. The reference command continues to increase, until all the satellites are in their forward flight configurations. Collected data will be analyzed and evaluate how effective the system maintained equal spacing. Any deficiencies or errors will be simulated to observe how those errors would impact an unconstrained system. If the data reflects positively, then the next round of testing begins.

Collective Commands: With equal spacing accomplished, the next tests perform more elaborate coordinated flight maneuvers; starting with collective commands, because they are the easier outer-loop control process. Begin with the slower dynamic response mode. The system starts in its hover equilibrium state, and then a reference command increases the thrust from the propulsion units. The data should demonstrate that all the satellites still maintain equal spacing, and their angular rates and elevation changes happen in unison with one another. Next, consider the faster dynamic mode, elevator commands. Once the system is in equilibrium, the operator increases the elevator reference signal, and the satellites begin to climb together. Collected data will indicate whether the satellites maintain the same elevation and attitude during their ascent.

Cyclic Commands: After demonstrating collective commands, attention is given to cyclic commands. Again, begin with the slower dynamic response mode. Once in hover, the operator issues the command, and the satellites adjust their complementary ailerons cyclically. The data should show that each satellite attains high and low elevations at the same point in the rotation, and that each satellite observes a consistent altitude change while navigating around the hub. Next, test the faster dynamic mode. The system is brought to hover, and the operator issues a cyclic stabilizer

command. Because the pole constrains the translation of the hub, there will be a minimal observable response. However, the collected data should show changes in the satellite roll angle, which would reveal whether the tension on the tether was changed cyclically.

6.3.4 Free Flying TURN

Everything up to this point has paved the way for the pinnacle of the prototype testing: a completely unconstrained free flight of the TURN system. All the restraints have been removed, so the system is fully operational. This series of test marks the completion of each series of prototype, so the information gathered here is intended to aid with the next round of prototype development. Now that the system is flying on its own, the final set of testing focuses on pushing the boundaries of the vehicle capabilities. Assessing how it behaves in the real world, how to improve its performance under ideal conditions, and how to mitigate uncertainty under non-ideal conditions, are the focus of these concluding tests.

Waypoint Navigation: Having a free flying vehicle, leads into the next round of testing: waypoint navigation. Thus far, everything focused on maintaining a hover equilibrium state, so this next test will assess the system dynamics outside of the hover condition. The procedure is extremely straight forward; start the vehicle in one location and command it to go to another point. Prescribed response characteristics are designed into the controller; including, rise time, overshoot, damping ratio, etc. The goal is to compare the physical behavior to the prescribed response and confirm that the controller is implementing the desired closed-loop dynamics.

Optimal Control: Once the vehicle is able to navigate to a desired location, the next most pertinent issue is how efficiently it gets there. Early controllers use pole placement techniques, which exactly dictates the characteristic response of the system. This strategy helped reduced risk with early flights, because the controller had enough authority to overcome any unexpected disturbances or modeling errors. However, this additional responsiveness comes at the price of increased control energy. For a long endurance vehicle, minimizing the control effort is a primary consideration. Rather than using a pole placement feedback controller, the next test will implement an optimized control law where the gains are obtained through a linear quadratic regulator (LQR) design. The experiment runs the system with the same waypoint navigation, but collects data on the control signals used to navigate to that point.

Adaptive Control Assessment: Adaptive control is an important control technique to mitigate modeling uncertainty for both the prototype development and for the final full scale TURN vehicle. Understanding the capabilities and limitations of the adaptive controller helps to ensure stability and to avoid unacceptable transient responses. Previous system identification tests obtained the actual plant dynamics, which can be used as a baseline comparison. For this test, the controller gains are designed with slightly erroneous values. The adaptive controller should recognize discrepancy and adapt to the correct characteristics. Because the correct vehicle dynamics are already known, the performance of the adaptation process can be evaluated against the true parameters.

Chapter 7

Conclusion

If this research document has served its purpose, then there is little need for a lengthy *Conclusion* chapter; rather, all the pertinent points have already been clearly addressed. Thus, this chapter only contains two sections, to complete this document. Section 7.1 provides a *Chapter Recap*, which reiterates the main points from this Tethered Uni-Rotor Network (TURN) dissertation research. It summarizes the motivation and preliminary analysis material from the *Introduction*, the currently available research presented within the *Literature Review*, the multibody dynamic modeling effort developed within the *Plant Development*, the methodology and various control structures derived within the *Controls Analysis*, the assessment of the system performance from the *Simulation Study*, and the future prototype development and testing outlined within the *Prototype Development Plan*. Section 7.2 is a collection *Final Thoughts*, which highlight the importance of this work and how it contributes to society.

7.1 Chapter Recap

Each chapter included a great deal of detail, which provided a complete assessment of the presented research project. Having amassed all the specifics of the development effort, it is prudent to recap the highlights, and to convey a big picture overview of how all the pieces fit together. Following is a summary of the most important points to takeaway from each chapter development.

7.1.1 Introduction

This research document opened with *Chapter 1: Introduction*, which described the desire for attaining eternal flight, and laid the foundation for the remainder of this dissertation project.

First, this chapter provided the motivation for eternal flight, which is the primary focus of the TURN concept system. It discussed existing and future satellite demand, and described the various classes of satellites; including: geosynchronous satellites which have the farthest orbits, low Earth orbit satellites which need an entire fleet to be operational, and atmospheric satellites which

require a currently unrealized eternal flight capability. There is much commercial interest in attaining an eternal flight capability, which is evidenced by the number of current research projects; including; Project Loon, DARPA ISIS and Vulture, QinetiQ Zephyr, and other aerospace company efforts. However, severe limitations are present with existing approaches, which requires a complete paradigm shift to solve this aeronautic challenge.

Then, this chapter introduced the radical new TURN concept vehicle. It discussed the features of glider and helicopter designs, and illustrated how the TURN concept embodies the best of both methodologies. It introduced the TURN vehicle layout, and described modes of operation for: hover, flight, and takeoff and landing. It outlined the prominent design considerations, and touted the primary system benefits; including: high aspect ratios, centrifugal stiffening, aerodynamic efficiency from a tether, high lift-to-drag ratio, and increased payload capacity from a rotating system.

Finally, this chapter presented several alternative embodiments which would directly utilize a TURN methodology. It showcased several various TURN vehicle sizes to meet different mission requirements, and highlighted a particular embodiment that would provide direct competition with existing commercial unmanned aerial vehicle (UAV) platforms. Of the many different applications for such a system, it specifically described how the TURN concept could directly and immediately benefit airborne wind energy (AWE) platforms.

7.1.2 Literature Review

Following the introduction was *Chapter 2: Literature Review*, which presented various bodies of research, and laid the foundation from which this project was built upon.

High-altitude long-endurance (HALE) aircraft have received a great deal of attention in the past years, but only recently have people begun to envision these vehicles as providing an eternal flight capability. The trouble is that a great majority of these designs, simply look to push the envelope of new and exotic structural materials, which are applied to conventional tube-and-wing structures. Many references within the literature cite energy collection and storage as the limiting factors, such that this design methodology has very little chance for success, until both battery and solar cell technologies see substantial breakthroughs.

This chapter also reviewed models developed for tethered systems. As the main entity which ties all of the TURN pieces together, this component required special attention within the simulation environment. However, most of the available research presented on tethered systems, focused on space applications, where forces from gravity and aerodynamic drag were not included within the models. To work around this deficiency, this research looked to an alternative modeling strategy: one that uses multibody dynamics.

Many different methods are available to model multibody dynamic systems. Predominant techniques typically use Kane's method or Lagrangian mechanics, but both strategies require cumbersome derivations which are not easily modified for new or revised models. Others use simplifying

assumptions to link rigid bodies together, but these linearized approaches do not accurately convey the nonlinearities within the simulation environment. This research adopted a novel technique, which encompasses the entire nonlinear system dynamics within a matrix framework, is easily extended to different models and number of rigid body elements, and is suitable for implementation within a numerical simulation routine.

Mitigating modeling uncertainty and unknown aerodynamic properties is handled through adaptive control techniques. Although the goal of adaptive control is to reduce the amount of *a priori* knowledge needed for a dynamic system, many model reference adaptive control (MRAC) designs still need some knowledge of the plant to proceed. An attractive means of incorporating this plant uncertainty within the adaptation process, is to use a decomposition of the high frequency gain (HFG) matrix. Several prior publications on this subject were presented, which served as a starting point for the adaptive controller development applied to the TURN platform.

Finally, several publications from the author were presented. Some were focused on the earliest embodiments of the TURN system, which described the modeling and initial controller designs. Other publications, were originally developed for quadrotor vehicles, but the theoretical derivations for the controller architectures were subsequently utilized within the TURN control loops.

7.1.3 Plant Development

Before diving into the controls analysis, the document covered *Chapter 3: Plant Development*, which provided a complete description of the nonlinear dynamics within the simulation environment.

The TURN system was modeled as various subcomponents. Some served as rigid bodies within the simulation routine, while others were used to represent the forces and moments that arose from the aerodynamics. A complete system overview was provided, which then led into descriptions for the hub, tether, and satellite bodies. Each of the aerodynamic surfaces were accounted for, and assembled together using a modular satellite configuration within the simulation.

After outlining the system model, the research presented the system dynamics, which describe the equations of motion for each component. It presented an overview of how the forces map into moments, and then listed the most common forces acting on each entity. Then it specifically described the forces on the hub, tether and satellite. Finally, it yielded models for the: propulsion system, skin friction drag, lift and drag profiles, and aerodynamic surfaces.

The dynamics were implemented within a multibody dynamic simulation model. This section motivated the particular development path and introduced preliminaries for the derivations. A general structure was presented which began with two rigid bodies, graduated to a multiple rigid body structure, and then presented a technique for redundant state elimination. Finally, it described each of the TURN models used during the simulation study: a single unconstrained satellite, a tethered vehicle, and the full TURN system model.

Identifying equilibrium points required a trimmed vehicle solution, but multibody models have unique hurdles that must be addressed. The research presented the problem formulation which

outlined trimming limitations, an alternative optimization technique, and an overview of the novel process. It described the implementation that was used for a tether force balance, tether projection, satellite force balance, and hub force balance. Then, initial guess values were calculated using the satellite lift force, velocity, and position, which yielded the angular rate and hub anchor forces.

Linearizing multibody problems experience many of the same limitations as trimming. It utilized a Taylor series expansion as the mechanism for the linearization process, and it illustrated how the linearized model forms the state space representation of the system. Finally, the specifics of the linearization process were implemented on the TURN simulation model.

All of the theoretical developments were implemented within a Matlab simulation environment. The sizing and parameters for simulated system were summarized, plots of trimmed systems were displayed, and the state space model used for subsequent controls analysis was provided.

7.1.4 Controls Analysis

The primary concern confronting this concept was addressed in *Chapter 4: Controls Analysis*, which formulated a complete strategy for successfully coordinating all the TURN components.

First, a general description was provided. The control methodology delivered an alternative perspective, redefined standard conventions, outlined translation within the inertial frame, and described how satellites are used to manipulate forces on the hub. Three control loops were defined; such that: stabilization was applied to each satellite, an inner-loop control managed each tether arm, and outer-loop control coordinated the efforts on the central hub. Each of these control loops had a parallel with both the simulation study and the prototype vehicle development.

Then, attributes of the plant were discussed. It described the mathematical model of the plant, and how it is related to the interactor matrix and HFG matrix. An LDS decomposition was presented, which allows for a more flexible MRAC architecture; and the conditions required to implement the controllers, were outlined within the plant assumptions.

Derivations for an LDS based MRAC architecture were presented. It parameterized the control law, and formulated the LDS decomposition process, which was applied to all three TURN control loops. The derivation included an error model for both tracking and parameter error, the adaptive laws to update the parameter estimates, and a stability analysis to ensure closed-loop stability throughout the entire system.

The first assessment was applied to the unconstrained satellite, which is the foundation for all control loop development. It defined the states, inputs, and outputs, which make up the state space model; and presented control input mixing to achieve stronger input/output correlations. Properties including controllability, observability, and the relative gain array, were reviewed; the desired system response was established; and the plant was shown to satisfy the necessary conditions for implementing the controller architectures.

Stabilization of each satellite is accomplished with state feedback MRAC. The availability of all system states for measurement, provides the motivation for using state feedback. A nominal state

feedback controller depicted state tracking, with its matching condition limitations; and then output tracking, which relaxes those matching conditions. Finally, an adaptive state feedback controller design was reviewed, which covered the control structure and provided remarks concerning the performance of such an MRAC architecture.

Managing the tether arms is accomplished with the inner-loop, which uses output feedback MRAC. The relative positions of the satellites are not specifically measured, which provides motivation for using output feedback control. A nominal output feedback controller depicted the reference model, controller structure and parameters, and the fixed control design. Finally, and adaptive output feedback controller was reviewed, which presented the parameter matrices and regressor signal, and commented on the features of incorporating plant uncertainty within the adaptation process.

Coordinating the efforts of multiple tether arms, thus influencing the translation of the central hub, is handled with the outer-loop controller, which uses a novel controls technique adapted from a complementary filter methodology. The motivation for such an approach arises from the two distinct control modes that need to be seamlessly integrated together. Limitations with existing approaches are discussed, followed by the alternative approach utilizing high-pass and low-pass filter techniques. The derivations for a standard complementary filter were provided, and then shown how they were revised and implemented within the TURN controller structure.

7.1.5 Simulation Study

The capabilities of the controller design, were assessed within *Chapter 5: Simulation Study*, which presented numerous simulations of the control strategy applied to the nonlinear system dynamics.

First, a preliminary analysis was performed prior to running the simulations. It introduced the vehicle sizing and parameter values that were implemented within the simulation routine. An unconstrained satellite vehicle was trimmed, which yielded the states and control inputs to maintain a level flight condition. The outcome of the linearization process provided the state space model of the subsystem, which was used to confirm controllability and observability of the satellite vehicle.

The first set of simulations focused on the stabilization controller implemented on the free flying satellite. A desired system response was established for each degree of freedom, which was used to obtain the appropriate controller gains. The controller was implemented on the nonlinear simulation system, where a set of impulse disturbances were used to evaluate the robustness of the controller. A comparison between SISO and MIMO controller performance illustrated the benefits of a multivariable controller architecture.

Then the simulations graduated to the inner-loop control structure, which manages the relative positions of each tether arm. After trimming the tether arm, a set of multisine control inputs were generated to help evaluate the capabilities of the adaptive controller. Signal injection was superimposed with the LDS based MRAC architecture and the parameter convergence was investigated. Finally, a simulation demonstrated the output tracking ability of a satellite to track relative positions which is required for implementing the outer-loop controller.

7.1.6 Prototype Development Plan

This research is only the first step toward eternal flight, so subsequent research efforts are described in *Chapter 6: Prototype Development Plan*, which layout an immediate commercialization development plan by developing a series of prototype vehicles.

The simulation is the primary analysis tool available for the TURN system design, so several improvements are anticipated within the near future. A more accurate depiction of the propulsion model is needed, and a computational fluid dynamics (CFD) analysis will shed insight into unknown aerodynamic features. Future satellite vehicles will utilize a flexible and non-symmetrical wing design, and the vertical takeoff and landing (VTOL) and transformational flight capabilities still need to be addressed.

A spiral development methodology will work with several prototype vehicles, which are designed to mitigate risk through incremental steps. An acrobatic model airplane is the easiest means of testing new avionics, sensors, and controls algorithms. A half scale prototype is more representative of the TURN concept, which will help validate simulation and aerodynamic models. Finally, a full system demonstrator will showcase the capabilities of a commercial TURN unmanned system.

Each new prototype vehicle progresses through a testing plan, which is also designed to mitigate risk through incremental steps. The first set of testing works with a free flying satellite, which is used to evaluate hover, transition, and forward flight capabilities. Next, comes a single constrained satellite, which studies the tether dynamics through doublets, signal injection, and disturbance rejection tests. Multiple satellites make up a constrained TURN system, which demonstrate coordinated maneuvers such as equal spacing, collective commands, and cyclic commands. Finally, a free flying TURN system evaluates system performance with waypoint navigation, optimal control, and adaptive control assessment.

7.2 Final Thoughts

The journey to attaining eternal flight, or even one that just develops a new concept vehicle from scratch, is a long and arduous path. Traditional aircraft design methodologies follow a linear progression which have extremely large upfront costs. These commonly include labor for detailed nonlinear dynamic modeling, hundreds of thousands of dollars spent on scaled wind tunnel prototypes, wind tunnel testing costs at $10k per hour, and months of post processing from a team of engineers. Alternatively, spiral development provides an efficient means of developing new concept aircraft through an iterative design path, which reduces these upfront costs. It addresses the largest concerns, embodied within the lowest risk platforms, learns about the current system, and then makes incremental and manageable improvements over time. The TURN design methodology utilizes such a spiral development process, and this dissertation research represents the first step within that iterative cycle. Although this concept began with no existing foundation, this document provides a comprehensive analysis of the first research effort. It provides a very reasonable

representation of the system dynamics and maintains nonlinearity within the model. Various simulations demonstrated that a viable control strategy can be implemented, where each of the control loops successfully accomplished reference tracking and mitigated unknown disturbances, even in the presence of plant uncertainty. With this foundation in place, the TURN system is ready for the next level of improvements. The next phase of development has manageable milestones and reasonable expectations, because it minimizes risk within both the prototype vehicle design and the testing plan. Continuing the spiral develop process will demonstrate quantifiable results.

In addition to implementing a new spiral development approach, which can be applied to other novel aircraft concept design programs, the modeling and controls effort developed for the TURN system, is equally applicable to other research domains. For instance, the LDS based MRAC derivations were originally developed for a quadrotor platform, but its flexible structure made it equally appealing for all three control loops within the TURN application. The general nature of the derivations allows this approach to be utilized on other types of systems as well. Incorporating the LDS decomposition within the adaptation process, reduced the amount of *a priori* knowledge needed for the plant, allowed the controller to accommodate unmodeled dynamics, and permitted the system to adapt to changing equilibrium points. Similarly, the complementary filter can be adopted for any control problem that needs to efficiently and seamlessly incorporate dual control modes into a single unified architecture. The novel multibody dynamic structure, which encompasses the TURN nonlinear dynamics, is also sufficiently general for other modeling and simulation efforts. Both flexible bodies and entities with articulated joints, can be easily constructed, and then assembled together to model extremely complex systems. The matrix structure is easily modified for revised models, and extremely well suited for numerical environments like Matlab. After presenting this modeling approach at NASA Langley, an identical process is currently used to depict the dynamics of a three-legged robotic lander system, which is part of their asteroid recovery vehicle project.

Attaining eternal flight is an ambitious endeavor, and despite extensive current research efforts, this feat has yet to be realized. It is clear that existing methodologies are not sufficient to attain this goal; rather, a completely new breed of aircraft design is needed. The TURN concept vehicle represents such a paradigm shift. Higher aspect ratio, improved lift-to-drag ratio, benefits of centrifugal stiffening, and an increased payload capacity; are some of the notable benefits this vehicle has to offer. In turn, these benefits lead to: reduced initial and operational costs, VTOL capability for routinely scheduled maintenance, increased number of potential applications, station keeping abilities, and lower signal latency; which are all features that offer better capabilities than our existing satellite technology. This research has demonstrated that a TURN platform is ready to be commercialized in the short run, but the long term implications are far more astounding. Putting this system into practice would not only replace our existing and antiquated satellite network, but could also allow for unprecedented weather observation, enable practical alternative wind energy platforms, deliver internet access across the entire planet, and achieve a milestone in aviation history.

This document closes with several quotes as they pertain to this TURN research project. Albert Einstein is known to have said that, “Problems cannot be solved with the same mindset that created them,” and that “Imagination is more important than knowledge.” Both of these precepts are embodied within this research, where a paradigm shift was needed to conceive of a new approach to

an existing problem, and innovation was needed to put it into practice. As a cofounder of aviation, Wilbur Wright once said, "The desire to fly is an idea handed down to us by our ancestors... who looked enviously on the birds soaring freely through space... on the infinite highway of the air." But even he and his brother had a hard time conceiving of an aircraft capable of transoceanic flight, let alone one with an eternal flight capability. Finally, Robert Browning claimed, "But a man's reach should exceed his grasp," advocating that humanity is constantly striving for the unattainable. But history has shown us, that on rare occasions, the impossible becomes reality.

Appendix A

Control Theory Fundamentals

This appendix introduces concepts that analyze the plant from a controls perspective. It introduces the idea of a plant, and describes the state space and transfer function forms. It covers the characteristic polynomial of the system, the process for determining system eigenvalues, and how those relate to the poles and zeros of the system. Finally, it addresses controllability, observability, and decentralized control.

A.1 Plant Description

The plant is the physical system to be controlled. It is a mathematical model that relates the control inputs $u(t)$ to the system outputs $y(t)$. A linear time-invariant (LTI) model of a physical system is expressed in state space form as

$$\dot{x}(t) = Ax(t) + Bu(t), \quad y(t) = Cx(t) + Du(t) \tag{A.1}$$

where $x(t) \in \mathbb{R}^n$ is the state vector, $u(t) \in \mathbb{R}^m$ is the control input, $y(t) \in \mathbb{R}^q$ is the system output, $A \in \mathbb{R}^{n \times n}$ is the state matrix, $B \in \mathbb{R}^{n \times m}$ is the input matrix, and $C \in \mathbb{R}^{q \times n}$ is the output matrix. The most general form of a state space system includes a feedforward matrix, $D \in \mathbb{R}^{q \times m}$. However, this term does not appear in physical systems, and is dropped from subsequent derivations. The dynamics in (A.1) describes a multiple-input multiple-output (MIMO) system. For single-input single-output (SISO) systems, the control input $u(t)$ and system output $y(t)$ become scalar values, and the B and C matrices reduce to vectors of appropriate dimensions.

A.2 Transfer Function/Matrix

The transfer function $G(s)$ of a LTI state space model expresses the relationship between the control input and the system output of the system with zero initial condition and zero point equilibrium; and can be obtained directly from the state space model. Convert the time domain representation

of (A.1) to the frequency domain, with the Laplace transform

$$sX(s) = AX(s) + BU(s), \quad Y(s) = CX(s) \tag{A.2}$$

solve for $X(s)$ as

$$\begin{aligned} sX(s) - AX(s) &= BU(s) \\ (sI - A)X(s) &= BU(s) \\ X(s) &= (sI - A)^{-1}BU(s) \end{aligned} \tag{A.3}$$

substitute $X(s)$ into the output equation

$$Y(s) = C(sI - A)^{-1}BU(s) \tag{A.4}$$

and define the transfer function $G(s)$ as

$$G(s) = C(sI - A)^{-1}B \tag{A.5}$$

which satisfies the relationship $G(s) = Y(s)/U(s)$ as desired. For a SISO system, $G(s)$ is single a rational polynomial that relates a single input to a single output. For MIMO systems, $G(s)$ becomes a transfer matrix which is populated with rational polynomials within the matrix elements.

A.3 System Eigenvalues

Transfer function $G(s)$ has an equivalent representation formed by replacing the inverse term

$$G(s) = \frac{C[\text{Adj}(sI - A)]B}{\det(sI - A)} = \frac{z(s)}{p(s)}. \tag{A.6}$$

The denominator $p(s) = \det(sI - A)$, called the characteristic polynomial, describes the response characteristics of the system. It is calculated as

$$\begin{aligned} p(s) &= |sI - A| \\ &= \begin{vmatrix} s - a_{11} & -a_{12} & \cdots & -a_{1n} \\ -a_{21} & s - a_{22} & \cdots & -a_{2n} \\ \vdots & & \ddots & \vdots \\ -a_{n1} & -a_{n2} & \cdots & s - a_{nn} \end{vmatrix} \\ &= s^n + p_{n-1}s^{n-1} + \cdots + p_1 s + p_0 \\ &= (s + \lambda_1)(s + \lambda_2)\cdots(s + \lambda_n) \end{aligned} \tag{A.7}$$

and solving for $p(s) = 0$ yields the system eigenvalues, λ_i for $i = 1, 2, ..., n$. Eigenvalues, also called system poles, have real and imaginary parts, and their location in the complex plane dictates

the response characteristics of the system. The real part of a pole, $\texttt{Re}[\lambda_i]$, determines its horizontal position. Poles in the Left Half Plane (LHP) are stable, poles on the vertical axis produce a bounded oscillation, and poles in the Right Half Plane (RHP) are unstable. The imaginary part of a pole, $\texttt{Im}[\lambda_i]$, form complex conjugate pairs above and below the horizontal axis. The greater the magnitude away from the axis, the greater the frequency of oscillation.

A.4 Poles and Zeros

The numerator and denominator polynomials of a SISO transfer function determine the poles and zeros of the system. The roots of the numerator $z(s)$ are system zeroes, and the system poles are the roots of the denominator $p(s)$, which is the characteristic equation. Poles of SISO systems are also the eigenvalues of the state matrix A. Transfer matrix poles and zeros carry slightly different meaning from their transfer function counterparts. For nearly all s, a MIMO transfer matrix $G(s) = Z(s)/p(s)$, has $\texttt{rank}[G(s)] = \texttt{min}\{m, q\}$. System zeros are defined such that $Z(s)$ drops rank, and system poles are $p(s) = \texttt{det}(sI - A) = 0$. The Smith-McMillan Form transforms the transfer matrix $G(s)$ into a useful form for evaluating poles and zeros. Given $\epsilon_i(s)$ and $\delta_i(s)$ are a pair of monic and coprime polynomials, $\epsilon_i(s)$ is a factor of $\epsilon_{i+1}(s)$, and $\delta_i(s)$ is a factor of $\delta_{i-1}(s)$, and $r = \texttt{rank}(Z(s))$, then the Smith-McMillan form of $G(s)$ is described by

$$G_{SM}(s) = \texttt{diag}\left\{ \frac{\epsilon_1(s)}{\delta_1(s)}, \cdots, \frac{\epsilon_r(s)}{\delta_r(s)}, 0, \cdots, 0 \right\}. \tag{A.8}$$

A.5 Controllability

Controllability describes whether the control inputs can influence the states of the system. It is an important tool for system transformations and implementing MIMO state feedback. The controllability matrix $\mathbb{C}$ is given by

$$\mathbb{C} = \left[B,\, AB,\, A^2B, \cdots, A^{n-1}B \right] \in \mathbb{R}^{n \times nm} \tag{A.9}$$

and the system (A, B) is controllable if $\mathbb{C}$ is full rank, because $\texttt{rank}(\mathbb{C}) = n$, signifies that all rows and columns are linearly independent. Controllability indexes perform a bookkeeping function while working with MIMO systems. Define column vectors of B as

$$B = [\, b_1,\, b_2, \cdots, b_m \,], \quad b_i \in \mathbb{R}^n \tag{A.10}$$

then, select the first n linearly independent columns of $\mathbb{C}$, and reorder them as

$$\left[b_1,\, Ab_1, \cdots, A^{\mu_1 - 1}b_1, \cdots, b_m, \cdots, A^{\mu_m - 1}b_m \right] \in \mathbb{R}^{n \times n} \tag{A.11}$$

where $\mu_i,\ i = 1, \ldots, m$ are controllability indexes.

A.6 Observability

Observability describes whether initial states can be inferred indirectly from the system outputs. It is an important tool for state estimation when states are not directly measured. The observability matrix $\mathbb{O}$ is given by

$$\mathbb{O} = \left[C,\, CA,\, CA^2,\, \cdots,\, CA^{n-1} \right]^T \in \mathbb{R}^{nq \times n} \tag{A.12}$$

and the system (A, C) is observable if $\mathbb{O}$ is full rank, because $\texttt{rank}(\mathbb{O}) = n$, signifies that all rows and columns are linearly independent. Observability indexes serve the same function as controllability indexes. Define row vectors of C as

$$C = [\, c_1,\, c_2,\, \cdots,\, c_q,\,]^T, \quad c_i^T \in \mathbb{R}^n \tag{A.13}$$

then, select the first n linearly independent rows of $\mathbb{O}$, and reorder as

$$\left[c_1,\, c_1A,\, \cdots,\, c_1A^{\nu_1 - 1},\, \cdots,\, c_q,\, \cdots,\, c_qA^{\nu_q - 1} \right]^T \in \mathbb{R}^{n \times n} \tag{A.14}$$

where $\nu_i,\ i = 1, \ldots, q$ are observability indexes.

A.7 Decentralized Control

Developing MIMO control theory is more involved than SISO control theory, so applying SISO design techniques to a MIMO system is attractive. Significant coupling between inputs and outputs means SISO techniques are not appropriate. However, when there is strong correlation between input and output pairs, and little cross coupling elsewhere, then decentralized control is a valid technique. The objective is to identify one-to-one mappings between control inputs and system outputs, with little coupling between other inputs and outputs. Strong correlations permit SISO design techniques.

For example, consider a generic system

$$Y(s) = G(s)U(s) \tag{A.15}$$

which can be expanded into

$$\begin{bmatrix} y_1(s) \\ y_2(s) \end{bmatrix} = \begin{bmatrix} g_{11}(s) & g_{12}(s) \\ g_{21}(s) & g_{22}(s) \end{bmatrix} \begin{bmatrix} u_1(s) \\ u_2(s) \end{bmatrix}. \tag{A.16}$$

Decentralized control is appropriate when the elements of $g_{12}(s)$ and $g_{21}(s)$ are "small," because it indicates that $u_1(s)$ maps into $y_1(s)$, and $u_2(s)$ maps into $y_2(s)$. The Relative Gain Array (RGA) is a matrix Λ that quantifies the subjective term "small." Denote the elements of Λ as λ_{ij}, and define them through the relationship

$$\lambda_{ij} = [G(0)]_{ij} \left[G^{-1}(0) \right]_{ji} \tag{A.17}$$

where $G(0)$ is the DC gain of the transfer function, and $G^{-1}(0)$ is its inverse. Then the RGA is described by the matrix

$$\Lambda = \begin{bmatrix} \lambda_{11} & \dots & \lambda_{1m} \\ \vdots & \ddots & \vdots \\ \lambda_{m1} & \dots & \lambda_{mm} \end{bmatrix} \tag{A.18}$$

where large positive terms on the matrix diagonal indicate strong mappings, and nearly zero values for off-diagonal elements imply little coupling between the other input and output channels.

Appendix B

SISO State Feedback

Single-input single-output (SISO) systems have one control input $u(t)$, any number of states $x(t)$, and one system output $y(t)$. These systems are less complex than multiple-input multiple-output (MIMO) systems, so understanding the behavior of the SISO subsystems is a natural progression toward a more complex analysis. State feedback control is a well established control technique, straight forward to implement, and allows for arbitrary selection of the desired system response. Although, state feedback only utilizes a state gain K and a reference gain k, this control technique achieves any desired system response, within the physical limits of the control inputs. The simplicity of the controller, and the flexibility to design a prescribed system response, makes this controller an ideal starting point for many controller designs. This section introduces fundamental concepts needed to understand the theory implementing state feedback control.

B.1 Desired Response

Consider a generic system represented by a second order dynamic model, described by

$$G(s) = \frac{\omega_n^2}{s^2 + 2\zeta\omega_n s + \omega_n^2} \tag{B.1}$$

where ζ and ω_n are the damping ratio and undamped natural frequency, respectively. The characteristic polynomial is described by

$$p(s) = (s + \sigma + \omega j)(s + \sigma - \omega j) \tag{B.2}$$

where Re$[\lambda] = \sigma$, and Im$[\lambda] = \omega$. When designing a feedback controller, it is more convenient to specify the desired dynamics in terms of percent overshoot M_p, and settling time t_s, within 1% of steady state. However, implementing the controller requires knowledge of the system poles. Understanding the relationships between the system dynamics and the pole locations aids the design process. The settling time t_s dictates σ, the percent overshoot M_p yields ζ, and σ and ζ are used to

determine ω and ω_n, from the following relationships

$$\sigma = \frac{4.6}{t_s}, \quad \zeta = \sqrt{\frac{\ln(M_p)^2}{\pi^2 + \ln(M_p)^2}}, \quad \omega_n = \frac{\sigma}{\zeta}, \quad \omega = \omega_n\sqrt{1-\zeta^2}. \tag{B.3}$$

Starting with the desired system characteristics (t_s, M_p, ζ), the previous equations are used to find the system poles (σ, ω), which are needed for control design.

B.2 Canonical Transformation

Before developing the state feedback controller, the system must be transformed into a canonical form. This alternative description is equivalent to the original system, but has a special simplified structure used during the controls development. The plant transfer function $G(s)$, with n internal systems states, is expressed as rational polynomials of $z(s)$ and $p(s)$, with

$$G(s) = \frac{z(s)}{p(s)} = \frac{z_{n-1}s^{n-1} + \cdots + z_1 s + z_0}{s^n + p_{n-1}s^{n-1} + \cdots + p_1 s + p_0} \tag{B.4}$$

which forms an alternative state space realization with transformed matrices of the form

$$\check{A} = \begin{bmatrix} 0 & 1 & & 0 \\ \vdots & & \ddots & \\ 0 & 0 & & 1 \\ -p_0 & -p_1 & \cdots & -p_{n-1} \end{bmatrix}, \quad \check{B} = \begin{bmatrix} 0 \\ \vdots \\ 0 \\ 1 \end{bmatrix}, \quad \check{C}^T = \begin{bmatrix} z_0 \\ z_1 \\ \vdots \\ z_{n-1} \end{bmatrix}. \tag{B.5}$$

The control input can manipulate every state within the model, so the special structure of this realization guarantees the system (A, B) is controllable. An important point to note, is that similarity transforms do not alter the original system eigenvalues. Mappings between the controller canonical form and the original representation, is handled by a transformation matrix $T \in \mathbb{R}^{n\times n}$, where

$$\check{x} = Tx, \quad \check{A} = TAT^{-1}, \quad \check{B} = TB, \quad \check{C} = CT^{-1} \tag{B.6}$$

and the the transformed system is described by

$$\dot{\check{x}}(t) = \check{A}\check{x}(t) + \check{B}u(t), \quad y(t) = \check{C}\check{x}(t). \tag{B.7}$$

Transformation matrix T is obtained with the controllability matrix $\mathbb{C}$. Compute the last row of the controllability matrix inverse with, $t_n = [\,0,\, 0,\, \cdots,\, 1\,]\,\mathbb{C}^{-1}$, then the transformation matrix T is

$$T = \left[\; t_n,\; t_nA,\; \cdots,\; t_nA^{n-2},\; t_nA^{n-1} \;\right]^T \in \mathbb{R}^{n\times n} \tag{B.8}$$

which is used to obtain the transformed state space realization (B.7). The derivation began with a fully controllable realization, then developed the transformation. Therefore, when starting with the transformation to find the canonical form, the system (A, B) must be controllable.

B.3 State Feedback Development

The goal of state feedback is to generate a control input $u(t) \in \mathbb{R}^m$, using direct measurements of the states $x(t) \in \mathbb{R}^n$, to arbitrarily place the poles of the closed-loop system in prescribed locations. With a SISO LTI plant described by

$$\dot{x}(t) = Ax(t) + Bu(t) \tag{B.9}$$

define the control law $u(t)$ as

$$u(t) = Kx(t) + kr(t) \tag{B.10}$$

with bounded reference input $r(t) \in \mathbb{R}$, constant state gain vector $K^T \in \mathbb{R}^n$, and constant reference gain $k \in \mathbb{R}$. Substituting the state feedback control law (B.10) into the plant (B.9), produces the following closed-loop system

$$\dot{x}(t) = (A + BK)\, x(t) + Bkr(t) = \bar{A}x(t) + \bar{B}r(t) \tag{B.11}$$

where

$$\bar{A} = A + BK, \quad \bar{B} = Bk, \tag{B.12}$$

describes the state feedback matching condition. The design task is to find K such that the eigenvalues of the closed-loop system $\lambda_i(A + BK)$ match the eigenvalues of some desired characteristic polynomial $d(s)$, and to find k so the output $y(t)$ tracks a constant reference set point $r(t) = r$. The state gain K determines transient response, the reference gain k dictates the steady state response, and the resultant system follows the matching condition (B.12). When the system is expressed in controller canonical form $(\check{A}, \check{B}, \check{C})$, the closed-loop state matrix $\bar{A}$ is described by

$$\begin{aligned} \bar{A} &= \check{A} + \check{B}\check{K} \\ &= \begin{bmatrix} 0 & 1 & & 0 \\ \vdots & & \ddots & \\ 0 & 0 & & 1 \\ -p_0 + k_0 & -p_1 + k_1 & \cdots & -p_{n-1} + k_{n-1} \end{bmatrix} \end{aligned} \tag{B.13}$$

and the closed-loop characteristic polynomial is

$$\bar{p}(s) = s^n + (p_{n-1} - k_{n-1})s^{n-1} + \cdots + (p_1 - k_1)s + (p_0 - k_0). \tag{B.14}$$

This simplified structure allows for direct matching between coefficients in the closed-loop characteristic polynomial $\bar{p}(s)$, and coefficients in the desired characteristic polynomial $d(s)$

$$d(s) = s^n + d_{n-1}s^{n-1} + \cdots + d_1 s + d_0. \tag{B.15}$$

Select the transformed feedback gain $\check{K}$ as

$$\check{K} = [\ p_0 - d_0,\ \ p_1 - d_1,\ \ \cdots,\ \ p_{n-1} - d_{n-1}\ ] \tag{B.16}$$

which places the closed-loop poles of $\bar{A}$ in the desired locations. Because $\check{K}$ is designed for the canonical form, it must be transformed with $K = \check{K}T$ to work for the original system. The final step determines the reference gain k which achieves steady state set point tracking. The steady state of a system is described by the equilibrium point once the state derivatives settle to zero. The closed-loop state equation is expressed as

$$0 = \bar{A}x_e + \bar{B}r \quad \Rightarrow \quad x_e = -\bar{A}^{-1}\bar{B}r \tag{B.17}$$

and the output equation becomes

$$y_e = Cx_e = -C\bar{A}^{-1}\bar{B}r. \tag{B.18}$$

For y_e to track r, we need $-C\bar{A}^{-1}\bar{B} = 1$, which is equivalent to

$$-C(A + BK)^{-1}Bk = 1. \tag{B.19}$$

Solving for the reference gain k yields

$$k = -[C(A + BK)^{-1}B]^{-1} = -[C\bar{A}^{-1}B]^{-1} \tag{B.20}$$

which forces the steady state system output $y_e(t)$ to track the reference signal $r(t)$.

Appendix C

MIMO State Feedback

The theory for multiple-input multiple-output (MIMO) controllers is more involved than single-input single-output (SISO) controllers, but MIMO control accounts for coupling between inputs and outputs, which offers a more unified response. Most adaptive control and system identification theory is based on MIMO systems, so this controller is the next logical progression. State feedback for MIMO systems maintain the same structure as SISO state feedback. It still only utilizes two gains, and achieves any desired system response. The two gains become matrices K_x and K_r, accounting for additional inputs and outputs. Although the control structure is identical, obtaining the gain matrices requires additional derivations. This section presents the theory for developing MIMO state feedback, selecting a desired system response, and obtaining the gain matrices.

C.1 Theory Overview

Consider a MIMO linear time-invariant (LTI) system described by

$$\dot{x}(t) = Ax(t) + Bu(t), \quad y(t) = Cx(t) \tag{C.1}$$

where system matrices are known and constant, and all states are available for measurement. Define the control law as

$$u(t) = K_x x(t) + K_r r(t) \tag{C.2}$$

with control input $u(t) \in \mathbb{R}^m$, reference signal $r(t) \in \mathbb{R}^m$, state gain matrix $K_x \in \mathbb{R}^{m\times n}$ and reference gain matrix $K_r \in \mathbb{R}^{m\times m}$. Substitute (C.2) into (C.1) to obtain the closed-loop system

$$\dot{x}(t) = (A + BK_x)x(t) + BK_r r(t) = \bar{A}x(t) + \bar{B}r(t) \tag{C.3}$$

where $\bar{A} \in \mathbb{R}^{n\times n}$ and $\bar{B} \in \mathbb{R}^{n\times m}$ are the reference state and input matrices which achieve the desired closed-loop system response. These relationships form the following matching conditions

$$\bar{A} = A + BK_x, \quad \bar{B} = BK_r \tag{C.4}$$

which mirrors the SISO relationships in the previous appendix. The design task is to place the closed-loop eigenvalues, $\lambda_i(\bar{A}) = \lambda_i(A + BK_x)$, at some prescribed locations, and to have the output signal $y(t) \in \mathbb{R}^m$, track a constant reference set point, $r(t) = r$. To implement this control architecture, the system (A, B) must be controllable, with $\texttt{rank}(B) = m$.

C.2 Canonical Transformation

Identical to the SISO development, this process begins by putting the system into a canonical form through a transformation matrix $T \in \mathbb{R}^{n\times n}$. The transformed arrays and the transformed system are identical to those developed for the SISO case in the previous appendix. With (A, B) controllable, a transformation T exists for the MIMO system, such that

$$\check{A} = A_0 + B_0 U T^{-1}, \quad \check{B} = B_0 R \tag{C.5}$$

with

$$A_0 = \texttt{diag}\{\, A_{01},\, A_{02},\, \cdots,\, A_{0m}\,\}, \quad B_0 = \texttt{diag}\{\, B_{01},\, B_{02},\, \cdots,\, B_{0m}\,\} \tag{C.6}$$

where A_{0i} and B_{0i} are given by

$$A_{0i} = \begin{bmatrix} 0 & 1 & 0 & \cdots & 0 \\ 0 & 0 & 1 & & 0 \\ \vdots & & & \ddots & \vdots \\ & & & & 1 \\ 0 & \cdots & & 0 & 0 \end{bmatrix} \in \mathbb{R}^{\mu_i \times \mu_i}, \quad B_{0i} = \begin{bmatrix} 0 \\ 0 \\ \vdots \\ 0 \\ 1 \end{bmatrix} \in \mathbb{R}^{\mu_i} \tag{C.7}$$

for $i = 1, \ldots, m$, where μ_i are controllability indexes.

C.3 Matrix Formulation

Parallel to the SISO derivations, the MIMO theory utilizes a modified controllability matrix as an intermediate step toward finding the gain matrices. Form an auxiliary matrix as

$$M^{-1} = \left[\, b_1,\; Ab_1,\; \cdots,\; A^{\mu_1 - 1} b_1,\; \cdots,\; b_m,\; \cdots,\; A^{\mu_m - 1} b_m \,\right] \in \mathbb{R}^{n\times n} \tag{C.8}$$

and define row vectors as $M = [\, M_1,\, M_2,\, \cdots,\, M_n\,]^T \in \mathbb{R}^{n\times n}$ and $T = [\, T_1,\, T_2,\, \cdots,\, T_m\,]^T \in \mathbb{R}^{n\times n}$. Matrix M determines the sub matrices of T with

$$T_i = \begin{bmatrix} M_{\mu_1 + \cdots + \mu_i} \\ M_{\mu_1 + \cdots + \mu_i} A \\ \vdots \\ M_{\mu_1 + \cdots + \mu_i} A^{\mu_i - 1} \end{bmatrix} \in \mathbb{R}^{\mu_i \times n} \tag{C.9}$$

and populates matrices U and R by

$$U = \begin{bmatrix} M_{\mu_1} A^{\mu_1} \\ M_{\mu_1+\mu_2} A^{\mu_2} \\ \vdots \\ M_{\mu_1+\cdots+\mu_m} A^{\mu_m} \end{bmatrix} \in \mathbb{R}^{m\times n}, \quad R = \begin{bmatrix} M_{\mu_1} A^{\mu_1-1} B \\ M_{\mu_1+\mu_2} A^{\mu_2-1} B \\ \vdots \\ M_{\mu_1+\cdots+\mu_m} A^{\mu_m-1} B \end{bmatrix} \in \mathbb{R}^{m\times m}, \tag{C.10}$$

which yields all the matrices needed to put the system into the canonical form.

C.4 Closed-Loop Response

The closed-loop response is dictated by $\bar{A}$ where

$$\bar{p}(s) = \mathtt{det}(sI - \bar{A}) = s^n + \bar{p}_{n-1}s^{n-1} + \cdots + \bar{p}_1 s + \bar{p}_0 \tag{C.11}$$

and the desired system response is described by

$$d(s) = s^n + d_{n-1}s^{n-1} + \cdots + d_1 s + d_0. \tag{C.12}$$

The closed-loop state matrix $\bar{A}$, indirectly determines the state feedback gain $\check{K}_x$, defined as

$$\check{K}_x = -R^{-1}UT^{-1} + R^{-1}P \tag{C.13}$$

where P is given by

$$P = \begin{bmatrix} e_{\mu_1+1} \\ e_{\mu_1+\mu_2+1} \\ \vdots \\ e_{\mu_1+\cdots+\mu_{m-1}+1} \\ [\, -d_0,\ -d_1,\ \cdots,\ -d_{n-1}\,] \end{bmatrix} \in \mathbb{R}^{m\times n} \tag{C.14}$$

where e_j are the j^{th} row of an $n \times n$ identity matrix, and d_i are the coefficients of the desired characteristic polynomial (C.12). This canonical form leads to

$$\bar{A} = A_0 + B_0 P = A_0 + B_0(UT^{-1} + R\check{K}_x) \tag{C.15}$$

so the closed-loop eigenvalues are given by

$$\lambda_i(\bar{A}) = \lambda_i(\check{A} + \check{B}\check{K}_x) = \lambda_i(A + BK_x) \tag{C.16}$$

where $K_x = \check{K}_x T$, which places the system poles in the desired locations. The final step calculates the reference gain K_r, so the system output $y(t)$ tracks a constant reference set point $r(t) = r$.

Steady state equilibrium is dictated by

$$y_e = -C\left(A + BK_x\right)^{-1} BK_r r \tag{C.17}$$

so, define the reference gain as

$$K_r = -\left[C\left(A + BK_x\right)^{-1} B\right]^{-1} = -\left[C\bar{A}^{-1}B\right]^{-1} \tag{C.18}$$

which forces the steady state system output $y_e(t)$ to track the reference signal $r(t)$.

Appendix D

State Estimation

Up to this point, state feedback theory assumes all states $x(t) \in \mathbb{R}^n$ are available for measurement. In practice, many systems have states that are not directly measured, so full state feedback cannot be directly implemented. State estimation is a powerful control technique that can overcome these short comings. It is designed to make use of all the available measurements and then estimate states that are not measured. The theory is a direct extension of state feedback, so it builds heavily upon the previous foundation. This section introduces the general theory for full state estimation, shows the error reduction process, and expands the theory to a reduced order estimator which only estimates the unknown states.

D.1 Theory Overview

State estimation uses information from the system output $y(t) \in \mathbb{R}^q$, the control input $u(t) \in \mathbb{R}^m$, and the state space matrices (A, B, C), to find the estimate $\hat{x}(t)$ of $x(t)$, such that

$$\lim_{t \to \infty} (\hat{x}(t) - x(t)) = 0 \tag{D.1}$$

exponentially. The dynamics of the multiple-input multiple-output (MIMO) linear time-invariant (LTI) system are still described by

$$\dot{x}(t) = Ax(t) + Bu(t), \quad y(t) = Cx(t) \tag{D.2}$$

but now the control law becomes

$$u(t) = K_x \hat{x}(t) \tag{D.3}$$

which uses the state estimate $\hat{x}(t)$ to calculate the control input $u(t)$. Substituting the control law (D.3) into the plant description (D.2), forms the closed-loop system as

$$\dot{x}(t) = Ax(t) + BK_x \hat{x}(t) + BK_r r(t). \tag{D.4}$$

Now, define the estimation system as

$$\dot{\hat{x}}(t) = A\hat{x}(t) + Bu(t) + K_e\left(C\hat{x}(t) - y(t)\right) \tag{D.5}$$

with initial condition $\hat{x}(0) = \hat{x}_0$, and an estimation gain of $K_e \in \mathbb{R}^{n\times q}$. The estimation system (D.5) has a very specific form. Notice $\hat{y}(t) = C\hat{x}(t)$ is the estimate of $y(t) = Cx(t)$. When the state estimate $\hat{x}(t)$ equals the true state value $x(t)$, then $\hat{y}(t) = y(t)$, the final term becomes zero, and K_e has no influence. Similarly, when the estimate has no error, the other terms in (D.5) reduce to (D.2).

D.2 Error Reduction

The goal is to select K_e so the state estimate $\hat{x}(t)$ tracks the actual state $x(t)$, and maintains stability within the system. Define the estimation error as

$$\tilde{x}(t) = \hat{x}(t) - x(t) \tag{D.6}$$

and solve for its derivative

$$\begin{aligned}
\dot{\tilde{x}}(t) &= \dot{\hat{x}}(t) - \dot{x}(t) \\
&= \left[A\hat{x} + Bu + K_e\left(C\hat{x} - y\right)\right] - \left[Ax + Bu\right] \\
&= A\hat{x} - Ax + K_eC\hat{x} - K_ey \\
&= A(\tilde{x} + x) - Ax + K_eC(\tilde{x} + x) - K_ey \\
&= (A + K_eC)\tilde{x}
\end{aligned} \tag{D.7}$$

The estimation system dynamics are described by $\lambda_i(A + K_eC)$, so the current task is to select K_e to achieve a desired response. Notice the similarity between state estimation $(A + K_eC)$ and state feedback $(A + BK_x)$. Duality between controllability and observability, means selecting K_e follows the same process as selecting K_x. With (A, C) observable, it is known that (A^T, C^T) controllable. The estimation structure is identical to state feedback formulation, so the previous process to find the state feedback gain K_x from (A, B), can find the state estimator gain K_e from (A^T, C^T).

D.3 Reduced Order Estimator

All feedback controlled systems have some states available for measurement, so full order estimators have redundancy while estimating states that are directly measured. A reduced order estimator is more efficient because it uses the direct measurements and only estimates the unknown states. Apply a transformation where T is selected to achieve a special form of $\check{C}$, such that

$$\check{C} = \left[\ I_q,\ 0_{q\times(n-q)}\ \right] \in \mathbb{R}^{q\times n} \tag{D.8}$$

which leads to $\check{x} = [\, x_m^T,\, x_e^T \,]^T$ where $x_m \in \mathbb{R}^q$ are measured states, and $x_e \in \mathbb{R}^{n-q}$ are estimated states. The measured states directly map to the system outputs, so $y = x_m$. The expanded transformed system is described by

$$\begin{aligned} \dot{\check{x}}(t) &= \check{A}\check{x}(t) + \check{B}u(t) \\ \begin{bmatrix} \dot{x}_m \\ \dot{x}_e \end{bmatrix} &= \begin{bmatrix} A_{mm} & A_{me} \\ A_{em} & A_{ee} \end{bmatrix} \begin{bmatrix} x_m \\ x_e \end{bmatrix} + \begin{bmatrix} B_m \\ B_e \end{bmatrix} u \end{aligned} \tag{D.9}$$

where (A_{ee}, A_{me}) must be observable, which is known to be true when (A, C) is observable. The reduced order estimator has a special structure for the transformed measurement matrix $\check{C}$, so the previous estimation system (D.5) cannot be used. Notice that $\check{y} = \check{C}\check{x} = x_m = y$; therefore, $y - \check{C}\check{x} = 0$, so an estimator gain has no influence on this system. To alleviate this concern, select a substitution variable

$$w(t) = x_e(t) + K_o\, x_m(t) \tag{D.10}$$

where $K_o \in \mathbb{R}^{(n-q)\times q}$ and $w(t) \in \mathbb{R}^{n-q}$. Then, the estimated states are determined from the relationship $x_e(t) = w(t) - K_o\, x_m(t)$. The substitution variable dynamics are described by

$$\begin{aligned} \dot{w} &= \dot{x}_e + K_o \dot{x}_m \\ &= [A_{em}x_m + A_{ee}x_e + B_e u] + K_o\,[A_{mm}x_m + A_{me}x_e + B_m u] \\ &= [A_{em}y + A_{ee}(w - K_o y) + B_e u] + K_o\,[A_{mm}y + A_{me}(w - K_o y) + B_m u] \\ &= (A_{ee} + K_o A_{me})\, w + (B_e + K_o B_m)\, u + (A_{em} + K_o A_{mm} - (A_{ee} + K_o A_{me})\, K_o)\, y \end{aligned} \tag{D.11}$$

with $w(0) = w_0$. To evaluate the stability of the substitution variable, solve for $w(t)$ as

$$\begin{aligned} w(t) = \; & e^{(A_{ee}+K_oA_{me})t}w(0) + (sI - A_{ee} - K_oA_{me})^{-1}\,(B_e + K_oB_m)\,[u](t) \\ & + (sI - A_{ee} - K_oA_{me})^{-1}\,(A_{em} + K_oA_{mm} - (A_{ee} + K_oA_{me})\,K_o)\,[y](t) \end{aligned} \tag{D.12}$$

where the stability of $A_{ee} + K_o A_{me}$, ensures that

$$\lim_{t\to\infty} e^{(A_{ee}+K_oA_{me})t}w(0) = 0. \tag{D.13}$$

Define the estimation system as

$$\dot{\hat{x}}_e = [A_{em}x_m + A_{ee}\hat{x}_e + B_e u] + K_o\,[(A_{mm}x_m + A_{me}\hat{x}_e + B_m u) - \dot{x}_m] \tag{D.14}$$

where $\hat{x}_e(t)$ is the current value of the estimated state $x_e(t)$. Just like (D.5), this estimation system has a very special structure. Notice that when the estimate $\hat{x}_e(t)$ equals the true value $x_e(t)$, the last term drops to zero and K_o has no influence on the system. Similarly, when the estimate has zero error, the other terms in (D.14) become the bottom row of (D.9). The estimation error is defined as

$$\tilde{x}_e(t) = \hat{x}_e(t) - x_e(t) \tag{D.15}$$

and the estimation error dynamics are obtained by taking the derivative of (D.15), and substituting in both rows of (D.9) and (D.14). This yields

$$\dot{\tilde{x}}_e(t) = \dot{\hat{x}}_e(t) - \dot{x}_e(t) = (A_{ee} + K_o A_{me})\, \tilde{x}_e(t) \tag{D.16}$$

which also has the same structure as the full state feedback and full state estimator designs. When (A_{ee}, A_{me}) observable, finding the value of K_o from (A_{ee}^T, A_{me}^T) follows an identical procedure as selecting K_x given (A, B), or K_e given (A^T, C^T).

Before closing this appendix, a few comments are in order, which motivate how an output feedback controller is a direct extension of the reduced order estimator architecture. An alternative expression for the substitution variable $w(t)$, as seen in (D.12), can be rewritten as

$$w(t) = \frac{G_u(s)}{\Lambda(s)}[u](t) + \frac{G_y(s)}{\Lambda(s)}[y](t) + e^{(A_{ee}+K_o A_{me})t} w(0) \tag{D.17}$$

where $G_u(s) \in \mathbb{R}^{(n-q)\times m}$, and $G_y(s) \in \mathbb{R}^{(n-q)\times q}$, are polynomial matrices, and

$$\Lambda(s) = \texttt{det}\,(sI - A_{ee} - K_o A_{me}) = s^{n-q} + \lambda_{n-q-1} s^{n-q-1} + \cdots + \lambda_2 s^2 + \lambda_1 s + \lambda_0 \tag{D.18}$$

captures the denominator of the inverse terms. The original control law $u(t) = K_x x(t)$, is now replaced with $u(t) = K_x \hat{x}(t)$, which generates the control signal using the state estimates $\hat{x}(t)$, where $\hat{x}_e(t) = w(t) - K_o y(t)$ and $x_m(t) = y(t)$. In light of (D.17), the control law can be parameterized as

$$u(t) = K_x \hat{x}(t) = \Theta_{\hat{u}} \hat{u}(t) + \Theta_{\hat{y}} \hat{y}(t) + \Theta_y y(t) \tag{D.19}$$

with filtered system signals given by

$$\hat{u}(t) = \frac{g(s)}{\Lambda_0(s)}[u](t), \quad \hat{y}(t) = \frac{g(s)}{\Lambda_0(s)}[y](t) \tag{D.20}$$

which is comprised of a numerator polynomial operator, defined as

$$g(s) = \left[1,\, s,\, s^2,\, \cdots,\, s^{n-q-1}\right]^T \tag{D.21}$$

a chosen monic stable polynomial $\Lambda_0(s)$, of degree $n - q$, with zeros that represent the desired eigenvalues of $A_{ee} + K_o A_{me}$, and

$$\Theta_{\hat{u}} \in \mathbb{R}^{m\times m}, \quad \Theta_{\hat{y}} \in \mathbb{R}^{m\times q}, \quad \Theta_y \in \mathbb{R}^{m\times q} \tag{D.22}$$

which are some constant parameter matrices. This parameterized control law structure will be expanded upon in a subsequent appendix which covers output feedback controller architectures.

Appendix E

System Identification

Thus far, all the controllers have assumed perfect knowledge of the plant dynamics. However, with new and unique vehicles, the dynamics of these system are largely unknown due to their novel design. Modeling provides a good starting point, but when there is very little research and no wind tunnel data to compare against the simulations, system identification can offer an attractive means of validating the dynamics of a prototype system. System identification is a type of adaptive control which uses measured signals to determine system characteristics. Values like polynomial coefficients and elements within state space matrices, can validate computer models and aid with future prototype designs. These architectures are deigned to adjust controller parameters in real time, so the controller starts with an imperfect model, and adapts to the true physical plant. This section introduces the concept of system identification and focuses on adaptive control which performs parameter estimation. It also presents a stability analysis, and the conditions that must be present for the parameters to converge to their true values.

E.1 Parameter Estimation

The purpose of parameter estimation is to obtain unknown values of the plant. This theory builds upon state feedback control, and will yield the values of the elements within the A and B matrices. These values represent the partial derivatives of the system, so their physical significance is especially useful developing prototypes and validating simulations.

The goal of parameter estimation is to generate a control input $u(t) \in \mathbb{R}^m$, using direct measurements of the states $x(t) \in \mathbb{R}^n$, to determine the unknown elements within the state space matrices. Consider a multiple-input multiple-output (MIMO) linear time-invariant (LTI) plant described by

$$\dot{x}(t) = Ax(t) + Bu(t) \tag{E.1}$$

with a full state feedback control law $u(t)$, defined as

$$u(t) = K_x x(t) + K_r r(t) \tag{E.2}$$

with a bounded reference input $r(t) \in \mathbb{R}^m$, a constant state gain matrix $K_x \in \mathbb{R}^{m \times n}$, and constant reference gain matrix $K_r \in \mathbb{R}^{m \times m}$. Let $\hat{A}$ and $\hat{B}$ be the estimates of A and B, respectively. Substitute the matrix estimates into the matching condition, which becomes

$$\bar{A} = \hat{A} + \hat{B}K_x, \quad \bar{B} = \hat{B}K_r \tag{E.3}$$

solve explicitly for $\hat{A}$ and $\hat{B}$ as

$$\hat{A} = \bar{A} - \bar{B}K_r^{-1}K_x, \quad \hat{B} = \bar{B}K_r^{-1} \tag{E.4}$$

and rearrange the control law (E.2) in terms of the reference signal

$$r(t) = -K_r^{-1}K_x x(t) + K_r^{-1}u(t). \tag{E.5}$$

The reference system

$$\dot{\hat{x}}(t) = \bar{A}\hat{x}(t) + \bar{B}r(t) \tag{E.6}$$

is identical to a traditional MIMO state feedback reference system, except the actual states are replaced by reference states $\hat{x}(t)$. Eliminate the state and reference gains by substituting the reference signal (E.5) into reference system (E.6), so that

$$\begin{aligned} \dot{\hat{x}}(t) &= \bar{A}\hat{x}(t) + \bar{B}\left[-K_r^{-1}K_x x(t) + K_r^{-1}u(t)\right] \\ &= \bar{A}\hat{x}(t) + (\bar{A}x(t) - \bar{A}x(t)) - \bar{B}K_r^{-1}K_x x(t) + \bar{B}K_r^{-1}u(t) \\ &= \bar{A}\hat{x}(t) + (\hat{A} - \bar{A})x(t) + \hat{B}u(t). \end{aligned} \tag{E.7}$$

When $\hat{A} = A$, $\hat{B} = B$, and $\hat{x} = x$ the system reduces down to (E.1). This suggests the adaptive laws should update time varying estimates $\hat{A}(t)$ and $\hat{B}(t)$. Designing the adaptive observer requires that $\bar{A}$ is stable, such that all eigenvalues observe $\mathtt{Re}[s] < 0$, and the control input $u(t)$ and state $x(t)$ are bounded. Traditional state feedback ensures these conditions are satisfied, because the closed-loop desired characteristics are reflected in $\bar{A}$, which is designed to be stable. The boundedness of the control input $u(t)$ and the state $x(t)$ were demonstrated in the MIMO state feedback development.

E.2 Estimation Errors

Define the parameter estimate errors as

$$\tilde{A}(t) = \hat{A}(t) - A, \quad \tilde{B}(t) = \hat{B}(t) - B \tag{E.8}$$

with the following column vectors

$$\tilde{A}(t) = [\ \tilde{a}_1(t),\ \cdots,\ \tilde{a}_n(t)\ ], \quad \tilde{B}(t) = [\ \tilde{b}_1(t),\ \cdots,\ \tilde{b}_m(t)\ ]. \tag{E.9}$$

Because A and B are constant, the parameter estimate error derivatives are given by $\dot{\tilde{A}}(t) = \dot{\hat{A}}(t)$ and $\dot{\tilde{B}}(t) = \dot{\hat{B}}(t)$. The state estimate error is defined as

$$\tilde{x}(t) = \hat{x}(t) - x(t) \tag{E.10}$$

with dynamics described by

$$\begin{aligned}\dot{\tilde{x}}(t) &= \dot{\hat{x}}(t) - \dot{x}(t) \\ &= [\bar{A}\hat{x}(t) + (\hat{A}(t) - \bar{A})x(t) + \hat{B}(t)u(t)] - [Ax(t) + Bu(t)] \\ &= \bar{A}\tilde{x}(t) + \tilde{A}(t)x(t) + \tilde{B}(t)u(t).\end{aligned} \tag{E.11}$$

Define the estimation errors $\epsilon(t)$, from the dynamic system as

$$\epsilon(t) = \left[\, \tilde{x}^T,\, \tilde{a}_1^T,\, \cdots,\, \tilde{a}_n^T,\, \tilde{b}_1^T,\, \cdots,\, \tilde{b}_m^T \,\right]^T \in \mathbb{R}^{(1+n+m)n} \tag{E.12}$$

which is used for stability analysis.

E.3 Adaptive Laws

Select an arbitrary square matrix $Q \in \mathbb{R}^{n\times n}$ where $Q = Q^T > 0$. Find $P \in \mathbb{R}^{n\times n}$, which is the solution to the Lyapunov equation $P\bar{A} + \bar{A}^T P = -Q$, where $P = P^T > 0$. Then, the adaptive laws for $\hat{A}(t)$ and $\hat{B}(t)$ are described by

$$\dot{\tilde{A}}(t) = \dot{\hat{A}}(t) = -\Gamma_A P\tilde{x}(t)x^T(t), \quad \dot{\tilde{B}}(t) = \dot{\hat{B}}(t) = -\Gamma_B P\tilde{x}(t)u^T(t) \tag{E.13}$$

where $\Gamma_A, \Gamma_B \in \mathbb{R}^{n\times n}$ are arbitrary constant adaptive gain matrices, such that $\Gamma_A = \Gamma_A^T > 0$ and $\Gamma_B = \Gamma_B^T > 0$.

E.4 Stability Analysis

Define a positive definite function V in terms of the estimation errors $\epsilon(t)$ as

$$V(\epsilon) = \tilde{x}^T P\tilde{x} + \Sigma_A + \Sigma_B \tag{E.14}$$

where

$$\Sigma_A = \sum_{i=1}^{n} \tilde{a}_i^T \Gamma_A^{-1} \tilde{a}_i = \mathtt{tr}\left[\tilde{A}^T \Gamma_A^{-1} \tilde{A}\right], \quad \Sigma_B = \sum_{j=1}^{m} \tilde{b}_j^T \Gamma_B^{-1} \tilde{b}_j = \mathtt{tr}\left[\tilde{B}^T \Gamma_B^{-1} \tilde{B}\right] \tag{E.15}$$

and solve for the derivative of V as

$$\dot{V} = 2\tilde{x}^T P\dot{\tilde{x}} + 2\mathtt{tr}\left[\tilde{A}^T \Gamma_A^{-1} \dot{\tilde{A}}\right] + 2\mathtt{tr}\left[\tilde{B}^T \Gamma_B^{-1} \dot{\tilde{B}}\right]. \tag{E.16}$$

Substituting (E.11) into the first term of (E.16) yields

$$2\tilde{x}^T P\dot{\tilde{x}} = 2\tilde{x}^T P\left[\bar{A}\tilde{x} + \tilde{A}x + \tilde{B}u\right] = 2\tilde{x}^T P\bar{A}\tilde{x} + 2\tilde{x}^T P\tilde{A}x + 2\tilde{x}^T P\tilde{B}u \tag{E.17}$$

which yields three new terms. The first term is

$$2\tilde{x}^T P\bar{A}\tilde{x} = -\tilde{x}^T Q\tilde{x} \tag{E.18}$$

the second term yields

$$\begin{aligned} 2\tilde{x}^T P\tilde{A}x &= 2\mathtt{tr}\left[\tilde{x}^T P\tilde{A}x\right] \\ &= 2\mathtt{tr}\left[x\tilde{x}^T P\tilde{A}\right] \\ &= 2\mathtt{tr}\left[\tilde{A}^T P\tilde{x}x^T\right] \\ &= 2\mathtt{tr}\left[\tilde{A}^T\Gamma_A^{-1}\Gamma_A P\tilde{x}x^T\right] \end{aligned} \tag{E.19}$$

and the third term follows the same derivation

$$2\tilde{x}^T P\tilde{B}u = 2\mathtt{tr}\left[\tilde{B}^T\Gamma_B^{-1}\Gamma_B P\tilde{x}u^T\right]. \tag{E.20}$$

Substitute all the manipulated terms back into (E.16), so $\dot{V}$ becomes

$$\begin{aligned} \dot{V} = &-\tilde{x}^T Q\tilde{x} \\ &+ 2\mathtt{tr}\left[\tilde{A}^T\Gamma_A^{-1}(\Gamma_A P\tilde{x}x^T)\right] + 2\mathtt{tr}\left[\tilde{A}^T\Gamma_A^{-1}(\dot{\tilde{A}})\right] \\ &+ 2\mathtt{tr}\left[\tilde{B}^T\Gamma_B^{-1}(\Gamma_B P\tilde{x}u^T)\right] + 2\mathtt{tr}\left[\tilde{B}^T\Gamma_B^{-1}(\dot{\tilde{B}})\right] \end{aligned} \tag{E.21}$$

where the adaptive laws from (E.13) cancel all of the trace terms leaving

$$\dot{V} = -\tilde{x}^T Q\tilde{x} \tag{E.22}$$

which shows that $\dot{V}$ is negative semi-definite. This means the equilibrium state $\epsilon = 0$ of the closed-loop system is uniformly stable, and the solution $\epsilon(t)$ is uniformly bounded. It also proves that $\tilde{A}(t)$, $\tilde{B}(t)$, and $\dot{\tilde{x}}(t)$ are all bounded. Finally, (E.22) implies that $\tilde{x}(t) \in L^2$, so $\lim_{t\to\infty}\tilde{x}(t) = 0$.

E.5 Parameter Convergence

The stability analysis shows that all the closed-loop signals are bounded; however, Barbălat Lemma does not ensure $\lim_{t\to\infty}\tilde{A}(t) = 0$ and $\lim_{t\to\infty}\tilde{B}(t) = 0$. Ensuring the parameter estimates converge to their true values requires persistent excitation to make the signal "rich" enough. Multisine signal injection accomplishes this task. The process applies sinusoidal control inputs to the system, which excites the system dynamics so the adaptation continues with new measurements. The control

input is persistently exciting if it contains at least $f = n + m + 1$ frequencies. A constant control input contains a single frequency at zero. Sinusoidal inputs with frequency ω and amplitude σ, contribute two frequencies at $\pm\omega$. Therefore, the minimum number of sine inputs f_0 is the smallest integer that satisfies $f_0 \geq (n + m + 1)/2$. Specify the control input as

$$u(t) = \sum_{i=1}^{f_0} \sigma_i \sin(\omega_i t) \tag{E.23}$$

where $\sigma_i \neq 0$, and ω_i are all distinct, for $i = 1, 2, \cdots, f_0$. Once the persistently exciting signal is introduced into the system, $\lim_{t\to\infty} \tilde{A}(t) = 0$ and $\lim_{t\to\infty} \tilde{B}(t) = 0$, exponentially.

Bibliography

Ahrens, Uwe, Moritz Diehl, and Roland Schmehl (eds.) (2013). *Airborne Wind Energy*. Springer Science and Business Media. URL: http://www.springer.com/us/book/9783642399640.

Barr, Alistair and Reed Albergotti (2014, Apr 14). *Google to Buy Titan Aerospace as Web Giants Battle for Air Superiority*. Website. URL: http://www.wsj.com/articles/SB10001424052702304117904579501701702936522.

Cesnik, Carlos E. S. and Weihua Su (2005). "Nonlinear Aeroelastic Modeling and Analysis of Fully Flexible Aircraft". In: *46th AIAA/ASME/ASCE/AHS/ASC Structures, Structural Dynamics and Materials Conference*. Apr 18-21. Austin, TX. URL: http://gust.engin.umich.edu/Papers/2005/AIAA-2005-2169.pdf.

Chen, Yi, Rui Huang, Liping He, Xianlin Ren, and Bin Zheng (2014). "Dynamical Modelling and Control of Space Tethers: A Review of Space Tether Research". In: *Nonlinear Dynamics*. Vol. 77, No. 4, pp. 1077–1099. URL: http://dx.doi.org/10.1007/s11071-014-1390-5.

Costa, Ramon R., Liu Hsu, Alvaro K. Imai, and Petar Kokotovic (2003). "Lyapunov-Based Adaptive Control of MIMO Systems". In: *Automatica*. Vol. 39, No.7, pp. 1251–1257. URL: http://www.sciencedirect.com/science/article/pii/S0005109803000852.

Durham, Wayne (2013). *Aircraft Flight Dynamics and Control*. Hoboken, NJ: John Wiley and Sons. URL: http://www.wiley.com/WileyCDA/WileyTitle/productCd-1118646819.html.

Eshel, Tamir (2013, Aug 13). *Solar HALE Drones Turn into Atmospheric Satellites*. Website. URL: http://defense-update.com/20130813_solar_hale_atmospheric_satellites.html.

Etherington, Darrell (2014, Apr 14). *Google Acquires Titan Aerospace, the Drone Company Pursued by Facebook*. Website. URL: https://techcrunch.com/2014/04/14/google-acquires-titan-aerospace-the-drone-company-pursued-by-facebook/.

Euston, Mark, Paul Coote, Robert Mahony, Jonghyuk Kim, and Tarek Hamel (2008). "A Complementary Filter for Attitude Estimation of A Fixed-Wing UAV". In: *Intelligent Robots and Systems*. Sept 22-26. Nice, France. URL: http://ieeexplore.ieee.org/document/4650766/.

Fletcher, Seth (2008, Mar 6). *DARPA's New Goal: A Plane That Flies for Five Years*. Website. URL: http://www.popsci.com/military-aviation-space/article/2008-03/darpas-new-goal-plane-flies-five-years.

Franklin, Gene F., J. David Powell, and Abbas Emami-Naeini (2010). *Feedback Control of Dynamic Systems*. 6th ed. Upper Saddle River, NJ: Pearson Education. URL: http://www.

mypearsonstore . com / bookstore / feedback – control – of – dynamic – systems – 9780136019695.

Garside, Juliette (2014, Mar 28). *Facebook Buys UK Maker of Solar Powered Drones to Expand Internet*. Website. URL: https://www.theguardian.com/technology/2014/mar/28/facebook-buys-uk-maker-solar-powered-drones-internet.

Goodwin, Graham C., Stefan E. Graebe, and Mario E. Salgado (2001). *Control System Design*. Upper Saddle River, NJ: Prentice Hall. URL: https://www.pearsonhighered.com/program/Goodwin-Control-System-Design/PGM110008.html.

Guo, Jiaxing, Yu Liu, and Gang Tao (2009). "Multivariable MRAC With State Feedback For Output Tracking". In: *IEEE American Control Conference*. Jun 10-12. St Louis, MO. URL: http://ieeexplore.ieee.org/document/5160489/.

Guo, Jiaxing, Gang Tao, and Yu Liu (2011). "A Multivariable MRAC Scheme with Application to a Nonlinear Aircraft Model". In: *Automatica*. Vol. 47, No. 4, pp. 804–812. URL: http://www.sciencedirect.com/science/article/pii/S0005109811000847.

Holt, Jeffery (2017). *Linear Algebra with Applications*. 2nd ed. New York, NY: W. H. Freeman and Company. URL: http://www.macmillanlearning.com/Catalog/product/linearalgebrawithapplications-secondedition-holt.

Hovakimyan, Naira and Chengyu Cao (2010). *L1 Adaptive Control: Guaranteed Robustness with Fast Adaptation*. Philadelphia, PA: Society for Industrial and Applied Mathematics. URL: http://bookstore.siam.org/dc21/.

Hsu, Liu, Ramon R. Costa, Alvaro K. Imai, and Petar Kokotovic (2001). "Lyapunov-Based Adaptive Control of MIMO Systems". In: *IEEE American Control Conference*. Jun 25-27. Arlington, VA. URL: http://ieeexplore.ieee.org/document/945743/.

Hughes, Peter C. (1986). *Spacecraft Attitude Dynamics*. Hoboken, NJ: John Wiley and Sons. URL: http://store.doverpublications.com/0486439259.html.

Imai, Alvaro K., Ramon R. Costa, Liu Hsu, Gang Tao, and Petar Kokotovic (2001). "Multivariable MRAC Using High Frequency Gain Matrix Factorization". In: *IEEE Conference on Decision and Control*. Dec 4-7. Orlando, FL. URL: http://ieeexplore.ieee.org/document/981047/.

Ioannou, Petros and Jing Sun (1996). *Robust Adaptive Control*. Upper Saddle River, NJ: Prentice Hall. URL: http://store.doverpublications.com/0486498174.html.

Johnson, Roger A. (1960). *Advanced Euclidean Geometry*. Mineola, NY: Dover Publications. URL: http://store.doverpublications.com/0486462374.html.

Keshmiri, M., A. K. Misra, and V. J. Modi (1996). "General Formulation for N-body Tethered Satellite System Ddynamics". In: *Journal of Guidance, Control, and Dynamics*. Vol. 19, No. 1, pp. 75–83. URL: http://arc.aiaa.org/doi/10.2514/3.21582.

Khalil, Hassan K. (2002). *Nonlinear Systems*. 3rd ed. Upper Saddle River, NJ: Prentice Hall. URL: https://www.pearsonhighered.com/program/Khalil-Nonlinear-Systems-3rd-Edition/PGM298535.html.

Lardinois, Frederic (2017, Feb 16). *How Alphabet's Project Loon Ballons Learned to Loiter*. Website. URL: https://techcrunch.com/2017/02/16/how-googles-project-loon-balloons-learned-to-loiter/.

Lawson, Charles L. and Richard J. Hanson (1995). *Solving Least Squares Problems*. Orig published by: Prentice Hall, Upper Saddle River, NJ (1974). Philadelphia, PA: Society for Industrial and Applied Mathematics. URL: http://bookstore.siam.org/cl15/.

Mattos, Bento Silva de, Ney R. Secco, and Eduardo F. Salles (2013). "Optimal Design of a High-Altitude Solar-Powered Unmanned Airplane". In: *Journal of Aerospace Technology Management*. Vol. 5, No. 3, pp. 349–361. URL: http://www.jatm.com.br/ojs/index.php/jatm/article/view/223.

Mirkin, Boris M. and Per-Olof Gutman (2005). "Output Feedback Model Reference Adaptive Control for Multi-Input-Multi-Output Plants with State Delay". In: *Systems and Control Letters*. Vol. 54, No. 10, pp. 961–972. URL: http://www.sciencedirect.com/science/article/pii/S0167691105000241.

Morelli, Eugene A. (2000). "Real-Time Parameter Estimation in the Frequency Domain". In: *Journal of Guidance, Control, and Dynamics*. Vol. 23, No. 5, pp. 812–818. URL: http://arc.aiaa.org/doi/abs/10.2514/2.4642.

– (2003). "Multiple Input Design for Real-Time Parameter Estimation in the Frequency Domain". In: *Conference on System Identification*. Aug 27-29. Rotterdam, Netherlands. URL: https://pdfs.semanticscholar.org/5a67/07a6467027d7e4e3df0c0bc2915a3290a942.pdf.

Nickol, Craig L., Mark D. Guynn, Lisa L. Kohout, and Thomas A. Ozoroski (2007). "High Altitude Long Endurance Air Vehicle Analysis of Alternatives and Technology Requirements Development". In: *45th Aerospace Sciences Meeting and Exhibit*. Jan 8-11. Reno, NV. URL: http://arc.aiaa.org/doi/abs/10.2514/6.2007-1050.

Noll, Thomas et al. (2004, Jan). *Investigation of the Helios Prototype Aircraft Mishap*. NASA Mishap Report. URL: https://www.nasa.gov/pdf/64317main_helios.pdf.

Ortega, Romeo, Liu Hsu, and Alessandro Astolfi (2001). "Adaptive Control of Multivariable Systems with Reduced Prior Knowledge". In: *IEEE Conference on Decision and Control*. Dec 4-7. Orlando, FL. URL: http://ieeexplore.ieee.org/document/980846/.

Pepitone, Julianne (2014, Mar 4). *Facebook to Buy Drone Company Titan Aerospace for $60 Million*. Website. URL: http://www.nbcnews.com/tech/social-media/facebook-buy-drone-company-titan-aerospace-60-million-n44056.

Pizarro-Chong, Ary and Arun K. Misra (2008). "Dynamics of Multi-tethered Satellite Formations Containing a Parent Body". In: *Acta Astronautica*. Vol. 63, pp. 1188–1202. URL: http://www.sciencedirect.com/science/article/pii/S0094576508002452.

Ricciardi, Anthony P., Mayuresh J. Patil, Robert A. Canfield, and Ned Lindsley (2013). "Evaluation Quasi-Static Gust Loads Certification Methods for High-Altitude Long Endurance-Aircraft". In: *Journal of Aircraft*. Vol. 50, No. 2, pp. 457–468. URL: http://arc.aiaa.org/doi/abs/10.2514/1.C031872?journalCode=ja.

Ridden, Paul (2010, Dec 29). *World Record For QinetiQ Zephyr UAS Now Official*. Website. URL: http://newatlas.com/qinetiq-zephyr-world-records-ratified/17396/.

Schutte, Aaron D. and Brian A. Dooley (2005). "Constrained Motion of Tethered Satellites". In: *Journal of Aerospace Engineering*. Vol. 18, No. 4, pp. 242–250. URL: http://ascelibrary.org/doi/pdf/10.1061/(ASCE)0893-1321(2005)18%3A4(242).

Selfridge, Justin M. and Gang Tao (2014a). "A Multivariable Adaptive Controller for a Quadrotor with Guaranteed Matching Conditions". In: *IEEE American Control Conference*. Jun 4-6. Portland, OR. URL: http://ieeexplore.ieee.org/document/6859355/.

– (2014b). "A Multivariable Adaptive Controller for a Quadrotor with Guaranteed Matching Conditions". In: *System Science and Control Engineering*. Vol. 2, No. 1, pp. 24–33. URL: http://www.tandfonline.com/doi/pdf/10.1080/21642583.2013.879050.

– (2015a). "Centrifugally Stiffened Rotor: A Complete Derivation and Simulation of the Inner Loop Controller". In: *AIAA Guidance, Navigation, and Control Conference*. Jan 5-9. Kissimmee, FL. URL: http://arc.aiaa.org/doi/abs/10.2514/6.2015-0073.

– (2015b). "Centrifugally Stiffened Rotor: A Complete Derivation of the Plant Model with Nonlinear Dynamics". In: *AIAA Aviation Technology, Integration, and Operations Conference*. Jun 22-26. Dallas, TX. URL: http://arc.aiaa.org/doi/abs/10.2514/6.2015-2735.

– (2016). "Multivariable Output Feedback MRAC for A Quadrotor UAV". In: *IEEE American Control Conference*. Jul 6-8. Boston, MA. URL: http://ieeexplore.ieee.org/document/7524962/.

Stoneking, Eric (2007). "Newton-Euler Dynamic Equations of Motion for a Multi-Body Spacecraft". In: *AIAA Guidance, Navigation and Control Conference and Exhibit*. Aug 20-23. Hilton Head, SC. URL: http://arc.aiaa.org/doi/abs/10.2514/6.2007-6441.

Tao, Gang (2003a). "A Unification of Multivariable MRAC Based on High Frequency Gain Matrix Decompositions". In: *IEEE American Control Conference*. Jun 4-6. Denver, CO. URL: http://ieeexplore.ieee.org/abstract/document/1239708/.

– (2003b). *Adaptive Control Design and Analysis*. Hoboken, NJ: John Wiley and Sons. URL: http://www.wiley.com/WileyCDA/WileyTitle/productCd-0471274526.html.

Teal Group (2015, Aug 14). *Teal Group Predicts Worldwide UAV Production Will Total $93 Billion in Its 2015 UAV Market Profile and Forecast*. Website. URL: http://www.prnewswire.com/news-releases/teal-group-predicts-worldwide-uav-production-will-total-93-billion-in-its-2015-uav-market-profile-and-forecast-300128745.html.

– (2016, Jul 7). *Teal Group Predicts Worldwide Civil UAS Production Will Total $65 Billion in Its 2016 UAS Market Profile and Forecast*. Website. URL: http://www.prnewswire.com/news-releases/teal-group-predicts-worldwide-civil-uas-production-will-total-65-billion-in-its-2016-uas-market-profile-and-forecast-300295255.html.

Woo, Pamela and Arun K. Misra (2013). "Mechanics of Very Long Tethered Systems". In: *Acta Astronautica*. Vol. 87, pp. 153–162. URL: http://www.sciencedirect.com/science/article/pii/S0094576513000568.

Xian-Zhong, Gao et al. (2013). "Parameter Determination for Concept Design of Solar-Powered, High-Altitude Long-Endurance UAV". In: *Aircraft Engineering and Aerospace Technology*. Vol. 85, No. 4, pp. 293–303. URL: http://www.emeraldinsight.com/doi/abs/10.1108/AEAT-Jan-2012-0011.

Xiongfeng, Zhu, Guo Zheng, Fan Rongfei, Hou Zhongxi, and Gao Xianzhong (2014). "How High Can Solar-Powered Airplanes Fly". In: *Journal of Aircraft*. Vol. 51, No. 5, pp. 1653–1659. URL: http://arc.aiaa.org/doi/abs/10.2514/1.C032333.

Zhao, Zhenjun and Gexue Ren (2011). "Multibody Dynamic Approach of Flight Dynamics and Nonlinear Aeroelasticity of Flexible Aircraft". In: *AIAA Journal*. Vol. 49, No. 1, pp. 41–54. URL: http://arc.aiaa.org/doi/abs/10.2514/1.45334?journalCode=aiaaj.

Glossary

adaptive control Control method whereby the controller uses an adaptive update law which is designed to adjust controller parameters that can be initially uncertain or varying over time.

aileron Hinged flight control surface, typically located on the trailing edge of a fixed-wing aircraft, influencing the roll of the vehicle.

airborne wind energy Alternative energy concept where a typical wind turbine is suspended in the air without a tower structure; achieving higher altitudes, and greater velocity and persistence of wind.

airfoil Cross-sectional profile of a wing or rotor, which determines the aerodynamic lift and drag forces acting on the surface.

airship Type of lighter-than-air vehicle that achieves lift using large balloons filled with gas that is less dense than surrounding air.

angle of attack Angle between the chord line of an airfoil and the relative motion between the surface and the surrounding air.

aspect ratio For an aeronautic wing; ratio of its wingspan to its mean chord, such that a long and narrow wing has a high aspect ratio, while a short and wide wing has a low aspect ratio.

atmospheric satellite Aircraft that run for extended periods of time at high atmospheric altitudes, and provide services traditionally found on conventional satellite technology which orbit in space.

attitude Description of the rotational orientation of a vehicle, typically described in terms of roll, pitch, and yaw angles.

bending moment Induced reaction when an external force or moment is applied to a structural member, thus causing the element to bend.

center of gravity Also called *center of mass*; geometric property of an object, which is the unique point where the distributed mass sums to zero, such that an applied force moves the object without rotation.

centrifugal stiffening Design approach utilizing the physical phenomenon where rotating a rigid body element increases the stiffness and structural integrity of the member.

chord Also described as *chord length*; refers to a straight imaginary line connecting the leading and trailing edges of an airfoil.

collective input In rotorcraft terminology; refers to the scenario where all the rotor blades change equally, at the same time, and independently of their rotational position.

complementary filter Signal processing technique, which is the combination of two filtered signals, such that one is subjected to a high-pass filter, and the other is subjected to a low-pass filter.

complementary input Opposite of a *differential input*; type of coupled control input, where a single command adjusts the paired control inputs in the same directions and with equal magnitudes.

computational fluid dynamics Branch of fluid mechanics, that uses numerical techniques, applied to fluid dynamic models, which simulate the interactions between a fluid and a predefined set of boundary surfaces.

control surface Articulating hinged surface intended to deflect airflow across an aerodynamic surface, which alters the attitude of an aircraft.

controllability Property of a dynamic system, where investigating the rank of the controllability matrix, will indicate whether control inputs can influence the states of the system.

cross-coupling Phenomenon in multivariable systems, where an applied input excites some auxiliary outputs, which are not part of the primary input/output channel mapping.

cutoff frequency Boundary within the frequency response of a system, that transitions from a range which allows signals to pass through, into a range where signals are attenuated.

cyclic input In rotorcraft terminology; refers to the scenario where rotor blades change in a sinusoidal manner throughout the cycle, but each has the same disposition at the same rotational position.

decentralized control Controls approach applied to multivariable systems, with strong input/output mappings, and little cross-coupling, where the system is decomposed into several individual SISO controllers.

differential input Opposite of a *complimentary input*; type of coupled control input, where a single command adjusts the paired control inputs with equal magnitudes but in opposite directions.

disk loading Ratio of the weight of the vehicle over the rotor disk area, yielding the average pressure change across the actuator disk.

downwash Change in direction and downward deflection of an airstream by an aircraft wing or helicopter rotor blade, as part of the process for producing lift.

drag Aerodynamic force arising from the pressure distribution over a moving body, acting in the direction of fluid freestream flow.

drag coefficient Dimensionless value, used in the drag equation, to quantify the amount of drag resistance experienced by an object as it moves through a fluid environment.

drag equation Formula used to determine the amount of drag force acting on an object as it moves through a fluid environment.

drone See definition for *unmanned aerial vehicle*.

elevator Hinged flight control surface, typically located on the horizontal stabilizer of an aircraft, which influences pitch of the vehicle.

elevon Type of control surface which combines the functionality of both an elevator and an aileron into a single aerodynamic structure.

elliptic loading Type of of force distribution on an aerodynamic structure that resembles an elliptical shape in the spanwise direction, resulting in the least amount of induced drag acting on the surface.

energy kites Component found on an airborne wind energy device which performs the same function as a traditional wind turbine used to harvest wind energy.

equations of motion Mathematical relationships that represent the dynamic response of a physical system, where its motion is a function of time.

equilibrium point Also called a *trim point*; constant solution to a set of differential equations where the derivatives are exactly zero, thus an operating point where a dynamic system is in a steady state.

eternal flight Currently sought-after capability for aircraft, where solar energy collection during the day is sufficient enough to power the vehicle throughout the night.

Euler angles Set of three angles that dictate a rotation sequence around principle axes, which describes the orientation of one coordinate frame relative to another.

finite element analysis Numerical technique that provides approximate solutions from partial differential equations while analyzing how applied stresses impact a material or object.

fixed-wing Heavier-than-air type of aircraft, such that the wings remain in a static position with respect to the the vehicle, and where the system requires forward airspeed to generate lift.

flying wing Type of tailless fixed-wing aircraft with no definitive fuselage structure, where all the aircraft components are stored within the primary wing structure.

free-space optical Emerging communication technology for telecommunications or computer networking, which wirelessly transmits data using light propagating across free space.

geometric center Also called a *centroid*; mean position of all points in a shape, and conceptually similar to center of gravity, but for a plane figure.

geosynchronous satellite Type of satellite that remains in a geosynchronous orbit, meaning it maintains the same orbital period as the Earth, thereby remaining in a relatively fixed position within the sky.

glider Also described as a *sailplane*; type of fixed-wing aircraft that does not include an engine, and is characterized by high aspect ratio wings and extreme aerodynamic efficiency.

heavier-than-air Type of aircraft, such as airplanes and helicopters, that do not generate lift from buoyant gases, rather they counteract gravity with aerodynamic surfaces or thrust from engines or rotors.

high-altitude long-endurance Description applied to aircraft that fly at very high altitudes and operate for uncharacteristically long periods of time.

high-frequency gain Property of a dynamic system, which defines the gain between the system input and the system output, under the idealized conditions of an infinite input frequency.

high-pass filter Construct which passes signals with frequencies above a defined cutoff frequency, and attenuates signals with frequencies below the cutoff frequency.

human powered aircraft Class of aircraft characterized by a high power-to-weight ratio, which lacks a formal power system, and instead relies on human-power for propulsion.

induced drag Also described as *lift-induced drag*; aerodynamic drag force that arises from an object deflecting airflow to achieve lift.

inner-loop In reference to a traditional aircraft control system; responsible for stabilizing the attitude and angular rates of the vehicle.

laminar flow Describes a scenario in fluid dynamics where a fluid flows in predominantly parallel paths, without disruption between the layers, and lacks eddies or swirls within the flow path.

laminar separation Also called *flow separation*; phenomenon where fluid flow detaches from a boundary surface, and laminar flow paths are replaced with eddies and vortices, resulting in increased drag.

leading edge Foremost edge of an airfoil, thus the section that makes first contact with the airstream.

left half plane Portion of the complex plane, where the real part of the complex number is negative; the entire region left of the vertical axis.

lift Aerodynamic force component which acts perpendicular to the airflow as a fluid moves past the surface of an object; most commonly used on wings to counteract the force of gravity.

lift coefficient Dimensionless value, used in the lift equation, which relates the amount of lifting force exerted on an object, to the fluid density, fluid velocity, and an associated reference area.

lift equation Formula used to determine the amount of lift force acting on an object as it moves through a fluid environment.

lift-to-drag ratio Amount of lift produced from a wing over the amount of aerodynamic drag created while moving through the air; where high lift-to-drag indicates less power yields greater amounts of lift.

lighter-than-air Type of aircraft, such as balloons, nonrigid airships, and dirigibles, which achieve lift by displacing air with a sufficient volume of gas that is less dense than air, thereby creating buoyancy.

linear time-invariant Describes a linear system, which can be characterized entirely by a single impulse response function, and where the output does not depend explicitly on time.

linearization Process that yields a linear approximation from a nonlinear system, which is valid within a small region around the specified operating point.

low earth orbit satellite Satellite system that commonly operates within an altitude range of 400-1000 miles, travels at extremely high speeds, and is not fixed in space in relation to the surface of the earth.

low-pass filter Construct which passes signals with frequencies below a defined cutoff frequency, and attenuates signals with frequencies above the cutoff frequency.

matrix decomposition Also called *matrix factorization*; factorization of a matrix into a product of matrices with a simplified structure, which is often used to implement efficient matrix algorithms.

model reference adaptive control Closed-loop control technique, where a system output is compared to a desired reference model response; based on the error, control parameters are updated through an adaptive law.

multibody dynamics Mathematical relationships that prescribe the motion of a system consisting of several rigid body elements connected together through joints with various degrees of freedom.

multiple-input multiple-output Also known as a *multivariable system*, within the field of controls engineering; refers to a dynamic system that has several control inputs which map to several system outputs.

multirotor Generic term describing any rotorcraft vehicle with more than two rotors; where quadrotor, hexrotor, and octarotor designate multirotor systems with four, six, and eight rotors, respectively.

multisine signal injection Type of supplementary control input, that superimposes a summation of sinusoidal signals, which excite the system dynamics at several frequencies, and facilitate system identification.

observability Property of a dynamic system, where investigating the rank of the observability matrix, will indicate whether initial states can be observed from the system outputs.

outboard horizontal stabilizer Aircraft design technique which places a horizontal stabilizer within the vortex wake of a wingtip; which helps reduce drag, and can contribute additional lift for the vehicle.

outer-loop In reference to a traditional aircraft control system; adjusts the altitude, airspeed, and heading, used for vehicle navigation.

output feedback Similar to *model reference control*; control theory method which applies gains to the system output signals, such that the closed-loop response matches a desired reference model.

output tracking Controls architecture where the control objective is to have each output in the dynamic system track a desired reference output.

parasitic drag Drag force that resists an object moving through a fluid, which generally increases with greater velocities, and is a combination of skin friction drag, form drag, and interference drag.

pitch Rotation of an aircraft about a lateral axis, where the vehicle will nose up/down about an axis running from wing to wing.

planform Layout of the shape or outline of an aircraft wing, as seen from above, and projected onto a horizontal plane.

plant Within controls theory; dynamic system to be controlled, where the relationship between input signals and output signals are modeled through a transfer function or transfer matrix.

pole placement See definition for *state feedback*.

power-to-weight ratio See definition for *specific power*.

prop wash Current of fluid pushed aft by the action of a propeller or rotor, which is a byproduct of thrust generated by a propulsion unit.

quadrotor Type of multirotor aircraft that utilizes four propellers.

relative gain array Matrix from an element-wise product of the transfer function matrix and its inverse transpose; for each input-output, provides a measure coupling and an indication of suitable pairings.

Reynolds number Dimensionless quantity which expresses the ratio of inertial forces to viscous forces, and helps identify the laminar-turbulent transition point.

right half plane Portion of the complex plane, where the real part of the complex number is positive; the entire region right of the vertical axis.

roll Rotation of an aircraft about a longitudinal axis, where the vehicle tilts left/right about an axis running from nose to tail.

rotor disk area Area swept out by the blades of a rotor.

rotorcraft	Heavier-than-air rotary-wing type of aircraft, which uses lift generated by rotor blades spinning about a mast; for example, a helicopter or an autogyro.
rudder	Hinged flight control surface, typically located on the vertical stabilizer of an aircraft, which influences yaw of the vehicle.
ruddevator	Type of control surface which combines the functionality of both a rudder and an elevator into a single aerodynamic structure.
sailplane	See definition for *glider*.
signal latency	Time delay between when a signal originates at the transmitting end, and when it arrives at the receiving end.
single-input single-output	Within controls theory; describes a simple dynamic system with exactly one control input and exactly one system output.
spar	Main structural member in an aerodynamic surface, used predominantly in fixed-wing aircraft, typically running spanwise for the entire length of the surface.
specific power	Used as a measure of performance between alternative vehicle designs; it is the ratio of the system power requirements divided by the weight of the vehicle.
spiral development	Risk-driven research and development process, which at first uses simple models and prototypes, and then incrementally advances to increasingly complex milestones.
stabilizer	Aerodynamic surface used on aircraft to provide longitudinal or directional stability; commonly recognized as the vertical and horizontal tail structure on tube-and-wing style aircraft.
state estimation	Control theory technique where the algorithm yields an estimate of the unknown system state variables.
state feedback	Also referred to as *pole placement*; control theory method which applies gains to the system state signals such that closed-loop poles are moved to prescribed and desirable locations.
state space	Mathematical model of a physical system, where a series of first-order differential equations describe the relationships between the system inputs, states, and outputs.
state tracking	Controls architecture where the control objective is to have each state in the dynamic system track a desired reference state.

state variable	Part of a set of variables, when working with state space form, which mathematically describes the state of a dynamic system.
station-keeping	Describes an ability of a vehicle to maintain a position relative to a reference point; for satellites and aircraft, this typically refers to holding a prescribed orbit or a fixed point over the earth.
steady state	Describes a condition where the system state variables, which dictate the behavior of the plant, are unchanging over time.
system identification	Technique used in control engineering to build mathematical models of physical systems directly from measured data.
tail-sitter	Transformational flight vehicle with VTOL capabilities, where the aircraft takes off and lands on its tail, and rotates to a horizontal disposition for forward flight.
tensegrity	Design methodology that minimizes compressional loads and achieves structural integrity by placing members in tension.
tethered uni-rotor network	Radical new aerial vehicle concept which combines the best attributes of both fixed-wing and rotorcraft features, by forming a single rotor from a network of tethered systems.
thickness-to-chord ratio	Characteristic of an airfoil, which is the ratio between the maximum thickness and its chord length, expressed as a percentage of the chord length.
thrust	Reaction force described by Newton's second and third laws, where a system accelerating mass in one direction, experiences a force of equal and opposite magnitude acting on the body.
thrust vectoring	Control technique where a vehicle changes the direction of thrust to manipulate the attitude or angular rate of the system.
trailing edge	Rearward edge of an airfoil, thus the section that has final contact with the airstream.
transfer function	Mathematical function that relates the single input signal of a SISO system to its single output response.
transfer matrix	Matrix whose elements are populated with transfer functions, which relates the multiple input signals of a MIMO system to the multiple output response.
transformational flight vehicle	Class of aircraft that has the ability to change its configuration or geometry as part of its normal flight operation.

transient state	Describes a condition where the system state variables, which dictate the behavior of the plant, are changing over time.
triangular loading	Type of of force distribution on an aerodynamic structure that resembles a triangular shape in the spanwise direction, resulting in a greater amount of induced drag acting on the surface.
trim point	See definition for *equilibrium point*.
trimming	Process to identify a trim point, which is an equilibrium point.
tube-and-wing	Most commonly used aircraft configuration, easily recognized with wings extending outward from a defined central fuselage.
unmanned aerial vehicle	Commonly known as a *drone*; type of remotely or autonomously operated aircraft without a human pilot aboard.
vertical takeoff and landing	Term that describes a type of aircraft with the ability to hover, and takeoff and land vertically, without the need for a runway.
wing root	Structural connection point found on on fixed-wing aircraft, which secures the wing surface to the fuselage, and generally bears the largest bending moment on the vehicle.
wing spar	Spar structural element specifically located in a wing surface.
wing weight fraction	Characteristic of an aircraft, which is the percentage of the wing weight with respect to the weight of the entire vehicle.
wingspan	Dimension of an aircraft measured from wingtip to wingtip.
yaw	Rotation of an aircraft about its vertical axis, where the vehicle will nose left/right about an axis running up and down.